The relationship of subsurface bubble plumes to wind speed and sea state in the open ocean

Adrian Victor Matei

A thesis presented for the degree of

Doctor of Philosophy

Department of Mechanical Engineering

University College London

January, 2020

Declaration

I, Adrian Victor Matei, confirm that the work presented in this thesis is my own. Where information has been derived from other sources, I confirm that this has been indicated in the thesis.

Abstract

When winds blow over the ocean, surface waves grow as energy and momentum are transferred from the air to the sea surface. The waves steepen as energy is added and may eventually break, generating turbulence and plumes of bubbles in the near-surface ocean. This thesis focuses on measurements made during a six-week research trip in the North Atlantic Ocean, in a wide range of wind speeds (8–30 m/s). The complex effects of wind speed, wave age, wind sea wave height and subsurface turbulence on the structure, penetration depth, duration and production rate of bubble plumes are investigated in this thesis. The major data set used here was collected using an upward-pointing sonar during three separate four-day deployments.

Individual bubble plumes were detected using an algorithm based on simultaneous sonar and resonator acoustic signals from subsurface bubbles. The acoustical backscattering caused by bubble plumes decays approximately exponentially with depth. The decay constant is related to the bubble entrainment in the water column. The entrainment of a larger void fraction may lead to a lower backscattering decay constant due to the possibility of multiple scattering.

Higher wind speed induces younger, rougher waves and higher turbulence, which generate deeper bubble entrainment that promotes longer-lasting plumes ($>$ 100 seconds). The plume production rate is amplified by low-medium wind speeds ($<$ 20 m/s) in a non-linear way, reaching up to 32 plumes per hour. However, at very high winds ($>$ 20 m/s), the plume production rate is significantly reduced to only 8 plumes per hour in the presence of younger less developed seas. The duration variation of these plumes is associated with large scatter. The wave height was found to influence the bubble-plume activity only in a sea state where swell does not contaminate the wind-driven waves. Given the complex and often chaotic sea state in the open ocean, wind speed remains the main factor that controls the bubble plume structure.

During the persistent storms, it is difficult to directly assess the effect of individual breaking waves on subsurface bubble plumes because the upper ocean may become supersaturated with gas, and plumes are often advected from a side into the sonar sample volume. In supersaturated seas (at wind speeds $>$ 20 m/s), the plumes become continuous fields of bubbles persisting for very long times (minutes or tens of minutes), without a clear separation between individual events. The total backscatter distribution along the water column (0–8 metres, which was the distance from the sonar to the sea surface) varies with plume penetration depth. Most

of the backscatter signal (over 90%) is contained in the upper one metre when the plume is shallow and dense, spreading down the water column more evenly as the plume deepens and becomes more acoustically transparent.

Impact Statement

Breaking-wave injected subsurface bubbles can influence the air-sea exchange of Greenhouse gases such as carbon dioxide. These sinking regions are present in almost all oceans, especially in oceanic locations dominated by high winds and rough seas (Takahashi et al., 2002). Knowledge of the detail of ocean bubbles can help reduce the uncertainty of gas fluxes (from the atmosphere to the ocean) at high winds ($> 15\ m/s$). This can have a key impact on the modelling and prediction of gas transfer across the air-sea interface by ocean-atmosphere coupled models, with a net effect on the total carbon dioxide budget in the atmosphere. This important because the ocean can thus regulate the atmospheric carbon dioxide concentration, impacting the climate system. The better uptake of carbon from the atmosphere via bubble injection (but also other shallow injection processes) may also have an impact on deeper sea sequestration of carbon dioxide, with possible effects on marine life (Haugan and Drange, 1992) and ocean acidification.

Bursting bubbles at the sea surface can also eject particles that can electrify the atmosphere (Blanchard, 1963). There are many types and sizes of marine particles that are transported in the atmosphere via bursting bubbles. Most particles are sea salt aerosols, but also biological particles produced by bacteria and algae (Bigg and Leck, 2008). These marine aerosols can serve as cloud condensation nuclei and influence the formation of clouds (O'Dowd and Smith, 1993). The evaporation of sea spray and aerosols above the sea surface can also affect the heat budget in the atmospheric boundary layer. This can influence total heat and energy available for the formation of clouds and weather systems.

Since the bubbles injected in the ocean mostly contain air (oxygen and nitrogen), there are often supersaturated conditions in the ocean that are caused by bubble-mediated gas flux (Woolf, 2005). This can have an influence on the oxygenation of the ocean, with various impacts on marine life such as corals. Moreover, bubble-mediated nitrogen flux can also have an impact on the ratio of nitrogen fixation to denitrification, which influences biological activity in the ocean. This effect has a critical role in determining the net biologically mediated exchange of carbon dioxide between atmosphere and ocean (Falkowski, 1997).

The injection of significant quantities of air as waves break leads to high void fraction in the upper ocean. This limits the usefulness of sonar backscatter measurements of bubbles

because of partial and even total acoustical extinction by high void fraction regions. Consequently, there is a critical threshold above which no acoustical signal can arrive back at the receiver in high void fractions. Bubbles in the ocean can also be photographed, so specialised underwater cameras have been designed to capture bubbles (their size, shape, etc.).

Understanding the meteorological and sea conditions that drive the dynamics of bubbles below breaking waves is essential to better assess all these vast impacts. The results of bubble, wind speed, sea state and breaking-wave measurements from independent sensors, presented in this thesis, contribute to our understanding of some of the physical mechanisms controlling the subsurface bubbles.

Publications

Journal papers

- Blomquist B. W., Brumer S. E., Fairall C. W., Huebert B. J., Zappa C. J., Brooks I. M., Yang M., Bariteau L., Prytherch J., Hare J. E., Czerski H., **Matei A.** and Pascal R. W. (2017), *Advances in quantifying air-sea gas exchange in environmental forcing*, published in Journal of Geophysical Research

- **Matei, A.**, Czerski, H., Brooks, I. M., Gunn, S., Al-Lashi, R., Pascal, R. and Blomquist, B. W., *Dynamics of bubble plumes controlled by wind speed and sea state* (in preparation)

Conference presentations

- **Matei A.**, Czerski H., Al-Lashi R., Gunn S., Brooks I. M., Amison M. J., Pascal R. W., Blomquist B. W., Bariteau L., *Comparison of bubble plume data with foam measurements, gas ux data and aerosol measurements*, AMS 19th Conference on Air-Sea Interaction, 4-8 January, Phoenix, USA, 2015

- **Matei A.**, Czerski H., Gunn S., Brooks I. M., Pascal R. W., Blomquist B. W., *Comparison of bubble plume data with wind/wave parameters, foam measurements, and carbon dioxide concentration*, Air-Sea Gas Flux: Progress and Future Prospects, 6-9 September, Brest, France, 2016

- **Matei A.**, *Big data in physical sciences*, Science & Engineering South, Southampton, UK, September 2015

- **Matei A.**, Departmental PhD conference, Department of Mechanical Engineering, UCL, London, UK, June 2014 (presentation and poster)

- **Matei A.**, Departmental PhD conference, Department of Mechanical Engineering, UCL, London, UK, June 2015 (presentation and poster)

Acknowledgements

During the last five years of my PhD I have learnt the most in my life about science, reality and life, in general. Coming in London and pursuing this PhD was the best decision I could make, helping me to grow as a professional and as a person.

I am very grateful to my supervisor, Helen Czerski, who accepted me as her PhD student. I still remember how happy I was when I received the acceptance email from her. It meant the world for me, and for good reason. Helen invested a lot of interest in guiding me properly, and she thought me how to communicate the science better, both verbally and in writing. Without Helen's key scientific insights for my research, I could have not finish this thesis. Going to sea in North Atlantic with Helen and the rest of the crew, to conduct measurements in storms, was one the most exciting times in my life. I also want to thank my second supervisor, Chris Brierley, who helped a lot in shaping my thesis. I appreciate his intellectual honesty, and I owe him a good deal for making me a better critical thinker and scientific writer. Without the data provided by collaborators from HiWinGS project, my work could not have been done, so I want to thank them all.

Finishing a PhD is never easy. All this time, I felt many types of emotions, like joy, excitement, anger, frustration. I shared all these moments with one special person, my future wife, Andreea Topor, who supported me unconditionally during all this time. I could not have gone through all the ups and downs to finish this thesis without Andreea. I want to thank my mother, Viorica Matei, for always encouraging me to follow my passion. She always supported me and lifted my morale, helping me however she could to get over difficult times. I also want to thank my father, Florin Matei, for teaching me to be more pragmatic and efficient in dealing with situations. Both my parents' affection helped me to keep going and accomplish my goals. I also want to mention my brother, Daniel Matei, and my nephews, Eric and Anais, who are also very dear to me. I want to thank my future mother and father in law, Dana Topor and Mircea Topor, respectively, whom I consider like my parents. Their support and care during my thesis writing-up was essential, and I am very grateful to them.

Great friends, like Simona Cazan and Adrian Cazan, were constantly beside me, offering advice, supporting and helping me to see that life is not so grim, but it can also be real fun. I have spent most of my working days at the office, where friendships were forged. There-

fore, I especially want to thank my good friends and colleagues, John Vardakis and Anjana Kothandaraman, with whom I shared many frustrations, but also moments of inspiration and fun.

x

Contents

List of Figures

List of Tables

Glossary of Terms

α_a	Sound attenuation due to absorption (dB)
α_{bs}	Emprical backscattering coefficient
α_b	Excess attenuation rate per unit distance (dB/m)
α_g	Sound attenuation due to geometric spreading (dB)
α_{PM}	Phillips constant
α_S	Otswald gas solubility
α_s	Sound attenuation due to scattering (dB)
α_t	Total sound attenuation (dB)
α_{wave}	Wave phase (deg)
α_{wind}	Function of wave components and reference wind speed
β	Surface tension (N/m)
β_{bs}	Empirical backscattering coefficient
β_s	Coefficient of wind-induced wave growth
β_t	Dimensionless variable dependent on turbulent water
χ	Frequency ratio
Δf_{wave}	Wave frequency interval (s^{-1} and Hz)
δ	Total damping coefficient
δ_r	Damping coefficient due to acoustic re-radiation
δ_t	Damping coefficient due to thermal dissipation
δ_v	Damping coefficient due to shear viscosity
δ_w	Range of wind-driven waves
ϵ	Extension of a string (m)
$\epsilon_b(c_w)$	Spectral rate of energy loss per unit area per crest velocity (m^{-1} Hz^{-1})

$\epsilon_b(k_{wave})$	Spectral rate of energy loss ($m^2\ s^{-1}$)
ϵ_{Plant}	Empirical coefficient proposed by Plant (1982)
ϵ_{Snyder}	Empirical coefficient proposed by Snyder et al. (1981)
ϵ_t	Turbulent dissipation rate ($m^2\ s^3$)
η_0	Zero up-crossing of random crest elevation (m)
η_{crest}	Random crest elevation (m)
η_{wave}	Random surface elevation (m)
γ	Heat capacity ratio
γ_d	Numerical constant introduced by Phillips (1985)
γ_{enh}	Peak enhancing factor
^{3}He	Helium isotope
Λ	Dimensionless coefficient decribing complex thermal conductivity effects
λ	Acoustic wavelength (m)
$\Lambda_b(c_w)$	Breaking crest length per unit area per crest velocity (s/m^2)
$\bar{f}_0$	Mean zero-crossing wave frequency (s^{-1} and Hz)
$\bar{f}_{\eta^*}$	Mean up-crossing wave frequency through level η^* (s^{-1} and Hz)
$\bar{T}_{\eta^*}$	Mean up-crossing wave period through level η^* (s)
μ	Total compressibility (m^2/N and Pa^{-1})
μ_d	Numerical constant introduced by Phillips (1985)
μ_g	Compressibility of gas (m^2/N and Pa^{-1})
μ_m	Compressibility of mixture (m^2/N and Pa^{-1})
μ_w	Compressibility of water (m^2/N and Pa^{-1})
∇	Nabla operator
ν_w	Kinematic viscosity of seawater (m^2/s)
ω	Acoustic angular frequency (Hz)
ω_R	Acoustic resonance angular frequency (Hz)
Ω_{wc}	Unknown coefficient that encompasses statistical properties of whitecaps
Π_a	Absorption power (J/s)
Π_s	Scattered power (J/s)
ρ	Density (kg/m^3)
ρ^*	Ambient density (kg/m^3)

ρ_a	Density of air (kg/m^3)
ρ_t	Total density (kg/m^3)
ρ_w	Density of water (kg/m^3)
σ_a	Absorption cross-section (m^2)
$\sigma_{bs,full}$	Full backscattering cross-section (m^2)
σ_{bs}	Backscattering cross-section (m^2)
$\sigma_{bs}(sonar)$	Backscattering cross-section in a sonar depth voxel (m^2)
σ_e	Extinction cross-section (m^2)
σ_s	Scattering cross-section (m^2)
τ	Pulse duration (s)
τ_w	Wind shear stress (N/m^2)
θ_{wave}	Wave direction (deg)
θ_{wind}	Wind direction (deg)
a	Bubble radius (m)
A_0	Maximum area of whitecap foam (m^2)
a_0	Bubble radius at equilibrium (m)
$a_{\epsilon 0}$	Bubble radius at non-equilibrium (m)
a_ϵ	Bubble radial displacement (m)
a_f	Final bubble radius (m)
a_i	Initial bubble radius (m)
a_{max}	Maximum bubble radius (m)
a_{min}	Minimum bubble radius (m)
a_{noise}	Proportion of average amplitude of signal noise
a_{src}	Source amplitude parameter
A_T	Area of transducer (m^2)
a_{wave}	Wave amplitude (m)
b	Dimensionless coefficient describing thermal conductivity effects during resonant bubble pulsations
$B(\theta)$	Beam pattern
$B_s(k_{wave})$	Saturation level
B_t	Sonar beam thickness (m)

B_w	Sonar beam width (m)
BL_t	Thermal boundary layer (m)
br	Breaking-wave numerical constant
BSD	Bubble size distribution
BSD_s	Scaled bubble size distribution
c	Sound speed (m/s)
c_0	Bubble-free water sound speed (m/s)
C_α	Empirical coefficient inversely proportional to g^2
C_a	Gas concentration in the air-side (mol/m^3)
C_D	Drag coefficient
$c_{g,x}$	Group velocity in x direction (m/s)
$c_{g,y}$	Group velocity in y direction (m/s)
c_{mhf}	Mixture sound speed at high frequency (m/s)
c_{mlf}	Mixture sound speed at low frequency (m/s)
c_m	Mixture sound speed (m/s)
C_p	Specific heat capacity at constant pressure (J/K)
c_p	Wave phase velocity (m/s)
C_v	Specific heat capacity at constant volume (J/K)
C_w	Gas concentration in the water-side (mol/m^3)
c_w	Wave crest velocity (m/s)
CO_2	Carbon dioxide
d	E-folding depth (m)
d_{bc}	Distance from the bubble centre (m)
D_g	Thermal diffusivity of encapsulated gas (m^2/s)
D_m	Molecular diffusivity (m^2/s)
D_{wave}	Wave duration (s)
E	Particle displacement (m)
$E(k_{wave})$	Energy density per wave number ($kg\ m^3/s^2$ and $J\ m$)
E_0	Acoustic wave amplitude (m)
$E_{k,max}$	Maximum kinetic energy of radially displaced water shell ($kg\ m^2/s^2$ and J)
E_k	Kinetic energy of radially displaced water shell ($kg\ m^2/s^2$ and J)

$E_{net,x}$	Net energy import in x direction ($kg\ m^2/s^2$)
$E_{net,y}$	Net energy import in y direction ($kg\ m^2/s^2$)
$E_{p,max}$	Maximum potential energy of bubble wall ($N\ m$)
E_p	Potential energy of bubble wall ($N\ m$)
E_v	Echo intensity in a voxel
F	Force (N)
f	Acoustic frequency (Hz)
F_a	Force applied to a string (N)
F_b	Bubble restoring force (N)
F_g	Gas flux ($mol\ m^{-2}s^{-1}$)
f_{PM}	Peak Pierson-Moskowitz frequency (s^{-1} and Hz)
f_{RA}	Acoustic resonance frequency in adiabatic conditions (Hz)
f_R	Acoustic resonance frequency (Hz)
F_s	Force exerted by a string (N)
f_{wave}	Wave frequency (s^{-1} and Hz)
f^*_{wave}	Peak wave frequency (Hz)
$Fd(\eta_{crest})$	Cumulative distribution function of wave crests
$fd(\eta_{crest})$	Probability density function of wave crests
$fd(\eta_{wave})$	Gaussian probability density function of the surface elevation
$Fd(H)$	Cumulative distribution function of wave height
$fd(H)$	Probability density function of wave height
FN	False negative
FP	False positive
G	Gain (dB)
g	Gravitational acceleration (m/s^2)
G_d	Software display gain
G_s	Hardware start gain (dB)
G_u	User-defined gain coefficient
H	Wave height (m)
H_{ss}	Significant wave height of swell (m)
H_{sw}	Significant wave height of wind-sea (m)

H_s	Significant wave height (m)
I	Sound intensity ($J/s\ m^{-2}$)
i	Imaginary number
I_N	Noise intensity (dB)
I_p	Incident plane wave intensity ($J/s\ m^{-2}$)
I_S	Signal intensity (dB)
J	Jacobian
j	Stiffness of a string (N/m)
j_b	Bubble stiffness (N/m)
K	Bulk modulus (N/m^2)
k	Acoustic wave number (m^{-1})
$k_{g\ 660}$	Transfer velocity at a Schmidt number $Sc = 660$ (m/s)
K_g	Thermal conductivity of gas ($W/m\ K^{-1}$)
k_g	Gas transfer velocity (m/s)
k_R	Wave number at resonance (m^{-1})
k_{wave}	Wave number (m^{-1})
L	Face length of transducer (m)
l	Acoustic path (m)
L_{bin}	Depth bin length (m)
L_b	Total breaking length per unit area per crest velocity (s/m^2)
L_p	Pulse length (m and cm)
L_{wave}	Wavelength (m)
m	Mass (kg)
m_{0s}	Swell spectral moment (m^2)
m_{0w}	Wind-sea spectral moment (m^2)
m_0	Zeroth-order moment of the variance spectrum (m^2)
M_e	Extinction cross-section per unit volume (m^{-1})
m_n	Moment of the variance spectrum of order n (m^2)
M_v	Backscattering cross-section per unit volume (m^{-1})
m_w	Mass of water displaced from bubble (kg)
$N(a)$	Bubble size distribution (number of bubbles per a per m^3)

$N_{\eta_{crest}>\eta^*}$	Number of up-crossings through level η^*
N_b	Number of quantization levels
N_{crests}	Total number of crests
NL	Noise level (dB)
p	Pressure (N/m^2 and Pa)
$P(\theta)$	Directional pressure amplitude ($N/m^2\ deg^{-1}$ and Pa/deg)
P_0	Pressure amplitude at a reference range (N/m^2 and Pa)
p_0	Reference pressure (N/m^2 and Pa)
p_a	Ambient pressure (N/m^2 and Pa)
P_d	Plume duration (s)
P_f	Plume frequency (h^{-1})
p_g	Equilibrium pressure inside a bubble (N/m^2 and Pa)
p_i	Incident plane pressure wave (N/m^2 and Pa)
p_L	Laplace pressure (N/m^2 and Pa)
p_s	Spherical pressure wave (N/m^2 and Pa)
p_t	Total pressure (N/m^2)
p_w	Equilibrium pressure in water (N/m^2 and Pa)
$Pr\{\eta_{crest} > \eta^*\}$	Probability of wave crests exceeding level η^*
$Pr\{\eta_{crest} \leq \eta^*\}$	Probability of wave crests not exceeding level η^*
$Q_{s,U}$	Source terms of wind generation ($m^2/Hz\ s^{-1}$)
$Q_{s,wc}$	Source terms of dissipation due to whitecapping ($m^2/Hz\ s^{-1}$)
$Q_{s,ww}$	Source terms of wave-wave interaction ($m^2/Hz\ s^{-1}$)
Q_s	Source terms of wave energy density ($m^2/Hz\ s^{-1}$)
R	Range (m)
r	Radius of bubble water shell (m)
R_0	Reference range (m)
$r_{digital}$	Digital resolution (V)
R_H	Wave Reynolds number
$RMSE$	Root mean square error
$S(f_{wave})$	One-dimensional total variance density spectrum (m^2/s)
$S(f_{wave}, \theta_{wave})$	Directional total variance density spectrum ($m^2/Hz\ deg^{-1}$)

$S^*(f_{wave})$	One-dimensional energy density spectrum ($kg\ m^{-2}m^2/Hz\ s^{-2}$)
$S^*(f_{wave}, \theta_{wave})$	Directional total variance density spectrum ($kg\ m^{-2}m^2/Hz\ s^{-2}\ deg^{-1}$)
$S_{1D}(f_{wave})$	One-dimensional variance density spectrum (m^2/s)
$S_{2D}(f_{wave}, \theta_{wave})$	Directional variance density spectrum ($m^2/Hz\ deg^{-1}$)
$S_{JONSWAP}(f_{wave})$	JONSWAP spectrum (m^2/s)
S_{max}	Measured maximum spectral energy ($kg\ m^{-2}m^2/Hz\ s^{-2}$)
S_{max}^{PM}	Pierson-Moskowitz maximum spectral energy ($kg\ m^{-2}m^2/Hz\ s^{-2}$)
$S_{PM}(f_{wave})$	Pierson-Moskowitz fully-developed spectrum (m^2/s)
S_{vb}	Backscattering cross-section per unit volume from measured bubble size distribution (m^{-1})
S_v	Backscattering cross-section per unit volume in a sonar voxel (m^{-1})
$S_v(0)$	Surface backscattering level (m^{-1})
Sc	Schmidt number
SD	Standard deviation
SL	Sound pressure level (dB)
SNR	Signal-to-noise ratio (dB)
t	Time (s)
$T(k_{wave})$	Transfer coefficient as a function of wave number
T_0	Zero-crossing wave period (s)
t_r	Return time (s)
t_w	Whitecap decay time (s)
TL	Transmission loss (dB)
TL_b	Bubble transmission loss (dB)
TN	True negative
TP	True positive
TS	Target strength (dB)
u	Particle velocity (m/s)
u_*	Friction velocity (m/s)
U_{10N}	Neutral wind speed at 10 metres height (m/s)
U_{10}	Wind speed at 10 metres height (m/s)
V	Fluid volume (m^3)

V_{b0}	Bubble gas volume at equilibrium (m^3)
$V_{b\epsilon}$	Bubble gas volume at non-equilibrium (m^3)
V_b	Bubble gas volume (m^3)
V_f	Void fraction
v_j	Jet velocity on wave face (m/s)
V_{voxel}	Volum of sonar voxel (m^3)
v_w	Velocity of bubble water shell (m/s)
w_d	Empirical coefficient introduced by Phillips (1985)
W_f	Whitecap fraction
X	Thermal diffusivity ratio
X_0	Sonar calibration parameter
Y_1	Incident plane wave amplitude (m)
Y_2	Spherical wave amplitude (m)
$Y_{enh}(f_{wave})$	Peak enhancing function
Z	Acoustic imepdance ($N\ s/m^5$)
z	Depth (m)
z_{bl}	Bubble layer depth (m)
ADC	Analog-to-digital converter
ADCP	Acoustic Doppler Current Profiler
ADV	Acoustic Doppler velocimetre
CIRES	Cooperative Institute for Research in Environmental Sciences
CTD	Conductivity, temperature and depth
DMS	Dimethyl sulphide
ECMWF	European Centre for Medium-Range Weather Forecast
ESRL/PSD	Earth System Research Laboratory's Physical Sciences Division
GPS	Global Positioning System
HiWinGS	High Wind Gas Exchange Study
JONSWAP	JOint North Sea WAve Project
NOAA	National Oceanic and Atmospheric Administration
NOC	National Oceanography Centre
PML	Plymouth Marine Laboratory

R/V	Research vessel
SST	Sea surface temperature
TVG	Time varying gain
UK	United Kingdom
USA	United States of America

Chapter 1

Introduction

1.1 Motivation

As wind exerts stress over the ocean surface, the ocean waves grow and become steeper, so they have an increased likelihood of breaking. Wind stress causes vertical flux of horizontal momentum across the air-sea interface (Geernaert, 1990); e.g. a breaking wave generates a region of mixed air and water, which carries additional horizontal and vertical velocity as it is injected into the upper ocean (Holthuijsen, 2007). The wave boundary layer is a shallow part of the atmospheric boundary layer where air flow is shaped by the waves and where the air-sea drag cannot be neglected. This momentum transfer occurs between the wave boundary layer and the sea surface. A net transfer of momentum from the wave boundary layer to the sea surface is associated with an increase of the roughness at the sea surface (Donelan et al., 1993), and turbulent kinetic energy is enhanced within the shallow subsurface layer. The surface breaking waves usually entrain air in the form of bubble plumes (mixture of gas and water), which exist in the upper few metres but may extend downward 10 metres or more (Trevorrow, 2003; Vagle et al., 2010). The bubbles in plumes are known to enhance air-sea gas exchange (Farmer et al., 1993; Woolf, 1997), decrease upper ocean sound propagation (Macpherson, 1957; Medwin, 1974), increase acoustical scattering and attenuation (Hall, 1989; McConnell and Dahl, 1989; Medwin, 1977*c*), impact sonar performance (Deane, 2016; Trevorrow, 2003). Bubble plumes also affect optical scattering (Terril et al., 2001) and therefore also affect photographic and satellite measurements. They produce marine aerosols (Cipriano and Blanchard,

1981; Mason, 2001).

Bubbles in these plumes can inject significant amounts of air into the ocean, the majority of which is nitrogen. Indeed, bubble plumes are known to enhance the nitrogen fluxes from the atmosphere to ocean (D'Asaro and McNeil, 2007; McNeil and D'Asaro, 2007; Vagle et al., 2010). One of the important roles of nitrogen gas is that it can influence the evolution of biogeochemical cycles in the ocean (Falkowski, 1997). Subsurface bubbles are also known to enhance the transfer of more soluble gases during the occurrence of breaking waves, such as carbon dioxide (Woolf and Thorpe, 1991). The injection of bubbles transfers turbulent kinetic energy (energy dissipation) from the breaking wave to the subsurface region. The initial turbulence as a wave breaks acts on large bubbles and causes fragmentation (Deane and Stokes, 2002), followed by the formation of fully developed (acoustically quiescent) bubble plumes. Small bubbles within fully developed plumes can subsequently be transported by turbulent eddies, so these bubbles can act as tracers of turbulent motion (Thorpe, 1982, 1992). Bubble plumes can thus be used to infer the connection between waves, turbulence and upper ocean dynamics without directly assessing the flow field (Thorpe, 1992). Bubble plumes can also act as tracers when trapped in upper ocean organised circulation flow known as Langmuir circulation (Zedel and Farmer, 1991), which is an important mechanism for mixing the upper ocean. Understanding the mechanisms by which environmental parameters affect bubble plumes is necessary for better parameterisation of the processes mentioned above.

1.1.1 Research objectives

The goal of this thesis is to provide a description of the deep bubble plumes, and quantify the relationship of bubble dynamics with wind speed (in the $8-30\ m/s$ range) and sea state. This thesis examines the structure and dynamics of average backscatter vertical profiles to estimate e-folding depth (a backscatter decay rate factor) associated with bubble populations created by breaking waves. Statistics characterising plume morphology, including plume penetration depth, duration and production rate, are produced in this thesis. The bubble plume penetration depth is defined as the vertical extension of the bubble entrainment (Thorpe, 1982, 1986). The plume duration can be defined as the time interval for which a bubble plume exists (the time over which the plume is detected by a sensor). The plume production rate is the num-

ber of plumes occurring in a given time interval. The relationship of these bubble factors with wind speed and sea state will be assessed here. This thesis also highlights the analysis, over shorter periods, of the evolution of individual bubble plumes, present in the water column, with respect to the occurrence of individual breaking waves. We use analysis from three observation periods (storms), with data from measurements taken over about 18 days in total. The implications for air entrainment, parameterised using e-folding depth, will be considered. Plume evolution was tracked via time-series measurements of acoustical backscatter using a sonar within the upper 8 metres of the ocean. The connection between subsurface void fraction within plumes, measured at different depths by a high-speed bubble camera and an acoustical resonator, and the shape of plumes, measured by the sonar, will be explored in this thesis.

Measurements and calculation of detailed bubble parameters in such a wide range of wind speed and sea state are relatively uncommon in the literature (especially at high wind speed), so these results can be used to examine some of the uncertainty in bubble dynamics and bubble-mediated physical fluxes in more extreme environmental conditions. Given the importance of air entrainment and bubble evolution to air-sea gas exchange, the results presented in this thesis have the potential to improve the current parameterisations that are used in the air-sea interaction and climate models.

1.1.2 Scientific background

Gases and particles are continuously exchanged across the air-sea interface. Air-sea gas exchange is of high interest because of its importance to climate, weather and biogeochemical processes (Wanninkhof et al., 2008). It also has engineering applications related to sonar performance (Deane, 2016) and the interpretation of optical measurements. A flux at the air-sea interface can be defined as the amount of gas that is transported across the surface per unit area per unit time. The direction of this gas flux can be from the atmosphere to the ocean (invasion) and vice-versa (evasion). The flux can be expressed as the product between a quantity called the gas transfer velocity, k_g (m/s), and the gas concentration difference between air and water (Wanninkhof, 1992; Wanninkhof et al., 2008; Wanninkhof and Jessup, 1999),

$$F_g = k_g(C_w - \alpha_S C_a), \tag{1.1}$$

where C_w (in mol/m^3) is the gas concentration in the water-side, C_a is the gas concentration in the air-side, and $\alpha_S = (C_w/C_a)_{eqm}$ is the dimensionless Ostwald gas solubility in water at equilibrium.

Equation (1.1) shows that solubility is a significant consideration for gas transfer, implying that dominant physical mechanisms may be different for various gases. For more soluble gases, the flux is influenced by air-side processes rather than water-side ones (McGillis et al., 2000). The presence of bubbles and the associated bubble-mediated flux is strongly dependent on gas solubility (Jeffrey et al., 2000), because a gas with higher solubility would escape much faster from the interior of a bubble, while poorly soluble gases would be expected to remain inside the bubble for longer (Asher et al., 1996; Wanninkhof et al., 1995), particularly when bubbles reside in the water for long periods and therefore the probability of dissolution is increased.

Water temperature has a strong influence on the gas solubility, with a decline in gas solubility with increasing water temperature. Early observations of the relationship between solubility and water temperature hlshow a decreased dissolution rate of oxygen and nitrogen with increasing temperature of distilled water (Weiss, 1970). In seawater, the temperature dependence of nitrogen and argon solubility was shown by Weiss (1970). The oxygen solubility dependence on seawater temperature was reported by Weiss (1970), Carpenter (1966) and Green and Carritt (1967). Thermodynamically, the dissolution rate of a gas in a solvent (water) can be explained as the difference between the internal energy (enthalpy hlterm) and the entropy term of the solution (gas-water mixture). The lower solubility of a gas in water with a higher temperature is the result of an exothermic process that characterises the dissolution of most gases, leading to an increase of thermal energy into the solution and thus overcoming the attractive forces between the gas and water molecules.

Persistent bubble plumes can lead to an asymmetry in gas exchange (Blomquist et al., 2017; Keeling, 1993; Woolf and Thorpe, 1991). Submerged bubbles enhance gas invasion (flux from the atmosphere to ocean) and suppress gas evasion (flux from the ocean to atmosphere) (Blomquist et al., 2017). The gas invasion is weaker for low-solubility gases, which tend to stay contained in bubbles for a longer time, leading to supersaturation of nitrogen (Blomquist et al., 2017; McNeil and D'Asaro, 2007), hland less gas is transferred in a water volume that is already super-saturated. Thus, the very persistent bubble plumes present in

the upper ocean are thought to be significant for the ocean's capacity to uptake poorly-soluble gases like oxygen and nitrogen.

Transfer velocity, k_g, is controlled by the air and water boundary layers (thin layers above and below the free surface level with a thickness of few centimetres), which depends on the near surface turbulence and molecular diffusivity (Jeffrey et al., 2000). However, k_g has been parameterised in many different ways, but none of which produce a satisfactory result in all conditions. One way of parameterising k_g, which combines turbulence, shear and molecular effects, can be expressed as following (Wanninkhof and Jessup, 1999):

$$k_g = \frac{1}{\beta_t} \frac{1}{Sc^n} u_*, \tag{1.2}$$

where β_t is a dimensionless variable dependent on the turbulence in water (which decreases with increasing turbulence), u_* is the friction velocity (units of m/s) hlwhich accounts for the shear stress exerted at the surface (more details will be discussed in Section 1.2.3) and Sc is the Schmidt number. The exponent n of Schmidt number in Equation (1.2) decreases from 0.67 when the water surface is smooth, to 0.4 when water surface is broken and a regime with bubbles dominates (Wanninkhof and Jessup, 1999). The dimensionless Schmidt number is inversely proportional to molecular diffusivity D_m (in units of m^2/s) and can be expressed as following (Woolf, 2005):

$$Sc = \frac{\nu_w}{D_m}, \tag{1.3}$$

where ν_w is the kinematic viscosity of seawater (in units of m^2/s). Equation (1.3) shows that gases with high solubility (thus high mass diffusivity) are associated with a lower Schmidt number.

Figure 1.1 sets out the contributions to the process of air-sea gas flux, which is driven by thermodynamic forcing (the difference in gas concentrations) where the gas is transferred diffusively across an unbroken surface, and kinetic forcing (the transfer velocity) where a two-phase (bubbles/gas and water) turbulent entrainment dominates the gas transfer (Deike et al., 2017). Since it can produce oxygen, biological activity in the ocean can induce an imbalance in the oxygen concentration difference across air-sea interface (Wanninkhof et al., 2008), affecting the net transfer of oxygen, so biological activity must be taken into account when the total oxygen budget and concentration gradients are being calculated. The influences of biological activity and gas solubility on the thermodynamic forcing are sketched in the diagram

from Figure 1.1.

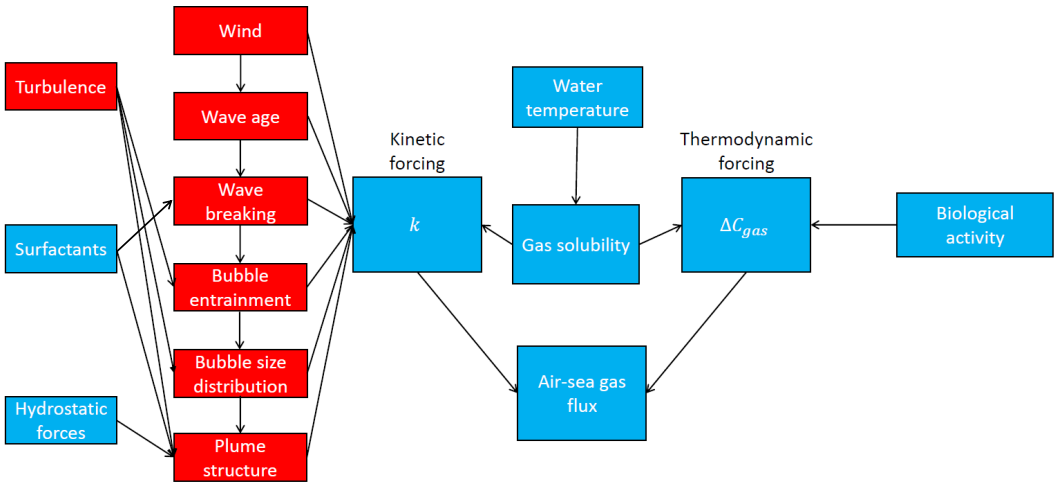

Figure 1.1: Diagram showing the contributions of kinetic and thermodynamic forcing to air-sea gas fluxes. The direction of the arrows show the direction of influence of the parameters. The process (highlighted in red squares) that links wind, wave and bubble parameters is complex, and is affected by turbulence, surfactants and hydrostatic forces. The red rectangles indicate processes investigated in this thesis.

The gas fluxes between ocean and air are often parameterised by combining air-sea gas concentrations with a transfer velocity that encompasses only wind speed (Liss and Merlivat, 1986; Wanninkhof, 1992; Wanninkhof et al., 1985). However, recent studies (Brumer et al., 2017) suggest that wind speed is not the only parameter that must be incorporated in the effect of transfer velocity on gas fluxes. However, especially air-sea fluxes of climatically active gases like CO_2 and DMS (dimethylsulphide), reported by Wanninkhof (1992), are 40% to 85% larger than the fluxes observed by Liss and Merlivat (1986), and there is no consensus on an adequate parameterisation.

The Schmidt number is usually used to normalize the transfer velocity to make different datasets inter-comparable. The technique often used is the transfer velocity normalized to a Schmidt number $Sc = 660$ ($k_{g\ 660}$) which is then related to wind speed. The value 660 is the Schmidt number value for a water temperature of $20°C$. Figure 1.2, produced by Wanninkhof et al. (2008), shows many observations of the relationship between wind speed and $k_{g\ 660}$ of ^{3}He from different ocean regions. It can be observed in Figure 1.2 that, at low wind speed ($3 - 8\ m/s$), the measurements fall within a narrow range. However, as wind blows more

strongly over the sea surface, the variability in the measured transfer velocity increases (shown by larger error bars in Figure 1.2) because of complex mechanical forcing that includes wave breaking, turbulence and bubble injection. There is a growing consensus that sea state, wave breaking characteristics and bubble processes should be considered in the parameterisation of gas transfer velocity.

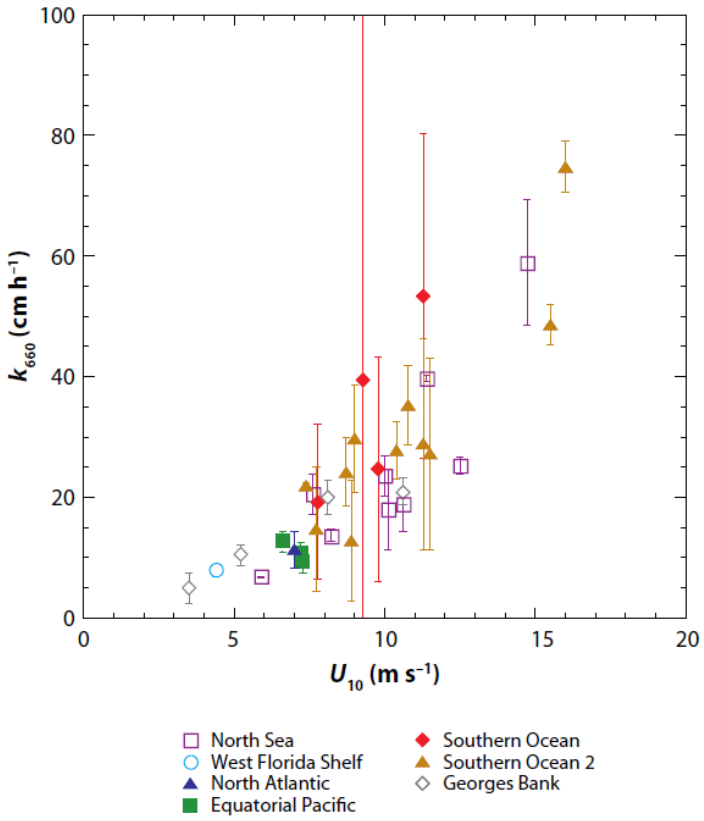

Figure 1.2: Open ocean observations of the variation of transfer velocity, based on $^3He/SF_6$ dual tracer, with wind speed. Each symbol denotes a different ocean region, and the error bars represent the standard deviation. Although conducted independently and in different ocean regions, the gas transfer velocity generally shows an increase with wind speed. However, this relationship shows large variance (shown by the large error bars) caused by the uncertainty of estimating the transfer velocity only using wind speed when other parameters such as sea state, wave breaking and subsurface bubbles also have a more direct impact. Figure 3 from Wanninkhof et al. (2008).

The gas transfer velocity that includes bubble processes via wave breaking is a complicated result of a long chain of processes that influence each other. Wind exerts stress and drag over the sea surface, influencing the development of waves, which is a process characterised by wave age (more details on the derivation of wave age are given in Section 1.2.4.2). Usually, younger waves are steeper, so they are more likely to break (Terray et al., 1995), leading

to bubble injection and turbulence that further entrains bubbles with depth. The largest and most buoyant bubbles rapidly rise back at the sea surface (Monahan and Lu, 1990), leaving a population of bubbles of different sizes (Deane and Stokes, 2002). Bubble fragmentation will be discussed in more detail in Section 1.3.1.

The entire chain of causality that links wind speed, wave age, wave breaking, bubble entrainment, turbulence, and plume structure is incompletely described in the literature, inducing great uncertainty in the estimation of gas fluxes especially at high winds. The physical interaction between bubble processes (bubble entrainment and plume structure) and environmental parameters (wind speed, wave age and wave Reynolds number) will be considered in this thesis. Results from the direct comparison between individual breaking waves and simultaneous occurrences of bubble plumes, together with the relationship between whitecap fraction and bubble entrainment (via backscatter decay), will also be examined in this thesis.

1.2 Waves in the open ocean

The bubbles of interest here are generated by breaking waves, so the methods for characterising ocean waves will be set out in this section. Usually, waves are recorded as a surface elevation signal in a time-series. These signals show that a wave is the profile of the surface elevation between two successive downward zero-crossings of the elevation (Holthuijsen, 2007).

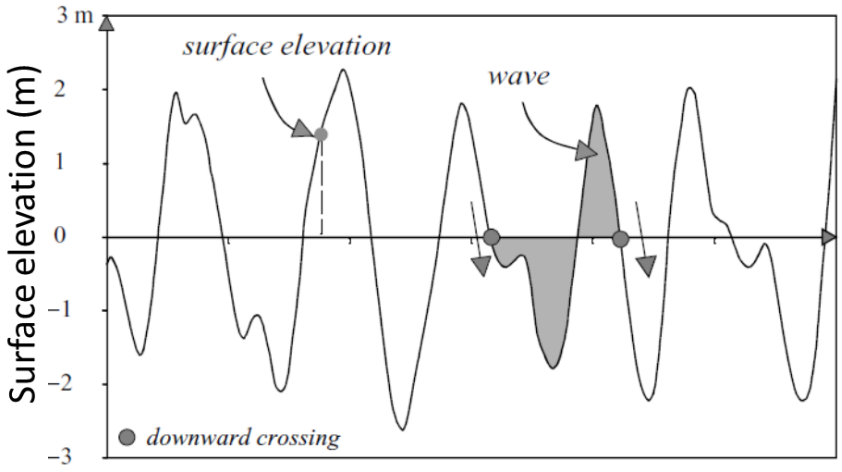

Figure 1.3: Surface elevation and a wave profile. Figure extracted from Holthuijsen (2007).

A zero-crossing is the point where the wave intersects the mean of surface elevations, and it is referred to as ”downward” because the measurement is taken in the downward direction of the wave. Figure 1.3 shows a wave profile with a downward zero-crossing. In the same way, there can be an upward zero-crossing when the intersection point is on the upward side of the wave.

The zero-crossing concept depends on the existence of the mean surface elevation, which can be statistically estimated under the assumption that the surface elevation is a stationary, Gaussian pattern. Since the surface elevation in the open ocean is generally viewed as random (Holthuijsen, 2007), the assumption that its variation is Gaussian is reasonable.

1.2.1 The wave spectrum

The analysis of the details of few local wave observations cannot offer a consistent picture of the wave field in the open ocean. However, describing ocean waves with a spectrum permits the analysis of the sea surface as a stochastic event where all the possible observations that could have been made under specific oceanic conditions are characterised (Holthuijsen, 2007).

The harmonic components, usually present in the open ocean, have randomly distributed amplitudes and phases. In a time-series of wave observations with the duration of wave, D_{wave}, the surface elevation, varying in time at one location, $\eta_{wave}(t)$ (in metres), can be represented as the sum of discrete number of many harmonic components with random amplitudes and phases (Holthuijsen, 2007)

$$\eta_{wave}(t) = \sum_{i=1}^{N} a_{wave,i} \cos(2\pi f_{wave,i} t + \alpha_{wave,i}), \tag{1.4}$$

where $a_{wave,i}$, $\alpha_{wave,i}$ and $f_{wave,i}$ are the wave amplitude, wave phase and wave frequency, respectively, of individual waves. The frequency interval is, therefore, $\Delta f_{wave} = 1/D_{wave}$, and the frequency can also be represented as $f_{wave} = 1/T_0$ for each wave. where T_0 is the zero-crossing wave period (this parameter is defined in Section 1.2.2.1).

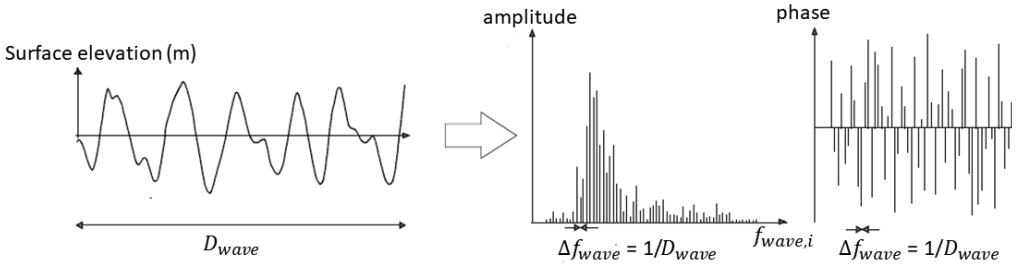

Figure 1.4: The conversion of a surface elevation time-series into the amplitude and phase spectra. Figure 3.4 extracted from Holthuijsen (2007).

The amplitude of a wave is the vertical distance between a peak and the zero-crossing point. Using Fourier analysis, the values of amplitude and phase from Equation (1.4) can be determined for each frequency, thus obtaining the distributions of amplitude and phase for all frequencies. These distributions form the amplitude and phase spectrum (Figure 1.4).

Since the surface elevation is stochastic, a repeated surface elevation measurement under identical oceanic conditions will vary, so the amplitude spectrum would vary as well (Holthuijsen, 2007). For it to converge (approach a constant shape), the amplitude spectrum must be averaged over many experiments (M) as following:

$$\bar{a}_{wave} = \frac{1}{M} \sum_{m=1}^{M} a_{wave,m}, \tag{1.5}$$

where $a_{wave,m}$ is a value of the amplitude spectrum in the experiment with sequence number m. This average amplitude spectrum can be obtained for all frequencies.

1.2.1.1 One-dimensional wave spectrum

A more useful approach is to use the variance of each wave component, $\frac{1}{2}a^2_{wave}$. One reason is that the variance can offer a more relevant statistical description of the spectrum, e.g. the sum of variances of the wave components is equal to the variance of the sum of the wave components (Holthuijsen, 2007). The variance also provides an estimate of the uncertainty of the behaviour of the wave components, because the standard deviation is derived from the variance. Another reason for using variance is that, according to the linear theory of surface gravity waves, the energy of the waves is proportional to the variance (Holthuijsen, 2007). The variance spectrum is discrete (e.g. fixed frequency intervals Δf_{wave} are present), but all frequencies are present. To represent all frequencies, a first approach would be to distribute

the variance, $\frac{1}{2}a_{wave}^2$, over the frequency band, Δf_{wave}, thus obtaining a variance density at each frequency (Holthuijsen, 2007). Although the variance is now distributed over all frequencies, it still varies, in fixed amounts, from one frequency band to the next (it is discontinuous). The variance density distribution becomes continuous when an infinitesimal frequency band is present (Δf_{wave} approaches zero). This continuous distribution is the 1-dimensional variance density spectrum, $S_{1D}(f_{wave})$ (in units of m^2/Hz), defined as following (Holthuijsen, 2007):

$$S_{1D}(f_{wave}) = \lim_{\Delta f_{wave} \to 0} \frac{1}{\Delta f_{wave}} E\left\{\frac{1}{2}a_{wave}^2\right\} \tag{1.6}$$

where $E\left\{\frac{1}{2}a_{wave}^2\right\}$ is the expected value of the random amplitude. The average of the amplitude has been replaced by the expected value because the number of the repetitions of the measurement is very large (approaches infinity).

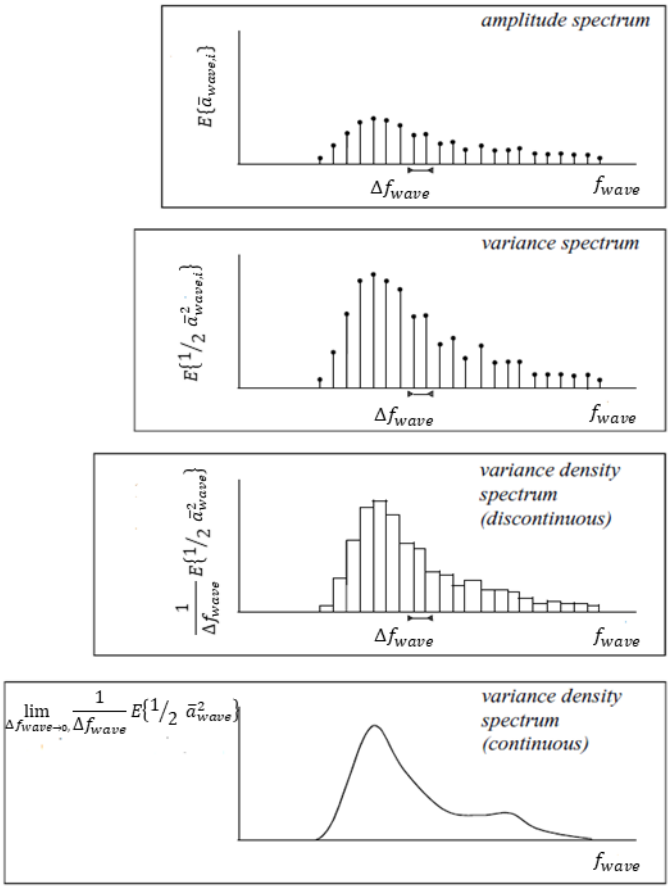

Figure 1.5: The transition from a discrete amplitude spectrum to a continuous variance density spectrum. Figure 3.7 extracted from Holthuijsen (2007).

The expected value is the average amplitude in the Rayleigh probability distribution at each frequency. The variance density spectrum is formed from all the expected values extracted

from the probability distributions at all frequencies. To ensure that it is always a positive quantity when calculating the expected value, the amplitude, in the variance spectrum, is squared. The wave phase is ignored from the variation density spectrum because it has a uniform distribution (Holthuijsen, 2007). The transition of wave spectrum from the discrete amplitude spectrum to the continuous variance density spectrum is shown in Figure 1.5.

Given the assumption that the surface elevation is a stationary Gaussian process, the variance density spectrum provides a complete statistical description of the elevation of ocean waves (Holthuijsen, 2007). The total continuous variance density spectrum (total variance of the random surface elevation) is obtained via the integration of the 1-dimensional variance density spectrum over infinitesimal frequency increments, df_{wave}, as following:

$$S(f_{wave}) = \int_0^\infty S_{1D}(f_{wave}) df_{wave}, \tag{1.7}$$

where $S(f_{wave})$ has units of m^2/Hz.

The energy of a harmonic wave, per unit horizontal ocean surface, is the total surface elevation variance multiplied by density of water, ρ_w, and gravitational acceleration, g. Consequently, the 1-dimensional total variance density spectrum can be multiplied by $\rho_w g$ to obtain the 1-dimensional energy density spectrum as (Holthuijsen, 2007)

$$S^*(f_{wave}) = \rho_w g S_{1D}(f_{wave}). \tag{1.8}$$

The 1-dimensional energy density spectrum characterizes the wave energy (distributed over all frequencies) as a function of time and only at one geographic location, and it has units of $kg\ m^{-2} m^2/Hz\ s^{-2}$. The wave energy spectrum, defined in Equation (1.8), encompasses both the kinetic and potential energy of the wave field composed of many wave components (Holthuijsen, 2007).

Assuming a stationary Gaussian wave model and a linear theory of surface gravity waves, the variance density spectrum is used to describe the statistical characteristics of the waves, and the energy density spectrum is used to describe the physical properties of the waves. These assumptions are usually realistic for wind-generated waves (Holthuijsen, 2007), so the wave spectrum described in this section is appropriate for this study.

1.2.1.2 Directional wave spectrum

To characterize the 3-dimensional moving waves (towards and from any direction, so they are no longer confined at one location), the direction of wave propagation needs to be considered.

The random surface elevation of waves that propagate, in time t, in x–y space, and in direction θ_{wave} relative to positive x-axis (normal to the wave crest of each individual component) is expressed as the sum of these propagating harmonic wave components (Holthuijsen, 2007),

$$\eta_{wave}(x, y, t) = \sum_{i=1}^{N} \sum_{j=1}^{M} a_{wave,i,j} \cos(f_{wave,i} t - k_{wave,i} x \cos\theta_{wave,j} - k_{wave,i} y \sin\theta_{wave,j} + \alpha_{wave,i,j}), \tag{1.9}$$

where $k_{wave} = 2\pi / L_{wave}$ is the wave number of each wave component (where L_{wave} is the wavelength of the harmonic wave), and θ_{wave} is the direction of wave propagation. In Equation (1.9), the indices i and j represent the summation over all frequencies and directions, respectively. The construction of a 3-dimensional random sea surface, via the summation of many waves propagating with different amplitudes and in different directions across the ocean surface, is sketched in Figure 1.6.

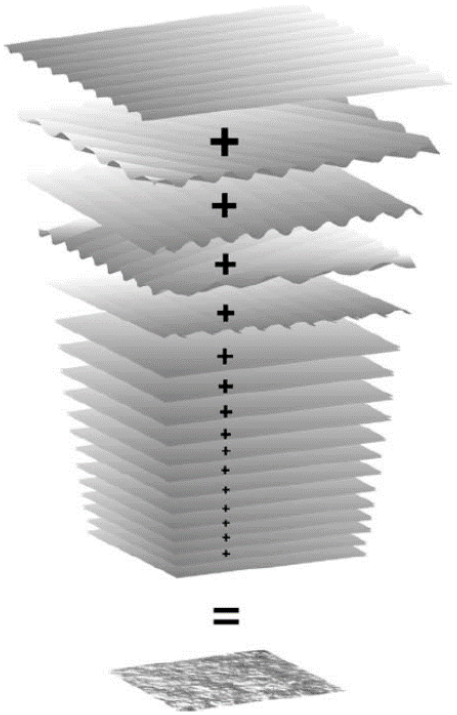

Figure 1.6: The summation of wave fields with many types of waves with different amplitudes and directions. Figure 3.10 extracted from Holthuijsen (2007).

Using the same technique as for the 1-dimensional wave spectrum, the discrete 2-dimensional

amplitude spectrum can be converted into a continuous 2-dimensional variance density spectrum (Holthuijsen, 2007),

$$S_{2D}(f_{wave}, \theta_{wave}) = \lim_{\Delta f_{wave} \to 0} \lim_{\Delta \theta_{wave} \to 0} \frac{1}{\Delta f_{wave} \Delta \theta_{wave}} E\left\{\frac{1}{2} a^2_{wave}\right\}. \tag{1.10}$$

Similarly to the 1-dimensional spectrum, the total directional variance density spectrum shows the distribution of the variance of surface elevation over all frequencies and directions (Figure 1.7). The total directional variance density spectrum is, therefore, obtained via the integration of directional variance density spectrum over all possible frequencies and directions (from 0 to 2π) as following:

$$S(f_{wave}, \theta_{wave}) = \int_0^{\infty} \int_0^{2\pi} S_{2D}(f_{wave}, \theta_{wave}) d\theta_{wave} df_{wave}, \tag{1.11}$$

where $S(f_{wave}, \theta_{wave})$ has units of $m^2/Hz\ deg^{-1}$.

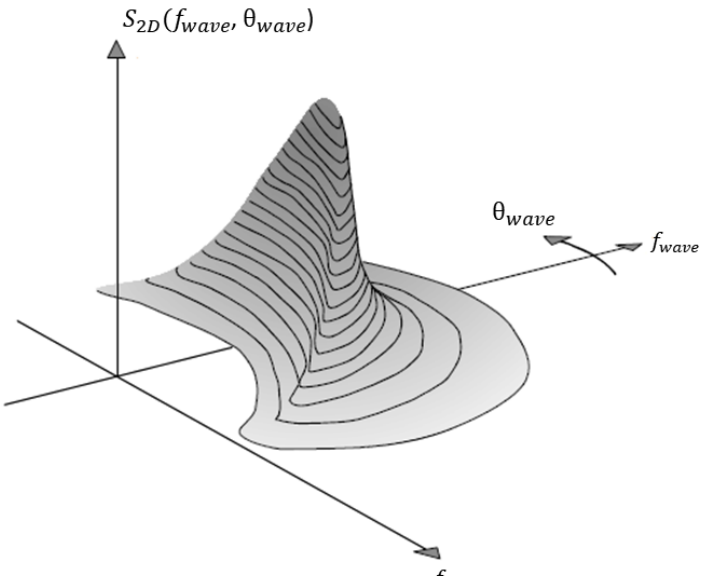

Figure 1.7: The shapes of amplitude and phase spectrum. Figure 3.11 extracted from Holthuijsen (2007).

Finally, the physical properties of the propagating waves across the sea surface are characterized by the directional wave energy spectrum. This is obtained by multiplying the directional variance density spectrum by $\rho_w g$,

$$S^*(f_{wave}, \theta_{wave}) = \rho_w g S(f_{wave}, \theta_{wave}), \tag{1.12}$$

where $S^*(f_{wave}, \theta_{wave})$ has units of $kg\ m^{-2} m^2/Hz\ s^{-2}\ deg^{-1}$.

1.2.1.3 Wind-sea and swell waves

The appearance of the wave field can be inferred from the shape of the wave spectrum. The waves are smoother and more regular as the spectrum becomes narrower, and more irregular as the spectrum widens.

The transition of the spectrum from single-frequency smooth, regular waves (Delta-Dirac function) to multiple-frequency, irregular waves (wide) is shown in Figure 1.8. The wind-generated waves (which have been described, in this section, in terms of spectrum) are of two types: wind-sea and swell waves. The waves that are generated by local wind are referred to as wind-sea waves, while the waves that are generated from remote storms (and have propagated over large distances) are known as swell waves (Holthuijsen, 2007; Portilla et al., 2008).

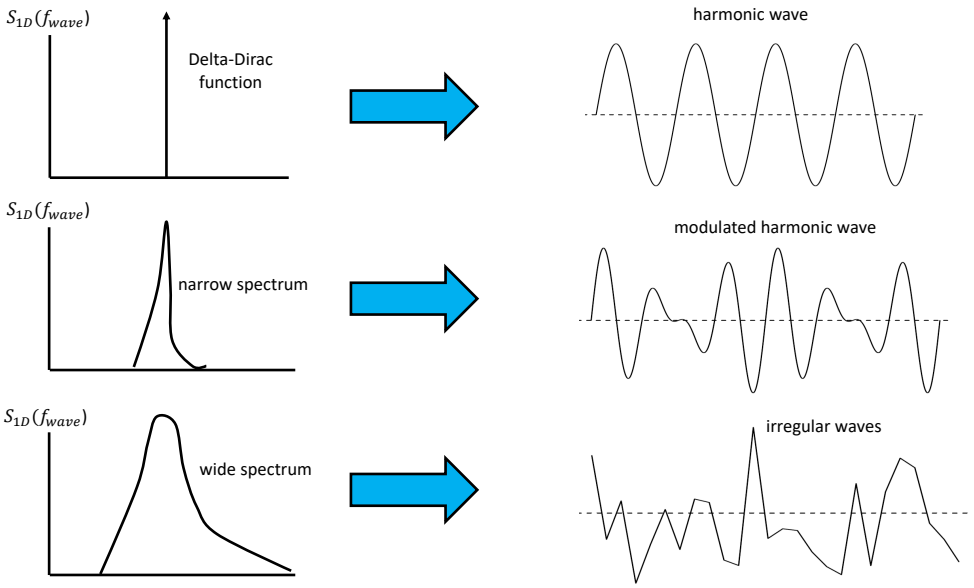

Figure 1.8: Types of waves and the shape of their spectrum. The waves found in the ocean are usually described by narrow and wide spectra. Figure adapted after Figure 3.9 from Holthuijsen (2007).

A wave field dominated by wind-sea waves is characterised by irregular waves with many frequencies. Swell waves are more regular/smoother, usually have a much lower frequency, because high frequencies are attenuated more quickly, and they also contain fewer frequencies than wind-sea waves (Holthuijsen, 2007; Portilla et al., 2008). Wind-sea waves also usually move from different directions, while swell waves are generally propagating from a narrow range of directions (Figure 1.9). These characteristics allow wind-sea and swell waves to be

clearly separated (Holthuijsen, 2007).

This separation is shown in the shapes of both the 2D and 1D wave spectrum from Figure 1.9. The spectrum of wind-sea waves is significantly wider, with both frequency and direction, than the spectrum of the swell waves (Figure 1.9). In the case of swell waves, the highest energy in the wave spectrum is contained at a clearly lower frequency band than the wave energy spectrum of wind-sea waves (Figure 1.9).

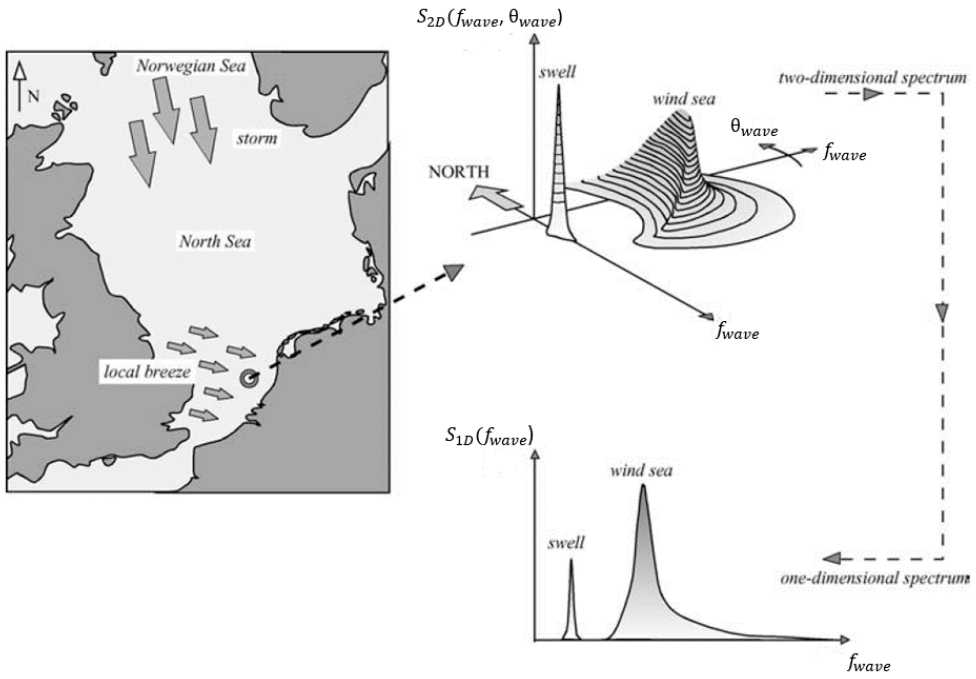

Figure 1.9: The spectra of wind-sea and swell waves. Figure 3.13 extracted from Holthuijsen (2007).

1.2.1.4 Fully-developed spectrum

The fully-developed spectrum refers to the spectrum which shows the maximum spectral energy of a locally wind-driven wave field present at higher frequencies. This represents an equilibrium of the waves with the wind if the wind steadily blows for a long time and over a large ocean surface. In this wind-wave equilibrium, the kinetic energy input and turbulent dissipation loss are equal. One of the most important contributions to the derivation of the fully-developed spectrum is from JOint North Sea WAve Project (JONSWAP), conducted by Hasselmann et al. (1973). The JONSWAP spectrum is obtained via the normalisation (with respect to peak energy and peak frequency, f^*_{wave}) of multiple spectra measured at many fetches (distances from the storm).

The peak frequency is the frequency at which the energy/variance density of the spectrum is maximum. The shape of the JONSWAP spectrum shows the evolution of the observed spectra with fetch (Holthuijsen, 2007). As the spectrum evolves with increasing fetch, the shape of the spectrum becomes sharper and the peak is present at lower frequencies (upper panel in Figure 1.9). The JONSWAP spectrum is the result of scaling the observed spectra (in magnitude and frequency), so that they collapse on to a single distribution (bottom panel in Figure 1.10).

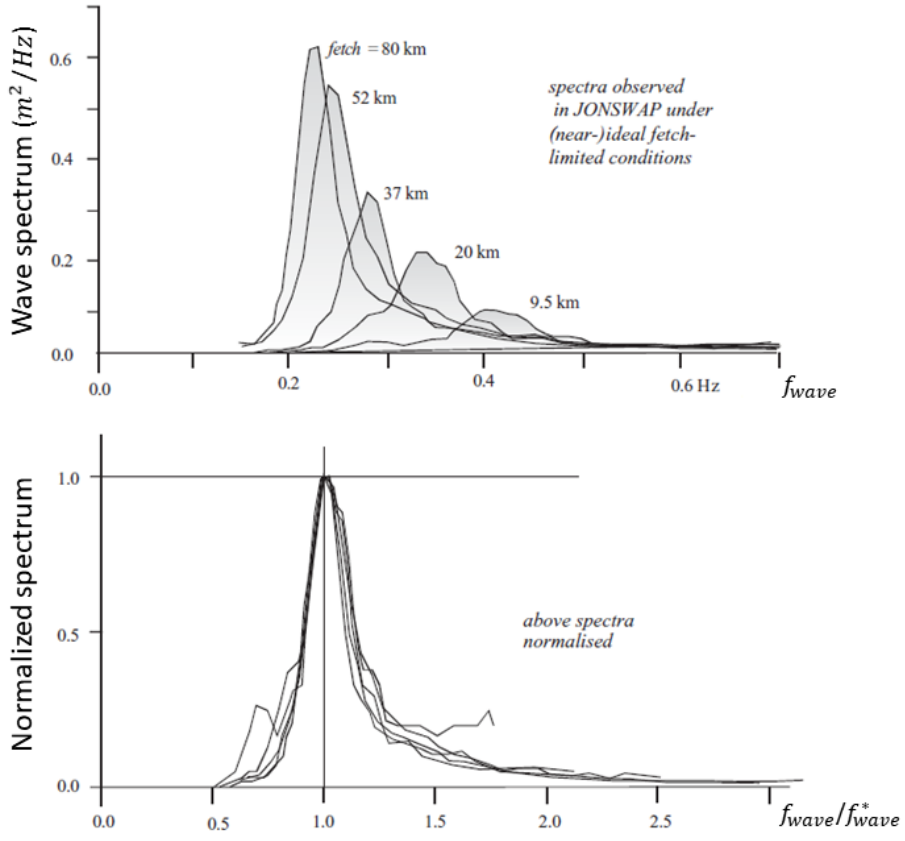

Figure 1.10: The JONSWAP spectrum dependent on fetch (upper panel) and the normalized JONSWAP panel (lower panel). Figure extracted from Holthuijsen (2007).

The high-frequency tails of these spectra were studied by Phillips (1958), who derived the shape of these tails using dimensional analysis. Phillips (1958) hypothesised that wave breaking limits the spectral level (energy) at higher frequencies (Holthuijsen, 2007). This would translate in to the dependency of the variance spectrum on the frequency, f_{wave}, and gravitational acceleration, g, as wave breaking is dominated by gravitational acceleration. The

expression of this dependency is $S(f_{wave}) \sim g^{x_1} f_{wave}^{x_2}$. Since the dimension of the variance density spectrum is $[m^2/Hz] = [m^2 s]$, Phillips (1958) obtained the coefficients $x_1 = 2$ and $x_2 = -5$, so the inferred relationship for a breaking-dominated spectral tail (high frequency tail) becomes (Holthuijsen, 2007)

$$S(f_{wave}) \propto g^2 f_{wave}^{-5}. \tag{1.13}$$

Using a definition for wave breaking based on the wave propagation speed and the forward speed of the water particles at the surface, Thornton (1977) obtained the same result for the high frequency tail.

To parameterise the observed fetch-dependent spectra, a spectral function which shows the shape of the fully-developed spectrum is used. This function is known as the Pierson-Moskowitz spectrum, and was proposed by Pierson and Moskowitz (1964). A smoothing cut-off factor, known as the Phillips constant, has been used to preserve f_{wave}^{-5} at high frequencies. The Pierson-Moskowitz parameterisation for a fully-developed spectrum is, thus, expressed as (Hasselmann et al., 1973; Holthuijsen, 2007)

$$S_{PM}(f_{wave}) = \alpha_{PM} g^2 (2\pi)^{-4} f_{wave}^{-5} \exp\left[-\frac{5}{4} \left(\frac{f_{wave}}{f_{PM}} \right)^{-4} \right], \tag{1.14}$$

where α_{PM} is the Phillips constant (energy scale) and f_{PM} is the peak Pierson-Moskowitz (PM) frequency.

The spectra observed by Hasselmann et al. (1973) during the JONSWAP experiment have a more elongated and narrow peak than the Pierson-Moskowitz spectrum. To account for this effect in the Pierson-Moskowitz spectrum, the expression in Equation (1.14) was further multiplied by a peak enhancing function, $Y_{enh}(f_{wave})$ (Holthuijsen, 2007),

$$Y_{enh}(f_{wave}) = \gamma_{enh}^{\exp\left[-\frac{1}{2} \left(\frac{f_{wave}/f_{PM}^{-1}}{\sigma_{enh}} \right)^2 \right]}, \tag{1.15}$$

where $\gamma_{enh} = S_{max}/S_{max}^{PM}$ is a peak enhancing factor (the maximum spectral energy measured during JONSWAP divided by the Pierson-Moskowitz maximum spectral energy) and σ_{enh} is a peak width parameter.

Two peak width parameters are used to account for the marginally different widths on the two sides of the spectral peak: $\sigma_{enh} = \sigma_a$ for $f_{wave} \leq f_{PM}$ and $\sigma_{enh} = \sigma_b$ for $f_{wave} > f_{PM}$. This peak enhancement does not affect the shape of the Pierson-Moskowitz spectrum, as it only enhances the magnitude of the spectral peak (Figure 1.11).

This extended version of Pierson-Moskowitz spectrum is known as the JONSWAP spectrum (Hasselmann et al., 1973; Holthuijsen, 2007),

$$S_{JONSWAP}(f_{wave}) = \alpha_{PM} g^2 (2\pi)^{-4} f_{wave}^{-5} \exp\left[-\frac{5}{4}\left(\frac{f_{wave}}{f_{PM}}\right)^{-4} \right] Y_{enh}(f_{wave}), \qquad (1.16)$$

where $Y_{enh}(f_{wave})$ was defined in Equation (1.15).

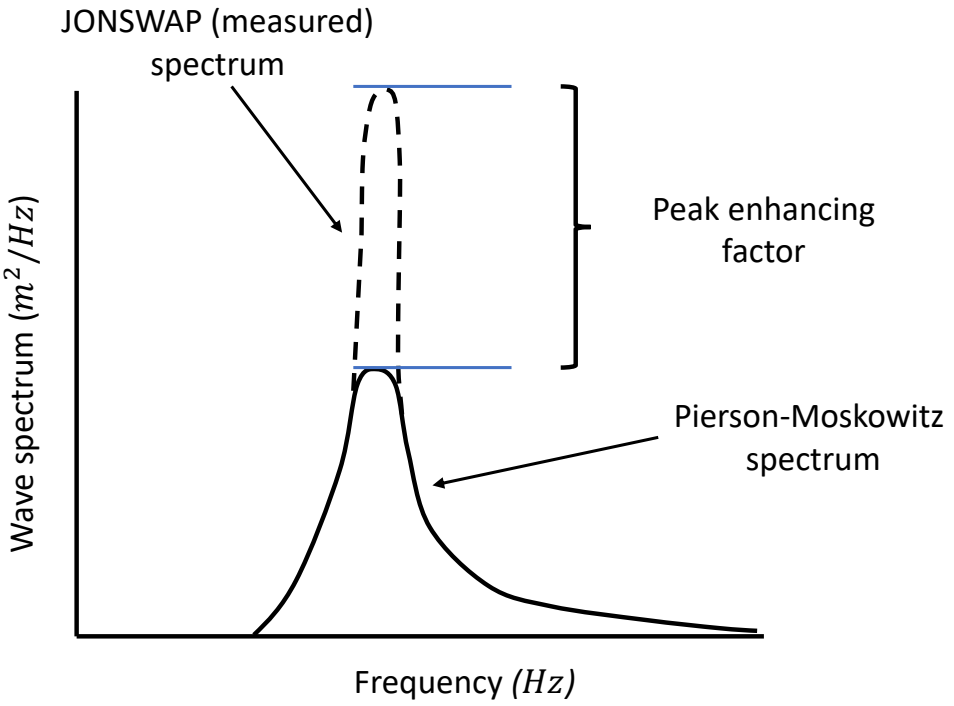

Figure 1.11: The Pierson-Moskowitz (theoretical) spectrum has a similar shape to that of the (measured) JONSWAP when a peak enhancing factor is applied. Figure adapted after Holthuijsen (2007).

Given the limited fetch, a fully developed spectrum dependent on fetch only was not observed during the JONSWAP experiment (Hasselmann et al., 1973). However, the spectrum becomes fully-developed (a JONSWAP spectrum) via non-linear wave-wave interactions (see more details in the next section), compensating the dependency on a limited fetch. The JONSWAP spectrum does not include swell waves (Holthuijsen, 2007), and the spectrum for swell is therefore usually found at the lower frequencies (on the left hand-side of the fully-developed spectrum).

1.2.2 Significant wave height and wave period

1.2.2.1 Measured parameters

The wave height, H, is defined as the vertical distance between the lowest and the highest surface elevation in a wave profile (Holthuijsen, 2007). Usually, the wave height is measured for many waves, thus the average wave height, $\bar{H}$, of a N_w number of waves is

$$\bar{H} = \frac{1}{N_w} \sum_{i=1}^{N_w} H_i, \tag{1.17}$$

where i is the sequence number in a wave record. A more useful wave height is the significant wave height, H_s (Holthuijsen, 2007). For a time-series with a given N_w number of waves, the significant wave height is defined as the mean of the highest one-third of wave heights (Forristall, 1978; Holthuijsen, 2007)

$$H_s = \frac{1}{N_w/3} \sum_{j}^{N_w/3} H_j, \tag{1.18}$$

where j represents the waves ranked based on their heights.

A wave has been defined in terms of the downward zero-crossing, so the wave period is defined as the time interval between two successive downward zero-crossings (Holthuijsen, 2007). The wave period, defined with zero-crossings, is called the zero-crossing period, T_0, and it is the wave period regularly used in the literature, including this thesis. Since there is usually a record with many waves measured, the zero-crossing wave period is averaged over a N_w number of waves as following:

$$\bar{T}_0 = \frac{1}{N_w} \sum_{i=1}^{N_w} T_{0,i}. \tag{1.19}$$

1.2.2.2 Parameters derived from the wave spectrum

The statistical description of wave period, wave height, and significant wave height is based on the wave variance spectrum. Using this approach, the wave period and wave height can be extracted from probability density distributions. This can be achieved using moments of the variance spectrum. Firstly, consider the distribution of the random instantaneous surface elevation, which is Gaussian. The Gaussian probability density function of the surface elevation (with a zero mean) can be expressed as

$$fd(\eta_{wave}) = \frac{1}{\sqrt{2\pi m_0}} \exp\left(- \frac{\eta_{wave}^2}{2m_0} \right), \tag{1.20}$$

where m_0 is the zeroth-order moment of the variance spectrum (variance of the surface elevation), and $\sqrt{m_0}$ is the standard deviation of the surface elevation. The zeroth-order moment is, then, the variance spectrum (Holthuijsen, 2007; Wang and Hwang, 2001) or, more physically, the area under the spectral curve,

$$m_0 = \int_0^\infty S(f_{wave}) df_{wave}. \tag{1.21}$$

Higher order moments can also be expressed in terms of the variance spectrum as (Holthuijsen, 2007; Wang and Hwang, 2001)

$$m_n = \int_0^\infty f_{wave}^n S(f_{wave}) df_{wave}, \tag{1.22}$$

where $n = 1, 2, 3, \ldots$ and m_n is the nth-order moment of the variance spectrum. Equation (1.22) shows that the higher order moments express the variance of the surface elevation oscillating at higher frequencies. One consequence of the varying frequency weighting expressed in the various moments is that the high-order moments are sensitive to noise in the high-frequency range of the spectrum (Holthuijsen, 2007).

The fraction of time the surface elevation is above a certain positive level, η^*, is expressed by the up-crossing wave period through that level. This time interval is usually averaged, so the mean up-crossing wave period through that level, $\bar{T}_{\eta^*}$, can be obtained, which is expressed in terms of the spectrum as (Holthuijsen, 2007; Rice, 1954)

$$\bar{T}_{\eta^*} = \sqrt{\frac{m_0}{m_2}} \left(\exp\left(-\frac{\eta_{wave}^2}{2m_0} \right) \right)^{-1}, \tag{1.23}$$

where m_2 is the second-order spectral moment, and the exponential is the denominator. The mean frequency of these level crossings is the inverse of the mean wave period, $\bar{f}_{\eta^*} = (\bar{T}_{\eta^*})^{-1}$, so it has the following form:

$$\bar{f}_{\eta^*} = \sqrt{\frac{m_2}{m_0}} \exp\left(-\frac{\eta_{wave}^2}{2m_0} \right) \tag{1.24}$$

It was previously shown that zero-crossing wave period, $\bar{T}_0$ can be obtained from measurements (see Section 1.2.2.1), but it can also be derived from the spectrum. The zero-crossing concept was already discussed in the introduction of Section 1.2. In the expression of zero-crossing wave period, the exponential of the surface elevation in Equation (1.23) will therefore disappear, so $\bar{T}_0$ is defined purely based on the moments of the spectrum (Holthuijsen, 2007),

$$\bar{T}_0 = \sqrt{\frac{m_0}{m_2}}. \tag{1.25}$$

The mean zero-crossing frequency, $\bar{f}_0$, is the inverse of $\bar{T}_0$, giving the following expression:

$$\bar{f}_0 = \sqrt{\frac{m_2}{m_0}}. \tag{1.26}$$

To derive the significant wave height from the wave spectrum, the wave crest height can be firstly considered. A wave crest is the maximum point in the surface elevation (Holthuijsen, 2007). Each crest has a height, η_{crest}, which is always positive for a narrow spectrum (swell waves which are smooth). If the spectrum is wide (wind-sea waves which are irregular), a crest height can also be negative (Holthuijsen, 2007), because this spectrum contains waves with small local spikes/maxima, below the zero/mean level, that are represented as crests (the local maxima are counted). However, if the definition of a wave as the surface elevation between two successive up-crossings/down-crossings through the zero/mean level (see introduction of Section 1.2) is considered, the negative local maxima within a wave are discarded. Only the positive maxima are present in a wave signal, so the maximum elevation of each wave signal can be extracted. This definition allows for a smoothing of the waves with a wide spectrum, so the retrieval of a positive wave crest height is possible for a wide spectrum as well.

The above definition of a wave implies that the total number of crests is the number of up-crossings through the zero level for waves with both narrow and wide spectra,

$$\frac{N_{\eta_{crest}>\eta^*}}{N_{crests}} = \frac{\bar{f}_{\eta^*}}{\bar{f}_0}. \tag{1.27}$$

Equation (1.27) shows that the number of high crests can be extracted from the wave spectrum via the ratio between the mean frequency of the waves crossing through the η^* level and the mean frequency of the waves crossing through the zero level. These high crests (relative to the positive level, η^*) are shown in the time-series from Figure 1.12.

The ratio in Equation (1.27) can be interpreted as the probability of the wave crests, in a time-series, exceeding the level η^* (Holthuijsen, 2007). Since it is the inverse of the cumulative distribution function, the probability density function of wave crests, $fd(\eta_{crest})$, can be then obtained as the derivative of cumulative distribution function of wave crests not exceeding η_{crest} (Casas-Prat and Holthuijsen, 2010; Holthuijsen, 2007; Longuet-Higgins, 1952),

$$fd(\eta_{crest}) = \frac{\eta_{crest}}{m_0} \exp\left(-\frac{\eta_{crest}^2}{2m_0}\right), \tag{1.28}$$

which is a Rayleigh probability density function.

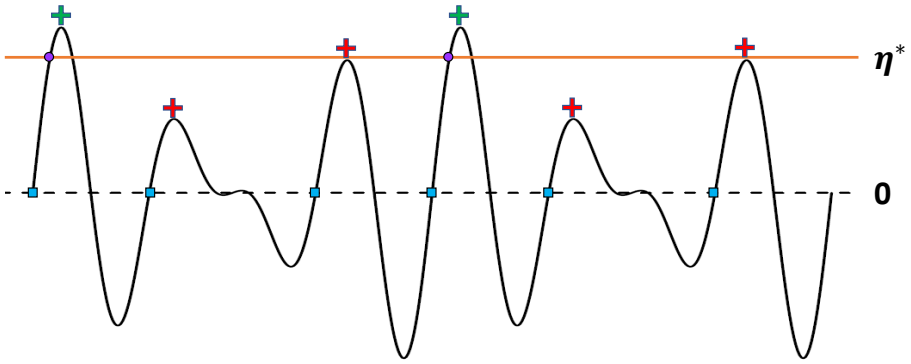

Figure 1.12: The detection of wave crests (local maxima) using a positive threshold. The green crosses indicate a successful detection, while the red ones indicate that these wave peaks are not classified as crests (they are below the threshold). Figure adapted after Holthuijsen (2007).

For waves with narrow spectrum in deep water (open ocean), the wave height is approximated to be equal to twice the wave crest, $H \sim 2\eta_{crest}$ (Casas-Prat and Holthuijsen, 2010; Holthuijsen, 2007). The probability density function of wave height, $fd(H)$, can be transformed from $fd(\eta_{crest})$ using a Jacobian, J, assuming that the integrals (areas under the curves) of $fd(H)$ and $fd(\eta_{crest})$ are conserved. The final expression of the probability density function of individual wave heights is

$$fd(H) = \frac{H}{4m_0} \exp\left(-\frac{H^2}{8m_0}\right), \tag{1.29}$$

which is also a Rayleigh distribution (Casas-Prat and Holthuijsen, 2010; Holthuijsen, 2007). Considering $\eta_{crest} = H/2$, the cumulative distribution of wave height (the probability that the wave height does not exceed a certain level) is

$$Fd(H) = 1 - \exp\left(-\frac{H^2}{8m_0}\right). \tag{1.30}$$

As indicated in Section 1.2.2.1, the significant wave height is defined as the mean value of the highest one-third of wave heights, which can be determined from the Rayleigh distribution given in Equation (1.29) as follows (Casas-Prat and Holthuijsen, 2010; Holthuijsen, 2007):

$$\int_{H^*}^{\infty} fd(H)\, dH = \frac{1}{3}. \tag{1.31}$$

Ultimately, the significant wave height, H_s, is defined in terms of the spectrum as (Casas-Prat and Holthuijsen, 2010; Holthuijsen, 2007)

$$H_s = \frac{\int_{H^*}^{\infty} H\, fd(H)\, dH}{\int_{H^*}^{\infty} fd(H)\, dH}, \tag{1.32}$$

resulting in a simple expression for significant wave height:

$$H_s = 4\sqrt{m_0}. \tag{1.33}$$

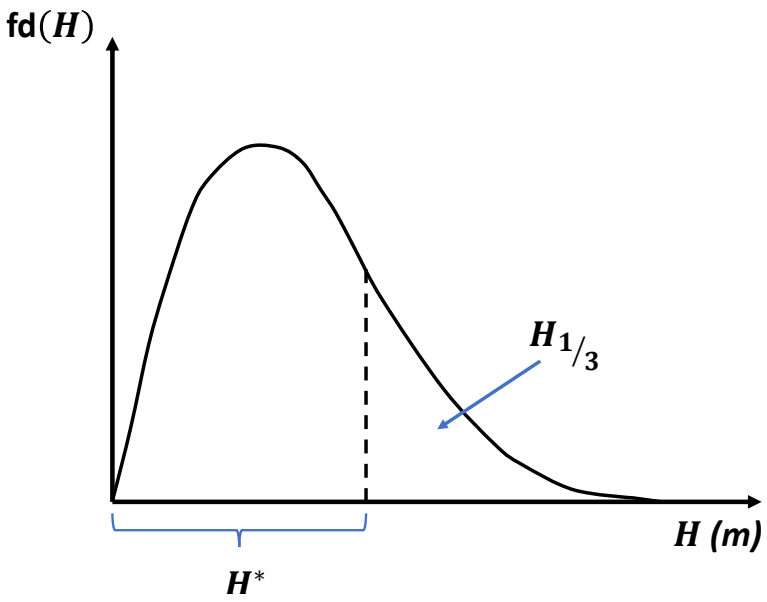

Figure 1.13: Rayleigh probability density function of wave height. The top one third of this probability is attributed to the significant wave height. Figure adapted after Holthuijsen (2007).

The spectral moment, m_0, can be determined from both a spectrum for swell waves (narrow spectrum) and a spectrum for wind-sea waves (wide spectrum), so the swell and wind-sea spectral moments are just the special cases of the definition in Equation (1.21). Therefore, the swell spectral moment, m_{0s}, is the variance spectrum for swell waves, and the wind-sea spectral moment, m_{0w}, is the variance spectrum for wind-sea waves. Using these definitions of the spectral moments and the definition of H_s in Equation (1.33), the swell significant wave height, H_{ss}, is expressed as (Wang and Hwang, 2001)

$$H_{ss} = 4\sqrt{m_{0s}}, \tag{1.34}$$

and, similarly, the wind-sea significant wave height, H_{sw}, is defined as (Wang and Hwang, 2001)

$$H_{sw} = 4\sqrt{m_{0w}}. \tag{1.35}$$

Some observations should be noted as following: for a narrow spectrum of waves (smoother random signal with mainly positive crests/peaks), $fd(\eta_{crest})$ and $fd(H)$ tend toward a Rayleigh distribution (the crest statistics are more easily resolved); for a wide wave spectrum (sharper

random signal with equally as many positive and negative crests/peaks), $fd(\eta_{crest})$ and $fd(H)$ approach a Gaussian distribution (the crest statistics are more complicated).

1.2.3 Friction velocity and wave Reynolds number

1.2.3.1 Friction velocity

The effect of the wind on the sea surface (in terms of its drag) is accounted for using the friction velocity, u_*, which relates to the wind shear stress, τ_w, as following (Charnock, 1955):

$$\tau_w = \rho_a u_*^2, \tag{1.36}$$

where ρ_a is the air density. Wind shear stress can be parameterised based on drag coefficient, C_D, and wind speed at 10 metres, U_{10}, as follows:

$$\tau_w = \rho_a C_D U_{10}^2, \tag{1.37}$$

where the drag coefficient is usually linearly related to wind speed (Yelland and Taylor, 1996). Using Equation (1.36), friction velocity, u_*, can be expressed as

$$u_* = \sqrt{\frac{\tau_w}{\rho_a}}. \tag{1.38}$$

In this subsection, the friction velocity was only mathematically defined as part of a parameterisation for wind shear stress. The details about the mechanism of wind shear stress (and friction velocity) will be explained, in terms of wind-induced wave growth, in Section 1.2.4.2.

1.2.3.2 Wave Reynolds number

The wave Reynolds number is a dimensionless parameter that combines wind and wave data, and is used as a non-dimensional representation of ocean-atmosphere interaction processes, particularly those related to wave breaking. Wave Reynolds number combines friction velocity and significant wave height, providing information about the wind shear stress over the ocean and the available wave energy. Since it is derived from a wide spectrum (which contains more irregular waves that are more susceptible to dissipation by wave breaking – see Section 1.2.4.3), the wind-sea significant wave height, defined in Section 1.2.2.2, is usually used in the formulation of wave Reynolds number. However, the wind-sea significant wave height does not specifically measure the energy/magnitude of breaking waves, but it provides

an average estimation of the magnitude of the variance/energy of wind-sea waves contained in a spectrum (which might be affected by wave breaking).

The wave Reynolds number was proposed by several authors, such as Zhao and Toba (2001) and Woolf (2005). The classical definition of Reynolds number is that it is the ratio between the inertial forces (combination of velocity and a length scale) and the viscous forces (kinematic viscosity). In this thesis, the wave Reynolds number, R_H, is treated as a special case for wind-sea waves, where the velocity and the length scale are represented by friction velocity, u_*, and wind-sea significant wave height, H_{sw}, respectively, so R_H is expressed as

$$R_H = \frac{u_* H_{sw}}{\nu_w}, \tag{1.39}$$

where ν_w is the kinematic viscosity of seawater, and it is a function of water temperature and salinity. Note that ν_w represents the kinematic viscosity at the sea surface. For this study, ν_w was computed using a seawater salinity estimate and the ship's measurements of sea surface temperature (SST). A seawater salinity at the sea surface of $34 - 35$ psu (g/kg) is usually measured in the open ocean, so a value of 35 psu was considered in this thesis. Using sea surface temperature and salinity as inputs, the kinematic viscosity of seawater was computed using the MATLAB Seawater Thermophysical Properties Library (Nayar et al., 2016).

1.2.4 The growth of waves

The balance between wave energy density, sources (wind, wave interaction) and sinks (dissipation) can be described by the radiative transfer equation. Both the energy density and the source terms, in the radiative transfer equation, must be integrated as the wave components travel along a wave ray at the group velocity. However, the source terms depend on both the wave component that is being followed along each ray and the directional spectrum, at each propagation point, which contains other wave components propagating along other wave rays and intersecting the wave ray that is being followed (Holthuijsen, 2007). The energy densities of these other intersecting wave components are not known (Holthuijsen, 2007), so the integration of the radiative transfer equation does not have a solution in this situation.

1.2.4.1 The radiative transfer equation

An approach that includes only a dependence on the wave component that is being followed along the ray and local wind, not other wave components, can be used to resolve the energy balance of the particular wave component. This technique uses an Eulerian formulation, in which the spectrum is computed at a large number of locations in the ocean simultaneously with a local energy balance at each of these locations, not only at a single specified point (Holthuijsen, 2007). Using the Eulerian technique, the energy balance of the waves is assessed on a geographic grid. The spatial resolution depends on the cell size of the grid. For simplicity, a smaller ocean surface area is treated here, so the geographic grid can be approximated as a Cartesian x–y grid, e.g. for larger areas, where the Earth's curvature becomes important, a more accurate approach would be to use a grid in spherical coordinates.

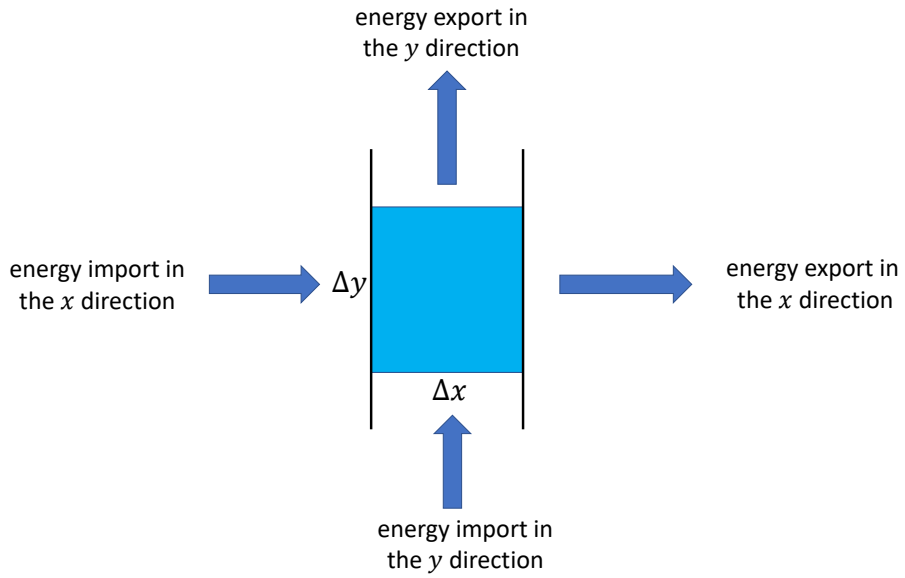

Figure 1.14: The balance of the wave energy flow through a cell grid.

The energy balance for each grid cell must be computed. For simplicity, only the energy balance of one grid cell is derived here. Consider any wave component propagating through this grid cell, where the variation of energy over a given time interval is balanced by the net import of energy and the local generation of energy (Holthuijsen, 2007). The net import of energy through the cell, during a time interval Δt, along x and y directions is shown in Figure 1.14.

In the x direction, the net import of energy is the difference between the energy import through the left-hand side of the cell, as a wave propagates with the group velocity, $c_{g,x}$ across the cell width, Δy, and the energy export through the right-hand side of the cell, as the energy

has been transported over the distance Δx (see Figure 1.14). Mathematically, this net energy import in x direction, $E_{net,x}$, in the Δt time interval, can be expressed as (Holthuijsen, 2007)

$$E_{net,x} = c_{g,x} S(f_{wave}) \Delta y \Delta t - \left(c_{g,x} S(f_{wave}) + \frac{\partial c_{g,x} S(f_{wave})}{\partial x} \Delta x \right) \Delta y \Delta t = -\frac{\partial c_{g,x} S(f_{wave})}{\partial x} \Delta x \Delta y \Delta t, \tag{1.40}$$

where the first term in the right hand-side is the wave energy (given, in this case, by the 1D spectrum, $S(f_{wave})$) imported in the cell along x direction, and the second term is the energy exported outside the cell along x direction. Similarly, the net import of energy in the y direction, $E_{net,y}$, by a wave propagating with the group velocity, $c_{g,y}$, over the time interval, Δt, is

$$E_{net,y} = -\frac{\partial c_{g,y} S(f_{wave})}{\partial y} \Delta x \Delta y \Delta t. \tag{1.41}$$

Finally, having the expressions for time variation of wave energy in cell, net import of energy and local generation of energy (source terms) in each grid cell, $\Delta x \Delta y$, the radiative transfer equation can be expressed as

$$\frac{\partial S(f_{wave})}{\partial t} \Delta x \Delta y \Delta t = -\frac{\partial c_{g,x} S(f_{wave})}{\partial x} \Delta x \Delta y \Delta t - \frac{\partial c_{g,y} S(f_{wave})}{\partial y} \Delta x \Delta y \Delta t + Q_s S(f_{wave}) \Delta x \Delta y \Delta t, \tag{1.42}$$

where $Q_s(f_{wave})$ includes the source terms of the 1-dimensional wave spectrum. Rearranging Equation (1.42) (and removing the cell's dimension, $\Delta x \Delta y \Delta t$), a more standard expression of the radiative transfer equation can be formulated, across any cell of the geographic grid, as following (Hasselmann et al., 1973; Holthuijsen, 2007):

$$\frac{\partial S(f_{wave})}{\partial t} + c_{g,x} \frac{\partial S(f_{wave})}{\partial x} + c_{g,y} \frac{\partial S(f_{wave})}{\partial y} = Q_s(f_{wave}), \tag{1.43}$$

where the summation of the terms in the left hand-side represents the material derivative of the wave energy, $dS(f_{wave})/dt$, balanced by the energy source terms (right hand-side). If the grid cells are 3-dimensional, Equation (1.43) can be rewritten in a compressed manner, using the Nabla operator, as (Melville, 1996; Phillips, 1977)

$$\frac{\partial S(f_{wave})}{\partial t} + c_g \nabla S(f_{wave}) = Q_s(f_{wave}). \tag{1.44}$$

The source and sink terms of the wave energy density consist of wind generation, $Q_{s,U}$, wave-wave interaction, $Q_{s,ww}$, and dissipation due to white-capping (wave breaking), $Q_{s,wc}$. These terms can be thus expressed, for any wave component, as

$$Q_s = Q_{s,U} + Q_{s,ww} + Q_{s,wc}, \tag{1.45}$$

where Q_s has units of $m^2/Hz\ s^{-1}$.

In this section (and also see the Appendix), the mechanisms associated with all the source terms in the right hand-side of Equation (1.44) will be explained in detail. However, the main focus will be on the influence of wind generation and dissipation terms on the wave spectrum, since this is the most relevant to this thesis.

The balance between the wave energy spectrum and the source terms can be visually observed in Figure 1.15a, where the source terms are superimposed on the JONSWAP spectrum. This balance implies that the summation of the shapes of the source terms acts to conserve the shape of this wave spectrum. The wave growth mechanisms are generally applied exclusively to the wind-sea waves, and the configuration of swell waves does not usually change significantly (for long propagation distances), so swell does not show much growth, since it is not locally influenced by wind.

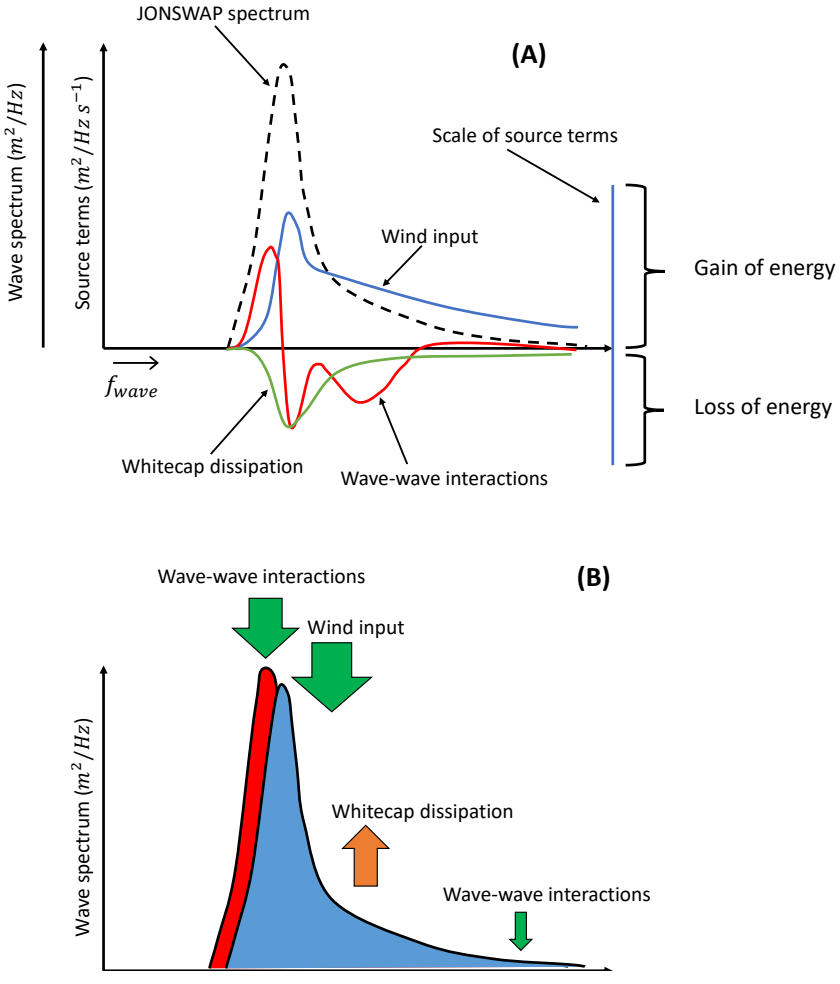

Figure 1.15: (A) The balance between source terms. (B) Energy flow within the spectrum. Figure adapted from Holthuijsen (2007).

Most of the energy gained by the waves from the wind, near the spectral peak and at mid-range frequencies, is removed by whitecap dissipation and wave-wave interactions (Figure 1.15a). The energy from wave-wave interactions is transferred to the higher and lower frequencies (Holthuijsen, 2007). There is a net loss of energy at mid-range frequencies, and the energy is distributed from the mid-range frequencies to the low frequencies (below the peak frequency). This flow of energy within the wave spectrum leads to a migration of the spectral peak towards the lower frequencies (Figure 1.15b).

The wave spectrum evolution is characterised by the migration of the spectrum from high to low frequencies via the mechanisms described above. As the wave spectrum migrates toward the lower frequencies, the frequency of a wave component with a fixed high frequency becomes the peak frequency. As this wave component frequency transitions to the peak frequency, that part of the spectrum grows exponentially due to wind-generation and wave-wave interactions mechanisms, and the energy eventually decays predominantly due to whitecapping. As the spectrum becomes fully-developed, the frequency of the wave component is eventually found in the high-frequency tail of the spectrum, which is characterised by a relative equilibrium (Holthuijsen, 2007). The difference between the equilibrium energy and the temporary peak energy of the wave component (when it reaches peak frequency) is known as spectral overshoot (Holthuijsen, 2007).

1.2.4.2 Wind generation and wave age

The wind-induced wave growth is the most important mechanism by which the sea state is evaluated in this thesis. Wave age is one of the main concepts that will be used to assess sea state in this thesis. It will be shown in this section, by referring to results from the literature, that wave age can be used as a reliable estimate for the wind-induced wave growth.

A mechanism for the wind generation term was suggested by Phillips (1957). This mechanism states that waves are generated by resonance between the propagating wind-induced pressure waves (air pressure) at the sea surface and the freely propagating water waves (Holthuijsen, 2007). This translates into a turbulent pressure field induced by the wind on the water surface. As it advects across the sea surface, this turbulent pressure field appears 'frozen' (Holthuijsen, 2007), because its propagation speed is clearly dominant over the turbulent circulations within the field (this effect is similar to the Taylor's hypothesis of 'frozen'

turbulence inside clouds). Phillips (1957) describes this turbulent pressure field as the superposition of many harmonic air pressure waves, which are oriented in different directions, but propagating in the wind direction. Within this pressure field, some pressure components have the same speed, wavelength and direction as the freely propagating water wave components (Holthuijsen, 2007). As they match together, the air pressure waves transfer energy to the sea surface waves by resonance. As the wind is constant over the sea surface, there is a constant transfer of energy in time, resulting in a linear growth of sea surface waves in time (Holthuijsen, 2007; Phillips, 1957),

$$Q_{s,U}(f_{wave}) = \alpha_{wind}, \tag{1.46}$$

where α_{wind} is a function of wave components and reference wind speed (measured at 10 metres height), U_{10}, so $\alpha_{wind} = \alpha_{wind}(f_{wave}, \theta_{wave}, U_{10})$. This is the case of energy transfer purely via wind-induced surface pressure, without any contribution of other initial waves to the linear growth. A more comprehensive description of the linear wave growth, which also includes initial contributing waves (propagating from different directions), is given in an empirical expression proposed by Cavaleri and Malanotte-Rizzoli (2010),

$$Q_{s,U}(f_{wave}, \theta_{wave}) = C_{\alpha}\Big[u_{*}\cos(\theta_{wave} - \theta_{wind})\Big]^{4} \tag{1.47}$$

for $|\theta_{wave} - \theta_{wind}| < 90^{\circ}$ and $f_{wave} > f_{PM}$. In Equation (1.47), C_{α} is an empirical coefficient that is inversely proportional to the squared gravitational acceleration, u_{*} is the air friction velocity and θ_{wind} is the wind direction. In Equation (1.47), there is a Pierson-Moskowitz lower frequency threshold to ensure that only wind-induced waves are growing through this mechanism. The angle difference between waves and wind is set to be lower than 90° to ensure there are no cases where the source term is zero.

The vertical wind profile that forms over the waves describes the bending of the wind streamlines as they encounter a wave (see Figure 1.16). The disturbance of the wind profile decreases with height, so the streamline bending becomes very small or non-existent at higher elevations (Figure 1.16).

The streamlines compress (come closer together) on the windward side of the wave crest (peak of the wave), so the air pressure at the surface reaches a maximum (Holthuijsen, 2007; Miles, 1957). On the other hand, the streamlines are further away from each other on the leeward side of the wave crest, so the air pressure is minimum at the sea surface (Holthuijsen,

2007; Miles, 1957). This pressure variation indicates that the wind pushes the sea surface down on the windward side of the wave crest and pulls the sea surface up on the leeward side of the crest (see Figure 1.16).

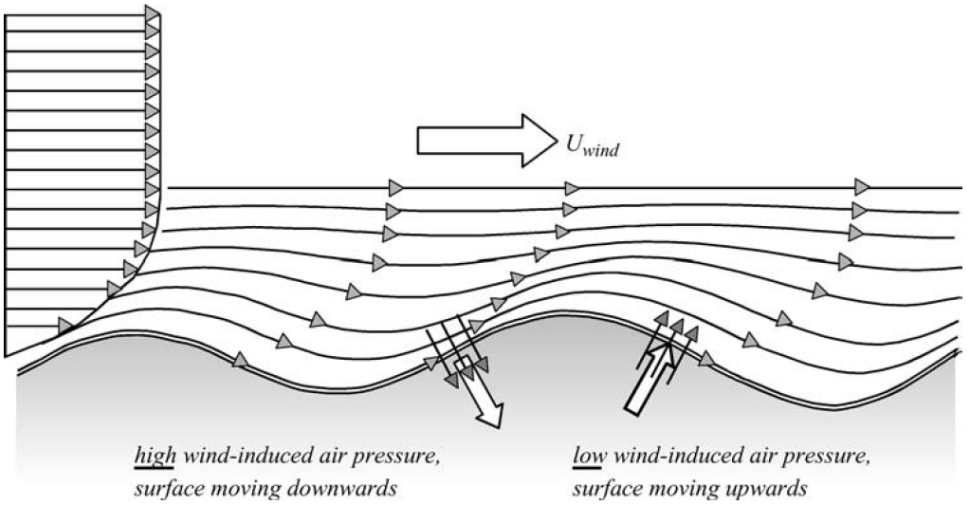

Figure 1.16: The action of wind shear stress over the waves. Figure extracted from Holthuijsen (2007).

Since the low and high pressure areas are not located in the wave trough and above the wave crest, an out-of-phase pressure/sea surface coupling system is formed. This coupling system transfers energy to the waves, which subsequently grow as they propagate forward. This transfer depends on the amplitude of the waves, so it becomes more effective as the waves grow (Holthuijsen, 2007). This leads to an even faster wave growth, so it is a process that enforces itself. This mechanism is formulated as (Holthuijsen, 2007; Miles, 1957)

$$Q_{s,U}(f_{wave}, \theta_{wave}) = \beta_s S(f_{wave}), \tag{1.48}$$

where β_s is the coefficient of wind-induced wave growth. This important coefficient was derived from independent field measurements conducted by Plant (1982) and Snyder et al. (1981). The expression for β_s, proposed by Plant (1982), is

$$\beta_s = \epsilon_{Plant} \frac{\rho_a}{\rho_w} \left[\frac{u_* \cos(\theta_{wave} - \theta_{wind})}{c_p} \right]^2 2\pi f_{wave}, \tag{1.49}$$

where ϵ_{Plant} is an empirical coefficient, ρ_a and ρ_w are the densities of air and water, respectively, and c_p is the wave phase velocity (which is the rate, in a given time interval, at which the phase propagates with distance). In deep water (open ocean), the wave phase velocity is expressed as $c_p = g/2\pi\ T_0$, where g is the gravitational acceleration and T_0 is the zero-crossing wave

period. Snyder et al. (1981) proposed the following expression for β_s:

$$\beta_s = \epsilon_{Snyder} \frac{\rho_a}{\rho_w} \left[28 \frac{u_*}{c_p} \cos(\theta_{wave} - \theta_{wind}) - 1 \right] 2\pi f_{wave}, \tag{1.50}$$

where ϵ_{Snyder} is an empirical coefficient, in this instance used by Snyder et al. (1981).

Equations (1.49) and (1.50) contain an important parameter known as wave age, which is the ratio of wave phase velocity and the friction velocity. This is a key parameter and it will be frequently used throughout the thesis to describe the sea state. In both expressions for wind-induced wave growth coefficient, the inverse wave age, u_*/c_p, is actually used. A significant number of laboratory and field measurements show a positive relationship between the wind-induced wave growth and inverse wave age (see Figure 1.17).

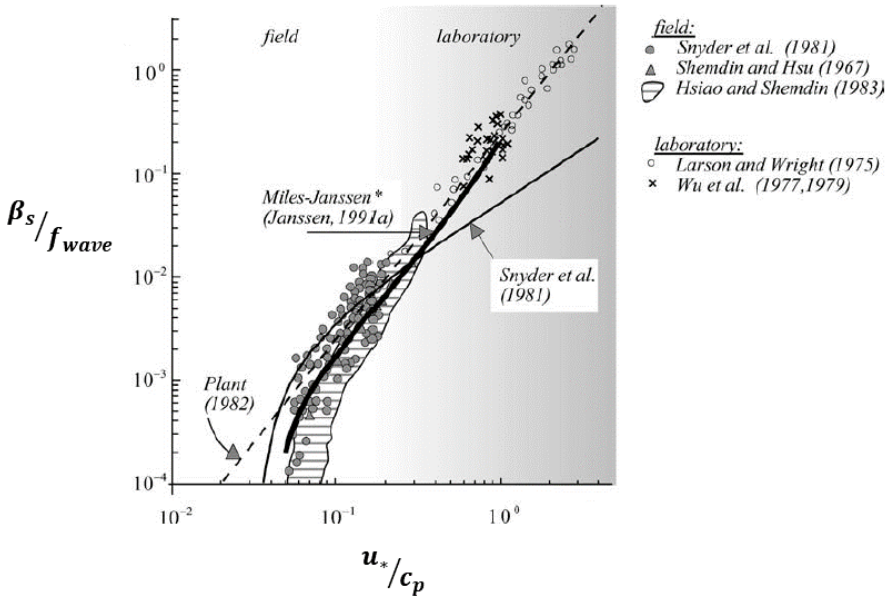

Figure 1.17: The relationship between wave growth and inverse wave age. These observations show that the wave growth parameter has a dependency on inverse wave age. Figure extracted from Holthuijsen (2007).

This mechanism is restricted to the transfer of energy from the wind to the waves only (positive wave growth), not vice-versa. Therefore, in many wave models, the value of β_s, given in Equation (1.55), is cut off at $\beta_s = 0$ to avoid a negative wave growth or the energy transfer from the waves to the wind (Holthuijsen, 2007). The β_s coefficient, given in Equation (1.54), is linearly related to the inverse wave age, while β_s from Equation (1.55) is non-linearly re-

lated to the inverse wave age (see Figure 1.17). Some aspects of the mechanism remain uncertain/unknown but inverse wave age is still a useful measure.

The wind generation source term is integrated over all directions (with the constraints imposed previously), and it can be summarized using the formulations from Phillips (1957), Cavaleri and Malanotte-Rizzoli (2010), Plant (1982) and Snyder et al. (1981), and based on the model developed by Miles (1957) (that explains the mechanism),

$$Q_{s,U}(f_{wave}, \theta_{wave}) = \alpha_{wind} + \beta_s S(f_{wave}, \theta_{wave}). \tag{1.51}$$

The shape of the wind generation source term, relative to the JONSWAP spectrum, shows that most of the energy transfer from the wind to the waves occurs near the spectral peak (see Figure 1.15a).

1.2.4.3 Dissipation via wave breaking

Wave breaking in the open ocean (deep water), also known as white-capping (Holthuijsen, 2007), is still a relatively poorly understood phenomenon. Various breaking criteria have been proposed in the literature, but none of them is universally accepted. Also, it is very difficult to reproduce an open ocean breaking wave, similar to the ones produced in the open ocean, in the laboratory, since the scales and environmental conditions are very different. In this subsection, the dissipative effect of wave breaking on the wave energy spectrum is discussed. It will cover wave breaking related to types, mechanics and statistics of breaking waves, along with the various criteria for wave breaking proposed in the literature.

The dissipative effect of wave breaking on the development of waves is highly non-linear (Holthuijsen, 2007). One of the most important models that describes this dissipation effect states that a whitecap acts as a pressure pulse on the sea surface downwind of the wave crest (Hasselmann, 1974; Holthuijsen, 2007). At that location above the wave, the whitecap exerts a downward force on the wave face (the whitecap has a weight), removing energy from the wave (the elevation of the wave is inhibited; see Figure 1.18).

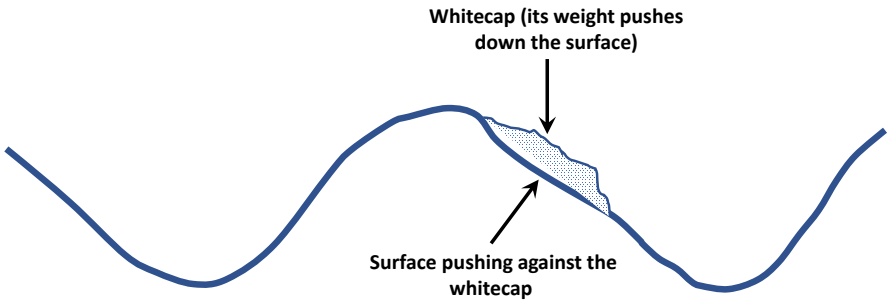

Figure 1.18: The action of a whitecap on a wave. Figure adapted after Holthuijsen (2007).

There is a quasi-symmetry between the whitecap dissipation and wind-induced growth related to the energy distribution relative to the wave. This implies that the whitecap extracts energy from the wave and transports it to the surface currents and turbulence at approximately the same location as where the wind transfers energy to the wave (Holthuijsen, 2007). This effect is not quite symmetric because the magnitude of energy draining induced by whitecaps is lower than that of energy input by wind, e.g. most whitecap energy dissipation occurs near the spectral peak (see Figure 1.15a). The dissipation near the spectral peak may not be a valid assumption in the open ocean, where the dissipation is shifted towards higher frequencies (towards the spectral tail). This quasi-symmetrical effect implies that the weight of the whitecap counteracts the pulling effect of the low air pressure area above the lee side of the wave crest (Hasselmann, 1974; Holthuijsen, 2007). This whitecap dissipation model, shown in Figure 1.18, can be expressed as the source term for the wave spectrum (Hasselmann, 1974; Holthuijsen, 2007),

$$Q_{s,wc}(f_{wave}) = -\Omega_{wc} k_{wave} S(f_{wave}), \tag{1.52}$$

where k_{wave} is the wave number and Ω_{wc} is an unknown coefficient that encompasses the statistical properties of breaking waves (whitecaps). This coefficient must be a quantity that represents the breaking wave/whitecap on the sea surface, and which must be integrated over the entire spectrum. The negative sign on the right hand-side of Equation (1.59) indicates the whitecap's tendency to remove energy from the wave spectrum. The statistic that is often used as a criterion to evaluate the potential of waves for breaking is wave steepness, which is defined as the ratio between wave height and wavelength. No clear dependency of breaking-wave initiation on wave steepness has been confirmed (Holthuijsen, 2007). How-

ever, even though the precise breaking onset is difficult to quantify, there are results in the literature showing a relationship between breaking strength and wave slope (Drazen et al., 2008; Romero et al., 2012). Deike et al. (2017) found that the entrained air volume (bubble injection) increases with breaking crest length as wave slope also increases. The whitecap dissipation source term will be further explored here in terms of a saturation level coefficient (which is a function of inverse wave age). The effects of the whitecap dissipation term on the breaking-wave statistics will be then evaluated.

1.2.4.4 Wave number spectrum and energy dissipation

The wave number spectrum has a similar shape and structure to that of the frequency spectrum, the difference being that the wave number spectrum represents the surface elevation continuously distributed at each possible wave number within a given range. Using inverse wave age, the saturation level coefficient can be expressed in the following form (Phillips, 1985):

$$B_s(k_{wave}) = \mu_d(\cos\theta_{wave})^m\Big(\frac{u_*}{c_p}\Big), \tag{1.53}$$

where μ_d is a numerical constant and the value of m is usually deduced from observational data. This saturation level coefficient represents the degree of saturation, so when the wave field reaches saturation, dissipation due to wave breaking occurs (at high frequencies and wave numbers). According to Equation (1.53), the saturation level depends solely on inverse wave age when the waves propagate from the same direction as the wind (there are no cross-propagating waves).

The whitecap dissipation can be expressed as a function of $B_s(k_{wave})$ (Phillips, 1985),

$$Q_{s,wc}(k_{wave}) = g\ k_{wave}^{-4}\ f(B_s(k_{wave})) = \gamma_d\ B_s^3(k_{wave}), \tag{1.54}$$

where γ_d is a numerical constant. Using the saturation level, the wave number spectrum, $S(k_{wave})$, is expressed as (Melville, 1996; Phillips, 1985),

$$S(k_{wave}) = \mu_d(\cos\theta_{wave})^m u_* g^{-1/2} k_{wave}^{-7/2}. \tag{1.55}$$

An now the dissipation term can be rewritten as (Phillips, 1985)

$$Q_{s,wc} = \gamma_d \mu_d^3(\cos\theta_{wave})^{3m} u_*^3 g^{-1/2} k_{wave}^{-5/2}. \tag{1.56}$$

The spectral rate of energy loss from the wave field is the product between frequency and dissipation term (Phillips, 1985), implying that the energy loss increases at higher frequencies via dissipation. Using the expression given in Equation (1.56) and the dispersion relation, $f_{wave} = \sqrt{g k_{wave}}$, the spectral rate of energy loss can be formulated as (Melville, 1996; Phillips, 1985)

$$\epsilon_b(k_{wave}) = f_{wave} Q_{s,wc} = \gamma_d \mu_d^3 (\cos\theta_{wave})^{3m} u_*^3 k_{wave}^{-2}. \tag{1.57}$$

Using the characteristics of the wave number spectrum, the energy loss from the wave field was derived. As this loss is distributed to surface turbulence and turbulent mixing, it affects the whitecap activity and bubble presence near the sea surface.

1.3 Breaking waves

Breaking waves act to disrupt the air-sea interface (Soloviev and Lukas, 2013) by injecting air from the atmosphere into the ocean in the form of bubbles. Having such an important effect on bubble generation, the breaking-wave process is of high relevance for the research in this thesis, so it is characterised in detail.

As high wind transfers energy from the air to the ocean, the surface waves may steepen and break. The momentum transfer from wind leads to water particles with a larger velocity than that of the forward speed of the wave, so the wave forward face begins to steepen beyond an equilibrium point and the wave eventually breaks. There are few types of breaking waves that occur in the open ocean, such as plunging, spilling breakers (Galvin, 1968), and even plunging/spilling hybrid breakers (Blenkinsopp and Chaplin, 2007). The most relevant for this thesis are plunging and spilling breaking waves, so these two types will be further discussed in more detail.

1.3.1 Plunging breaking waves

The detailed mechanism of a plunging breaking wave and subsequent air bubble injection is reported by Deane and Stokes (2002), and the process is shown in Figure 1.19. Seawater containing surfactants and biological material was used in the experiment conducted by Deane and Stokes (2002). The breaking wave crest generates a complicated two-phase flow that evolves with width, depth and time (Blenkinsopp and Chaplin, 2007; Deane and Stokes, 2002).

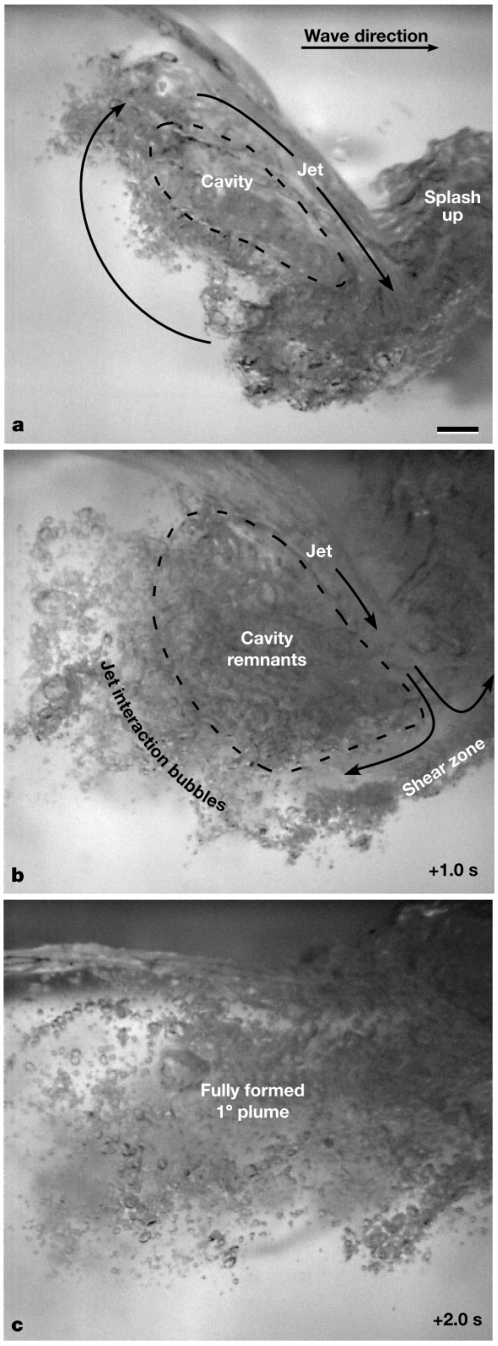

Figure 1.19: The evolution of a breaking wave and bubble injection during the acoustically active phase. (A) Bubble formation inside of a cavity of air trapped between the overturning wave crest and wave face. (B) The subsurface bubbles evolve during the collapse of the air cavity. (C) The end of the active wave breaking entrainment, when a fully formed bubble plume is present. The horizontal scale bar in (A) is 1 *cm*. Figure 2 extracted from Deane and Stokes (2002).

Plunging breakers often occur when the wave face has almost a vertical steepness, while the wave height also grows, so the wave crest bends (starts to overturn) over the face of the wave and, eventually, the crest plunges into the wave face (Galvin, 1968). The overturning wave crest forms and interacts with the wave face, trapping air from the atmosphere in a cavity

(Deane and Stokes, 2002).

Figure 1.19a shows the action of the plunging jet, when the crest overturns and impacts the forward face of the wave (Deane and Stokes, 2002; Duncan et al., 1994). The impact of the plunging leads to the bubble formation, as an air cavity is trapped between the overturning jet and the wave face (Figure 1.19a). The bubbles in the lower half of the cavity are formed by jet and drop impact at the wave face, further being advected around the cavity by a clockwise circulation caused by the rotational wave motion (Deane and Stokes, 2002).

Figure 1.19b shows the evolution, one second later, of breaking when the cavity has almost completely fragmented, and the plunging jet forms a shear layer on the wave face (Deane and Stokes, 2002). The cavity remnants are surrounded by a cloud of bubbles formed as a result of the interaction between the jet and wave face Deane and Stokes (2002). Finally, Figure 1.19c shows the process after two seconds, when the air cavity has collapsed, resulting in a more diffuse bubble plume. The dense bubble plumes which form during the active wave breaking entrainment in the first 1–2 seconds are known as alpha plumes (Deane and Stokes, 2002; Monahan and Lu, 1990). The alpha plumes rapidly evolve into the more diffuse plumes after the wave breaking induced entrainment ceases (after 1–2 seconds) which are known as beta plumes (Deane and Stokes, 2002; Monahan and Lu, 1990).

The beta bubble plumes exist for tens of seconds and longer after the wave breaks, so it is generally assumed that they evolve totally independently from breaking waves. However, there are still uncertainties with the characterisation of this post-breaking plume evolution.

The structure of these beta plumes is influenced by direct transportation of bubbles by Langmuir circulation (Farmer et al., 1993; Zedel and Farmer, 1991), bubble stability via surfactant coating and hydrostatic forces (Hanwright et al., 2005), and dissolution, buoyancy advection and bubble turbulent diffusion (Deane and Stokes, 2002), leading to persistent bubble plumes.

1.3.2 Spilling breaking waves

Due to wave shoaling near the water edge, most of breaking waves occurring near/at the coast are plunging breakers (they are well known to casual observers near the coast), but the spilling breaking waves dominate in the open deep ocean.

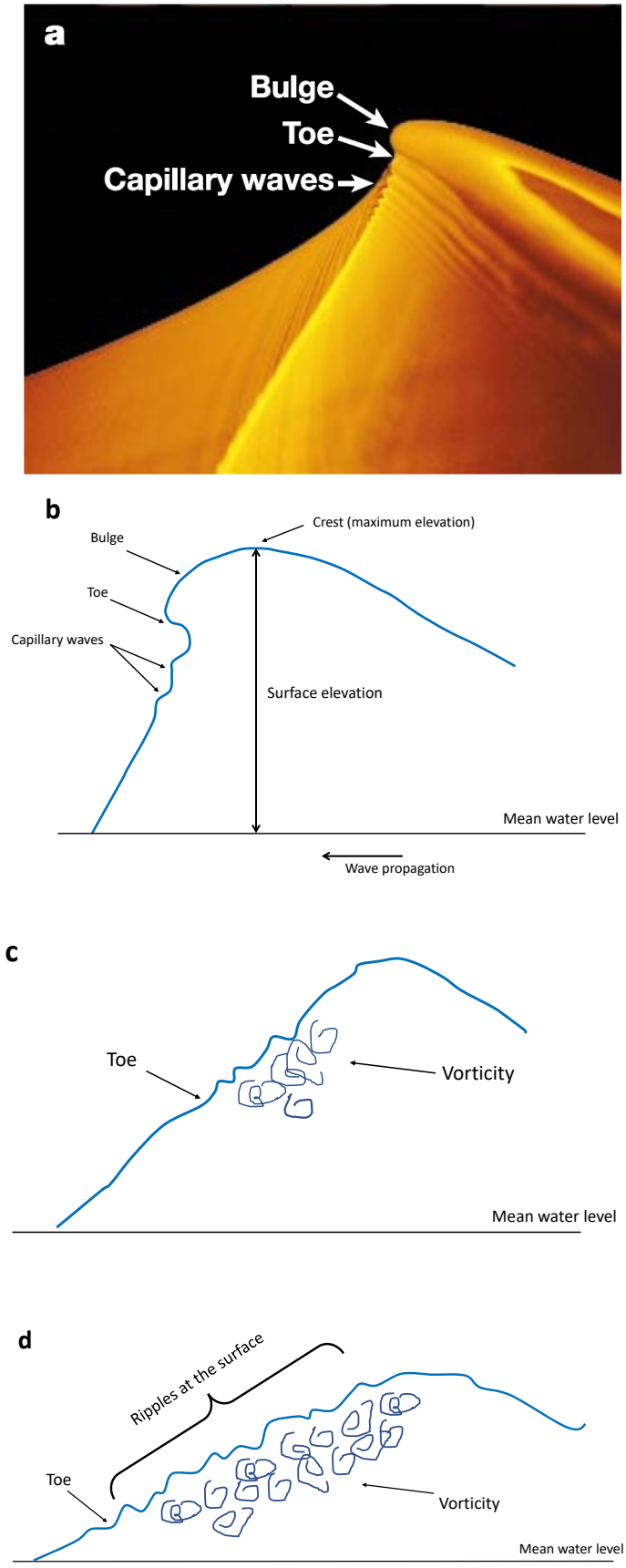

Figure 1.20: The evolution of a spilling breaker. (a) Image of the first evolution state, which was taken by Liu and Duncan (2003). (b)–(d) Schematic representations of the dynamics of the spilling breaker, which are adapted after Qiao and Duncan (2001).

The mechanism leading to the formation of spilling breaking waves is, however, less well understood (Duncan et al., 1994, 1999). Generally, spilling breakers in the open ocean are mostly driven by wind/sea surface drag, and foam, bubbles and turbulent water appear in the wave crest where spilling starts as a water sheet moves forward faster than the wave (Galvin, 1968).

In clean water, the spilling breaking waves break without the overturning of the free surface (Liu and Duncan, 2003, 2006). As the wave crest develops an asymmetric form (Qiao and Duncan, 2001), a bulge forms on the forward face of the wave crest and capillary waves upstream of the leading edge of the bulge (Duncan et al., 1994, 1999; Liu and Duncan, 2003, 2006). The leading edge of this bulge is called a toe (Liu and Duncan, 2003, 2006). An image (from the experiment conducted by Liu and Duncan (2003)) and a scheme of the wave with the bulge, toe and capillary waves are shown in Figure 1.20a and Figure 1.20b, respectively.

After a short time, the toe becomes sharp, a flow separation is triggered under the toe and turbulent vorticity develops (Figure 1.20c), while the toe rapidly moves down the wave face (Liu and Duncan, 2003, 2006; Qiao and Duncan, 2001). This flow separation (and the associated turbulent eddies) can be explained by a strong directional shear layer (the flow is reversed) between the descending toe and the upward flow of the underlying fluid (Qiao and Duncan, 2001). Liu and Duncan (2003) and Duncan et al. (1999); Liu and Duncan (2006) report that, as the toe moves down the wave face, ripples are generated between the toe and the crest (Figure 1.20d).

The resulting vorticity field generates a mixing region between the toe and the wave crest, at the air-sea interface and below the surface, where air is captured from the atmosphere and entrained down in the form of bubbles. Liu and Duncan (2003) studied spilling breaking waves in water contaminated by surfactants, and found significant changes in the breaking characteristics.

1.3.3 Bubble size distribution during breaking waves

Deane and Stokes (2002) observed 14 breaking waves and studied two mechanisms which determine the bubble size distribution during breaking waves. One mechanism is fragmentation in turbulence, which determines the size distribution of bubbles larger than about 1 mm,

resulting in the relationship between bubble density and bubble size described by a power-law of $-10/3$ (Deane and Stokes, 2002). The other mechanism is thought to be the result of jet and drop impact on the wave face, resulting in the bubble size varying with bubble density under a power-law of $-3/2$ (Deane and Stokes, 2002).

Since bubbles smaller than Hinze scale will not fragment, only bubbles larger than Hinze scale are susceptible to turbulent fragmentation (Deane and Stokes, 2002, 2008) because the distortion due to turbulence dominates the bubble surface tension. The Hinze scale is the bubble radius at which the distorting shear forces due to turbulent pressure fluctuations are balanced by the surface tension (Deane and Stokes, 2008), so the bubbles do not fragment further. The resulting bubble size distribution and the Hinze scale are shown in Figure 1.22.

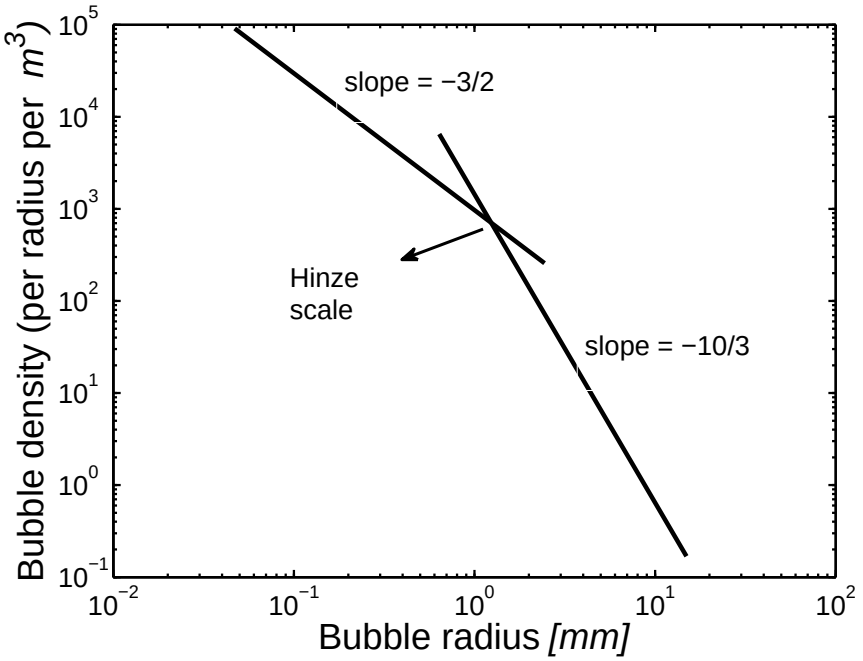

Figure 1.21: Two power-law fits estimating the shape of bubble size distribution. For bubbles smaller than about 1 *mm*, the power-law fit shows the bubble size distribution controlled by drop and jet mechanisms. For bubbles larger than 1 *mm* the power-law fit shows the bubble size distribution controlled by turbulent fragmentation. Fit lines copied from Figure 4 from Deane and Stokes (2002).

Mathematically, the bubble size distribution, $N(a)$, controlled by turbulence can be expressed in terms of wave breaking air volume entrained per volume of water per second, V_f (void fraction), and turbulent dissipation, ϵ_t, as follows (Deane and Stokes, 2002):

$$N(a) \propto V_f \epsilon_t^{-1/3} a^{-10/3}, \tag{1.58}$$

where a is the bubble radius. The bubble size spectrum controlled by jet and drop impact can be described for bubbles smaller than Hinze scale, where the surface tension β becomes important, as follows (Deane and Stokes, 2002):

$$N(a) \propto V_f \left(\frac{\beta}{\rho_w}\right)^{-3/2} v_j^2 a^{-3/2}, \tag{1.59}$$

where v_j is the jet velocity impacting the wave face, and ρ_w is the water density.

Void fraction, the gas volume occupied by bubbles in a given water volume sample, is a useful measure of bubble presence. Similar bubble size distributions where the Hinze bubble radius is also around 1 mm were also observed just below breaking waves (in alpha bubble plumes or shallow dense plumes) by Leifer et al. (2007). After the breaking-wave bubble creating mechanisms cease, the bubbles may become even smaller because they are compressed by hydrostatic forces as they are transported deeper. As will be shown in the results from chapters 5 and 6, these bubbles can persist for long times (tens of seconds to minutes) in the ocean, forming the plumes which are the subject of this thesis.

1.3.4 Breaking-wave statistics

Due to their rapid evolution and complicated fluid mechanical characteristics, breaking waves are difficult to characterise. The development of a statistical description of breaking waves is needed to understand the wave energy dissipation due to wave breaking, which influences the evolution of the wave spectrum (see Section 1.2.4.4) and is associated with turbulence and bubble production. In this section, the breaking-wave statistics are developed based on the theory proposed by Phillips (1985) in terms of breaking crest velocity, c_w, and breaking crest length per unit area, Λ_b (with units of m/m^2). With the latest development in imaging technology, the breaking crest velocity is a well defined quantity and can be measured by using, for example, infrared imaging which permits the tracking of image sequences of breaking crests moving over the sea surface during a time interval (Deike et al., 2017; Jessup et al., 1997; Zappa et al., 2012). On the other hand, Λ_b is much more difficult to measure, especially given its rapid change, because the thresholds, usually used to separate the breaking surface from a non-breaking surface, are mostly non-physical (although some are based on statistical inference) and are often arbitrarily chosen. Phillips (1985) proposed a way of indirectly deriving Λ_b mathematically considering the rate of energy loss in the equilibrium spectrum. The following

section will show that the fraction of whitecaps over the sea surface, produced by breaking crests, can be described by c_w and Λ_b.

The rate of spectral energy loss per each wave number element, dk_{wave}, is related to the rate of energy loss per unit area by wave breaking per crest velocity element, $\epsilon_b(c_w)dc_w$, as follows (Phillips, 1985):

$$\epsilon_b(k_{wave})dk_{wave} = \frac{1}{2}\epsilon_b(c_w)dc_w, \tag{1.60}$$

where the factor $1/2$ emerges if the direction of c_w varies between $-1/2\pi$ and $1/2\pi$, while that of k_{wave} ranges from $-\pi$ to π. Extracting $\epsilon_b(c_w)dc_w$ from Equation (1.60) and using the expression for the spectral energy loss from Equation (1.57) gives (Phillips, 1985)

$$\epsilon_b(c_w)dc_w = 4\gamma_d\ \mu_d^3(\cos\theta_{wave})^{3m}u_*^3c_w^{-2}dc_w. \tag{1.61}$$

The energy loss (dissipation), as a function of c_w, was quantified in terms of the temperature changes associated with the disruption and recovery of the surface thermal boundary layer, also known as the cool skin layer (Jessup et al., 1997).

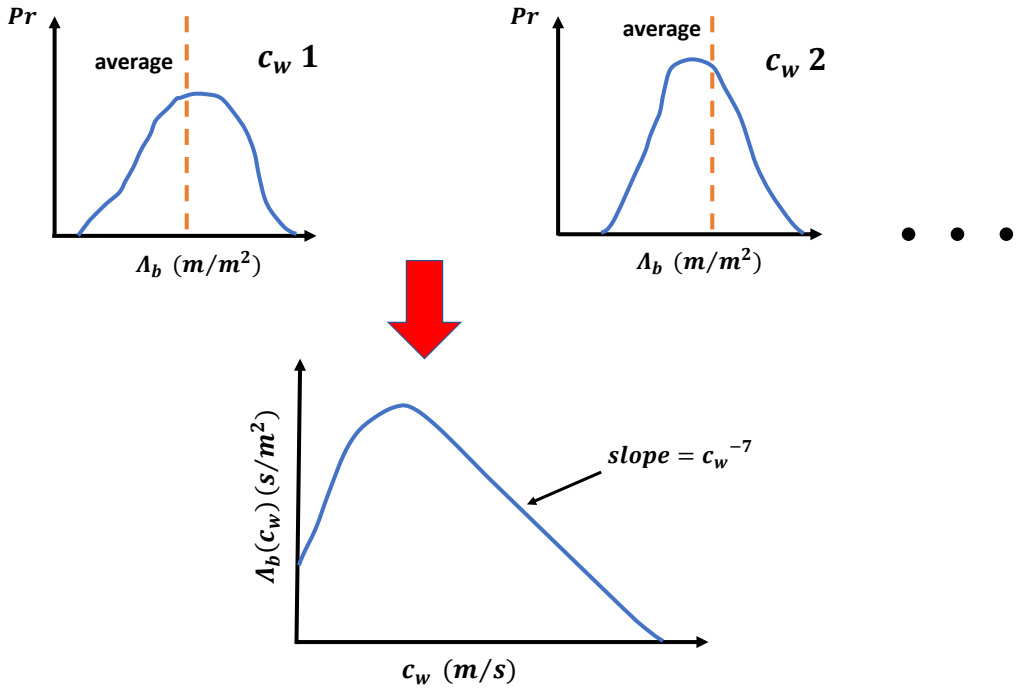

Figure 1.22: The derivation of the distribution of breaking crest length per unit area per velocity element. This continuous distribution (lower image) is created from the average values of breaking crest length per unit area for each possible crest velocity, as it is quantified by the probability density distributions (upper images). The approximate shape of the continuous distribution in the lower image (together with the c_w^{-7} slope) is adapted from Zappa et al. (2012).

Since the temperature of the cool skin layer is usually lower than the bulk temperature (in the water column few centimetres below), Jessup et al. (1997) used infrared imaging and observed that the cool skin layer can be momentarily disrupted by breaking crests, which overturn the free surface. This skin layer disruption is generated by turbulent mixing and energy dissipation, so the temperature is locally and momentarily increased.

The recovery time of the cool skin layer is associated with both the breaking crest velocity and energy dissipation (Jessup et al., 1997). This implies that faster breaking crests dissipate more energy, so will cause the recovery time of the cool skin layer to be delayed. The rate of energy loss per unit area by breakers moving with velocities between c_w and $c_w + dc_w$ is related to the distribution of breaking crest length per unit area per velocity element, $\Lambda_b(c_w)$, as following (Phillips, 1985):

$$\epsilon_b(c_w)dc_w = br\ g^{-1}c_w^5\Lambda_b(c_w)dc_w, \tag{1.62}$$

where br is a breaking-wave numerical constant determined in the laboratory (Duncan, 1981). Using the definition given in Equation (1.61), $\Lambda_b(c_w)$ can be extracted from Equation (1.62), and has the following form (Phillips, 1985):

$$\Lambda_b(c_w) = (4\gamma_d\ \mu_d^3\ br^{-1})(\cos\theta_{wave})^{3m}u_*^3 g\ c_w^{-7}. \tag{1.63}$$

Zappa et al. (2012) fitted breaking-wave observations to the $\Lambda_b(c_w)$ distribution, which shows that the distribution has a peak at low-mid-range crest velocities, followed by a steep decrease, with a slope of approximately c_w^{-7}, in the mid-high range crest velocities (Figure 1.22).

The total breaking length per unit area per velocity element, L_b, can be found by calculating the area under the $\Lambda_b(c_w)$ distribution curve as following (Phillips, 1985):

$$L_b = \int_0^\infty \Lambda_b(c_w)dc_w, \tag{1.64}$$

1.3.5 Whitecap fraction

The whitecap fraction is the proportion of surface area covered by bubbles (Phillips, 1985). Whitecap fraction can be assumed to vary with the spatial extension of the turbulent wake, as energy is dissipated by breaking crests that travel with different velocities. Most of the turbulent wake signatures of breaking crests, observed by Jessup et al. (1997), are approximately

circular, suggesting that the wake's dimension in the direction of the propagation can be approximated by the length of the breaking crest (Jessup et al., 1997). If bubbles, generated in the turbulent wake of the breaking crest (moving with a velocity c_w), persist for an average time, t_w (called whitecap decay time), on the sea surface, then the whitecap fraction (which is a non-dimensional quantity) is defined as (Phillips, 1985)

$$W_f = \int c_w \; t_w \; \Lambda_b(c_w) dc_w. \tag{1.65}$$

Whitecap fraction is perhaps the most frequently used breaking wave statistical quantity to indirectly parameterise bubble-mediated gas transfer by comparing it against wind speed, sea state or wave Reynolds number. However, the structure and statistics of bubble plumes, which contain and preserve the gas extracted by the breaking waves, are very poorly studied in relation to whitecaps. Little is known about the bubble-plume processes below breaking waves and whitecaps, so current attempts in quantifying the bubble-mediated gas transfer in terms of whitecap fraction, under the forcing of wind speed and sea state, ignore the direct mechanisms causing the gas flux. Therefore, additionally to whitecap fraction, a direct investigation of the dynamics and behaviour of bubble plumes with environmental conditions is clearly needed to better understand the gas content and saturation caused by breaking waves.

Optical imaging is the most commonly used for quantifying whitecap fraction over the sea surface. Individual whitecaps can be separated from the background water following a threshold algorithm (Callaghan et al., 2012), which is a widely used technique. This image analysis method identified supra-threshold regions associated with individual foam patches (Callaghan et al., 2012). The whitecaps are spatially patchy, so a single breaking wave is usually composed of multiple foam patches. The whitecap was identified from the breaking starting point (which is associated with uncertainty, as discussed earlier) until the foam had fully decayed, partially advected out of the image frame or was replenished by foam from a new breaking wave (Callaghan et al., 2012). Other techniques, such as the one proposed by Scanlon and Ward (2013), combine location relative to the crest, texture, shape and pixel intensity of each whitecap to separate them from the background water. Using these methods, the evolution of whitecap coverage can be quantified as varying from active (during wave breaking) to maturing (post wave-breaking, so the foam patch expands as an effect of surface dynamics) whitecaps. Given their transient nature, it is generally difficult to isolate the active whitecap fractions from

the total whitecap fraction – a high speed and high resolution whitecap camera is needed to record each small increment in the evolution of a whitecap.

One of the most important properties of whitecaps is the decay time, which can be extracted from the time evolving whitecap area by using a simple exponential model implemented as following (Callaghan et al., 2012):

$$A(t) = A_0 \exp \frac{-t}{t_w}, \tag{1.66}$$

where $A(t)$ is the time evolving area of whitecap foam during the decay phase, t is time where $t = 0$ occurs at the time when the foam patch area is at its maximum value A_0, and t_w is the whitecap decay time constant that usually ranges from 0.2 s to 10.4 s at wind speeds varying between 5.7 m/s and 13.7 m/s (Callaghan et al., 2012).

During the active breaking phase, the largest bubbles (larger than Hinze scale) having the highest rising speeds due to strong buoyancy, rapidly rise back at the sea surface (before turbulent fragmentation affects them) to feed the whitecaps. During the foam decay in the quiescent (post wave breaking) phase, the risen bubbles have fully formed the whitecap, but it is not clear if the bubble feeding from below has ceased. More direct ocean observations are needed to better understand this mechanism, as the current literature is very scarce in explaining this bubble feeding mechanism.

1.4 Bubble plumes

Bubble plumes are referred to in this thesis as the significantly more diffuse (lower bubble density) and deep plumes that occur after wave breaking has ceased. As shown in the previous section, the dense bubble plumes occurring during wave breaking are closely controlled by breaking-wave characteristics and wave breaking turbulent dissipation. However, the post-breaking fully-developed plumes are no longer directly controlled by wave breaking and intense dissipation, since they evolve a long time after the wave breaking processes cease, and their controlling mechanisms are still poorly understood. There are many interacting processes (physical, chemical and biological) that can influence the structure of bubble plumes. In this thesis, the effects of physical wind/sea state processes on plumes are explored, while acknowledging the contribution of other processes like gas solubility and biological activity.

Since the post-breaking fully-developed plumes are diffuse enough to be measured acoustically, subsurface bubbles and plumes are almost exclusively measured by sonars and other similar acoustical devices such as echo-sounders and ADCPs (Acoustic Doppler Current Profiler). These acoustical devices are an appropriate measurement technology at these low void fractions, partly because at higher void fractions the acoustical signals are completely absorbed.

1.4.1 Plume dynamics, structure and statistics

High temporal resolution analysis of individual bubble plumes can reveal the deepening rate of plumes with time. Open ocean observations show that bubble plumes generally start to deepen from a shallow bubble layer of about 1–2 metres (Crawford and Farmer, 1987; Dahl and Jessup, 1995; Farmer and Vagle, 1989; Thorpe, 1982; Zedel and Farmer, 1991) down to a maximum depth varying from about 3–4 metres (Thorpe, 1982) to 5–6 metres (Crawford and Farmer, 1987; Dahl and Jessup, 1995; Zedel and Farmer, 1991) and 7–8 metres (Farmer and Vagle, 1989) over a time span ranging between about 10–20 seconds (Crawford and Farmer, 1987) and up to 1-2 minutes (Dahl and Jessup, 1995; Farmer and Vagle, 1989; Thorpe, 1982; Zedel and Farmer, 1991). A diagram showing the evolution of a bubble plume long after the wave breaking moment, is shown in Figure 1.23. These kind of bubble plumes reach maturity and maximum penetration depth as they become more diffuse and can persist for a long time in the ocean.

The plume occurrence can be more periodic as Langmuir circulation – which is composed of circulation cells that converge at the sea surface where foam bands with a specific spacing are created – drag bubbles downward to form deep plumes (Zedel and Farmer, 1991). Turbulent overturning can also move bubbles downward. In some cases, the periodicity of bubble plumes appears to be connected to the spacing of Langmuir circulation foam bands that occur at the sea surface (Zedel and Farmer, 1991). Bubble plumes associated with Langmuir circulation bands were also observed by Osborn et al. (1992), however there is no clear evidence of a direct influence of Langmuir circulation on the downward spreading of bubbles, since the dataset is too small for a relevant statistical analysis. Osborn et al. (1992) observed bubble plumes penetrating down to 2–3 metres on average. Using the variation in the range of the

surface signal of a sonograph mounted on a submarine, Osborn et al. (1992) visually detected the individual bubble plumes as streaks of acoustic reflections apparently approaching the submarine.

Open ocean observations over long time periods (up to one month) reveal that the penetration depth of individual plumes varies, on average, between around 0 and up to 10 metres (Vagle et al., 2010). Many plume depth observations in this study were close to zero. The same is the case with the study conducted by Trevorrow (2003), who observed individual plumes penetrating, on average, between close to 0 and 10–12 metres. Since these individual plumes were statistically classified as such if the bubble penetration depth exceeded the mean plus 1 standard deviation (Trevorrow, 2003; Vagle et al., 2010), the plume depth can show anomalously low values (close to zero) which cannot physically contribute to the overall statistics. A depth threshold criteria can be used to identify individual plumes with non-zero penetration depth values, such as a novel technique, based on the comparison between independent sensor measurements, as it is proposed in this thesis (see Section 3.7). A wide plume maximum penetration depth range of 10 to 20 metres was observed by Thorpe (1992).

These plume depth observations show strong variations due to different types of acoustical devices and criteria of plume identification used by the above authors. The large observed plume depth range also depends on the varying wind speed and sea state conditions in which plumes were measured. The difficulty in comparing the above studies of bubble plumes is that the sonars all had different frequencies, and the threshold chosen for the edge of a bubble plume was arbitrary.

Following the discussion above, a schematic diagram showing the evolution stages of a bubble plume from the moment of wave breaking is presented in Figure 1.23. The stages comprise the short period of the highly dense shallow plume lasting for only 1–2 seconds, the period of plume deepening lasting for 10–30 seconds, and the period of the fully-developed diffuse bubble plume lasting tens of seconds to minutes or even tens of minutes.

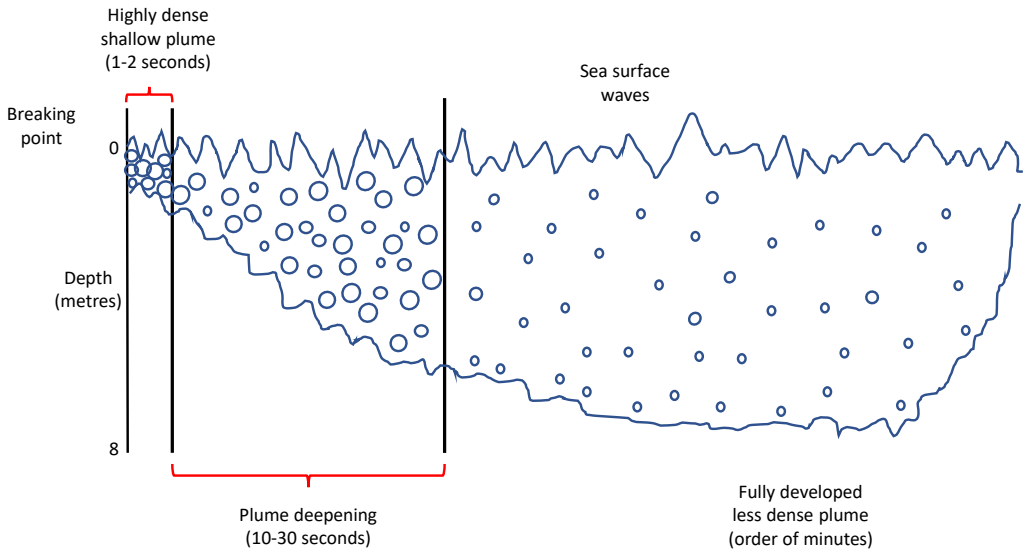

Figure 1.23: A diagram of the current understanding of the main evolution stages of a bubble plume from the moment of wave breaking.

The duration of individual bubble plumes, defined as the time interval between plume detection and plume vanishing (from the sonar's field of view), was observed in the open ocean to vary from about 10 to 80 seconds (Trevorrow, 2003), 20 to 70 seconds (Vagle et al., 2010), and 20 to 55 seconds (Osborn et al., 1992). The possible dependence of plume duration on air-sea interaction processes have not been found in the literature. Trevorrow (2003) only analyzed the relationship between plume duration and plume depth, which showed a mildly increasing trend of plume duration with plume depth, but with a large variability especially at larger values.

The plume production or frequency (number of plumes in a given time interval) can be used to understand how individual plume dynamics is connected to bubble injection by breaking waves under the forcing of wind speed and sea state. There are very few observations of plume frequency in the open ocean. Trevorrow (2003) and Vagle et al. (2010) reported tens of plumes produced in one hour. Moreover, there are some other plume frequency observations conducted by Thorpe and Humphries (1980) in the Loch Ness lake. Plume frequency (in *Hz*) was generally observed to vary between about 0.005 and 0.02 *Hz* (Thorpe and Humphries, 1980), indicating that plume occurrence is quite rare. Since, in this case, the measurements have been conducted in a lake (fresh water), the plume frequency may differ in a salty water environment (open ocean) where bubbles could persist for longer times.

However, there are relatively few plume frequency observations in relation to wind speed and sea state in the open ocean – with the associated possible environmental influences on plume frequency. For example, Thorpe and Humphries (1980) observed plume frequency (in *Hz*) variation with wind speed in a lake. A total of only nine observations averaged over 20 minutes were recorded – even so, plume frequency increased from about 0.006 *Hz* to 0.018 *Hz* as wind speed grew from about 6 to 12 m/s (Thorpe and Humphries, 1980).

The intrinsic structure of plumes can be quantified by detecting the acoustical scattering signal from the bubbles. As it will be shown in Section 2.4, the scattering signal inside plumes can be obtained by integrating the scattering cross-sections of bubbles along the water column where the plumes are present, yielding the quantity known as the volume scattering cross-section. Most authors use volume backscatter cross-section (given in units of decibels *dB*), which is the volume scattering signal generated by bubbles within plumes that reaches back to the sonar transducer. The volume backscatter cross-section is used to quantify the bubble physics within plumes, since the backscatter signal is sensitive to bubble size, compressibility and density. The backscatter signal within the bubble plumes decreases from close to the sea surface with increasing depth. There are measurements showing various maximum-minimum ranges of backscatter values. The backscatter signal within plumes can vary between about -15 and -50 *dB* (Farmer and Vagle, 1989; Thorpe, 1982; Vagle and Farmer, 1998). Lower backscatter values within plumes ranging between -30 and -60 *dB* have been observed by Trevorrow (2003). Larger range of backscatter signal (varying from -10 to -60 *dB*) was recorded in bubble plumes by Vagle et al. (2010).

The backscatter signal within the bubble layer has been found to approximately decrease exponentially with depth via fitting an exponential function to the observed backscatter values (Crawford and Farmer, 1987; Graham et al., 2004; Trevorrow, 2003; Vagle et al., 2010; Wang et al., 2011). The function that describes the rate of exponential decay of the backscatter signal over a given depth is known as e-folding depth (in metres). E-folding depth was found to increase within plumes that penetrate deeper, varying from about 0.1 to 2.7 metres (Crawford and Farmer, 1987; Graham et al., 2004; Trevorrow, 2003; Vagle et al., 2010; Wang et al., 2011). Larger values of e-folding depth indicate stronger bubble entrainment as larger backscatter signal propagates down the water column when plumes penetrate deeper. The bubble concentration variation with depth within entire plumes can be modeled using a combi-

nation between bubble density estimates at different local depths and continuous backscatter measurements within the plumes (Crawford and Farmer, 1987). However, the bubble density was estimated from a model of probability distribution as a function of bubble radius, not from a direct measurement from an independent sensor. This limitation can skew the estimation of the real bubble density when the ratio of large bubbles to small bubbles changes, which often occurs in the real ocean.

1.4.2 Wind speed and sea state dependencies of bubble plumes

There are only few studies that quantitatively assess the influence of wind speed on plume parameters in the literature. Within a low wind speed range, the plume penetration depth has been observed to increase from about 1 metre to 4.5 metres as wind speed increased from about 4 m/s to 12 m/s. These observations were conducted in the fresh water of lake Loch Ness by Thorpe (1982), so they may show some differences, in terms of plume depth rate of increase with wind speed, when compared to measurements in the open ocean. Extending the observations to a larger wind speed range and, but this time in the salty water just off-shore Oban, plume penetration was observed to also increase from about 1 metre to almost 10 metres as wind speed increased from about 3 m/s to almost 16 m/s (Thorpe, 1982). However, since these observations are close to the shore, the characteristics of wave breaking may differ, hence influencing the bubble injection and subsequent plume dynamics. Open ocean observations at high wind speeds (> 20 m/s) reveal an approximately linear increase of plume penetration to a maximum depth of about 10 metres as wind speed reaches 22–23 m/s (Vagle et al., 2010). Some variability was present in the relationship, as shown by $R^2 = 0.7$, but many data points were used, thus improving the significance of the relationship.

Plume depth measurements during the passage of a hurricane were reported by Wang et al. (2011), showing an increase in plume depth from about 5–6 metres to 25 metres as wind speed increased from about 12–13 m/s to 45 m/s. Wang et al. (2011) also observed that plume depth shows a weaker dependence on wind speed during steep both falling and rising winds (before and after the hurricane's eye). This may be caused by a delay in plume penetration as wind speed steeply shifted over a short time interval. Given the scarcity in the literature, clearly more observations of plume depth, duration and frequency variation with wind

speed in the open ocean and at higher wind speeds are needed to fill the lack of understanding of plume dynamics within a broad wind speed range.

Observations showing the dependence of subsurface bubbles on wave state are even more elusive in the literature. Wang et al. (2011) qualitatively observed an increasing trend of the bubble penetration depth down to about 20–25 metres as significant wave height increased to roughly 16–18 metres. Depending on wind speed, the bubble penetration depth is differently connected to the significant wave height H_s (Thorpe, 1992). At a wind speed of 6.9 m/s, the bubble penetration depth that reaches about 5 metres and 9–10 metres is equal to two times significant wave height ($2H_s$) and four times significant wave height ($4H_s$), respectively (Thorpe, 1992). As wind speed increases to 13.3 m/s, the wave states represented by $2H_s$ and $4H_s$ are now equivalent to a deeper bubble layer of 8 and 16 metres, respectively (Thorpe, 1992). A comparison of bubble layer depth against significant wave height and wave breaking frequency was reported by Farmer et al. (1993). The bubble layer depth gradually increased down to about 10 metres as significant wave height grew to almost 2 metres while wind was blowing at 12–14 m/s (Farmer et al., 1993). However, wave breaking frequency was only observed toward the end of the bubble layer evolution (when it already showed maximum penetration), not over the entire bubble penetration depth spectrum, so no clear trend of bubble layer depth with wave breaking frequency can be inferred from the results reported by Farmer et al. (1993).

This thesis will bring together independent records of bubble parameters, mentioned in the last section, wind speed, sea state and breaking waves to fill in the gaps in the understanding of the complex influence of meteorological and sea state processes on bubble-plume dynamics/evolution. This research is of even higher impact because these observations were collected within a large wind speed range (8–30 m/s) and complex wave field variability (with periods of interacting wind-sea and swell waves), conditions during which air-sea gas transfer presents a significant uncertainty.

1.5 Thesis plan

The main techniques for detecting and characterising bubbles, used in this thesis, are based on a sonar. Therefore, the fundamentals of underwater acoustics, like the propagation of sound and the properties of sound emission, the basic sonar functionality predicted by the sonar

equation, and the types of sonar used in the ocean are introduced in the first part of chapter 2. The last part of chapter 2 is dedicated to the detailed and comprehensive description of the literature containing many contributions on the acoustics of bubbles, where all the equations for computing the scattering cross-section from bubble populations are introduced.

The experimental design, with the utility of the measuring sensors attached on a floating spar buoy, are presented in chapter 3. Details on the functionality of the Delta T sonar, along with the measuring and post-processing sonar data techniques are also introduced in chapter 3. In the last part of chapter 3, a technique is developed for combining the sonar calibration characteristics obtained in Scandella et al. (2016) and bubble-plume sonar echo intensity signal for obtaining plume scale vertical sections of backscattering cross-section per unit volume. A simple signal filtering technique for detecting the bubble layer/plume base and its comparison to void fraction recorded, at different depths, by an underwater bubble camera and resonator are discussed in chapter 3.

Chapter 3 continues with the development of a technique for retrieving the sonar backscatter vertical profiles and bubble layer penetration with respect to the instantaneous sea surface. This approach will correct for the non-stationary sea level, providing a more realistic bubble dynamics below the real sea surface and not a stationary mean sea level. The backscatter output is used to quantify the exponential decay with depth of backscattering signal in bubble plumes. This backscatter exponential decay is described by a parameter called e-folding depth, which is sensitive to bubble entrainment in the water column. Chapter 3 ends with the description of an algorithm for the detection of individual bubble plumes combining simultaneous records from the sonar and resonator. This method enabled the computation of the variables characterising the bubble plume structure, which are the penetration depth, duration and production rate (frequency – number of plumes per hour) of bubble plumes.

Chapter 4 is mainly dedicated to the analysis of the change, in time, of the backscatter structure in varying wind and wave conditions. To parameterise the backscatter effects, the influence of wind speed and sea state on e-folding depth are statistically assessed in chapter 4. The analysis of the dependence of bubble plume structure on wind speed and sea state mainly composes chapter 5. Finally, chapter 6 was reserved for the analysis of four case studies where individual breaking wave events were compared with coincident subsurface bubble profiles; the breaking waves were analysed from photographic (a Foam Camera imaging the

sea surface) records, and the subsurface bubble measurements were extracted from a sonar. The kinematics and structure of individual bubble plumes evolving from initial breaking waves, along with possible plume lateral advection are discussed in chapter 6. The sonar performance during strong acoustical attenuation (and even extinction of backscatter signal), caused by expected high void fraction, is also discussed in chapter 6. The variation of backscatter signal, in the uppermost metre and full water column, with whitecap fraction is analysed towards the end of chapter 6.

Chapter 2

Underwater acoustics

2.1 Introduction

Underwater acoustics is used in a large range of applications, including scientific oceanographic research (such as observing the seabed structure, studying the shape and density of fish schools, and locating phytoplankton) and military applications (such as the underwater detection of weaponry and submarines).

This chapter will review the literature of underwater acoustics and set out the mathematical basis for the acoustics used in this thesis. In Section 2.2 the propagation of sound in the ocean will be discussed and mathematically described in terms of the acoustic wave equation. Using the water equation of state, the expression for the speed of sound, which is a key parameter in acoustical oceanography, has been also derived. Section 2.2 continues with the description of the main properties of sound, a necessary foundation for studying acoustical scattering and attenuation effects in bubbly water.

Sonar technology and functionality are further discussed in the following section. The return acoustic signal from a sonar transducer to a target in the ocean is mathematically described in terms of sonar equation.

The last part of this chapter will cover bubble acoustics in the ocean. The development of acoustical techniques will be extensively covered, starting from the acoustical characterisation of a single bubble oscillating in water and continuing towards the characterisation of entire bubble populations present within a given sample volume. The description of these bubble

acoustics techniques are the foundation for the methods that were developed in this thesis to quantify the scattering generated by many bubbles within the entire water column, with essential implications in the acoustical analysis of bubble presence. Acoustical measurements are sensitive to the attenuation caused by large bubble populations. The acoustical implications of sound speed variation and signal loss inside bubble assemblages of different densities will be discussed at the end of this chapter.

2.2 Underwater sound

2.2.1 Propagation of sound

Sound in water can be emitted by natural and artificial sources, but the most common method of generating artificial sound is using a device called transducer. A transducer is a device that converts one form of energy (such as a physical signal) into another. The main transducer types are defined as following:

- A uni-directional transducer (sensor) is a device that only receives a signal from a physical system. It converts the physical signal into an electronic signal, which can be used to infer the original source.
- A bi-directional transducer is a device that converts a type of physical signal into an electrical signal, and can also convert the electrical signal into a physical signal.

An acoustical transducer is the bi-directional type and is often composed of a quartz crystal (Leighton, 1994), a polycrystal (Medwin and Clay, 1997) or a ceramic material. This material deforms in shape when an electrical field is applied to it, and also generates a voltage signal when it is deformed by external processes. This leads to material displacements perpendicularly along the surface of the transducer.

After each displacement, the transducer is restored to the initial position and the process is repeated (Figure 2.1). These displacements are similar to the motion of a piston, which pushes the water particles (considered as very small water elements) further from the transducer, compressing them in in a direction perpendicular to the direction of travel (Figure 2.1). The compression peaks in these bands, also referred to as wave fronts, are described by the wave

pressure amplitude. The expansion region between two wave fronts is known as rarefaction and has lower pressure and density.

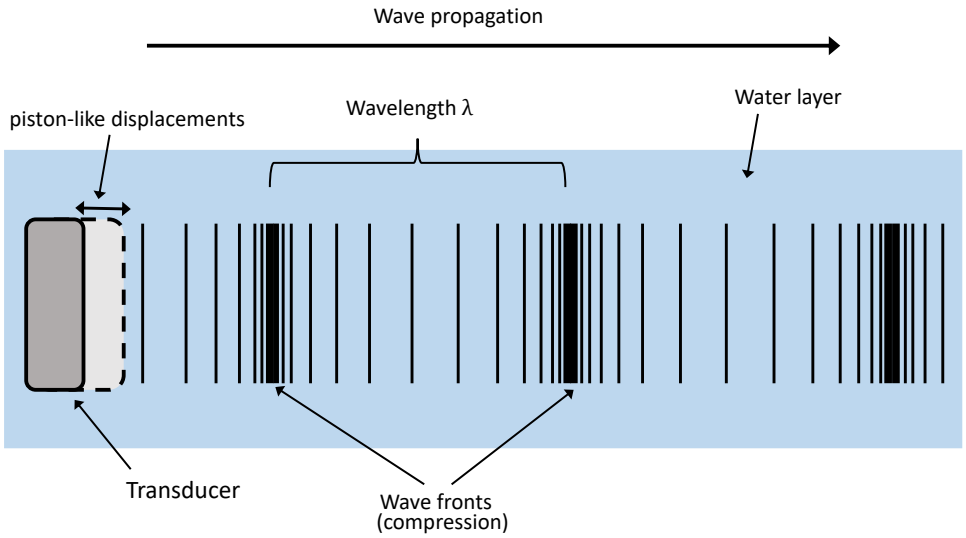

Figure 2.1: Simplified representation of the process of sound wave generation by a transducer with the associated propagation of sound. The line spacing indicates the magnitude of the relative pressure.

The distance between two wave fronts is the wavelength λ, which corresponds to a full oscillation cycle. The number of wave cycles passing a fixed point in one second is the frequency, f, and it is equivalent to the number of particle cycles in one second. Sound propagation depends on the pressure gradient between compression and rarefaction regions. The particles are accelerated from the higher pressure region (wave front) to the lower pressure region (rarefaction), and the process is repeated. This forces the particles to oscillate back and forth, while transferring momentum to neighbouring particles, so the wave continues to propagate. For sound to be generated, the distances over which the density and pressure change must be much larger than the distances over which the particles travel before colliding with other particles.

2.2.1.1 Acoustic wave equation

The acoustic wave equation describes the propagation of sound in a given medium. This equation predicts the evolution of pressure amplitude as a function of position and time. The derivation presented here follows that by Medwin and Clay (1997) and will consider a one-dimensional wave, but can be generalized to three dimensions.

Let us consider a region in a compressible medium (water) having volume ΔV, over which density and pressure change along direction x. The density, ρ, and pressure, p, result from the disturbances induced by sound propagation within the medium (Medwin and Clay, 1997). The density is a small increment (perturbation) relative to the ambient density (of the medium) ρ^*, so the total density is $\rho_t = \rho^* + \rho$, where $\rho \ll \rho^*$. The same is valid for the total pressure, which is $p_t = p_a + p$, where $p \ll p_a$.

2.2.1.2 Newton's second law

Given a fluid volume, $\Delta x \Delta y \Delta z$, the force acting on the fluid volume, F, is the difference between the pressure acting on the left hand-side of the fluid volume and the pressure acting on the right hand-side of the fluid volume (at this point, the pressure has changed with the width Δx of the fluid volume) along direction x,

$$F = p\ \Delta y \Delta z - \left(p + \frac{\partial p}{\partial x} \Delta x \right) \Delta y \Delta z. \tag{2.1}$$

Rearranging and dividing Equation (2.1) by the volume $\Delta x \Delta y \Delta z$, the force is then expressed as the pressure gradient on the horizontal (along direction x),

$$F = -\frac{\partial p}{\partial x}, \tag{2.2}$$

where the negative sign, on the right hand-side, indicates that the overall force F acts to compress the fluid volume (two opposing forces act on both sides of the fluid volume). Applying Newton's second law, $F = m\ddot{x}$ (where $\ddot{x}$ is the Newton's notation for the second derivative of x with respect to time), the net force above applied to the fluid particle is proportional to the particle acceleration (Medwin and Clay, 1997),

$$-\frac{\partial p}{\partial x} = \rho^* \frac{\partial u}{\partial t}, \tag{2.3}$$

where $\partial u / \partial t$ is the particle acceleration given by the partial time derivative of velocity u, ρ^* is the ambient density, and the increment of volume, ΔV, was cancelled from both sides of the equation.

2.2.1.3 Conservation of mass

The water particles disturbed by a sound wave move over a short distance across the fluid volume, but there is no net particle movement over many cycles. During this process, the

density due to the acoustical wave, within the volume, increases as $\partial\rho/\partial t\Delta V$ (Medwin and Clay, 1997). While the density increases, the net flow of particles (net mass flow) decreases as $-\rho^*\ \partial u/\partial x\ \Delta V$ (Medwin and Clay, 1997). Equating these variations provides the equation for conservation of mass inside the fluid volume,

$$-\rho^* \frac{\partial u}{\partial x} = \frac{\partial \rho}{\partial t}. \tag{2.4}$$

2.2.1.4 Equation of state

The equation of state for acoustics relates pressure p and strain (relative change in dimension) to the relative change of density ρ/ρ^* (Medwin and Clay, 1997). The bulk modulus, K, describes the resistance of a medium (such as water) to compression, and a large K indicates a less compressible medium. For small changes in ρ^* and p, the relationship between pressure and relative change in density is linear, as shown by the following equation:

$$p = \left(\frac{K}{\rho_a}\right)\rho. \tag{2.5}$$

The above equation is also known as the acoustic equation of state and is taken from the work conducted by Medwin and Clay (1997).

By operating on Equation (2.3) with the spatial partial derivative $\partial/\partial x$ and on Equation (2.4) with the time partial derivative $\partial/\partial t$, all physical laws described above can be combined to obtain the 1-dimensional wave equation as a second order partial differential equation,

$$\frac{\partial^2 p}{\partial x^2} = \frac{\rho^*}{K}\frac{\partial^2 p}{\partial t^2}. \tag{2.6}$$

A similar derivation as for Equation (2.6) can be employed for parameters such as ρ and velocity u. However, the above expression is the most suitable for acoustical study because pressure can be measured most easily.

2.2.1.5 Speed of sound

The speed of sound depends on the bulk modulus of the medium, K, defined above. Therefore, sound speed increases in a less compressible medium such as water (compared to air), and the 1-dimensional wave equation can be written in terms of sound speed as

$$\frac{\partial^2 p}{\partial x^2} = \frac{1}{c^2}\frac{\partial^2 p}{\partial t^2}, \tag{2.7}$$

where the sound speed c can be derived as

$$c = \sqrt{\frac{K}{\rho^*}}. \tag{2.8}$$

This definition implies that the sound speed in bubbly water can be significantly different to bubble-free water because of high bubble compressibility. This effect will be discussed in more detail in Section 2.4.2.2, where specific expressions will be derived.

2.2.1.6 Acoustic impedance

The distance over which the particle displacement occurs is labeled E, which is along the direction of wave travel. A one-dimensional and time dependent sinusoidal wave can be expressed as

$$E = E_0 \sin(kx - \omega t), \tag{2.9}$$

where E_0 is the wave amplitude, $k = 2\pi/\lambda$ is the wave number (in radians per metre), and $\omega = 2\pi f$ is the angular frequency (in radians per second); where f is the acoustical frequency. Taking the derivative of displacement E with respect to time gives the particle velocity in a harmonic wave,

$$u = \frac{\partial E}{\partial t} = -E_0\, \omega \cos(kx - \omega t). \tag{2.10}$$

When compressibility is considered, the velocity of water particles is related to the acoustic pressure in a harmonic wave,

$$p = -K\frac{\partial E}{\partial x} = -K\ E_0\ k \cos(kx - \omega t). \tag{2.11}$$

The meaning of the negative sign in Equation (2.11) is that the bulk modulus acts to reduce the displacement because it is a restoring force. The acoustic impedanceis defined as the ratio between applied pressure and the particle velocity, $Z = p/u$. This quantity is constant in water when there are no scatterers along the path. Substituting, in Z, the pressure p and velocity u with definitions from Equation (2.10) and Equation (2.11) respectively, gives

$$Z = \frac{Kk}{\omega}. \tag{2.12}$$

Let us consider the expression of speed of sound in Equation (2.7) with the expression of sound speed in terms of angular frequency and wave number, $c = \omega/k$. Substituting these in Equation (2.12) gives the relationship of impedance to ambient density and sound speed,

$$Z = \rho^*\ c. \tag{2.13}$$

The sound signal propagation is strongly affected at boundaries, where there is a high impedance gradient. An example would be the boundary between water and air, such as the sea surface, which produces a region of high sound reflectivity.

2.2.2 Properties of sound

2.2.2.1 Intensity of sound

The sound intensity is related to the pressure amplitude (acoustic pressure within wave fronts), and it is defined as the total energy (in Joules) crossing a unit area (1 m^2) per second. Intensity is the product of the particle velocity and pressure amplitude,

$$I = p\ u, \tag{2.14}$$

which gives the instantaneous sound intensity value (measured at one time instant). The definition of impedance leads to the following relationship:

$$p = \rho^*\ c\ u. \tag{2.15}$$

By extracting particle velocity u from Equation (2.15) and combining it with Equation (2.14), the relationship of instantaneous intensity and pressure amplitude p can be defined in a non-linear manner as

$$I = \frac{p^2}{\rho_a\ c}. \tag{2.16}$$

A relative unit of measure that is often used in measuring sound pressure level is the decibel (dB). However, care is needed because the reference pressure is different in air and water. The sound pressure level, SL, in dB, generated by a transducer, is the logarithmic ratio of the acoustic pressure, p, to a reference pressure, p_0, at a reference distance of 1 m,

$$SL = 20\ \log_{10}\left(\frac{p}{p_0}\right), \tag{2.17}$$

where p_0 is $20\ \mu Pa$ in air and $1\ \mu Pa$ in water. Therefore, when describing quantities such as the sound pressure level, the decibel is referenced to a pressure of $1\ \mu Pa$. The full expression is, then, dB relative to $1\ \mu Pa$ ($dB\ re:1\ \mu Pa$) when measuring a quantity. Sound usually occurring in ocean has a low pressure amplitude (in the order of $10^{-6} - 10^{-9}\ Pa$). For example, the sound generated by many bubbles at about one meter in depth and at distance from sound source of $8 - 10$ metres can reach about $-15\ dB\ re:1\ \mu Pa$, which is equivalent to $1.8 \times 10^{-7}\ Pa$. This

is a very small pressure, although the value of -15 *dB* is considered a loud sound in terms of passive bubble-plume measurements. However, when measuring bubbles in the ocean, another logarithmic quantity, known as the backscatter cross-section per unit volume, is often used (see Section 4.1). In this case, the decibel value is referenced to the bubble cross-section per unit volume.

2.2.2.2 Sound attenuation

The attenuation of sound represents the loss of energy as a wave propagates. Attenuation due to dense bubble populations will be considered in Section 2.4.2.2. Here, we only consider the simple attenuation along a path of bubble-free water. The total three-dimensional sound attenuation α_t is the result of the attenuation due to absorption α_a, the attenuation due to geometric spreading α_g and the attenuation due to scattering α_s,

$$\alpha_t = \alpha_a + \alpha_g + \alpha_s. \tag{2.18}$$

The quantity α_t can be used to assess the attenuation in time of a sinusoidal wave of amplitude E expressed as $E = E_0 e^{-\alpha_t t}$. Acoustical extinction is the sum of the scattering and absorption terms outlined in right hand-side of Equation (2.18).

2.2.2.3 Sound absorption

At higher frequencies, more energy is lost from a sound wave through the conversion of mechanical energy into heat. This leads to a typically linear increase in absorption rate for higher frequency sounds relative to lower ones. The absorption coefficient for seawater α is equal to about 4.6×10^{-2} dB/m at an acoustic frequency of 119 *kHz* (Clay and Medwin, 1977; Crawford and Farmer, 1987). The acoustic signal loss due to thermal and mechanical damping coefficients will be discussed further in Section 2.4.2.

2.2.2.4 Geometric spreading

Sound waves travelling from a sound source spread as they move outwards. The sound attenuation increases with sound wave spreading because of the increasing of area covered by the wave front. The pressure amplitude is inversely proportional to the distance travelled (range,

R), as shown in the following relationship for a sinusoidal wave (Medwin and Clay, 1997),

$$p = \frac{P_0 R_0}{R} \sin(\omega t - kR), \tag{2.19}$$

where P_0 is the pressure amplitude at reference range R_0. The range R can be simply defined as the distance over which the sound signal is travelling to the target at a constant sound speed.

2.2.2.5 Scattering and interference

An object can scatter sound in all directions when it is excited by an incident sound wave.

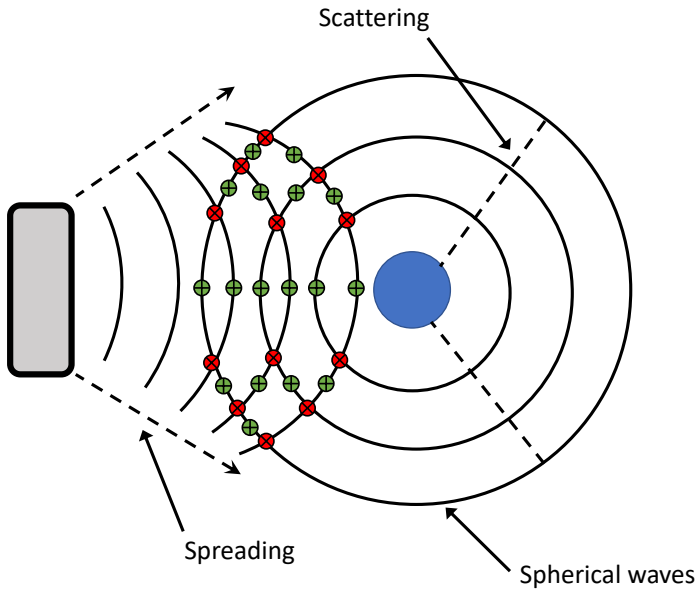

Figure 2.2: Interference of a spherical target (in blue) scattering a signal spreading with distance. The red 'x' dots indicate constructive interference, where the resultant signal is maximized. The green '+' dots indicate destructive interference, where the resultant signal is minimized.

The scattered acoustic signal will interact with the incident sound wave, generating a wave interference pattern is generated (Figure 2.2). When the sound waves overlap, the resulting amplitude is the sum of the input amplitudes, leading to constructive interference when peaks coincide and destructive interference when the peaks superimpose on the troughs (Figure 2.2). Note that scattering causes loss from the forward wave, but no loss of acoustical energy overall. Acoustical scattering from assumed spherical targets such as ocean bubbles will be discussed in Section 2.4.2.

2.3 Sonar

2.3.1 Sonar system

A sonar (SOund Navigation And Ranging) is a device used to detect nearby objects by exploiting their scattering or reflection properties. The sonar is designed to transmit sound forward and to receive the echo reflected by a target. For simplicity, an idealized perfectly spherical target is considered. The sonar generates the acoustic signal by using a transmitter which sends electrical current to the transducer. Due to its piezo-electric properties, the transducer produces electricity when mechanical stress is applied and vice versa. The electrical energy is converted by the transducer into acoustic pulses, initiating the forward propagating acoustic signal (Figure 2.3). The incident sound signal encounters the target, which has a different impedance to that of water, inducing changes in the speed of sound and density. In response, the target generates an echo (which is the contribution of both scattering and reflection) back to the transducer. The echo generated by the target is received by the transducer and converted back to electrical signal (voltage), which is amplified by an amplifier (Figure 2.3).

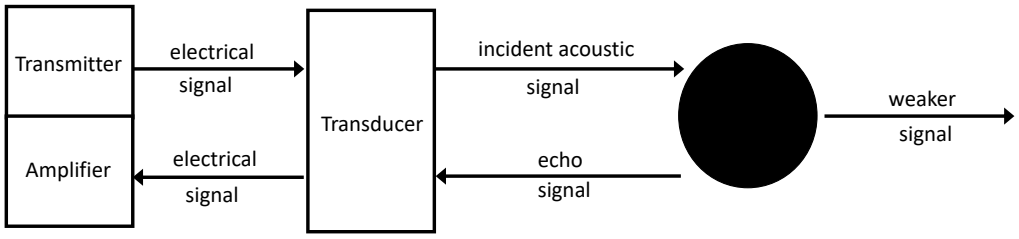

Figure 2.3: The process of target detection by a sonar, with the electrical to acoustical signal processing and vice-versa.

The impedance of the material which composes the transducer should be closely matched with the impedance of seawater, so transmission between transducer and water is maximized. This makes the sonar very efficient in detecting targets which have an impedance mis-match with the medium (seawater).

Each transducer displacement is usually repeated for a short time, generating a packet of sound waves as an acoustic pulse or ping. The time needed for the wave packet to pass a given point is the pulse duration, τ (in milliseconds). For a constant sound speed in water ($c = 1500\ m/s$ at a temperature of about $15^{\circ}\ ^{C}$), the pulse length (in centimetres) in water can

be defined as

$$L_p = c\,\tau. \tag{2.20}$$

The output of the sonar is the amplitude of the electrical signal converted from backscattering sound. This output is equivalent to the echo intensity amplitude in the sonar data. The range to target can be estimated from the time it takes the sound signal to travel to the target and return from the target at a constant sound speed. Measuring the return time t_r, one can estimate the range R of the sound signal as following:

$$t_r = \frac{2R}{c} \tag{2.21}$$

and

$$R = \frac{ct_r}{2}. \tag{2.22}$$

The above formulation of the estimation of range R was also used in Simmonds and MacLennan (2008).

2.3.1.1 Beam pattern

As it has a finite size, the transducer cannot act as a perfect point source of sound. Along with a range dependency, the sonar detection also has a directional dependency. The latter limitation is described by the beam pattern and the associated implications for signal transmission.

The shape of beam pattern is determined by sound spreading and wave interference. Sonars are commonly designed to form one main acoustic lobe and several side lobes. These lobes describe the magnitude of beam spreading and beam directivity. Figure 2.4 shows a typical beam pattern generated by a sonar. The acoustic axis perpendicular to the sonar transducer is called the main acoustic beam. It has a 0° directivity and it is measured in decibels. It is also called the 0 dB beam, which is used as the reference intensity for the rest of the beam pattern.

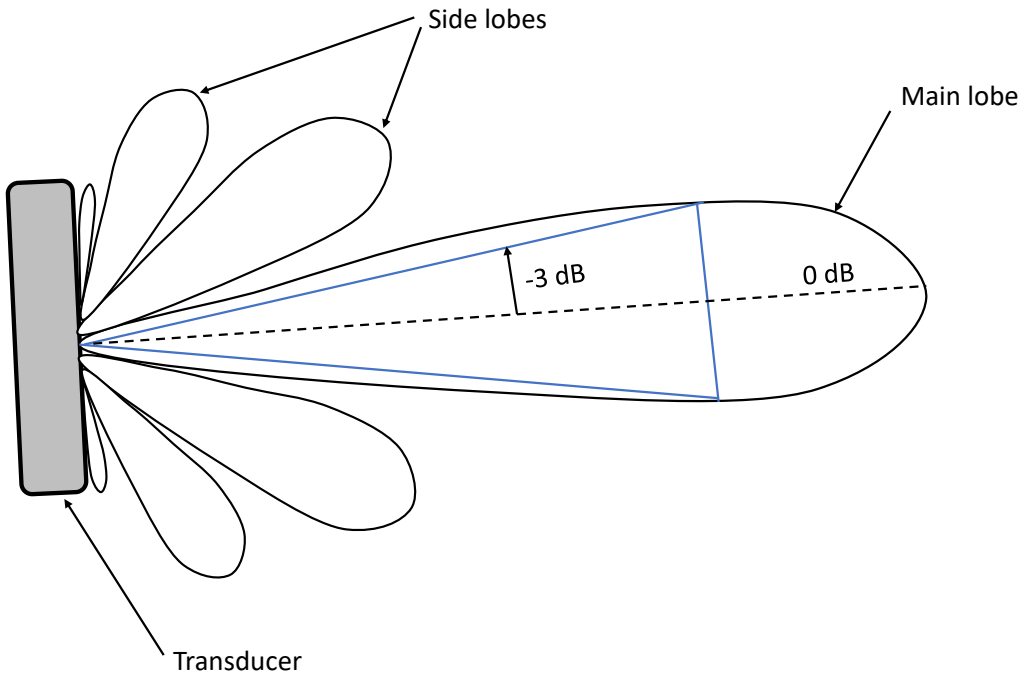

Figure 2.4: A typical sonar beam pattern showing acoustic lobes. The main lobe contains the main acoustic axis (dashed line) where the sound signal is the strongest. The side lobes are smaller and are associated with a lower sound signal. The beam spreading with range can be observed as well.

The main lobe depicted in Figure 2.4 shows the highest sensitivity in sound detection compared to the side lobes. Each position on the piston (transducer) acts as a separate point source. This causes interference between emitted signals from different positions of the sound source, decreasing (via destructive interference) or increasing (via constructive interference) the sound signal. Wave interference occurs more frequently in the side lobes, hence the signal decreases with directivity. Constructive interference is particularly present along the 0 dB beam where the sound signal is maximized. Destructive interference is especially present in the acoustic nulls, between lobes, where the sound signal is close to zero.

By considering the geometry of the main lobe, one can measure the beam width (in degrees). Hence, the beam width is defined by the angle at which the pressure amplitude (or sound intensity) of the main beam has been reduced by 3 dB on both sides of the main acoustic axis.

Reducing the beam width even by half of a degree could increase the strength of side lobes by up to 12 dB (Simmonds and MacLennan, 2008). This technique is called shading and it can be achieved by controlling the electrical gain applied to the signal. This is beneficial for

improving the sonar detection outside the main lobe because the magnitude of the side lobes is increased.

The beam width decreases with increasing acoustic pulse frequency. This can also be related to the dependency of beam width on the face length L of the transducer, in the case of rectangular transducers. Thus, the beam width is a function of L/λ, which means that transducers with a larger signal radiating surface and a higher operating frequency generate narrower beams.

The transducer radiates sound with a pressure amplitude P dependent on the angle θ relative to the main acoustic axis. The variation of $P(\theta)$ for a rectangular transducer can be expressed as

$$P(\theta) = \left[\frac{\sin\left(\pi \frac{L}{\lambda} \sin(\theta)\right)}{\pi \frac{L}{\lambda} \sin(\theta)} \right]^2 . \tag{2.23}$$

An equivalent version of Equation (2.23) was derived in terms of beam pattern, not pressure amplitude, by Simmonds and MacLennan (2008). In addition to narrower beams, a larger transducer with a high operating frequency also generates more acoustic lobes and a higher pressure amplitude at equivalent larger angles.

2.3.2 Sonar types

There are several ways in which the sonar design can be modified to optimize measurements in different underwater conditions. The main types of sonars that will be described here are the inverted echosounder, side-scan sonar and multibeam sonar.

2.3.2.1 Inverted echosounder

The inverted echosounder (IES) generates a single beam directed vertically upward (hence inverted) toward the sea surface (when measuring scatterers in the upper ocean). Due to easy deployment and low cost, these sonars are often used for various scientific purposes (such as biological sampling) and commercial applications. The IES produces point-like measurements, being a very efficient quantitative tool for estimating the distribution with depth of acoustic scatterers. The vertical range of a IES can extend over tens of meters (Trevorrow, 2003).

The measurement of scattering from bubble populations in the upper ocean is challenging due to intense motions of the sea surface, downward propagations of turbulence and

widespread acoustic extinction within a bubble layer. The acoustic extinction is the sum of the scattered and absorbed energy. It is possible that the incident acoustic signal is totally attenuated (the entire signal is scattered and absorbed), so the echo signal does not return to the sonar any more. Examples of measured acoustical attenuation/extinction within bubble plumes will be given in chapter 6.

For upper ocean measurements, the IES instruments are usually moored at larger depths where they are not affected by the destructive sea surface processes – see the work of Trevorrow (2003) and Vagle et al. (2010) who measured deep bubble plumes. The acoustic extinction is generally addressed by operating IES devices at high frequencies ($\geq$ 100 *kHz*). The frequency implication will be discussed in terms of high bubble density regime in Section 2.4.2.

2.3.2.2 Side-scan sonar

The side-scan sonar produces beams propagating horizontally on both sides of the instrument, which scan the target, so they produce intermittent rather than constant measurements (Figure 2.5b). These horizontal beams have a large swath extending with depth (within tens of meters), but their horizontal width is quite narrow (it is similar to the IES beam width). However, the horizontal range of the beams can extend over tens to hundreds of meters. This sonar can very efficiently detect both horizontal and vertical scattering distributions.

A device like this was used to measure how clouds of bubbles are organized by Langmuir circulation into rows aligned with the wind e.g. (Farmer et al., 1993; Zedel and Farmer, 1991). Note that the Langmuir circulation is an upper ocean turbulent process extending vertically (tens of meters in depth) and horizontally (over distances of hundreds of meters), and subsurface bubbles can act as tracers for this turbulent process. Figure 2.5b shows the use of the side-scan sonar in detecting the subsurface bubble and the foam windrows at the sea surface, both as a result of Langmuir circulation.

2.3.2.3 Multibeam sonar

The multibeam sonar uses many beams (tens to hundreds), and they are often used with their beams oriented downward to scan the sea-floor. However, for the upper ocean acoustics, these sonars can be also used with their beams oriented upwards towards the sea surface. The beams are usually organized in a fan-like shape, with the swath varying within 30°–40°

and up to $\geq 120°$. The clear difference between the beam coverage provided by the multibeam sonar and the one generated by the IES can be seen in Figure 2.5a.

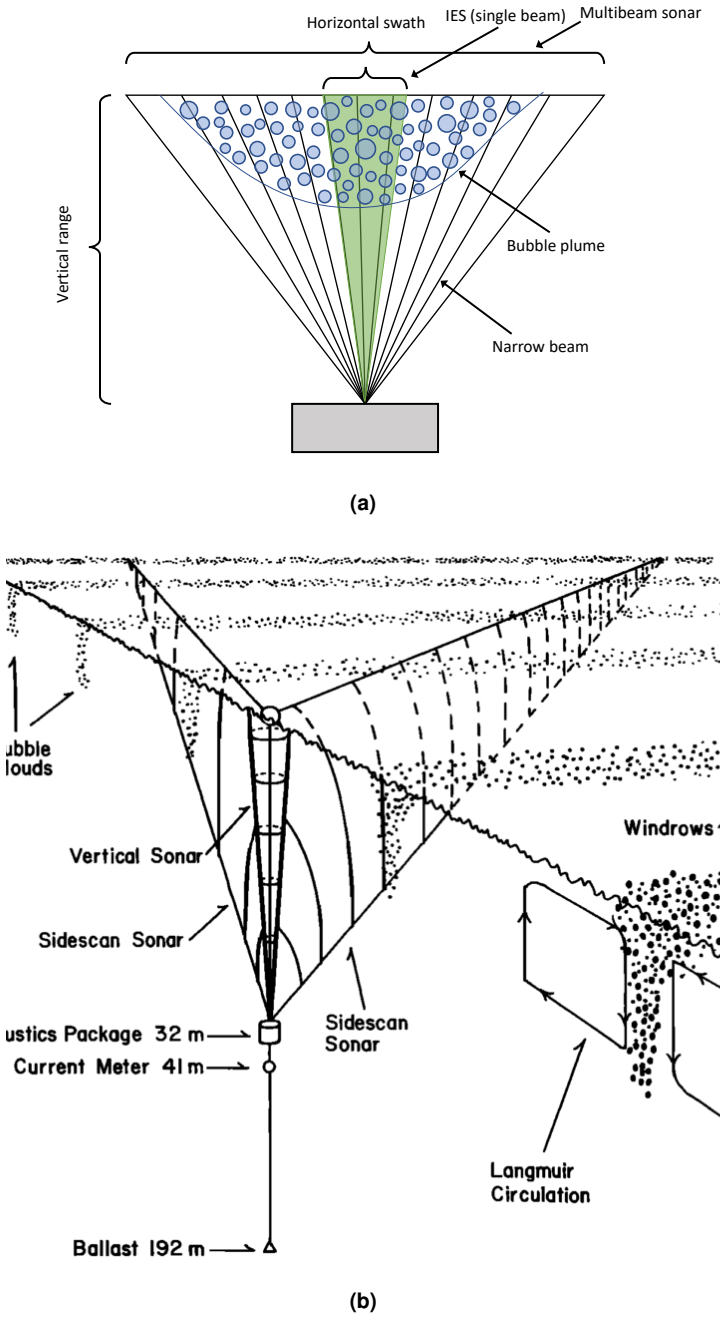

Figure 2.5: (A) Comparison between the swath of a multibeam sonar (with many narrow beams) and IES (the beam in green color) relative to the presence of a bubble plume. (B) Vertical cross section of two laterally spreading beams from a side-scan sonar, with both vertical and horizontal ranges extending over tens to hundreds of meters, so it can efficiently measure the Langmuir circulation, schematically shown here. Figure extracted from Zedel and Farmer (1991).

The beams forming the fan can be quite narrow ($\leq 1°$), providing a high resolution of the scatter distribution with depth and distance. This kind of sonar can provide complete radar-

like images of the shapes of entire bubble plumes, which are not available with IES systems. More details about the multibeam sonar model used in this study of bubble plumes will be discussed in Section 3.5. The physical and digital sonar characteristics, and the bubble acoustical scattering measured by a multibeam sonar, will be discussed in Section 3.5.

2.3.3 Sonar equation

The sonar equation accounts for the two-way sinks and sources of the forward transmitted signal to the target, and of the target-generated echo back to the receiver. The sonar equation can be used to quantify the signal-to-noise ratio (SNR) for a better prediction of sonar performance (Ainslie, 2004). The SNR of a sonar system can be written as the ratio between signal intensity I_S and noise intensity I_N in the form: $SNR = I_S/I_N$.

The sound pressure level (SL in dB), defined in Equation (2.17), is also known as the source level generated by the transducer at a reference distance of one meter. As the sound propagates further from the transducer, signal intensity is reduced. This effect is described by the transmission loss TL (in dB), which varies with range R as follows (Crawford and Farmer, 1987):

$$TL = 20\ \log(R) + \alpha_t R, \tag{2.24}$$

where α_t is the total sound attenuation in dB/m in water. In Equation (2.24), transmission loss is equivalent to the standard gain, which needs to be varied in time to compensate for the varying losses with distance. Note that gain is applied to the signal via post-processing. Therefore, as instrumental calibration is performed, time varying gain is applied to most sonars. This particularly useful especially when the measurements are more likely to be affected by scattering and attenuation (with distance) losses, but otherwise a time varying gain can also overestimate the signal received from the target.

A target is detected when a return signal is received by the transducer, contributing to the signal intensity I_S. The target strength is usually used to quantify the echo intensity in the sonar equation. The target strength TS is the logarithmic version (in dB) of scattering cross-section σ_{bs} (which will be described in detail in Section 2.4.2 in terms of bubble scattering),

$$TS = 10\ \log(\sigma_{bs}), \tag{2.25}$$

and it is the sound reflected and scattered by the target at a distance of one metre.

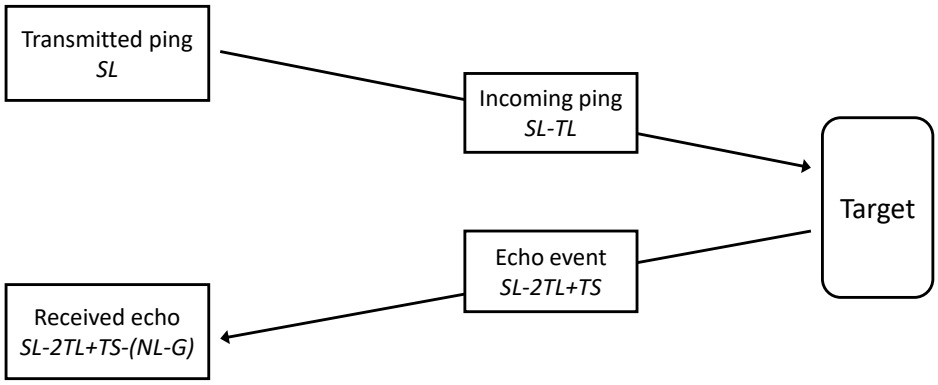

Figure 2.6: The main steps converting the transmitted signal to the received echo as described in the sonar equation.

As the reflected sound travels back to the receiver, the signal intensity I_S is again reduced by transmission loss, and it is described as the returned I_S as following:

$$I_S = (SL - TL) + TS - TL. \tag{2.26}$$

If noise level at the receiver is NL in dB, then the SNR becomes

$$SNR = (SL - TL) + TS - TL - NL. \tag{2.27}$$

The noise can be generated by instrumental reverberation, upper-ocean turbulence and thermal noise (Marage and Mori, 2013). Common sources of additional scattering in the upper ocean are very small bubbles (which have a negligible contribution to the total void fraction in the upper ocean) and by other scatterers (e.g. particulates or plankton).

Typically, to remove the noise from all other directions in SNR, a gain G (in dB) converted from an electrical signal can be applied, and the SNR is reinforced,

$$SNR = (SL - TL) + TS - TL - (NL - G). \tag{2.28}$$

The above steps in constructing the sonar equation are described by the scheme from Figure 2.6.

The gain G was shown by Marage and Mori (2013) to be proportional to the area of the transducer A_T,

$$G = 10 \ \log\left(\frac{4\pi}{\lambda^2} A_T\right). \tag{2.29}$$

2.3.4 Bubble measurements with the sonar

Sonars are often used to measure the acoustic signal generated by bubbles in the ocean, as mentioned in a vast literature on bubble acoustics (Crawford and Farmer, 1987; Farmer et al., 1993; Medwin, 1977*a*; Trevorrow, 2003; Vagle et al., 2010; Zedel and Farmer, 1991). Since bubbles are made of gas, they are highly compressible and create the conditions for a large impedance mismatch when measured in the ocean (Scandella et al., 2016). Therefore, bubbles can have a strong effect on sound propagation via a change in the refractive index and through scattering and absorption (Novarini and Bruno, 1982), so the return sonar signal is notably affected in the presence of bubbles.

Sonars are most effective in measuring low density bubble populations, and their functionality declines in the presence of acoustic attenuation when measuring denser bubble populations (Deane, 2016). The absorption and scattering of sound via bubbles present within the bubble layer at a depth of $13\ m$ can induce sound attenuation of about $40\ dB$ at a frequency of $10\ kHz$ and wind speed of about $13\ m/s$ (Novarini and Bruno, 1982). Moreover, measuring bubbles found at longer distances from the sonar also increases the likelihood of sound attenuation (Novarini and Bruno, 1982; Nützel et al., 1994). Therefore, bubble measurements by sonars are sensitive to environmental conditions and location of measuring.

Sonars may operate with different frequencies but, for bubble acoustics, high frequency sonars are commonly used (kHz frequencies). Using different frequencies, bubbles of many sizes can be detected (Farmer and Vagle, 1989). Higher frequency sonars can detect deeper plumes of bubbles because their signal is more sensitive to smaller bubbles which are usually present in deeper plumes (Trevorrow et al., 1994).

Understanding bubble acoustics is essential to better interpret the physical effects in the sonar measurements. Bubble acoustics is a crucial part in developing the techniques for the calculation of parameters that can be used to describe the structure and dynamics of bubble layers in the ocean.

2.4 Bubble acoustics

An underwater bubble can be defined as a gas cavity surrounded by liquid (water). The bubble is in equilibrium when is balanced by the surface tension, external pressure and the gas

pressure inside the bubble. In the ocean, bubbles are very often caused air entrainment in the presence of breaking waves (Leighton, 1994).

Acoustical techniques that determine the acoustical signal of a bubble as a physical obstacle, due to its geometric shape, known as scattering cross-section, will be presented here. A bubble at resonance can easily be distinguished from other objects in water because its acoustical scattering cross-section is 500–1000 times larger than its geometrical size (Medwin, 1977*b*; Medwin and Breitz, 1989; Vagle and Farmer, 1992). After calculating the cross-section for an individual bubble, the cross-sections from many bubbles of various sizes will be integrated over a unit volume to obtain the volumetric backscattering. This will permit the investigation of signal loss in dense bubble plumes (high void fraction). A linear assumption is used here, which assumes no interference between bubbles, so only single scattering is considered here, which is reasonable when measuring bubble populations with lower densities.

2.4.1 Bubble oscillator

Due to their high compressibility, bubbles contract and expand when they are forced by the acoustic pressure from an incident sound wave. This destabilizes the bubble to a non-equilibrium state, leading the bubble acting like a lightly damped harmonic oscillator (Leighton and Walton, 1959). Non-forced bubbles can also naturally behave like harmonic oscillators if perturbed from equilibrium, but only forced pulsating bubbles will be considered in this section. The bubbles that are not forced by an incident acoustic signal are studied using passive acoustics, while the ones that are excited by an acoustic signal can be studied using active acoustics.

The properties that are important for the behavior of a bubble as a mechanical oscillator are stiffness and inertia. The gas component inside the bubble and the surface coatings generates the stiffness (Leighton, 1994). The enclosed bubble gas can be considered to act like a spring when the bubble is disturbed from its equilibrium radius (Medwin, 1977*b*). The inertia is due to the mass of water surrounding the bubble (water shell) which must also oscillate as the bubble surface moves (Medwin, 1977*b*).

Bubbles have a natural frequency. If excited at that frequency, they resonate, and their oscillation amplitude is greatly increased. The combination of the effects of stiffness and inertia dictate the resonance frequency. This is an important parameter because an insonified bubble

(excited by a sound wave) at or near resonance frequency will absorb and scatter sound very effectively. Thus, resonance frequency is very important in determining the acoustical cross-sections of bubbles.

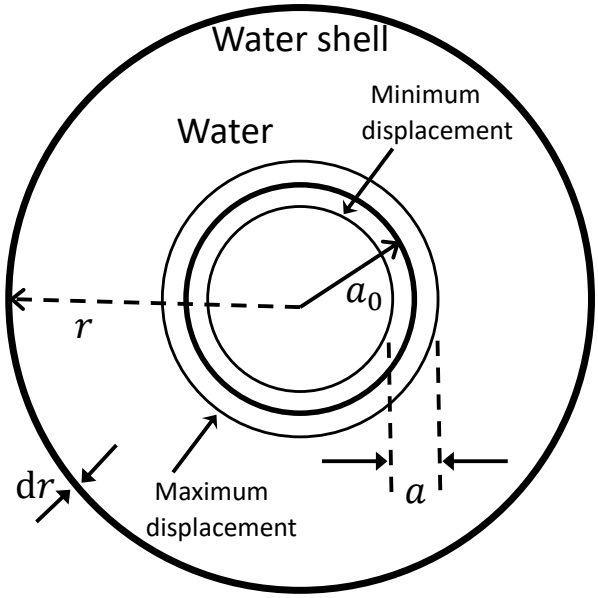

Figure 2.7: The scheme of a pulsating bubble, with the adjacent water layer which radiates relative to the bubble wall. The scale of the water shell is so large relative to the bubble size that it can be assumed to be infinite.

A diagram of a pulsating (insonified) bubble undergoing compression and expansion relative to its equilibrium radius, a_0, along with the surrounding water shell is shown in Figure 2.7. An increase in liquid pressure causes a decrease in bubble radius ($-a_{\epsilon 0}$), whereas a pressure decrease causes an increase in bubble radius ($+a_{\epsilon 0}$). The total radius, a, encompasses the bubble pulsating states (Leighton, 1994),

$$a = a_0 \pm a_{\epsilon 0} e^{i2\pi f_R t}. \tag{2.30}$$

For simplicity, one can also express the harmonic change in bubble radius as $a_\epsilon = \pm a_{\epsilon 0} e^{i2\pi f_R t}$. In the above equation, f_R is the resonance frequency of the bubble, which will be derived in the following section.

2.4.1.1 Resonant bubble

Bubble stiffness

Although there are different ways of deriving the bubble resonance frequency, a string analogy, proposed by Leighton (1994), was chosen to describe the mechanics of bubble oscillations. The force applied by an acoustic signal on a bubble is equivalent to the force applied to a string Leighton (1994),

$$F_a = j\,\epsilon, \tag{2.31}$$

where F_a is the force, in newtons (N), applied to the string, j is the stiffness of the string (which has units of N/m), and ϵ is the string extension (which has units of m). Since it is extended, the string exerts a balancing force F_s equivalent in magnitude but opposite to the applied force (Leighton, 1994),

$$F_s = -j\,\epsilon. \tag{2.32}$$

From Equation (2.32), stiffness of a string can be found as

$$j = -\frac{F_s}{\epsilon}. \tag{2.33}$$

In an equivalent manner, the stiffness of a bubble can be found by using the ratio in Equation (2.33) (Kinsler et al., 1982; Leighton, 1994).

Consider a bubble pulsating in equilibrium about the mean radius a_0. The compression of the bubble corresponds to a change of $-a_{\epsilon 0}$ in radius, from a_0 to $a_0 - a_{\epsilon 0}$, which is the radial displacement a_ϵ (the equivalent of the spring extension). The bubble volume changes by ΔV_b, from V_{b0} to $V_{b\epsilon}$. Here, V_{b0} and $V_{b\epsilon}$ are the bubble gas volumes at equilibrium and non-equilibrium, respectively. The gas pressure in the bubble also changes by Δp_g, which depends on the static equilibrium pressure p_w surrounding the bubble. For ocean bubbles, it is appropriate to consider the process adiabatic, $p_g V_b^\gamma = constant$, so there is no heat exchange between the interior gas and the surrounding water. Hence, the change in gas pressure inside a bubble is

$$\Delta p_g = -\frac{\gamma}{V_{b0}} p_w \Delta V_b, \tag{2.34}$$

where $\gamma = C_p/C_v$, with C_p and C_v being the specific heat capacities at constant pressure and volume, respectively (Leighton, 1994). The volume of the bubble while compressed and not in

equilibrium $V_{b\epsilon}$ can be found from the equilibrium volume $V_{b0} = 4\pi a_0^3/3$ as following (Leighton, 1994):

$$V_{b\epsilon} = \Delta V_b = 4\pi a_0^2 da = 4\pi a_0^2 a_\epsilon, \tag{2.35}$$

where da is a small change in bubble radius, which corresponds to the radial displacement, a_ϵ. For small perturbations, Equation (2.34) expresses the change (reduction) in bubble volume, ΔV_b, relative to the equilibrium volume, V_{b0} (Leighton, 1994),

$$\frac{\Delta V_b}{V_{b0}} = \frac{-4\pi a_0^2 a_\epsilon}{4\pi a_0^3/3} = -\frac{3a_\epsilon}{a_0}. \tag{2.36}$$

Using the above parameters and the string analogy, one can obtain the stiffness restoring force of the bubble F_b, which acts in the direction opposed to the bubble compression. This force changes the internal pressure as Δp_g, along with the change in bubble radius,

$$F_b = -4\pi a_0^2 \Delta p_g. \tag{2.37}$$

The substitutions of definitions from Equation (2.34) and Equation (2.36) in Equation (2.37) give

$$F_b = -12\pi\gamma a_0 p_w a_\epsilon. \tag{2.38}$$

We can now use the expression for F_b with Equation (2.33) to obtain the expression for bubble stiffness, j_b, in adiabatic conditions (Leighton, 1994; Medwin, 1977*b*),

$$j_b = 12\pi\gamma a_0 p_w. \tag{2.39}$$

The above description of an oscillating bubble is appropriate for a relatively small and spherical bubble. The bubble oscillates with a natural frequency, and the effects of hydrostatic pressure (which acts on a bubble with equilibrium radius, a_0), along with thermal and viscous damping were included in the bubble stiffness from Equation (2.39). However, the acoustic damping has been neglected in this simple treatment. The change of sound speed in the presence of bubbles will be discussed later in this section.

The result of the above derivation can be used for non-spherical bubbles as well because the sound wavelength is much larger the bubble radius, so the volume oscillation dominates. However, these large bubbles are unstable, and are likely to have rapidly varying shapes. In the real ocean, the bubble stiffness can be affected by an organic coating (bubbles scavenging biological material on their surface), which can also have an impact on the bubble natural

frequency. These effects can have a major role in the scattering properties of bubbles in the ocean.

2.4.1.2 Bubble inertia

The bubble water shell radial displacement is governed by the transfer of kinetic energy from a pulsating bubble to the water shell. In the ocean, a bubble is considered to be surrounded by many spherical water shells, each having radius, r, and infinitesimal width, dr (Figure 2.7). For simplicity, Figure 2.7 only shows one water shell surrounding a bubble. From Equation (2.30), a is the radius at the oscillating bubble wall. The kinetic energy of the radially displaced water shell integrates many spherical water shells (an infinite number of water shells can be approximated) starting from the bubble wall radius (Leighton, 1994),

$$E_k = \frac{1}{2}\int_a^\infty 4\pi r^2 \dot{r}^2 \rho_w dr, \tag{2.40}$$

where ρ_w is the density of the water surrounding the bubble, and $\dot{r} = dr/dt$. The above equation shows the mass of a water shell $4\pi r^2 \dot{r}^2 \rho_w$ changing with dr. The mass of the water shell flowing in time dt relative to the bubble surface is $4\pi r^2 \dot{r}^2 \rho_w dt$. This is the mass flow at the bubble wall where the boundary condition is (Leighton, 1994)

$$\frac{\dot{r}}{\dot{a}} = \frac{a^2}{r^2}. \tag{2.41}$$

Using the above equality, one can obtain the water velocity v_w at radius r across a water shell while a bubble pulsates at radius a,

$$v_w = \dot{r} = \frac{\dot{a}a^2}{r^2}. \tag{2.42}$$

In the above expression, the assumption of water incompressibility has been made. The density of surrounding water is much greater than that of the bubble, and its inertia must be considered. The assumption of incompressibility means that the water flux through any spherical water shell centered on the bubble is constant (Leighton, 1994). Thus, when a bubble pulsates, a considerable amount of water is displaced, and this will contribute to the inertia (Leighton, 1994). The assumption of incompressibility (or highly incompressible medium) leads to a much faster sound propagation in water compared to gas (air). However, water is not exactly incompressible, hence the sound speed is finite.

Applying the above boundary condition within the expression in Equation (2.41) gives the kinetic energy in terms of bubble radius a,

$$E_k = 2\pi a^3 \rho_w \dot{a}^2. \tag{2.43}$$

Replacing the bubble wall radius a with the equilibrium radius a_0, one can use the above expression and extract the mass of water displaced from the bubble (Leighton, 1994; Medwin, 1977*b*),

$$m_w = 4\pi a_0^3 \rho_w. \tag{2.44}$$

2.4.1.3 Resonance frequency

The pulsating gas and the spherical shells of water surrounding the bubble together form an oscillatory system. This is characterized by a resonance frequency when the amplitude response to an applied periodic external pressure is maximum. This leads to a maximum amount of energy extracted from the incident sound wave (Vagle and Farmer, 1992). The motions of the bubble oscillatory system are described by the kinetic and potential energies.

The potential energy E_p of the bubble wall displaced from the equilibrium radius a_0 by a distance equal to the displacement radius a_ϵ is the integration of the product of the applied force F_a and the incremental radius displacement da_ϵ (Leighton, 1994),

$$E_p = \int_{a_0}^{a_\epsilon} F_a da_\epsilon = \int_{a_0}^{a_\epsilon} j_b a_\epsilon da_\epsilon = \frac{j_b a_\epsilon^2}{2}. \tag{2.45}$$

The above relation states that potential energy E_p is proportional to bubble stiffness j_b.

As previously shown, the kinetic energy E_k is related to the inertia of the water shell (shells) surrounding the oscillating bubble (Leighton, 1994),

$$E_k = \frac{m_w \dot{a}_\epsilon^2}{2}, \tag{2.46}$$

where m_w is the mass of the water shell defined in Equation (2.44), and $\dot{a}_\epsilon = i\omega_R a_{\epsilon 0} e^{i\omega_R t}$ is the velocity of the bubble wall, and ω_R is the resonance angular frequency.

The kinetic energy is zero when the bubble wall is stationary, which occurs at the maximum radius displacement $a_\epsilon = \pm a_{\epsilon 0}$. In this state, the only energy is potential, which becomes maximum (Leighton, 1994),

$$E_{p,max} = \frac{j_b a_{\epsilon 0}^2}{2}. \tag{2.47}$$

On the other hand, the potential energy is zero at equilibrium radius a_0 where the displacement is zero ($a_\epsilon = 0$). When the equilibrium radius is reached, the kinetic energy is maximum. Considering the definition of the bubble wall velocity $\dot{a_\epsilon}$ given above, the expression of the maximum kinetic energy is (Leighton, 1994),

$$E_{k,max} = \frac{m_w \omega_R^2 a_{\epsilon 0}^2}{2}. \tag{2.48}$$

Assuming un-damped conditions, the bubble oscillation is the result of the continuous transformation of kinetic to potential energy and vice-versa. Applying the Lagrangian formalism, we have the equality between kinetic and potential energies,

$$\frac{m_w {\omega_R}^2 a_{\epsilon 0}^2}{2} = \frac{j_b a_{\epsilon 0}^2}{2}. \tag{2.49}$$

From the above equality, one can extract the resonance frequency ω_R as following:

$$\omega_R = \sqrt{\frac{j_b}{m_w}}. \tag{2.50}$$

The above expression states that resonance frequency depends on the ratio of bubble stiffness to water shell inertia. Substituting stiffness j_b and inertia m_w using Equation (2.39) and Equation (2.44), respectively, in Equation (2.50), one can obtain the natural frequency in adiabatic conditions Medwin (1977*b*),

$$f_{RA} = \frac{1}{2\pi a_0}\sqrt{\frac{3\gamma p_w}{\rho_w}}, \tag{2.51}$$

where the subscript A denotes the resonance frequency of a bubble pulsating adiabatically, and ω_R was replaced by $2\pi f_R$.

The above expression for resonance frequency of a pulsating bubble is appropriate for the condition $ka \ll 1$, where k is the wave number ($= 2\pi f/c$) and a is the bubble radius. This condition assumes linear and relatively small pulsations of spherical bubbles at low frequency, such that the bubble size is much smaller than the wavelength in the water (Ainslie and Leighton, 2011; Devin, 1959; Medwin, 1977*b*; Vagle and Farmer, 1992; Wildt, 1946). For example, the signal measured by sonars is generated by bubbles that mostly have sizes ranging between tens and hundreds of micrometres, so the condition $ka \ll 1$ is respected (Deane, 2016), and it can be used for most bubble measurements using sonars.

The number of smaller bubbles tends to increase when more particulates and surfactants are present in the water column (Thorpe et al., 1992). These particulates inhibit dissolution

(Thorpe et al., 1992) by stabilizing the bubbles. The longer-lived bubbles tend to have more time to scavenge particulates, so these bubbles are stabilized and become smaller as they are affected by the hydrostatic pressure. In time, the number of smaller bubbles eventually dominates the number of larger ones (Thorpe et al., 1992). In conclusion, it could be argued that, since they rise and burst more quickly, surfactants and particulates may have less of a stabilising effect on the behaviour of larger bubbles. The presence of larger bubbles is also associated with turbulence. Thorpe et al. (1992) observed a significantly higher turbulent energy dissipation in the shallower part of a bubble plume, where larger bubbles are usually present (compared to the ambient turbulence levels), but no significant difference between turbulence level in the deep part of the plume, where more smaller bubbles are usually present (down to about 10 metres), and that of the bubble-free surroundings. Other factors, such as temperature and gas saturation, may also affect the ratio between larger and smaller bubbles (Thorpe et al., 1992). Plumes of smaller bubbles are more likely to contain sizes which are resonant within the sonar beam and therefore will dominate the scattering profiles.

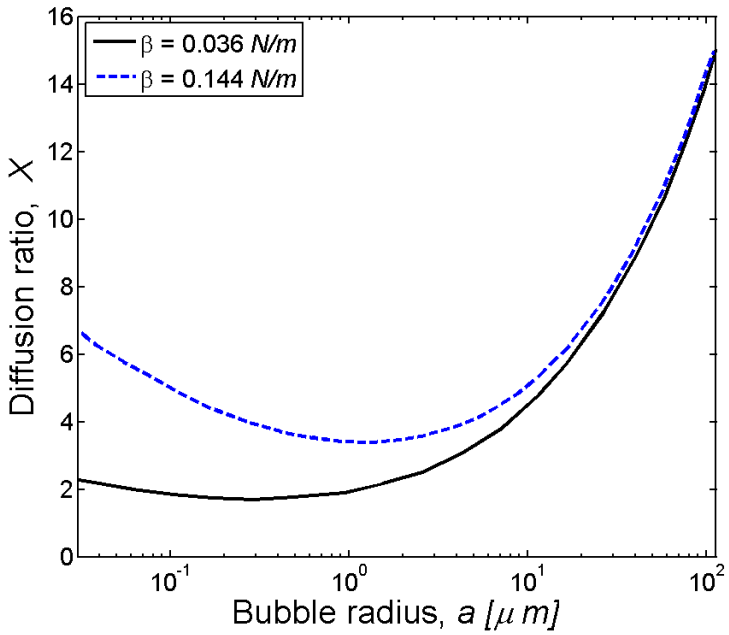

Figure 2.8: The evolution of diffusion ratio (vertical axis) with bubble radius (horizontal axis) for different values of surface tension β. Figure extracted from Ainslie Ainslie and Leighton (2011).

The adiabatic resonance frequency in Equation (2.51) is valid for bubble sizes much larger than the thickness of the thermal layer at the bubble boundary. Thus, bubbles pulsating adiabatically at resonance are considered as being thermally large bubbles (Ainslie and Leighton,

2011). The thermal boundary layer BL_t is proportional to the square root of thermal diffusivity of the encapsulated gas D_g at constant pressure (Ainslie and Leighton, 2011),

$$BL_t = \sqrt{\frac{D_g}{2\pi f}}, \tag{2.52}$$

where f is the incident acoustic frequency. The thermal diffusivity is proportional to thermal conductivity of gas K_g, and it is also defined in terms of equilibrium gas density ρ_g and its specific heat capacity at constant pressure C_p (Ainslie and Leighton, 2011),

$$D_g = \frac{K_g}{\rho_g(a_0)C_p}, \tag{2.53}$$

where ρ_g depends on equilibrium bubble radius a_0 due to the influence of surface tension on the gas pressure.

To assess bubbles that are thermally large, the condition $a_0 \gg BL_t$ is considered specifically for adiabatic resonance frequency. This condition can be verified by using the thermal diffusion ratio X, which is defined as the ratio of bubble equilibrium radius to the thermal boundary layer (Ainslie and Leighton, 2011; Medwin, 1977*b*),

$$X = \frac{a_0}{BL_t} = a_0\sqrt{\frac{4\pi f \rho_g C_p}{K_g}}. \tag{2.54}$$

Bubbles pulsate adiabatically at resonance when $X \gg 1$ (Ainslie and Leighton, 2011). This means that for an increasing bubble size, the thermal layer shows a relative decrease in thickness (Figure 2.8). Thus, larger bubbles radiate a smaller amount of heat relative to their size.

2.4.1.4 The connection between equilibrium pressure and resonance frequency

The equilibrium pressure inside a bubble p_g is defined as the sum of the equilibrium pressure in water, p_w, and the Laplace pressure, p_L, (Ainslie and Leighton, 2011; Chapman and Plesset, 1971; Leighton, 1994),

$$p_g = p_w + p_L = p_w + \frac{2\beta}{a_0}. \tag{2.55}$$

The Laplace pressure in Equation (2.55) is the gas pressure inside the bubble, and it includes the surface tension, β, which acts on the bubble by reducing its radius, a_0. The term, p_w, encapsulates the water pressure acting on the bubble (to deform the bubble wall) and the surface tension stabilizing the bubble wall, so both these effects lead to a net increase of p_g. Given this definition, it is assumed that the adiabatic resonance frequency is also valid when the Laplace pressure is much smaller than the equilibrium pressure in water ($p_L \ll p_w$).

Bubbles having similar sizes can be affected by different surface tension forces (Ainslie and Leighton, 2011), as shown in Figure 2.8. Hence, for bubbles influenced by stronger surface tension, the thickness of thermal boundary layer decreases due to lower thermal diffusivity, so the diffusion ratio increases at smaller bubble radii (Figure 2.8). As thermal diffusivity is inversely related to gas density, the Laplace pressure increases as the bubble becomes very small, thus increasing the gas density and decreasing its diffusivity. As the bubbles oscillate in a non-ideal medium (ocean), a standard bubble can never behave perfectly isothermally, as shown by the shape of diffusion ratio in Figure 2.8.

Given the above effects, the equation for the ideal adiabatic resonance frequency in Equation (2.51) must be changed to compensate for a varying thermal conduction and surface tension, which characterize bubbles pulsating at resonance. Therefore, γ in Equation (2.51) is replaced by the ratio of specific heats in the presence of thermal conductivity, γb, and p_w is replaced by the product of static pressure in water and surface tension, ζp_w (Medwin, 1977*b*),

$$f_R = \frac{1}{2\pi a_0}\sqrt{\frac{3\gamma b \zeta p_w}{\rho_w}}, \tag{2.56}$$

where ζ includes both surface tension and thermal conduction effects (Devin, 1959; Medwin, 1977*b*),

$$\zeta = 1 + \left(\frac{2\beta}{p_w}\right)\left[1 - \left(\frac{1}{3\gamma b}\right)\right]. \tag{2.57}$$

From Equation (2.57), one can observe the term $2\beta/p_w$, which is also known as Laplace radius at which the Laplace pressure is equal to the equilibrium pressure in water (Ainslie and Leighton, 2011). The first derivation of the unknown variable b, which describes the complex thermal conductivity effects during resonant bubble pulsations, is found in (Devin, 1959),

$$b = (1+\Lambda^2)^{-1}\left[1 + \frac{3(\gamma-1)}{X}\left(\frac{\sinh X - \sin X}{\cosh X - \cos X}\right)\right]^{-1}, \tag{2.58}$$

where the coefficient Λ is

$$\Lambda = 3(\gamma-1)\left[\frac{X(\sinh X + \sin X) - 2(\cosh X - \cos X)}{X^2(\cosh X - \cos X) + 3(\gamma-1)X(\sinh X - \sin X)}\right]. \tag{2.59}$$

To obtain the expressions in Equations (2.58) and (2.59), the definition of thermal diffusion ratio X from Equation (2.54) was used.

2.4.2 Bubble scattering measurements

2.4.2.1 Acoustical cross-sections

In order to understand the attenuation of sound by gas bubbles in the ocean, the fundamental processes by which pulsating bubbles dissipate their energy must be known (Devin, 1959). Energy is extracted from the incident sound wave when bubbles are present in water. A part of this energy is scattered by bubbles in all directions via acoustic re-radiation. Through sound absorption, a part is converted into heat during compressions and expansions of the enclosed gas. Finally, pulsating bubbles also lose energy through viscous dissipation, which occurs due to the shear exerted by the surrounding water on the bubble wall.

The acoustic dissipation processes described above can be estimated for individual bubbles of all sizes that are usually measured in the ocean. To estimate the amount of extracted energy from the incident sound wave which is dissipated by a bubble through scattering and absorption, one must obtain the extinction cross-section σ_e per bubble. Hence, σ_e is defined as the sum of scattering cross-section σ_s and absorption cross-section σ_a (Ainslie and Leighton, 2011; Medwin, 1977*b*; Vagle and Farmer, 1992, 1998),

$$\sigma_e = \sigma_s + \sigma_a. \tag{2.60}$$

The first comprehensive derivation of acoustical cross-sections mentioned above is found in Wildt (1946). For this derivation, an incident plane pressure wave, p_i, of amplitude, Y_1, travelling along a Cartesian x-axis is considered (Ainslie and Leighton, 2011; Wildt, 1946),

$$p_i = Y_1 \exp\left[i\omega\left(t - \frac{x}{c}\right)\right], \tag{2.61}$$

where ω is the angular frequency, t is time and c is the speed of sound. The incident acoustic pressure forces a bubble to scatter sound in the form of a spherical pressure wave, p_s, whose amplitude, Y_2, is inversely proportional to the distance, d_{bc}, from the bubble center (Ainslie and Leighton, 2011; Wildt, 1946),

$$p_s = \left(\frac{Y_2}{d}\right) \exp\left[i\omega\left(t - \frac{d_{bc}}{c}\right)\right]. \tag{2.62}$$

Both total scattering and absorption cross-sections are defined by the ratios of total scattered power Π_s and total absorbed power, Π_a, to the incident plane wave intensity, I_p, respectively

(Vagle and Farmer, 1992; Wildt, 1946),

$$\sigma_s = \frac{\Pi_s}{I_p}, \tag{2.63}$$

and

$$\sigma_a = \frac{\Pi_a}{I_p}. \tag{2.64}$$

Using the incident and spherical pressure wave parameters, the incident plane wave intensity I_p and the scattered power Π_s, respectively, can be expressed as following (Ainslie and Leighton, 2011; Wildt, 1946):

$$I_p = \frac{|p_i|^2}{2\rho_w c}, \tag{2.65}$$

and

$$\Pi_s = 4\pi a_0^2 \frac{|p_s|^2}{2\rho_w c}, \tag{2.66}$$

where ρ_w is the density in water and a_0 is the bubble equilibrium radius; here, $|p_i|$ and $|p_s|$ represent the absolute values of incident and scattered pressure waves, respectively. Substituting the definitions from Equations (2.65) and (2.66) in Equation (2.63), the total scattering cross-section of single bubbles can be partially derived. To obtain the final expression of total scattering cross-section, authors like Ainslie and Leighton (2011); Crawford and Farmer (1987); Dahl and Jessup (1995); Medwin (1977*b*); Vagle and Farmer (1992); Wildt (1946) additionally considered the ratio between resonance and operating frequencies, along with the effects of damping coefficients (which will be defined next), resulting in

$$\sigma_s = \frac{4\pi a_0^2}{[(f_R/f)^2 - 1]^2 + \delta^2}, \tag{2.67}$$

where f_R is the bubble resonance frequency, f is the incident acoustic frequency, and δ is the total damping coefficient of the bubble. Equation (2.67) shows that for an incident acoustical signal of frequency f, the bubble radius, a_0, has a strong effect on the scattering. Generally, the relevant output for acoustical measurements is backscattering cross-section σ_{bs}, which describes the amplitude of a backward-propagating signal generated by bubbles (Deane, 2016). The scattering from a bubble is isotropic, therefore the backscattering cross-section can be obtained from the scattering cross-section per steradian as following (Medwin, 1977*b*):

$$\sigma_{bs} = \frac{\sigma_s}{4\pi} = \frac{a_0^2}{[(f_R/f)^2 - 1]^2 + \delta^2}. \tag{2.68}$$

The definition of the total damping coefficient is the sum of contributions from acoustic re-radiation (δ_r), thermal dissipation (δ_t) and shear viscosity (δ_v),

$$\delta = \delta_r + \delta_t + \delta_v. \tag{2.69}$$

These components of total damping coefficient were derived as following (Devin, 1959):

$$\delta_r = ka_0, \tag{2.70}$$

$$\delta_t = \Lambda \left(\frac{f_R}{f} \right)^2, \tag{2.71}$$

$$\delta_v = \frac{4\eta_s}{\rho_w 2\pi f a_0^2}, \tag{2.72}$$

where η_s is the shear viscosity, k is the acoustic wavelength, and Λ is given in Equation (2.59). The absorption cross-section in terms of the above damping coefficients was also obtained (Medwin, 1977*b*; Vagle and Farmer, 1992),

$$\sigma_a = \frac{4\pi a_0^2 (\delta/ka_0 - 1)}{[(f_R/f)^2 - 1]^2 + \delta^2}, \tag{2.73}$$

The extinction cross-section of a single bubble was obtained by using the definition of scattering cross-section directly (Ainslie and Leighton, 2011; Crawford and Farmer, 1987; Medwin, 1977*b*; Vagle and Farmer, 1992),

$$\sigma_e = \sigma_s \frac{\delta}{ka_0} = \frac{4\pi a_0^2 \delta/ka_0}{[(f_R/f)^2 - 1]^2 + \delta^2}. \tag{2.74}$$

When there is minimum in damping, the bubble resonance frequency is maximum (Medwin, 1977*b*). The extinction and scattering cross-sections have large peaks at resonance bubble radius, a_R (Crawford and Farmer, 1987; Czerski, 2012; Medwin, 1977*b*; Thorpe, 1982; Vagle and Farmer, 1992). Furthermore, these large resonant cross-section values are also complemented by large non-resonant values at $a_0 \gg a_R$ at high acoustic frequencies (Medwin, 1977*b*). This extra contribution is caused by geometric scattering, which is the acoustic scattering resulting from the size of these large bubbles (Czerski, 2012; Leighton, 1994). This can induce limitations in the calculations of bubble size (discussed later in this section).

The extinction and scattering cross-sections at resonance were also measured at different frequencies (Medwin, 1977*c*; Vagle and Farmer, 1992). These authors observed that the measured radius of a resonant bubble decreases with increasing acoustic frequency. Furthermore, it was reported in Medwin (1977*b*) that the total damping coefficient increases with decreasing

resonance radius. The acoustical cross-sections are reduced for smaller resonance bubble radii and larger acoustical damping of bubbles. Consequently, results of a decline in both extinction and absorption cross-sections at resonance with increasing acoustic frequency are reported by Medwin (1977*b*); Vagle and Farmer (1992).

Organic material (from biological activity), which is sometimes present in the ocean in significant amounts, can be scavenged by smaller bubbles on their walls, thus they become coated by a layer. It has been observed that organic coatings affect the acoustic response of bubbles (Czerski, Twardowski, Zhang and Vagle, 2011; Hoff et al., 2000) because the coating stiffens the bubble. Consequently, it was showed in Czerski, Twardowski, Zhang and Vagle (2011) that a coated bubble has a higher resonance frequency and a lower extinction cross-section than an equally sized clean (assumed not to be contaminated by coating) bubble. Thus, among damping physical processes, the variability in oceanic biological activity also has an important influence over the variability of the acoustical cross-section values, particularly for small bubbles (not larger than about 100 μm). Note that, for the rest of this thesis, only clean bubbles are assumed. This is a common assumption, and for larger bubbles the difference is small.

2.4.2.2 Ensemble of bubbles

The experimental scatter measurements usually encompass many bubbles of different sizes which are simultaneously present in the ocean. It is therefore useful to define bubble density as the number of bubbles per radius per unit volume (usually 1 m^{-3}) for all measured bubble radii. In order to estimate bubble densities from acoustical backscattering, the number of backscattering cross-sections from bubbles of each radius a over increments of da equal to 1 μm must be integrated. This is also referred to as backscattering cross-section per unit volume M_v and is expressed as following (Crawford and Farmer, 1987; Trevorrow, 2003):

$$M_v = \frac{1}{4\pi} \int_0^\infty \sigma_s(a) N(a) da, \tag{2.75}$$

where $N(a)da$ is the number of bubbles per unit volume obtained for radii between a and $a+da$, and M_v is given in m^{-1}.

The excess attenuation rate per unit distance α_b due to bubbles (given in dB/m) is propor-

tional to the extinction cross-section per unit volume M_e (Medwin, 1977*b*),

$$\alpha_b = 4.34 M_e, \tag{2.76}$$

where the factor 4.34 is the result of the conversion to decibels per m^{-1} (Czerski, 2012; Medwin, 1977*c*, 2005). Here, M_e is the extinction cross-section per unit volume obtained in an equivalent manner as M_v in Equation (2.75),

$$M_e = \frac{1}{4\pi} \int_0^\infty \sigma_e(a) N(a) da. \tag{2.77}$$

Using the bubble attenuation rate per unit distance from Equation (2.76), the bubble transmission loss, TL_b (given in dB), which describes the attenuation of sound due to the presence of intermediary bubbles between a transducer device and the main scatterers, can be determined (Crawford and Farmer, 1987),

$$TL_b = 2 \int_0^l \alpha_b dl, \tag{2.78}$$

where dl is a very small increment of the distance along the acoustic path, l, between transducer and scatterers. This loss term becomes significant along nearly horizontal paths through denser and wider regions of the bubble plumes (Trevorrow, 2003). The bubble transmission loss can be further incorporated in the sonar equation. Thus, the subtraction of bubble transmission loss TL_b from the incident signal in the sonar equation from Equation (2.28) gives

$$SNR = SL + TS - 2TL - TL_b - (NL - G). \tag{2.79}$$

where $2TL$ represents the two-way transmission loss due to sound absorption by seawater, SL is the sound source level, NL is the noise level and G is the applied gain.

The typical bubble size used for the integrations in Equations (2.75) and (2.77) varies from about 10 μm to 500 μm (Farmer et al., 1998; Johnson and Cooke, 1979; Trevorrow, 2003), including both resonant and non-resonant bubbles. These wider bubble size ranges are specific for sonars which transmit signals at high frequencies. The above backscatter quantities were derived in the context of lightly damped spherical bubbles with clean walls (no organic coating) and located in an effectively infinite (very large) water volume. These bubbles are assumed to be far enough from each other that they do not acoustically interact, hence multiple scattering effects can be neglected. These assumptions are appropriate in the case of bubbles present in relatively low density plumes and far from the influence of sea surface.

2.4.2.3 Bubble population measurements and limitations

A bubble population can be estimated by inverting the acoustical attenuation it causes. Broadband attenuation measurement is required to infer a bubble size distribution with active acoustics. Many authors have used various inversion techniques to obtain the number and size of bubbles present in a population (Commander and McDonald, 1991; Commander and Moritz, 1989; Czerski, 2012; Medwin, 1977*a*).

The contribution to acoustical attenuation made by a single bubble size is very high at the bubble natural frequency, but the off-resonant scattering can also be significant, and even greater in some cases (Czerski, 2012). This can complicate the calculations of bubble size distribution. Consequently, a few inversion methods have been developed by several authors.

Medwin (1977*a*) assumed that the measured attenuation was dominated exclusively by resonant scattering. This author derived a simplified expression that directly connected measured attenuation to the number of resonant bubbles (Czerski, 2012). Larger bubbles that are resonant below the measuring frequency cannot be detected via their resonance, but they do present a geometrical obstacle and thus cause geometrical scattering. Thus, their geometrical scattering at the measuring frequency can be mis-interpreted as very small bubbles (Czerski, 2012). This can lead to the overestimation of the number of bubbles that are smaller than about 50 μm (Commander and Moritz, 1989). Consequently, Commander and Moritz (1989) also included the non-resonant contributions to the inversion technique in calculating the bubble density. One of the most frequently used method to include the contributions of non-resonant bubbles is that proposed in Commander and McDonald (1991). This method uses an iterative procedure to produce a stable result, but it is computationally demanding (Czerski, 2012).

It was shown by Czerski (2012) that another inversion method is much simpler, based on two principles: a bubble of single size causes attenuation over a narrow range of frequencies, and the resonant point is right at the peak of a frequency spacing (Figure 2.9a). This range is known as the resonance bandwidth. Each extinction cross-section is characterized by a single resonance bandwidth. The sum of many individual cross-sections is proportional to the total attenuation (Czerski, 2012).

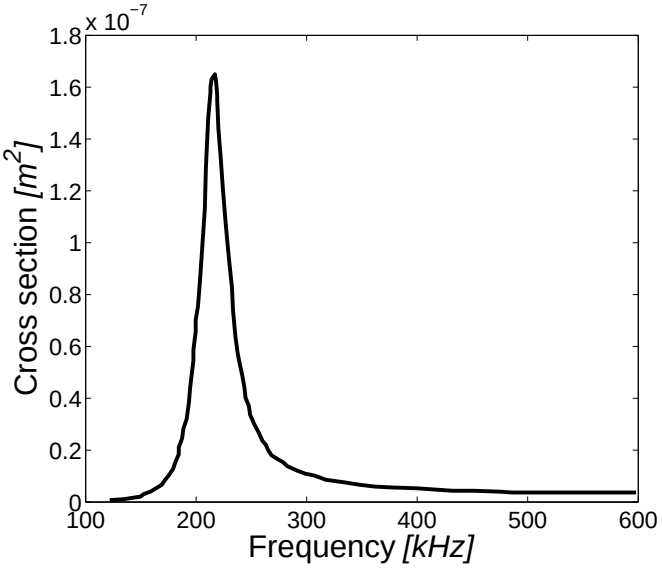

(a)

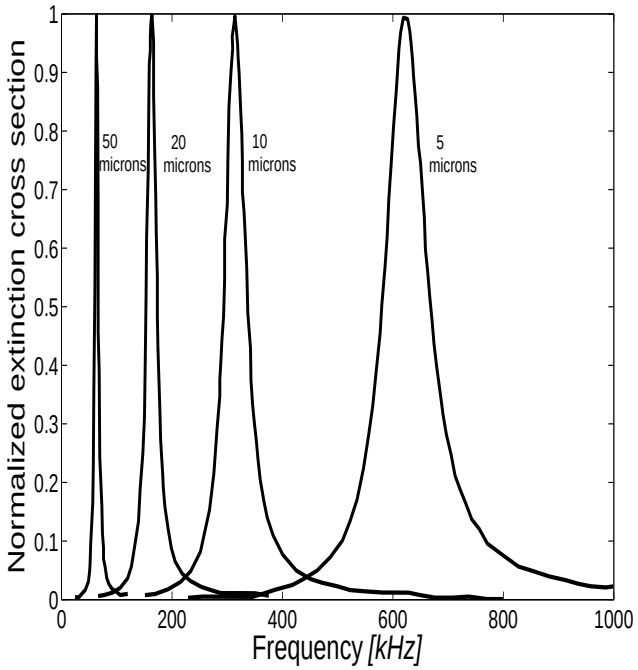

(b)

Figure 2.9: (A) Variation of the normalized extinction cross section with frequency for a single bubble with a radius of 15 μm and (B) for bubbles with different sizes, namely 50, 20, 10 and 5 μm from left to right peaks. Figure extracted from Czerski (2012).

The bubbles at fixed radius increments are associated with cross-sections of equal resonance bandwidths. This shows the importance of resonance bandwidth in determining the amount of overlap there is between bubble cross-sections separated by a fixed radius increment (Czerski, 2012). The resonance bandwidth is wider for bubbles with smaller radii (which

resonate at higher frequencies) than for larger bubbles, which resonate at lower frequencies (Czerski, 2012), as shown in Figure 2.9b. This shows that bubble cross-sections are not characterized by equal bandwidths, so the contribution to total attenuation will change. Thus, the different resonance bandwidths can be binned such that every bubble will be resonant in a bin, so the total attenuation can be inverted to produce the correct number of bubbles (Czerski, 2012).

Note that the above method for inversion reported by Czerski (2012) is not universal. There are other various techniques used to estimate the sizes of bubbles from given populations.

2.4.2.4 Comparison between resonator and sonar

For the measurement over a wide size range, acoustical resonators operating at a wide range of frequencies have been used. For example, every resonant peak provides a measurement of acoustical attenuation from bubbles, and resonators that have been used recently generate about 140 peaks between 20 and 800 kHz, providing a bubble radius range of $4 - 180\ \mu m$ (Czerski, 2012).

On the other hand, sonars usually provide only single-frequency measurements, so they do not have enough bandwidth to be used in estimating the bubble size distribution from acoustical attenuation measurements, e.g. the sonar used during our HiWinGS campaign measured bubble populations at a single frequency. In terms of sonar measurements, the depiction of bubble cross-section variation with frequency is relevant because, when using a sonar, the entire plume of bubbles is the target, and the sum of the contributions from individual bubbles is needed to asses the possible amplified response from resonant bubbles.

2.4.2.5 Bubble impact on the speed of sound

From the Newton-Laplace expression in Equation (2.6), it can be observed that the speed of sound in a medium increases with its resistance to compressibility (bulk modulus) of that medium. Water is considered to be compressible when discussing underwater acoustics, but for many applications, it can considered incompressible. Given that compressibility is much higher for air/gases than for water, the speed of sound propagating in bubbly liquids or dense plumes will be significantly lower compared to the sound speed in water.

Instead of bulk modulus, the speed of sound, c, can be also defined in terms of compressibility, μ, which is described in terms of volume change as a response to pressure variation. In this case, the speed of sound is inversely proportional to compressibility,

$$c^2 = \frac{1}{\rho_w \mu}, \tag{2.80}$$

where ρ_w is the density in water.

The void fraction, V_f, is defined in terms of bubble density, $N(a)$, which is given for every bubble of radius, a,

$$V_f = N(a)\frac{4}{3}\pi a^3. \tag{2.81}$$

Using void fraction, the density of the mixture, ρ_m, can be defined as (Wilson and Roy, 2008)

$$\rho_m = \rho_w - V_f \rho_w + V_f \rho_g, \tag{2.82}$$

where ρ_w is the density of water and ρ_g is the density of gas from bubbles. In the same manner, the compressibility of the mixture, μ_m, can be obtained as (Wilson and Roy, 2008)

$$\mu_m = \mu_w - V_f \mu_w + V_f \mu_g, \tag{2.83}$$

where μ_w is the compressibility of water and μ_g is the compressibility of gas.

Substituting the definition from Equations (2.82) and (2.83) into Equation (2.80), the expression for the mixture sound speed, c_m, in terms of void fraction was derived for the first time by Wood (1930), and it was reproduced by Wilson and Roy (2008) as following:

$$c_m^2 = \frac{1}{(\rho_w - V_f \rho_w + V_f \rho_g)(\mu_w - V_f \mu_w + V_f \mu_g)}. \tag{2.84}$$

The above expression for sound speed is valid for the entire void fraction range (0–1), and is also know as the Wood's equation. Figure 2.10 shows the Wood's equation prediction for sound speed in a bubble/water mixture varying over the full void fraction range. Wood's equation predicts that at zero void fraction the speed of sound is equal to that of bubble-free water. The minimum predicted sound speed is only 23 m/s and occurs at $V_f = 0.5$, but the sound speed is generally lower than 100 m/s across a very wide void fraction range (about 0.1–0.9) (Wilson and Roy, 2008). Thus, sound speed in bubbly water is at least a factor of two lower than sound speed in air (333 m/s). The reason for this effect is that bubbles considerably increase the compressibility of the mixture, while the density changes at a much lower rate (Wilson and Roy, 2008). The expression for the sound speed in bubbly water given

in Equation (2.84) is relevant for the entire process of bubble plume injection, covering both the acoustically active and the quiescent bubble plume states.

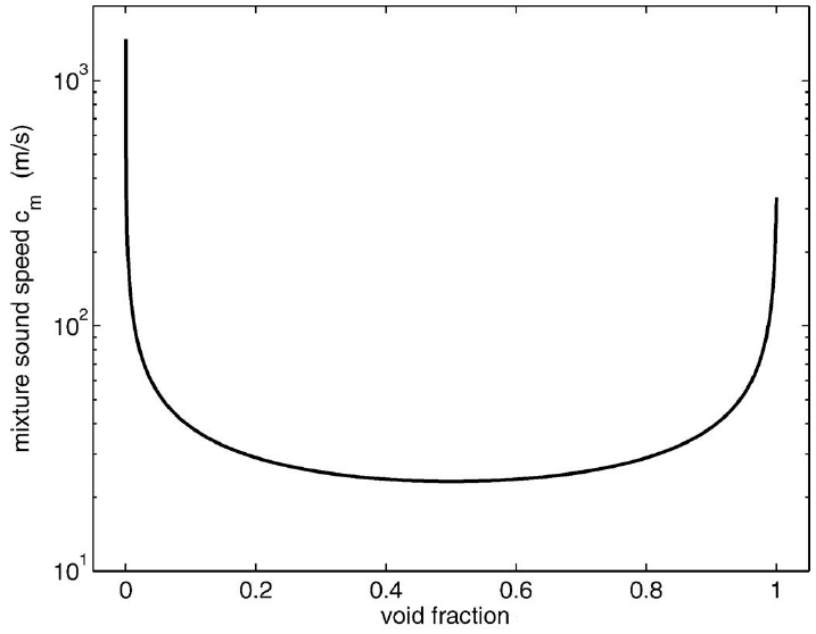

Figure 2.10: Speed of sound in a bubbly water given by Wood's equation (Equation (2.83)). This plot shows that sound speed propagates clearly slower in a bubble/water mixture than in pure gas (air) as explained in the text. Figure extracted from Wilson and Roy (2008).

Wood's model uses a narrow range of very low acoustical frequencies (200–1000 *Hz*) and a bubble size of about 1 *mm* (Wilson and Roy, 2008). This clearly limits the contribution to void fraction of bubbles with a wide range of sizes, which is usually found in oceanic bubble plumes (where most bubbles have sizes smaller than 1 *mm*). Furthermore, all bubbles in Wood's model are smaller than the resonant size corresponding to the acoustic frequency (Vagle and Farmer, 1998). Thus, Wood's model is valid only when the acoustic frequency is much less than the resonance frequency of bubbles. At this point, the speed of sound becomes nearly independent of frequency and bubble size, and it only depends on void fraction (Wilson and Roy, 2008).

The speed of sound in water-gas mixture in terms of void fraction V_f and individual bubble radius a for the case when the acoustic frequency f is much lower than bubble resonance frequency f_R ($f \ll f_R$) was derived as (Medwin, 1977*b*),

$$c_{mlf} = c_0 - \frac{3V_f c_0}{2a^2 k_R^2}, \tag{2.85}$$

where c_{mlf} is the mixture sound speed at low frequency, c_0 is the bubble-free water sound

speed, and k_R is the wave number at resonance. Here, the consequences for $f \ll f_R$ are equivalent to the ones of Wood's model. Equation (2.83) also shows that the mixture speed of sound for propagation at frequencies well below the bubble resonance frequencies is lower than in bubble-free water (Medwin and Breitz, 1989). The definition of the mixture sound speed when acoustic frequencies are much higher than bubble resonance frequencies ($f \gg f_R$) is (Medwin, 1977*b*)

$$c_{mhf} = c_0 + \frac{3V_f\chi^2 c_0}{2a^2k_R^2(1+\delta^2)}, \tag{2.86}$$

where $\chi = f_R/f$ is the ratio of resonance frequency to acoustic frequency, and δ is the damping coefficient. Here, bubbles are larger than the resonant size corresponding to the acoustic frequency. Therefore, bubbles do not affect the sound speed when the acoustic frequency is high enough (Medwin, 1977*b*). Consequently, the mixture speed of sound at frequencies well above the bubble resonance frequencies is higher than sound speed in bubble-free water (Medwin and Breitz, 1989).

One can generalize the definition of sound speed in a bubbly water of all radii. This can be accomplished by the integration of very small incremental changes of bubble density as $N(a)da$ and void fraction as $V_f(a)da$ both as functions of bubble radius, which gives the following speed of sound in water-gas mixture c_m (Medwin, 1977*b*):

$$c_m = c_0\left[1 - \frac{3}{2}\int_{a_i}^{a_f} \frac{\chi^2(\chi^2-1)V_f(a)da}{a^2k_R^2(\chi^2-1)^2+\delta_R^2}\right], \tag{2.87}$$

where δ_R is the total bubble damping coefficient at resonance. The integration in Equation (2.87) covers the bubble size range extending from an initial radius a_i to a final radius a_f. In the case of deep bubble plumes, the typical void fraction ($\sim 10^{-5}$) is too low to make a difference in the sound speed round trip propagation given in Equation (2.87).

2.4.2.6 Signal loss caused by high void fraction generated by oceanic bubbles

The assumptions regarding idealized bubbles used to compute the backscattering and extinction cross-sections per unit volume are no longer valid in high bubble densities. These regimes are common in actively breaking waves, which can contain void fractions up to 0.6, bubbles ranging from 10 μm to 1000 μm and large turbulent dissipation rates of $1\ W\ kg^{-1}$ (Deane, 2016). In these high densities, multiple scattering from many bubbles cannot be neglected anymore. Bubbles are now entrained by strong turbulent flows, which deform and

fragment the bubbles, thus their spherical shape cannot be assumed. Consequently, most of backscattering originates from large non-resonant bubbles with high buoyant rise speeds that interact with turbulence (Deane, 2016).

Bubble size can range from 60 μm to 6 mm measured beneath oceanic breaking wave crests (Bowyer, 2001; Deane, 2016) and in laboratory plunging breakers (Deane and Stokes, 2002). These bubbles are associated with void fractions exceeding 0.5 in actively breaking wave crests at sea (Gemmrich and Farmer, 1999) and in laboratory breaking waves (Blenkinsopp and Chaplin, 2007; Lamarre and Melville, 1991).

The incident acoustic signal loss is significant (43 dB) for void fraction in the range 0.03–0.06 and becomes maximum (losses of around 130 dB) for void fractions in the range 0.08–0.17 (Deane, 2016). The latter high void fractions occur in acoustically opaque regions within very shallow plumes (not more than few centimeters in depth) where the sonar data cannot be collected.

Bubbles are entrained and fragmented inside the breaking wave crest, which can referred to as the acoustically active phase (see Section 1.3). Once bubble production processes cease, the newly formed smaller bubbles become acoustically quiescent and evolve under the influence of turbulent diffusion, advection, degassing and dissolution (see Section 1.3). The latter bubbles are the ones which remain in the water column, and they mainly contribute to the scattering calculations mentioned earlier, forming the deep bubble plumes which are acoustically transparent enough for a sonar to probe them.

2.5 Summary and conclusions

The acoustic wave equation was derived by combining Newton's second Law and the acoustic equation of state to provide a theoretical characterization of the acoustic signal propagation in a given medium such as the upper ocean. One of the aims in this chapter was also to understand the physical implications of the main acoustical parameters in order to assess the variation in the incidence sound signal within medium with an impedance mismatch such as bubbly water. The physical characteristics of the attenuation of the sound signal, such as absorption, geometric spreading, scattering and interference, were discussed as an introduction to the causes of the effect on the sonar return signal. The structure and shape of the signal produced

by different types of sonars were discussed in terms of the beam pattern radiating from the transducer to better assess the sonar detection of various types of targets – different types of beam patterns can be used to detect targets of different shapes and sizes. This connects to the control of two-way signal propagation by applying a signal response enhancing gain to maximize the efficiency of detecting the target – this two-way signal process was described using the sonar equation.

Using the effect of a key physical property of a single bubble in water, such as bubble stiffness, on the water shell (surrounding the bubble) inertia, the resonance frequency of a single bubble was derived. This term is essential in predicting the size of a bubble pulsating with its resonance frequency when excited by a sound signal of a given frequency. This is very useful for determining if the return signal can be partly attributed to resonant bubbles.

Combining the incident and spherical pressure wave parameters along with the effect of damping, the scattering cross-section of a single bubble was derived. When considering entire population of different-sized bubbles, the scattering cross-sections from many bubbles are integrated over different sizes to obtain the backscatter signal generated from bubble populations. This backscatter acoustical technique will be generalized to the sonar data to generate full vertical cross-sections of bubble plume penetration depth (see Section 3.4). The backscatter signal is sensitive to the density of a bubble population, so it can be used (as will be shown in Chapter 4) to infer the bubble density and entrainment in the water column in different environmental conditions.

The bubble size and density are needed to compute void fraction, which is an important parameter used to estimate the gas content in a mixture of bubbles and water. Void fraction was also used to compute the total density of mixture, which influences the sound propagation (in terms of sound speed variation) as void fraction changes within the mixture. Void fraction is commonly estimated in bubble populations at local depths within the water column, with limits of the large scale assessment of void fraction within the entire water column.

Chapter 3

Methods and instruments

3.1 Experimental design

3.1.1 HiWinGS project

The physical mechanisms for air-sea interaction and gas transfer evolve as wind speed increases beyond $5 - 10\ m/s$, when breaking waves and bubble injection become important (Blomquist et al., 2017). Numerous parameterisations and some air-sea interaction models (such as the NOAA-COARE model which embeds some of these parameterisations) include these physical mechanisms, but they are based on a number of relatively limited field observations. The predicted and measured gas transfer (CO_2 is particularly of interest given its greenhouse potential) increases with wind speed, but it becomes highly uncertain at high wind speeds (see Figure 1.2). The poor understanding of this process highlighted the importance of measuring gas fluxes in high wind conditions, which primarily motivated the funding of the HiWinGS (High Wind Gas Exchange Study) project. Consequently, it is expected that the field results from HiWinGS would have the potential to inform and improve some of the current parameterisations at high wind speeds. The funding these experiments and HiWinGS cruise was offered by National Science Foundation (USA), Atmospheric and Geospace Sciences Division (USA, under grants AGS-1036062, AGS-1036006, AGS-1444294, OCE-1537890), NOAA Climate Program Office (USA) and Climate Observation Division (USA). The investigators involved in this field campaign are affiliated to institutions such as University of Colorado (CIRES), University of Hawaii (Department of Oceanography), University of Wisconsin (De-

partment of Chemistry), NOAA Earth Systems Research Laboratory (Physical Science Division, Boulder). Other investigators, involved in measuring and analysing wave breaking and wave physics during HiWinGS, are affiliated to Lamont-Doherty Observatory (Columbia University).

The large spar buoy (with the mounted acoustical and optical instruments) and Waverider were independent experiments designed by investigators from University College London (Department of Mechanical Engineering), National Oceanography Centre (Southampton) and University of Leeds (School of Earth and Environment) to provide important auxiliary information, which would offer context for a better understanding of the processes (particularly related to bubble and wave mechanisms) causing the observed gas fluxes. The sonar, which provided the bulk of data used for analysis is based on in this thesis, was a subset of the bubble measurements designed to observe the large scale context on the overall bubble field. Auxiliary measurements of gas fluxes, such as DMS flux, have been conducted by another investigator from Plymouth Marine Laboratory (Plymouth). The funding support for these experiments was offered by Natural Environment Research Council (UK, under grants NE/J020893/1, NE/J020540/1, and NE/J022373/1).

In terms of field work, the primary objective of HiWinGS was to deploy direct measurements of trace gas and physical fluxes with an independent suite of bubble layer and breaking-wave observations (collected by optical and acoustical instruments mounted on a spar buoy), and wave physics and sea state observations (collected by our collaborators from University of Leeds using a Waverider buoy). The HiWinGS cruise took place on the American ship R/V Knorr (Figure 3.1b), and the observations were conducted in North Atlantic and Labrador Sea, at a series of seven stations during storms along a cruise track from Nuuk, Greenland, to Woods Hole, USA, from October 9 to November 12, 2013. The times and dates, together with the locations of all seven stations, of the spar buoy deployments are also summarized in Table 3.1.

The ship spent most of the time in the Labrador Sea, south of Greenland (first $\sim$20 days of the cruise). At the first six stations the sea surface temperature (SST) was about 6–8 $^{\circ}C$, whereas the last station was associated with the much warmer waters from the Gulf Stream (south of Nova Scotia) where SST reached 20 $^{\circ}C$ (Figure 3.1a).

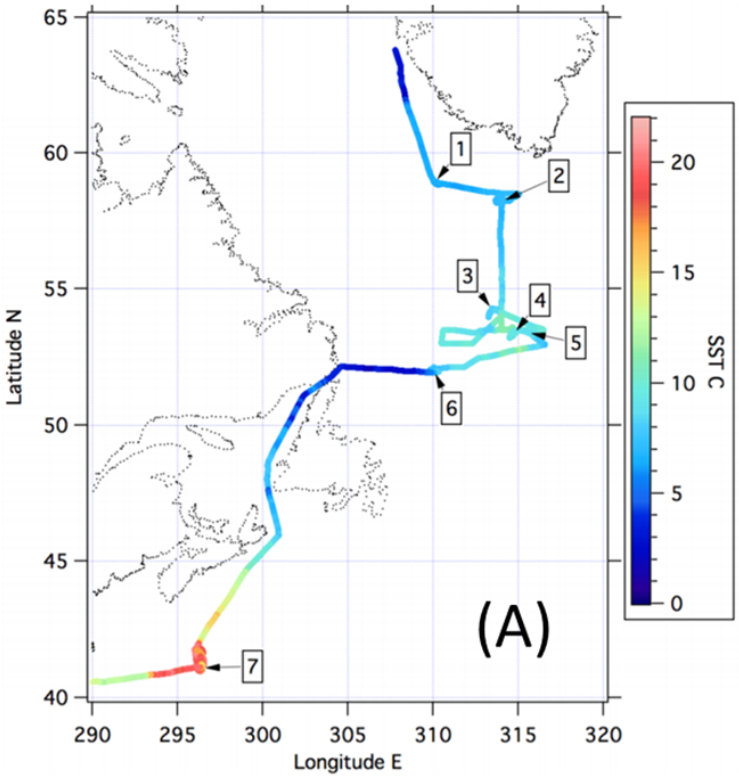

(B)

Figure 3.1: (A) Map of HiWinGS cruise route through all seven stations, from Nuuk, Greenland, to Woods Hole, USA, color-coded by *SST* (Blomquist et al., 2017). (B) The American ship R/V Knorr.

The Labrador Sea in October-November was selected for this measurement campaign because it is a location with frequent extra-tropical cyclones, high winds, frequent wave breaking, intense bubble entrainment and strong sink of atmospheric CO_2, associated with a large difference in partial pressure of CO_2 (ΔpCO_2) air-sea gradient. The itinerary of the ship was based on daily forecasts from European Centre for Medium-Range Weather Forecast (ECMWF) model provided by the Icelandic Met Office, aiming to identify and intercept the location with

maximum local winds generated by each storm system.

Buoys carrying observational sensors were usually deployed ahead of the storm, riding and drifting with the storm. The buoys were recovered in the calm periods between the storms and prepared for redeployment in the next storm system.

Table 3.1: Date and start time, and the location at each station along the cruise route. The deployment status of the Delta T sonar at each station.

Station	Date/Time (UTC)	Location (lat., long.)	Deployed sonar
1	Oct 11 2013 03:00	$58°N$, $48°W$	Yes (test)
2	Oct 14 2013 12:00	$58°N$, $46°W$	No
3	Oct 18 2013 18:00	$54°N$, $46°W$	Yes (contaminated)
4	Oct 23 2013 21:00	$53.5°N$, $45.5°W$	Yes (normal)
5	Oct 27 2013 20:00	$53.5°N$, $45°W$	No
6	Nov 01 2013 19:00	$52°N$, $50°W$	Yes (normal)
7	Nov 07 2013 09:00	$41°N$, $64°W$	Yes (normal)

The main work, conducted in this thesis, was based on data from a multibeam Delta T sonar (the characteristics of this sonar instrument will be described in detail in Section 3.4. The Delta T sonar was not deployed at all stations shown in Figure 3.1a, so there are no sonar measurements at stations 2 and 5 (Table 3.1). The sonar deployment at station 1 was only a test, so no data was used from this station (Table 3.1). The output visualized in the Delta T software for station 3 showed a contamination with acoustical reverberation consistently present in the laterally transmitted beams from the sonar profiles (Table 3.1). This led to unreliable acoustic datasets generated at the contaminated station, therefore these datasets will not be examined in this thesis (more details about this signal contamination is given in Section 3.5.4). The sonar output from stations 4, 6 and 7 did not contain reverberations (Table 3.1), so only the environmental conditions at these specific stations will be discussed in the following subsection. In total, about 98 hours of reliable data were collected from the sonar and compared with data from other independent sensors.

3.1.2 Environmental conditions

3.1.2.1 Time variation of wind/wave conditions

Figure 3.2 shows three time-series of 30-minute averaged wind speed at 10 metres height, U_{10N}, air-side (air density, ρ_a, was used) friction velocity, u_*, and significant wave height, H_s, respectively. The air-side friction velocity is proportional to the square root of wind stress, and it was calculated using Equation (1.43) (see Section 1.2.3). The significant wave height was partitioned in wind-sea (H_{sw}) and swell (H_{ss}) components. Details about the wave spectrum partition will be discussed in Section 3.4. The shading, in Figure 3.2, represents the periods, in stations 4 (Oct 24-25), 6 (Nov 02-03) and 7 (Nov 07-09), for which complete sonar measurements are available. Station 4 is characterized by the passage of the strongest recorded storm during this campaign ("St. Jude's Day" storm), with the production of the largest wind speed variation (in the $8 - 26\ m/s$ range).

The H_{sw} and H_{ss} time-series are fairly complete during the sonar deployment periods (shaded areas), with the exception of station 4, when the GPS reception from the Waverider buoy (the instrument that measured the waves, which will be described in Section 3.4.1) was frequently lost in the severe sea state conditions generated by Oct 24-25 storm (Figure 3.2c). At the peak of the large storm in station 4, the Waverider was intermittently dragged beneath the wave peaks, leading to the loss of GPS reception. Therefore, the data contaminated by the temporary loss of GPS reception was excluded from the time-series.

As the storm system advanced, U_{10N} gradually increased to 20 m/s throughout Oct 24. During this period, wind-sea significant wave height H_{sw} remained steady at about 2.5 m, with the presence of a slightly dominant swell. From Oct 25, wind speed sharply decreased to 10 m/s as the eye of the storm was approaching, while large swell waves of about 6–6.5 m were present (Figure 3.2a and Figure 3.2c). As the eye of the storm passed over the region, in a 3-hour time interval, U_{10N} decreased to 8 m/s, while u_* also diminished to a minimum value (Figure 3.2a and Figure 3.2b). After the passage of the eye of the storm, over about a 3-hour interval, wind speed rapidly increased to about 26–27 m/s, which is the maximum 30-minute averaged wind speed recorded in all stations. This rapid wind speed variation is associated with a steep growth of wind-sea waves up to about 6.5–7 m, coexisting with a swell of about 5.5–6 m.

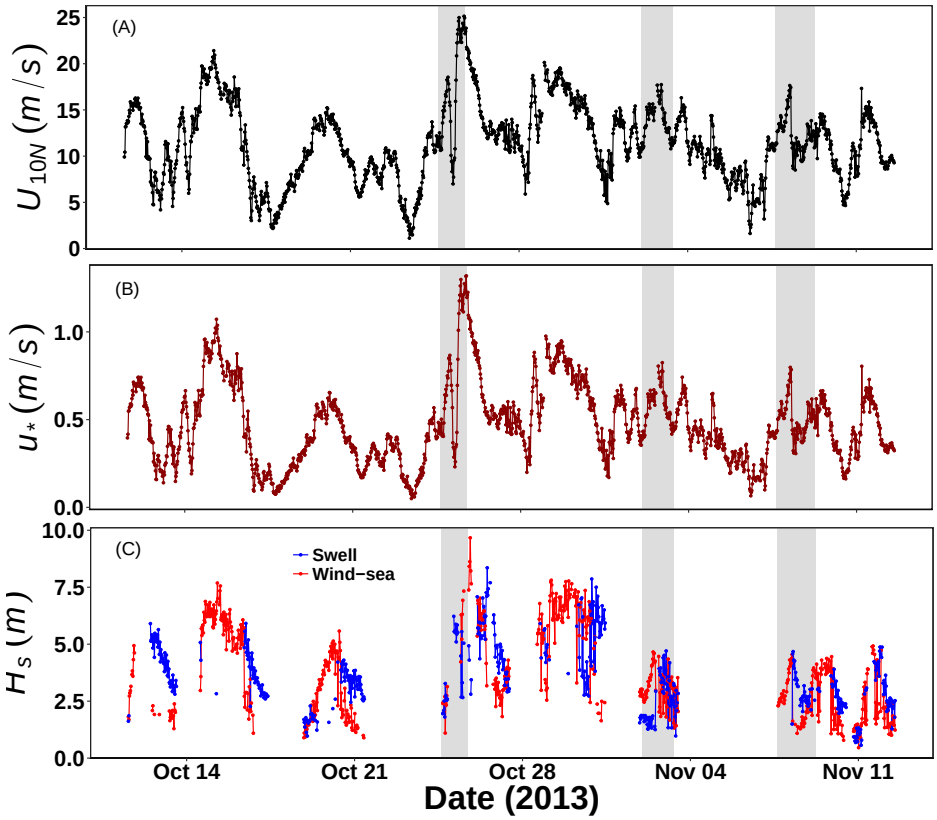

Figure 3.2: Time-series for the entire measuring campaign, from October 9 to November 12 2013, of wind speed (A), friction velocity (B) and significant wave height (C). In (C) the significant wave height is measured for wind-sea (red curve) and swell (blue curve). The time frames, corresponding to stations 4 (Oct 24-25), 6 (Nov 02-03) and 7 (Nov 07-09), for which we obtained complete bubble measurements are highlighted by the grey shades. This figure is produced using the wave spectra calculated by our collaborators from University of Leeds.

The location for station 6 was to the east of the Labrador Current in cooler waters ($SST = 6°C$). This storm occurred in the Nov 02-03 time interval and we observed relatively uniform winds of 16–18 m/s for most of the time (Figure 3.2b). At the beginning of the storm, over a 6-hour time interval on Nov 02, U_{10N} increased from a minimum of 11 m/s to the sustained level. Toward the end of the period, wind speed significantly decreased overnight, from Nov 02 to Nov 03. The sea state during this storm was partly characterized by the coexistence of wind-sea and swell, over a 12-hour time interval, from Nov 02 to Nov 03. In this time period, wind-sea waves decreased down to about 3 m under a relatively high wind stress (Figure 3.2b and Figure 3.2c). Through much of Nov 02, over a 15-hour time interval, a dominant wind-sea was present, characterized by waves of 3–4 m height.

Station 7 completed our cruise and was located in warm waters ($SST = 20°C$) under the

influence of Gulf Stream, south of Nova Scotia. As the cold front from the storm passed over the region, the air temperature behind the cold front decreased to 10°C over a much warmer sea surface, leading to significant convective instability in the atmosphere during Nov 08-09 interval. A wind speed of 11–14 m/s characterized most of the storm period, but U_{10N} increased to a maximum of 18 m/s on Nov 08 (Figure 3.2a). This storm almost exclusively produced a separated sea state (wind-sea and swell are not simultaneously present) where wind-sea was associated with the highest recorded wind speed at this station, over a 16-hour time interval, from Nov 07 to Nov 08. After reaching a peak of 4 m, wind-sea rapidly decreased as swell propagated, and wind stress maintained low for the rest of the time interval (Figure 3.2).

3.1.2.2 Wave field variability

Wave systems/components with different spectral energy densities and frequencies can influence the sea state and air-sea interaction processes. To better understand the wave field variability, the directional wave spectrum must be known, because this spectrum contains information about the variation of spectral energy density, $S(f_{wave}, \theta_{wave})$, with direction (in degrees) and frequency, f_{wave}. Figure 3.3 shows a sample directional wave spectrum (upper panel) and 1D wave spectrum (bottom panel), both extracted from a single 30-minute wave record. The directional spectrum, from Figure 3.3 (upper panel), indicates the coexistence of swell (gray shading) and wind-sea (no shading) components at 1715, Oct 24, when a low wind speed of about 11 m/s was present.

This directional wave spectrum has been smoothed by removing local peaks and noisy wave groups (the smoothing approach of Portilla et al. (2008) was used, which is described in Section 3.4.1). The directional wave spectrum shows the direction from which these wave components propagate. The 0° angle indicates the north coordinate. The swell and wind-sea waves are propagating from the north-west and south to south-west directions, respectively (Figure 3.3, upper panel).

The swell shows a larger spectral peak ($S(f_{wave}, \theta_{wave}) > 0.09\ m^2/Hz\ deg^{-1}$) than the wind-sea ($S(f_{wave}, \theta_{wave})$ of about $0.09\ m^2/Hz\ deg^{-1}$), but the wind-sea shows a wider spectral peak (and generally larger variability/spread of the spectral energy density) with direction. The spectral peak of swell waves is confined at $f_{wave} < 0.1\ Hz$, while the wind-sea spectral peak

exists in the 0.1–0.2 *Hz* f_{wave} range.

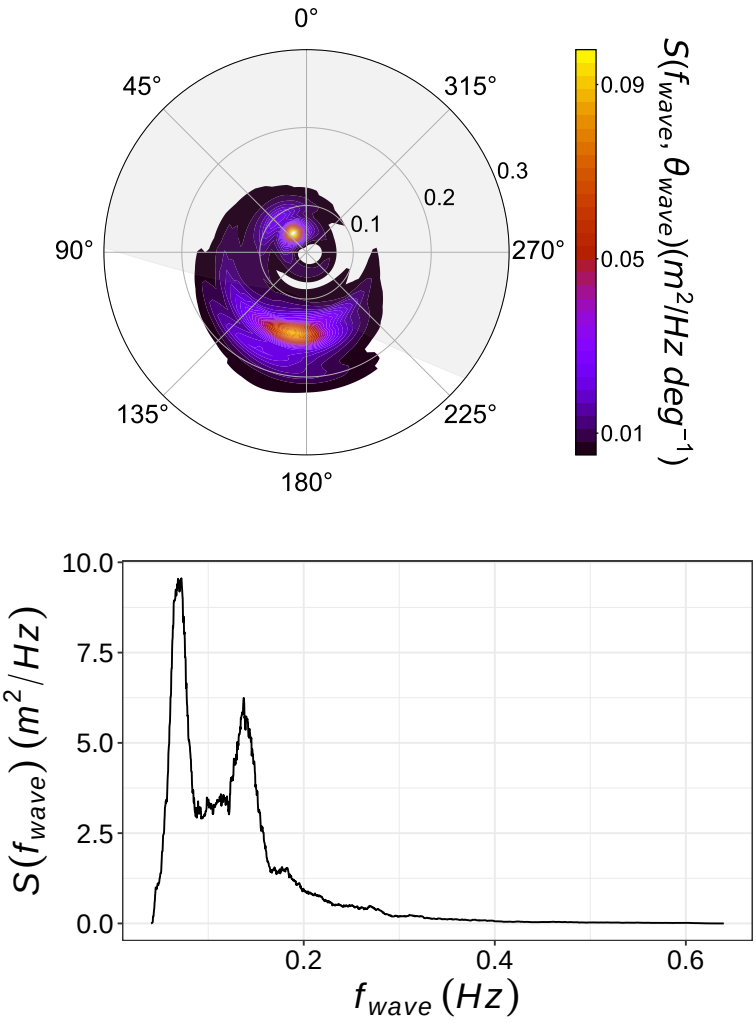

Figure 3.3: Directional (upper panel) and 1D (bottom panel) wave spectra. (Upper panel) The contours show different levels of $S(f_{wave}, \theta_{wave})$, the 0° angle represents the north coordinate, the radial ticks indicate different f_{wave} values and the gray shading indicates the swell wave component that coexists with wind-sea waves (not shaded). (Bottom panel) The variation of $S(f_{wave})$ with f_{wave}, which shows the presence of two spectral peaks (also observed in the directional spectrum).

Two spectral peaks can also be observed in the 1D spectrum (Figure 3.3, bottom panel). Since it was not smoothed (it is raw), the 1D spectrum initially showed large variability (with many oscillating peaks), so a moving average window with 55 frequency points has been used for smoothing. The wind-sea/swell partition has not been undertaken for the 1D wave spectrum, so no particular spectral peak can be attributed to whether swell or wind-sea. However, since the spectral peaks, in the 1D spectrum, are present at the same frequencies as in the directional spectrum, they can be considered as the same spectral peaks present in the direc-

tional spectrum. Similar to the directional spectrum, the spectral peak at the lower frequency ($< \ 0.1 \ Hz$) is larger ($S(f_{wave})$ of about 9 m^2/Hz) than the peak at $f_{wave} \ > \ 0.1$ (which only reached a $S(f_{wave})$ of about 6 m^2/Hz), as shown in Figure 3.3 (bottom panel).

3.2 Meteorological measurements

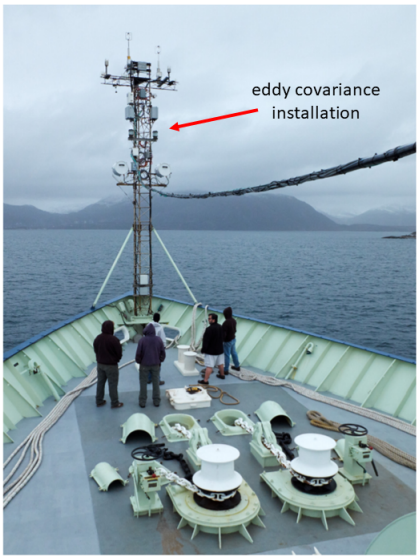

Figure 3.4: Eddy covariance equipment installed on the bow mast at 16 m above sea level.

R/V Knorr was equipped with instruments collecting meteorological, physical oceanographic and chemical (air and seawater) measurements operated by a shipboard technical team and other scientists from NOAA/ESRL/PSD. Meteorological measurements include 1-minute average bulk properties (air temperature, humidity, barometric pressure, down-welling solar radiation and rain rate) and wind speed, wind stress, momentum, energy and buoyancy fluxes via direct eddy covariance technique.

The chemical air-sea fluxes were obtained from eddy covariance measurements of CO_2, dimethyl sulfide (DMS), acetone and methanol. For both meteorological and chemical measurements, Blomquist et al. (2017) used a NOAA/ESRL/PSD wind-motion system, mounted on the bow mast at 16 m above the sea surface with rapid sampling sensors at 10 Hz, together with two additional sonic anemometers, namely a Gill model R2 from the University of Hawaii and a Gill Windmaster Pro from Plymouth Marine Laboratory (Figure 3.4). Using these ship instruments, 1-minute, 10-minute, 30-minute and 60-minute averages of neutral wind speed at

10 metres relative to the earth, U_{10N}, were obtained.

Table 3.2: The ship instrumentation and associated measurements conducted by groups from various institutions in North Atlantic in October-November, 2013.

Institution	Instrumentation	Measurements
NOAA/ESRL/PSD	wind-motion system laser system rain gauge, radiation sensor	wind speed, momentum and CO_2 fluxes 1D wave spectra bulk meteorological parameters
Univ. of Hawaii	wind-motion system and DMS chilled mirror hygrometer CTD	heat, momentum and DMS fluxes bulk humidity seawater DMS concentration
PML	wind-motion system	methanol and acetone fluxes
Univ. of Leeds	aerosol samplers	aerosol counting
Lamont-Doherty Lab.	whitecap camera	breaking waves and whitecap fraction

Physical oceanographic measurements encompass CTD profiles with measurements of temperature and salinity, ocean current profiles and wave breaking properties such as whitecaps imaged by two Mobotix MX-M24M IP cameras with 32 mm lenses mounted on the starboard side of R/V Knorr.

3.3 Wave measurements

3.3.1 Datawell Waverider

To better understand the wave field variability, the 1-dimensional and directional wave spectra have to be measured. During the HiWinGS cruise, a Datawell DWR-4G Waverider buoy, with a 0.4 m diameter and a transmitting and receiving GPS signal antenna mounted at the top, was deployed at each station by our collaborators from University of Leeds. During the deployments, with the exception of station 4 (the big storm), the Waverider was drifting freely within a range of about 5 km of the ship, covering the ship footprint of the gas flux measurements. At station 4, given the rough seas favoured by the big storm, the Waverider was deployed

tethered to the ship on 200 metres of propylene rope.

Figure 3.5: An image of the Waverider buoy – the observed long antenna is used for transmitting and receiving GPS signal.

This does not impact the measurements, but only when the tether remained slack and the ship maintained a relative position that avoided sheltering the buoy from incoming waves (deviations from the ships's relative position did occur during periods from station 4; see Section 3.1.2). The Waverider was functioning at a spectral frequency ranging from 0.025 Hz to 0.6 Hz, corresponding to waves with a wavelength larger than 4.3 m (Brumer et al., 2017). The deployment and recovery of the Waverider buoy were conducted by our collaborators from University of Leeds. The wave spectra and wave statistics, used in this thesis, were produced by our collaborators from University of Leeds and Columbia University – for more details on these measurements, see Brumer et al. (2017). An illustration of the Waverider is shown in Figure 3.5.

The Waverider, as it follows the shape of the waves, measures its displacement, at 1.28 Hz, by using the Doppler shift of the GPS signal. This signal is integrated to obtain a time-series of the 3-dimensional displacement of the Waverider from which the 1-dimensional and directional wave spectra and statistics, on 30-minute interval, were derived (Brumer et al., 2017). The directional wave spectra were calculated using the Extended Maximum Likelihood Method (Hashimoto et al., 1993). The directional wave spectra are calculated with a resolution of 1°

by 0.005 *Hz* and a frequency range of 0.04 to 0.64 *Hz*. Sparse spectral peaks occasionally occurred at very low frequency (periods of 10 seconds). These peaks are presumed to result from the integration of low frequency noise in the Waverider's velocity measurements. Before calculating the wave spectra, these noise peaks were suppressed by high-pass filtering the displacement time-series using a pass-band frequency of 0.05 *Hz*.

3.3.2 Spectral partitioning

Many schemes to separate the wind-sea and swell components of the wave spectrum have been proposed, with no clear best method. Many of these methods rely on identifying thresholds of frequency and direction for a single spectrum. These methods can fail particularly for measured spectra, which are usually noisy, may be non-stationary, and for which small changes in the averaging period can result in changes in spectral peak frequency direction, thus affecting their classification.

For the HiWinGS measurements, the partition of the directional wave spectrum was conducted following the approach of Hanson and Philips (2001) and Portilla et al. (2008). The spectra are divided into an arbitrary number of wave groups using an inverted watershed MATLAB function (Portilla et al., 2008), thus each point in the spectrum is associated with a local peak. Since measured spectra can be characterized by a large number of wave groups, Portilla et al. (2008) reduced these by smoothing the spectrum, applying a 3×3 element average (kernel) around each spectral estimate. Hanson and Jensen (2004) applied an 8-point connected smoothing function (*imhmax* function from MATLAB image processing toolbox) around each spectral estimate to remove local peaks less then some threshold value. The partitioning of the wave spectra, measured during HiWinGS, is a combination of the mentioned approaches. The partitioning starts with the implementation of the 3×3 element averaging kernel around each point, followed by the removal of the remaining local peaks of a magnitude less than 1.5% of the spectral maximum. This usually results in the return of fewer than 10 discrete wave groups. Any wave group contributing with less than 8% of the total spectral energy is then combined with a group with a peak closest to its own. All the remaining wave groups are finally partitioned into wind-sea and swell using the wave age criterion proposed by Hanson

and Philips (2001):

$$c_p \leq 1.5 U_{10N} \cos \delta_w, \tag{3.1}$$

where c_p is the wave phase velocity at the peak frequency of the wave group, and δ_w is the angle between the directions of the wind and the peak of the wave group. This was reformulated in terms of the peak frequency, f^*_{wave}, for deep water waves, as following:

$$f^*_{wave} \geq \frac{g}{2\pi}[1.5 U_{10N} \cos \delta_w]^{-1} \quad 0 \leq \delta_w \leq \frac{\pi}{2}. \tag{3.2}$$

The factor of 1.5 in Equation (3.1) ensures that most wind-sea peaks are identified (Hanson and Philips, 2001). The range of δ_w encapsulates only wind-driven waves, which always eventually tend to propagate in the direction (or at relatively small angles) of the wind.

3.4 Acoustical and optical measurements

3.4.1 Spar buoy

A National Oceanography Centre (NOC) spar buoy was deployed in all seven storms during HiWinGS cruise (Figure 3.6a) and floated freely during each deployment. More details about the design and calibration of the spar buoy are given by Pascal (2011). The spar buoy is an 11-metre metal platform which has a hollow and watertight hull with a circular cross-section. The buoy was freely floating in the ocean with an intentional tilt at $\sim 20^\circ$. The main purpose of this spar buoy was to serve as a platform for independent acoustical and optical measuring instruments vertically aligned during the deployments.

An attached weight forced the buoy to lean away from the wind. This tilt is important because it allows the spar buoy to orientate into the wind (by having a weight on one side to keep this orientation), permitting measurements to be made on the undisturbed upwind side of the buoy. This enabled the acoustical and optical sensors strapped to the spar buoy to measure wave breaking and the subsurface bubble activity within the entire 8-metre water column.

The spar buoy was floating with about 80% of its length submerged (Figure 3.6b) – that is $\simeq$8 m underwater from the bottom of the buoy to the mean sea surface – thus the mounted instruments were submerged at different depths. It took several crew members to deploy the spar buoy right before each storm. Between the storms, the spar buoy was recovered from

the ocean and the instruments were unstrapped from the buoy to upload the data to external hard-drives.

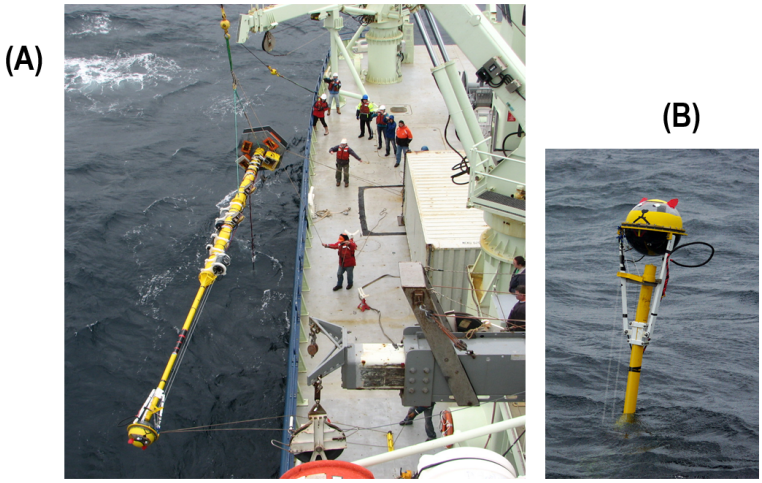

Figure 3.6: (A) Deployment of spar buoy, with all instruments attached, overboard R/V Knorr. (B) Free-floating spar buoy, after deployment, with about 80% of its length underwater – the observed slight tilt directed the spar buoy upwind to intercept the incoming waves.

3.4.2 Spar buoy instruments

Figure 3.7 shows a schematic diagram of the spar buoy together with all the acoustical and optical sensors vertically arranged from top to bottom as following: foam camera – embedded in a protective spherical capsule at the top of the buoy (~ 3 m above sea level) – recording whitecap coverage from active breaking waves; a bubble camera which was located at ~ 2 m below sea level, capturing subsurface bubble size distributions; two acoustical resonators submerged at about 4 m and 6 m, respectively, detecting deeper individual bubbles over a wide range of sizes; sonar, located at the bottom of the buoy at 8 m depth, was measuring large scale structures such as bubble plumes penetrating across the entire vertical range. All the spar buoy instruments and their measuring descriptions are summarized in Table 3.3.

During the cruise, 4-metre long capacitance wires (Figure 3.7) were operated by our collaborators from NOC to measure the water surface position relative to the buoy. Only small and short waves (< 2 metres) can be measured with higher certainty. The spar buoy itself was subject to strong vertical movement caused by the largest waves, so the wave wires cannot be used to extract overall wave spectra, but they can be used to extract the position of the instrument with time. These surface displacements, detected with the wave wires, were averaged to

obtain the mean sea level (with respect to the spar buoy). Using the mean sea level, the total submerged spar buoy's length of about 8 metres (80% of its length) can be retrieved, with all the mounted underwater instruments being submerged below this calculated mean sea level.

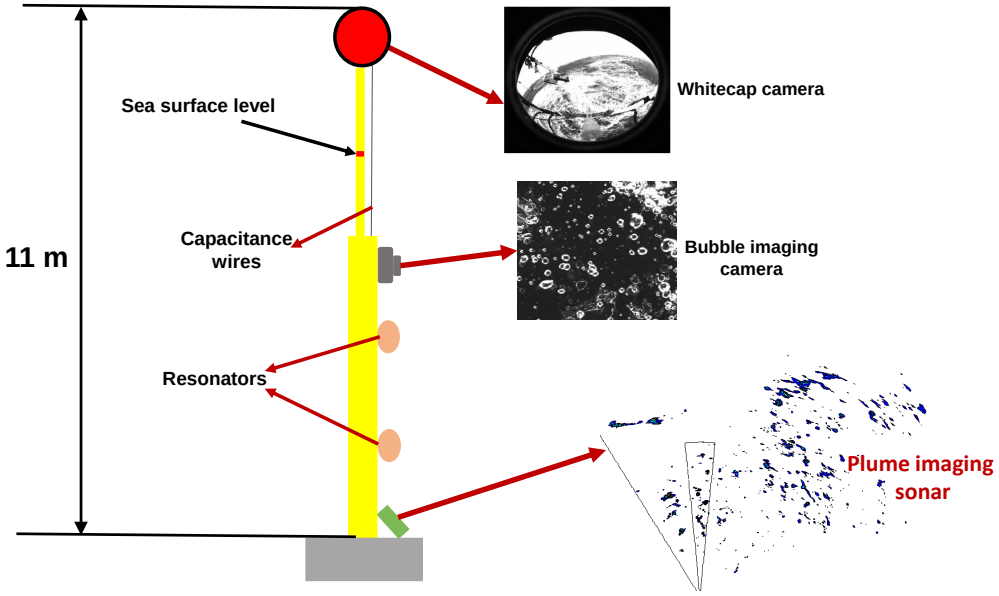

Figure 3.7: Scheme of the 11-m long upright spar buoy relative to the sea level, with all acoustical and optical instruments attached.

Table 3.3: The spar buoy instrumentation and associated measurements conducted by groups from various institutions in North Atlantic in October-November, 2013.

Institution	**Instrumentation**	**Measurements**
NOC Southampton	wave wires	wave spectra and time-series
Univ. of Southampton	bubble camera	large bubble size distribution
	acoustical resonators	small bubble size distribution
	multibeam sonar	bubble plume evolution
	foam camera	sea surface foam coverage
Univ. of Leeds	ADV current - turbulence probe	subsurface turbulence and current

3.4.3 Foam camera

Whitecaps, produced by fast rising bubbles at the surface during breaking waves, are strongly visible to optical sensors due to their intense brightness compared to the 'dark' ocean. The Foam Camera was built by our collaborators at University of Southampton (who also produced the whitecap images and developed a partial method for processing the images) to provide bulk measurements of the brightness intensity from foam patches (detailed information about this device is reported by Al-Lashi (2016)). The camera uses a wide-angle lens ($180°$) known as fish-eye lens that produces visual distortions to image incoming breaking waves. Having this wider angle of view, the camera was also able to image breaking waves propagating from the side. The Foam Camera had a 15 *Hz* sampling frequency, producing up to 40000 images per hour.

3.4.4 Underwater bubble camera

Accurate knowledge about bubble size distribution is needed for a better understanding of the void fraction variation just beneath breaking waves. In some cases of vigorous wave breaking, the extreme void fraction can reach values $\geq$ 0.5 (Deane, 2016) as a result of very large air volumes injected by breaking waves. Acoustical devices are not functional in such extreme bubble densities due to total bubble extinction (Deane, 2016; Trevorrow, 2003) and so optical instruments are used for measuring such bubble populations. A high-resolution bubble imaging camera was deployed to capture individual bubbles and retrieve the bubble density and a wide range of bubble radii. This optical instrument was designed and built in 2013 by our collaborators at University of Southampton and detailed information about the hardware components and functionality can be found in reports of Al-Lashi et al. (2016) and Al-Lashi et al. (2017). A picture and a scheme of the bubble camera are shown in Figure 3.8. The camera was mounted on the buoy at 2 metres below sea surface to measure the bubbles in the upper region of the bubble plumes.

The bubble camera comprises the camera with a mirror assembly connected to a computer. The images were stored in a specific format during recording (left image from Figure 3.8). The bubble camera computer could be operated via a running Linux operating system directly on a digital screen protected by a perspex lid (right image from Figure 3.8).

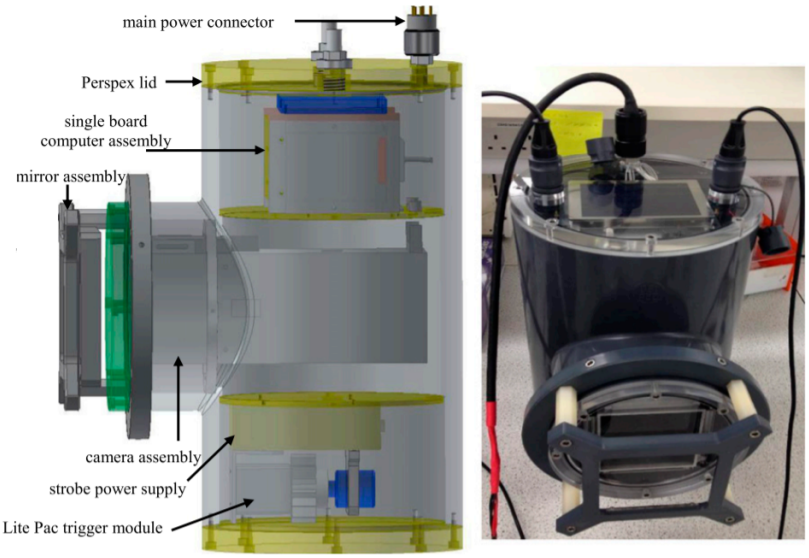

Figure 3.8: Scheme of bubble camera design and components (left), and an image of the actual bubble camera (right). Figure extracted from Al-Lashi et al. (2016).

The bubble camera was operating in preprogrammed measurement periods with 8.5 hours recording, and produced images at 15 frames per second during the deployments, enabling the analysis of about 850000 images (Al-Lashi et al., 2016). The sides of each image, generated by the bubble camera, have a length of 4 cm (Figure 3.9), so the sampling volume is 64 cm^3. During the cruise, timers were used to synchronize the power supplied to both the bubble camera and the foam camera, which permitted us to align the measurements of subsurface bubble presence and whitecap activity. A strong pulsed illumination system was built into the bubble camera, enhancing bubble visualization in the dark ocean by illuminating the bubbles with a light sheet. Generally, a limiting element of accurately capturing bubbles is the underwater non-uniform illumination, which can induce noise due to much brighter bubbles within the light sheet than bubbles outside (Al-Lashi et al., 2016; Leifer et al., 2003).

The bubble camera recorded images which were classified into three main categories: small-bubble, large-bubble and complex images, which are classified by an algorithm implemented by Al-Lashi et al. (2016). These complex images are usually associated with a larger bubble population captured as the buoy was going into the water (Figure 3.9d). The images show bubbles of different shapes, depending on their size; small bubbles are more likely spherical, whereas large bubbles tend to be non-spherical (Figure 3.9a). The bubble size range that this device can detect is from 20 μm radius (the size of a pixel) up to 10 mm, although we did not observe bubbles larger than about 300 μm during this cruise. The small spherical bubbles

that are not located in the light sheet provided by the illumination system are in the form of disks as shown in Figure 3.9b.

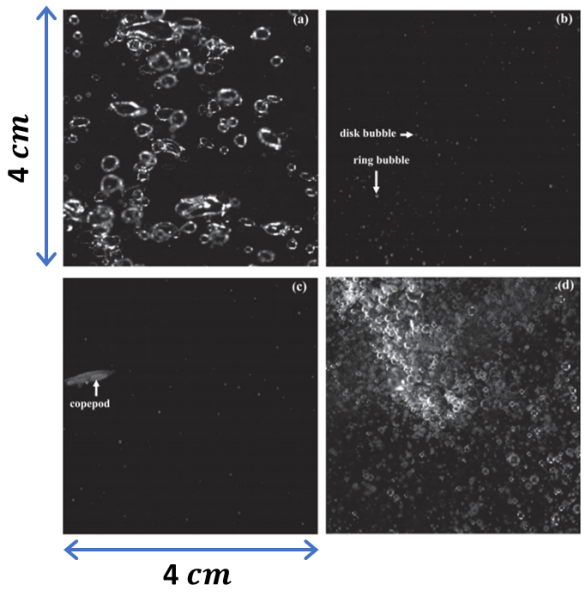

Figure 3.9: Types of images sampled by the bubble camera during one of the deployments: (a) non-spherical bubbles, (b) circular bubbles in the form of rings and disks, (c) a copepod, (d) complex image taken within a bubble plume. The size of of all 4 images is 4 $cm \times 4$ cm, as shown by the blue arrows. Figure extracted from Al-Lashi et al. (2016).

Although this imaging system has a high enough spatial resolution to measure a wide range of bubble sizes, there are even smaller bubbles than a single image pixel, hence the detection of the smallest bubble radius is limited by the pixel size (~ 20 μm). The camera captured images of bubbles in a water sample volume of $4 \times 4 \times 0.5$ cm^3 (Al-Lashi et al., 2016). The maximum measurable void fraction of the camera is 0.1, which is smaller by almost a factor of 3 than the device used by Stokes and Deane (1999).

3.4.5 Acoustical resonators

The persistent population of smaller bubbles (about $0.1 - 100$ μm in radius), which can remain for tens of minutes after the wave breaks (Blenkinsopp and Chaplin, 2011; Caruthers et al., 1999; Czerski, Twardowski, Zhang and Vagle, 2011), are usually contained in fully-formed mature bubble plumes. Acoustical resonators were used on this cruise to estimate the void fraction resulting from these deeper and more persistent bubbles. Due to some technical problems with its functionality, the resonator located deeper at about 6 m did not function

during the deployments. Nevertheless, the resonator positioned at 3.2 *m* depth was normally functioning and it could operate at 1 *Hz* sampling frequency, retrieving a wider range of void fraction (about 10^{-9}–10^{-5}); this void fraction is specific to fully-formed bubble plumes, which contain far less dense bubble populations than the ones present in active breaking waves.

The resonator is equipped with two transducers which essentially are two plates sensitive to pressure fluctuations. One of the transducers is a transmitter, sending the broadband noise with a frequency ranging between approximately 2 *kHz* and 1 *MHz*, and the other transducer receives the transmitted signal. Both transducers were recording for 0.25 seconds each second. Details about the physical characteristics of this acoustical resonator system and on sound attenuation techniques are provided by Czerski, Twardowski, Zhang and Vagle (2011) and Czerski, Vagle, Farmer and Hall-Patch (2011). The main author in these papers is responsible for the acquisition and processing of the resonator data used in this study.

Figure 3.10: An image with the two resonators strapped to the spar buoy before deployment, showing the pairs of transducers.

An image with the resonators strapped to the spar buoy just before a deployment is shown in Figure 3.10. The resonator sends a pulse of broadband sound into the water volume between the two plates. This sound signal is subject to attenuation due to bubbles which are close to their natural frequency, reducing the power spectral density of the signal. The underwater acoustical resonator is an open-sided echo chamber and it has the advantage that, by transmitting a continuous broadband input signal, it generates harmonic resonant peaks at many frequencies simultaneously (Czerski, Twardowski, Zhang and Vagle, 2011).

Every peak provides a sensitive measure of acoustical attenuation, and the resonator gen-

erates about 140 peaks between 20 and 800 kHz, measuring bubbles with radii in the range of 4–180 μm. The purpose of this instrument was to provide a bubble size distribution over that radius range once per second, allowing the void fraction to be calculated.

3.5 Delta T multibeam sonar

An Imagenex 837A Delta T 260 kHz imaging multibeam sonar was deployed for the measurement of subsurface bubbles that organize into deep plumes. This instrument is the main source of data used in this thesis. As described in Section 2.4, bubbles are very efficient in absorbing and scattering sound waves, thus acoustical devices such as sonars constitute very powerful tools in transmitting sound and receiving the scattered sound signals from oceanic bubbles.

The sonar produced measurements of full vertical cross-sections of the entire bubble layer evolving in time. Although the sonar can easily measure the shape and vertical variation of the large-scale bubble structures, it cannot directly detect the intrinsic properties of the bubble layer such as void fraction obtained from individual bubbles distributed within the bubble layer. The sonar was aligned on the vertical with the other underwater bubble measuring devices, such as the bubble camera and resonator, enabling a direct comparison of plume properties measured by different instruments.

3.5.1 Physical characteristics

The 837A Delta T multibeam sonar is an advanced electronics-acoustics system designed to provide video-like imaging of underwater structures and shapes. This system consists of an electronics package embedded in a stainless steel cylindrical recipient, and transducer which is both a transmitter and receiver of acoustical signal (Figure 3.11) similar to most sonars as discussed in the literature review from chapter 2. The transducer of this type of sonar consists of an array of receivers, which are designed to detect the incoming reflected signal from different angles (depending on the number of beams the sonar uses).

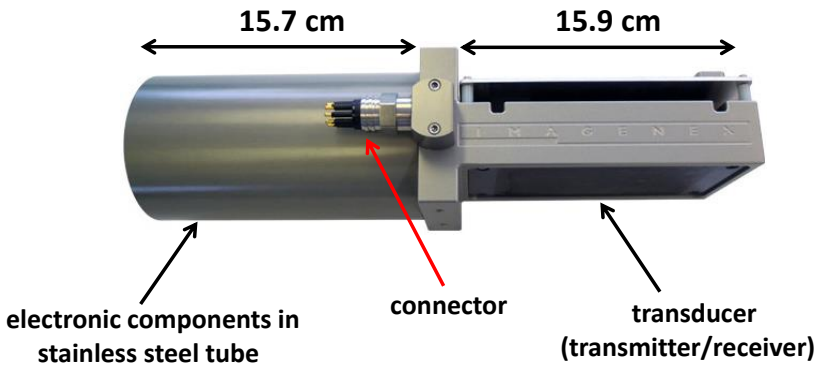

Figure 3.11: Image of the 837A Delta T multibeam sonar head (Imagenex Technology Corp.).

The electronics part is powered using a direct electrical current through a connector attached to the sonar head (Figure 3.10) from a 24-Volt power supply using about 0.4 A (Amperes) at 24 volts. The power arrives to the sonar head through a cable which comes with the unit along with an underwater connector to fit with the sonar connector. The transducer has a rectangular shape and the acoustic radiating surface can be calculated from the dimensions of the transducer given in Figure 3.11.

3.5.2 Operation principles

3.5.2.1 Analog-to-digital conversion

The electronics part of the sonar's transducer consists of an analog-to-digital converter (ADC), which is a system that converts analog signal (reflected sound) to digital signal. The ADC samples the input time-varying continuous voltage signal and converts it into a discrete signal. A quantization process is then used to map the sampled signal to a finite set of discrete values known as quantization levels. The number of quantization levels depend on the signal resolution, and is given by 2^{N_b}, where N_b is the number of bits (e.g., for 3-bit signal, there is binary output with three digits (combinations of 0s and 1s), which consists of 2^3 quantization levels ranging between 000 and 111). Following these processes, a digitally reconstructed signal is obtained, which resembles a step function that follows the original analog voltage signal. In-between quantization levels, there is a constant range of voltage values, known as step size (which is equivalent to the voltage signal resolution).

An ADC sampling rate significantly higher than the original signal frequency is generally

needed to reconstruct a digital signal that closely follows the original signal. Therefore, the step size decreases with the increasing number of quantization levels, generating a digital signal with a higher resolution. The Delta T sonar digitally processes the signal using 8 bits, so 256 quantization levels (ranging from 0 to 255) are used to generate the digital signal. The voltage signal resolution of the Delta T sonar is the result of the ratio between the full-range voltage amplitude (24 volts) and the number of quantization levels (256). This ratio gives a signal resolution of 0.09 volts, which represents the lowest voltage that can be resolved by the electronics part of the Delta T sonar.

3.5.2.2 Digital processing uncertainty

In general, the reconstructed digital signal does not exactly follow the pattern of the original analog signal, so an uncertainty always characterizes the digitization of the signal. This uncertainty is quantified by the quantization error (QE) of the digital signal. The difference between the signal input (original signal) and the corresponding digital values is referred to as the quantization error. Mathematically, QE can be expressed using the step size (or digital resolution), $r_{digital}$, and the number of quantization levels, 2^{N_b}, as following:

$$QE = \frac{r_{digital}}{2^{N_b}} \times 100. \tag{3.3}$$

With $r_{digital} = 0.09$ volts and 256 quantization levels, the quantization error, for the Delta T sonar, is 0.04%.

3.5.2.3 Spatial resolution setting

The Delta T multibeam sonar transmits sound pulses at 260 kHz. The transmitted pulse has a duration of 120 μs, with a rate of six transmitted pulses/pings per second (6 Hz sampling frequency). Using Equation (2.20) with the two-way speed of sound, a pulse length of 0.135 metres has been calculated for the Delta T sonar. The high temporal frequency of Delta T sonar provides more accurate estimates of the changes with time in the structure of the target. After the sonar transmits a pulse into the water, the receivers are turned on, and the bandwidth of the incoming signal is filtered to match the final resolution setting. The receiver channels are set to digitize/sample the return signal, in real time, at a rate much higher than the final resolution rate (personally communicated by Doug Wilson from Imagenex Tech. Corp.).

The ability of the sonar to distinguish between two targets is related to the pulse length. If two targets are within 0.135-metre spatial coverage and at the same angle from the sonar, then they would be difficult to distinguish. However, the high digitizing rate, known as oversampling, gives the ability to determine the range to a single target more precisely than the pulse length would suggest. For the Delta T sonar, the pulse length is about 2.5 times the oversampling resolution after signal processing and beam forming (personally communicated by Doug Wilson from Imagenex Tech. Corp.).

3.5.3 Multibeam structure

3.5.3.1 Beam geometry and sampling volume

The Delta T multibeam sonar uses 120 acoustical beams in a fan-shaped swath. The angular separation between two neighbour beams is 1°, hence the swath has a 120° total width (Figure 3.12). The maximum range of the Delta T sonar beams is factory-set to 20 metres, which is the limit set by the ping-receive time. Moreover, the beam swath is 3-dimensional, so it is also characterized by a thickness of 1.7°. Each beam is, therefore, described by a horizontal spacing – relative to the neighbour beam – as the width angle of 1° and a thickness with the angle of 1.7° (Figure 3.12).

The spatial resolution is given by the size of a sonar voxel (3-dimensional pixel) which is the 3-dimensional spatial sampling volume. The width of the voxel depends on the space between two beams, hence it is given by the 1° width angle, whereas the voxel thickness is given by the 1.7° angle. The height of the voxel (depth bin) has a value of 4 *cm* (0.04 *m*), so the maximum range is partitioned in 500 range bins (the range of a beam is incremented with 4 *cm* as distance increases from the sonar head).

Using the above voxel dimensions, the sampling volume for a sonar voxel has been computed. This sampling volume will be used in the conversion of the echo intensity signal into backscattering cross-section per unit volume in the sonar data. Each beam has an acoustical axis present along the centre of the beam, splitting the beam spacing in two. Thus, the 3-dimensional beam angular separation mentioned above yields a half power width angle of $1/2$ (the 1° width angle is split in two) and a half power thickness angle of $1.7/2$ (the 1.7° thickness angle is split in two) for each beam. In order to obtain the sampling volume, the beam

width B_w and beam thickness B_t were computed, both in meters at each beam range R, which increases from the sonar head with 0.04 m at each step along the 20-metre maximum range (in practice, the range used is 8 metres).

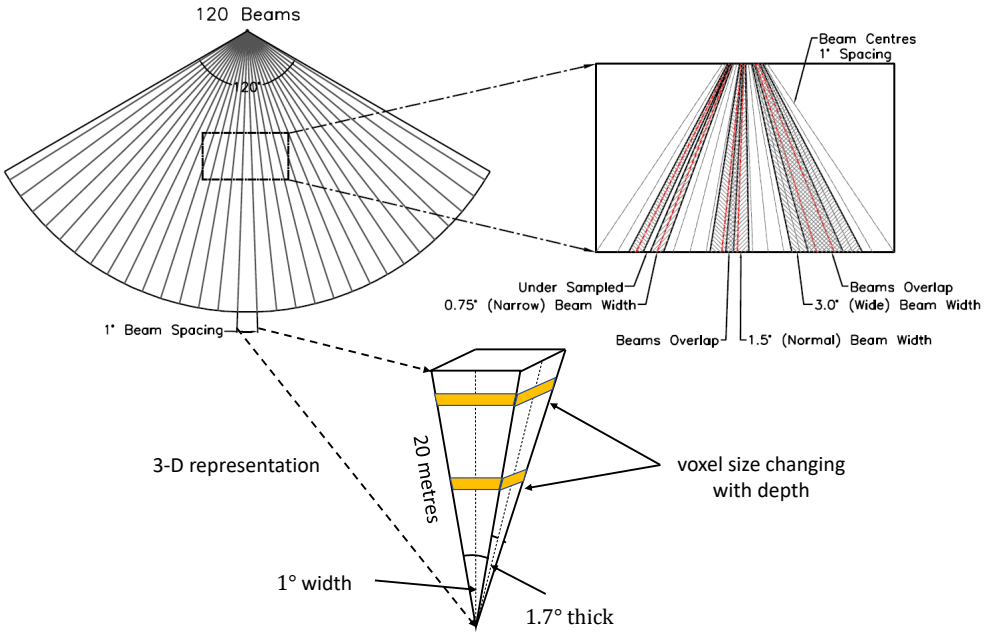

Figure 3.12: Scheme of all 120 Delta T sonar beams spreading, thus increasing the distance between two beams with range (top plot on the left, Imagenex Tech. Corp.). The structure of beam width for the Delta T multibeam sonar (top plot on the right, Imagenex Tech. Corp.). 3-dimensional representation of a single Delta T sonar beam with a 1° width and a 1.7° thick; the change, with depth, of the size of the sonar voxel (coloured in orange) is also shown (bottom plot).

The range bin, R, was then multiplied by the half power sines of $1/2$ for B_w and $1.7/2$ for B_t,

$$\begin{aligned} B_w &= R \times 2 \times \sin\left(\frac{1}{2}\right), \\ B_t &= R \times 2 \times \sin\left(\frac{1.7}{2}\right). \end{aligned} \tag{3.4}$$

Therefore, B_w and B_t are used to compute the sampling volume (also called insonified volume) in each sonar voxel V_{voxel} in m^3 for a single beam as following:

$$V_{voxel} = B_w \times B_t \times L_{bin}, \tag{3.5}$$

where L_{bin} is the length of a depth bin (range bin) equal to 0.04 m. Given the depth at which the sonar was deployed, the beam range from the sonar to the mean sea level (8 metres) is partitioned in 200 depth bins. Figure 3.12 shows that the sampling volume increases due to beam spreading with increasing distance from the sonar to the sea surface. Therefore, the

maximum sampling volume in a voxel is found at/near the sea surface (a maximum value of 0.0013 m^3 was calculated for the Delta T sonar).

A larger number of beams, at a constant angular range, yields a smaller beam spacing thus, as the size of the voxel also becomes smaller, the spatial resolution is improved. Although the Delta T sonar has a high spatial resolution, in terms of sonar technology, a bubble area cross-section can be still more than two orders of magnitude smaller than a sonar depth bin. Hence, especially in higher bubble density regimes – which is often the case within a bubble plume – a single voxel can insonify many bubbles. The backscatter intensity within a voxel is mostly dependent on the density and compressibility of bubbles, and the result of a backscatter intensity value is the cumulative scattering from all the bubbles insonified by a voxel. Thus, a larger cluster of insonified bubbles yields a higher backscatter intensity in the voxel.

3.5.3.2 Beam pattern

The Delta T sonar echo returns have a directionality dependency. Each beam has a different sensitivity in the return signal, yielding a specific beam pattern for the Delta T sonar. The shape of the beam pattern must be known in order to obtain the backscatter amplitude in a 1-degree beam, varying with the directionality of the beam.

The beam pattern of the Delta T sonar was measured by Scandella et al. (2016) in an ocean engineering tank using a 38.1 *mm* diameter tungsten-carbide calibration sphere, using a rotation pole to turn the sonar head horizontally and a motorized spool to raise and lower the sphere vertically. The calibration test was conducted with the sonar 120-beam fan oriented parallel to the sea surface at 4 *m* depth, showing a roughly Gaussian shape with a central peak and high-frequency oscillations that correspond to the sensitivity in each beam (Figure 3.13). According to this Gaussian result, the central beam – also called the main acoustic beam, located along the main acoustic axis, with a 0° directionality (see the general sonar description in Section 2.3) – is the most sensitive, and the backscatter intensity decreases in beams propagating laterally on both sides of the main beam (Figure 3.13).

The higher beam sensitivity closer to the main acoustic axis is also associated with significantly larger amplitude peaks (noise) and a weaker dependence on elevation angle (Figure 3.13). Although the signal is significantly weaker in the outer beams, the beam pattern noise is lower, and a more clear dependence on elevation angle is shown (Figure 3.13).

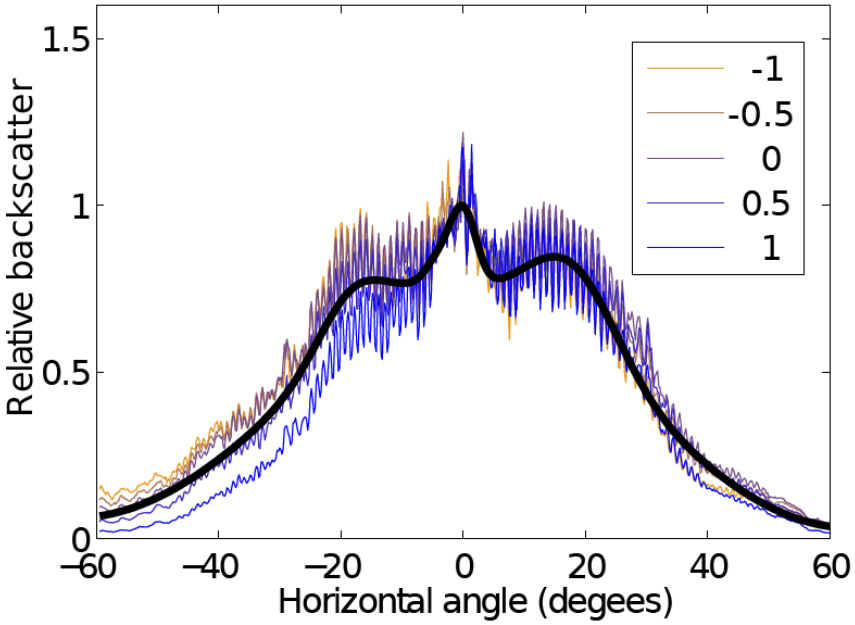

Figure 3.13: Beam pattern showing the signal strength across all 120 beams distributed on the x-axis. Negative degrees correspond to the beams at the left of the main acoustic beam (0° beam), whereas the positive degrees indicate the beams at the right of the 0° beam. A roughly Gaussian shape was obtained here for the relative backscatter (on y-axis) distribution, which shows the signal sensitivity within each beam. The different curves with high-frequency oscillations represent independent measurements at different elevation angles. Figure extracted from Scandella et al. (2016) (supporting information at page 10).

Following the calibration results, Scandella et al. (2016) found that the beam pattern has an overall uncertainty of $\sim 22\%$. The Delta T 120-beam setting provides a 3° beam width, which represents the width of the main acoustic beam. This indicates that the maximum backscatter intensity is maintained within a 3-degree span of the main acoustic beam.

3.5.3.3 Signal loss in beam pattern

As with any sonar, there are limitations in taking measurements near the face of the transducer. The previously seen (at a distance) beam pattern is not fully formed near the transducer face (at a distance of up to about 0.5 metres from the transducer face). There is an interference pattern where sound from different parts of the transducer face interfere with each other, causing the weakly formed or even completely cancelled beam pattern near the transducer face. In general, the beam pattern measurements should be undertaken at ranges greater than L/λ, where L is the area of the transducer face and λ is the sound wavelength (personally commu-

nicated by Doug Wilson from Imagenex Tech. Corp.). In our Delta T sonar measurements, the range at which the beam pattern is fully formed is around 0.5 metres. Since the sonar has only 8 bits of resolution in amplitude (about 48 *dB* full-range), it cannot form well a beam pattern with very low signal amplitudes (personally communicated by Doug Wilson from Imagenex Tech. Corp.).

3.5.4 Delta T software

The raw sonar returns can be visualized in a radar-like image provided by the Delta T visualization software, which uses rapid real time signal processing for converting the received acoustical-electrical signal to high resolution digital sonar images almost instantly. Each transmitted ping is an acoustic pulse which vertically scans the subsurface water layer up to the sea surface, yielding a sonar image; consequently, at a 6 *Hz* sampling frequency, there are six sonar images being generated every second.

As discussed in Section 2.3, the transmitted sound is attenuated in water as it travels over longer distances towards the acoustic target and also on the way back from the target. In some cases of extreme void fraction, the sound signal can undergo almost complete acoustical extinction due to bubble multiple scattering and absorption. To compensate for the sound attenuation loss, the Imagenex Delta T contains a time varying gain (TVG) which amplifies the echo return affected by attenuation – typically, there is a 40 *dB* gain, at most, in the TVG of Imagenex Delta T. To enhance the visualization, the Delta T software has a start gain of 20 *dB*, but it is adjustable within a $0 - 20$ *dB* range.

Figure 3.14 shows two sonar images generated by the Delta T software illustrating underwater conditions at an instant of time without the presence of a bubble plume (Figure 3.14a) and an event of a fully-developed bubble plume, which does not propagate deeper than about $4 - 5$ *m* (Figure 3.14b). The received echo returns are represented by the blue-green to orange-red colours, while the black background represents the absence of scattering. There is a difference of about 40 *dB* between black (no signal) and red (maximum signal) colours in the sonar images (personally communicated by Doug Wilson from Imagenex Tech. Corp.).

The acoustical extinction is minimum during the plume-free event, as the subsurface bubble scattering is very scarce in Figure 3.14a. This allows the incident sound pulse to travel through

the water column almost undisturbed until it encounters the sea surface where almost all of the sound hitting the sea surface is reflected back to the sonar. This effect can be observed in Figure 3.14a which shows a highly reflective sea surface with no bubble plume below. Additionally, two strongly reflective objects are also constantly present just above and below the 4-metre isobath on the left hand-side of the sonar fan as indicated in Figure 3.14b – these are the two resonators, so sound was strongly reflected by these solid objects in the trajectory of sonar beams propagating very close to the spar buoy.

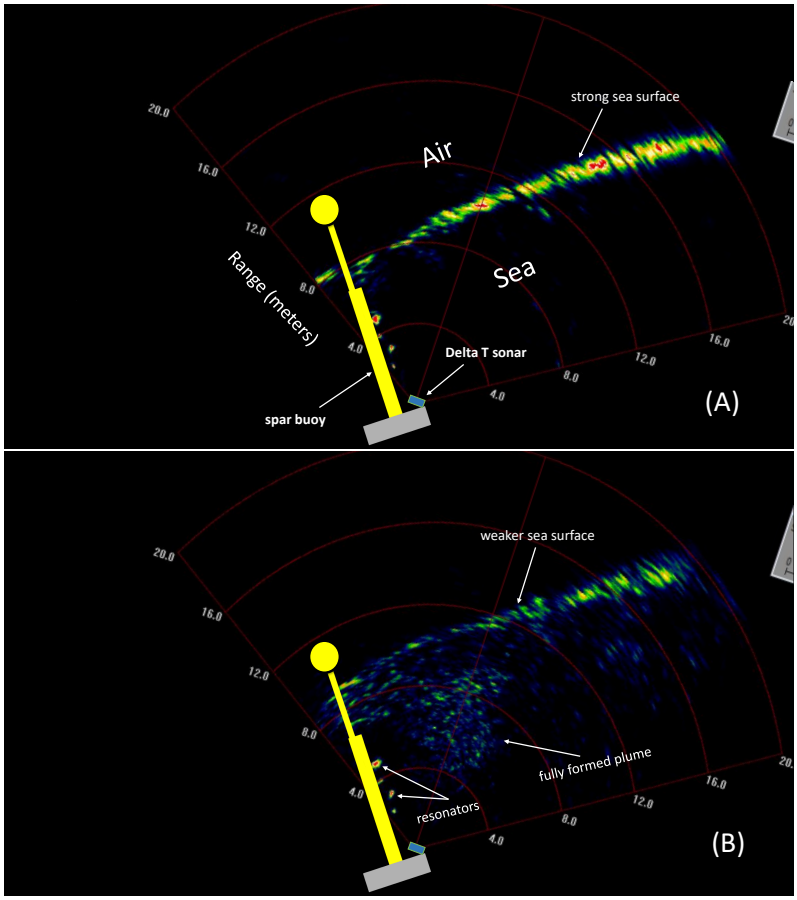

Figure 3.14: Sonar images, visualized with the Imagenex Delta T software, of (A) an instant of time without a bubble plume, hence no subsurface attenuation is present as indicated by the strong sea surface backscatter (yellow-red colors), and (B) a bubble plume event, which generates a lower backscatter level (blue-green colours), and induces significant attenuation that weakens the backscatter measured at the sea surface. The spar buoy (in yellow) is shown for scale comparison. Both images were rotated clockwise to realistically represent the localization of the 120-degree beam fan relatively to the tilted spar buoy while the instruments were submerged.

The sea surface acts like an acoustical mirror, so the sonar detects the reflection of what is in front of it, and the strength of the surface return is the result of a combination of bubble

surface concentration (these are usually large bubbles rising up at the sea surface), surface roughness over the sonar beam footprint and attenuation of sound due to bubble multiple scattering (Doug Wilson from Imagenex Tech. Corp., personal communication). A bubble plume is usually partially acoustically transparent, with a much lower void fraction than in breaking waves, yielding a much less reflective bubble plume. However, it can be observed that, as bubbles fill the water column below the sea surface when the bubble plume is present, multiple bubble scattering can reduce sound propagating towards the sea surface and back to the sonar, yielding a weaker surface return (Figure 3.14b).

3.5.4.1 Echo intensity

The Delta T sonar continuously recorded the underwater conditions during each storm from stations 4, 6 and 7 for a total of 98 hours, as mentioned in Section 3.1.1. The constant acoustical reverberations present in the side sonar beams generated two extra echo intensity bands, occurring without the contribution from bubbles or sea surface, in the sonar images from station 3, which were discarded from the sonar dataset. An example of this noisy output is shown in a time instant of a raw sonar image displayed by Delta T software (Figure 3.15).

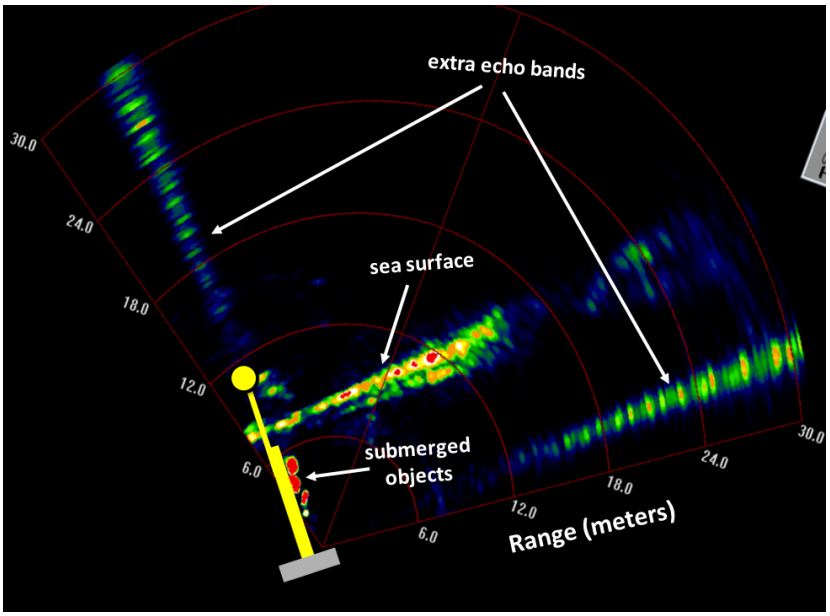

Figure 3.15: Delta T sonar digital image contaminated by two constantly present reverberation bands in the side sonar beams. The echo signal from sea surface, reverberation bands and subsurface spar buoy instruments is indicated in green-yellow and orange-red colors. The image of the buoy, in yellow, is at scale and is added for illustrative purposes.

The raw echo data in a sonar image is stored in a file with a format/extension specific to the Imagenex Delta T sonar model (.837 format). Each file typically contains a maximum of 73 minutes of recorded data, which means that there are 24999 sonar images in a single file (with some rare exceptions where the recording is shorter), so this corresponds to a total of 2×10^6 sonar images for all 98 hours of measurements. The Delta T software was used to process the digital raw data in the sonar images and convert it into quantitative echo intensity, enabling the assessment of non-zero echo intensity within the sonar sample volume. This was accomplished via the playback of all .837 files, which were automatically converted, by the Delta T software, into files with a binary format (with extension .83B). These binary files were eventually read using a computational tool (MATLAB) to extract the quantitative sonar output.

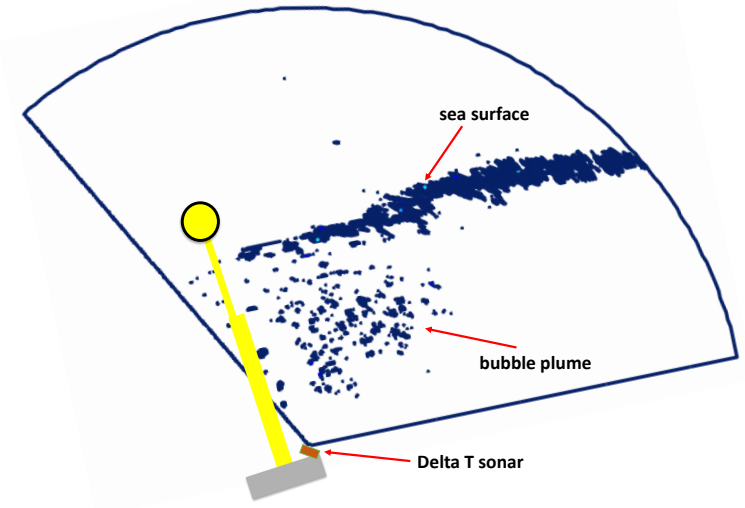

Figure 3.16: Multibeam sonar polar plot obtained by processing a raw sonar image – the figure here shows a contour polar plot of a fully-formed bubble plume. The image of the buoy, in yellow, is added for illustrative purposes.

The raw sonar echo intensity data was given in polar coordinates (Figure 3.16). Since it is easier to manipulate in Cartesian coordinates, the echo intensity in polar coordinates was converted into Cartesian coordinates as following:

$$\begin{aligned} x &= R\cos(\theta), \\ y &= R\sin(\theta), \end{aligned} \tag{3.6}$$

where x and y are the x-axis and y-axis converted from polar to Cartesian coordinates, R represents the range and θ is the beam angle (varying between 1° and 120°), with a 1-degree beam spacing. As a result, 500×120 echo intensity matrices were obtained, each matrix

corresponding to a single sonar image, hence a matrix was generated at each ping (six such matrices were generated per second).

The y-axis and x-axis correspond to the total number of range bins ($= 500$) and beam number ($= 120$), respectively. The raw sonar activity, characterized by a full bubble plume event was represented in the polar coordinates (Figure 3.16). These polar plots account for the echo intensity distribution with beam spreading across all 120 beams, being consistent with the illustrations from the raw sonar images shown in Figure 3.14.

3.5.5 Sonar matrix

An important limitation in the Imagenex Delta T measurements is induced by the tilt of the sonar head relative to the sea surface when deployed with the spar buoy. The sonar head was directed upward, but not perpendicular to the sea surface, because otherwise almost half of the transmitted beams would have interfered with the spar buoy, severely affecting the measurements.

3.5.5.1 Subset of sonar beams used for analysis

Because of this sonar tilt, the detection range is not consistent in all 120 beams, which means that the beams positioned at a larger angle from the actual spar buoy travel over longer distances before reaching the sea surface. This also further enhances attenuation of the sound signal in those beams. The real penetration depth of the bubble layer is, therefore, distorted because of the apparent much further sea surface (the penetration depth measurement is a relative quantity which depends on the accurate knowledge of the true position of the sea surface).

The bubble plumes constantly present closer to the sonar head induce an acoustical shadowing effect of the region behind these bubble plumes, so the very low acoustic detection in this region along the more distant beams usually leads to a significant underestimation of plume activity (Figure 3.17). Moreover, the 95–120 beams are not useful for these point measurements of bubble plume vertical cross-section because they propagate at very large angles. They are almost parallel to the sea surface – and do not reach the sea surface, so no subsurface plume structure data can be extracted from these beams (Figure 3.17).

To avoid all of the above limitations and maximize the accuracy of sonar detection with depth, a group of 10 beams was used, which propagated relatively close to the spar buoy, yet far enough away to avoid sound contamination from the two resonators and interference with the spar buoy. This group consists of beams numbered 25–35 from the total of 120, which are almost perpendicularly aligned to the sea surface and they are highlighted by the sub-domain within the sonar fan as indicated in Figure 3.17.

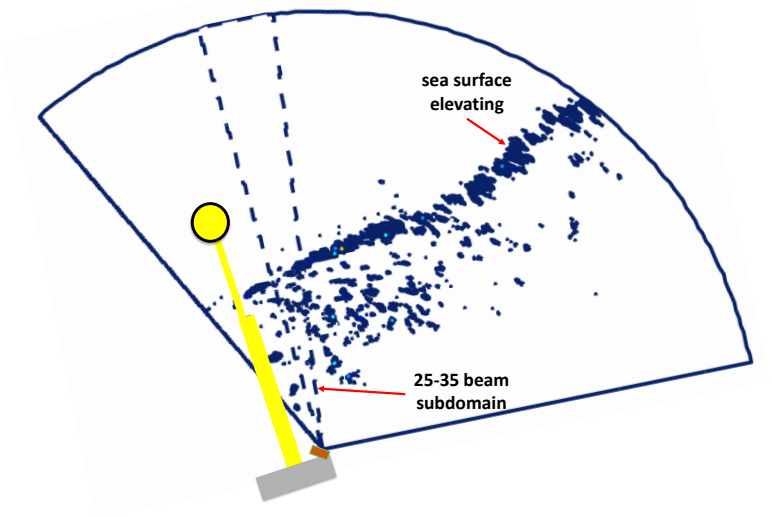

Figure 3.17: Sonar polar plot containing the 25-35 beam sub-domain (framed by the dashed lines), which will be used in the analysis of the sonar profiles in this thesis. The elevated sea surface can be seen propagating from distance (indicated by the red arrow), which is probably caused by the propagation of a large swell. A subsurface bubble plume is also present in the sonar image.

This 10-beam sub-domain was used to collect all sonar data in this study, providing essential information on the structure and properties of bubble plumes detected in the 10-beam range. To obtain the time evolution of bubble activity within the 10-beam sub-domain, the echo intensity, recorded in each beam across all 10 beams, was horizontally summed, so a single vertical profile, containing the total echo intensity distributed with depth for every transmitted ping, was obtained. This led to the construction of a 2-dimensional time-series of bubble-field penetration with depth, which we call the sonar matrix. An example of a bubble plume penetrating down to about 6 m and persisting for about 60 seconds is shown in the sonar matrix from Figure 3.18.

The largest values of echo intensity are mostly confined to the sea surface, which oscillates vertically (variation of free surface elevation), as indicated by the thick black contour

(Figure 3.18).

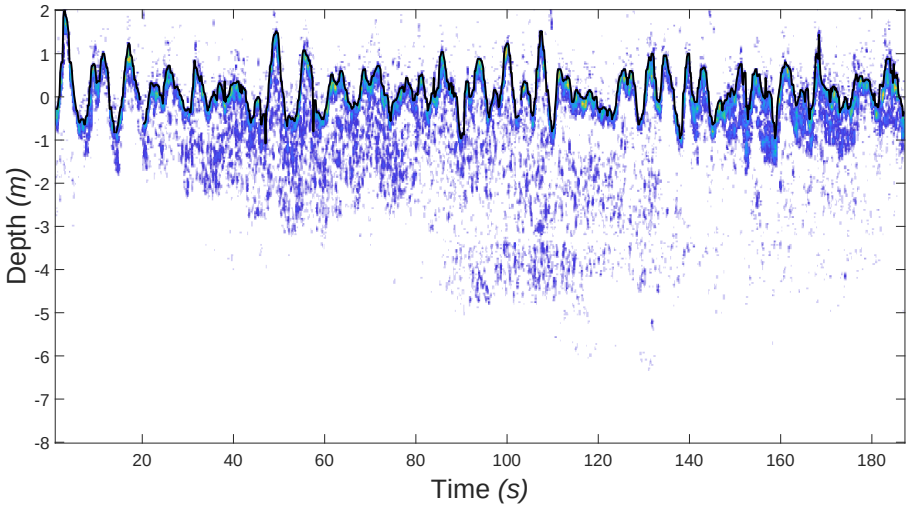

Figure 3.18: Sonar matrix showing the presence of a bubble plume event present in the time interval $\sim 50-180$ seconds (the depth of the plume is shown on the y-axis and the evolution in time on the x-axis), reaching maximum depth of 6 m after about 100 seconds. The sonar matrix was obtained by concatenating consecutive sub-domain vertical cross-sections of total echo intensity. The sea surface elevation is indicated by black thick contour evolving along the waves. The stronger echo intensity (yellow-red colours) is usually present within the surface waves, whereas the lower echo signal (blue-cyan colours) is more specific to the subsurface bubble plume.

3.6 Backscattering cross-section, bubble layer and void fraction

3.6.1 Measured bubble size distribution

The bubble density variation within the measured bubble layer is important for the understanding of the mechanisms for bubble injection with depth in different environmental conditions. We estimated the bubble density distribution with depth in terms of the contribution to total backscattering in a sonar voxel from individual bubbles contained/insonified in that voxel. For this backscatter estimation, a reference bubble size distribution must be known. Al-Lashi et al. (2016) used an algorithm that detects the bubbles of different sizes measured by the submerged bubble camera, producing a bubble distribution, BSD, over all measured radii.

Figure 3.19 shows the fits of all the normalised bubble size distributions recorded at 2

metres depth during all three deployments. The normalised bubble size distributions were calculated for each second, and divided by their own void fraction, V_f. Note that each bubble size distribution is scaled by its own void fraction. The scaling by void fraction shows that the bubble size distributions collapse into an uniform pattern, which shows that the bubble size distributions only show minor changes in time (their shapes collapse to a narrow range). This is a surprising result, and it will be discussed in more detail in an upcoming paper.

These *BSD* patterns are relevant for the sonar studies conducted in this thesis because it was observed that there were no bubbles with radii greater than 300 μm observed at any point at the bubble camera depth (even in the biggest storms). This confirms previous assumptions that large bubbles do not penetrate to these depths. Even more importantly, it also implies that sonar backscatter assumptions laid out in this thesis (about lack of multiple scattering, etc.) are appropriate in the depth range of $2 - 8$ m, and perhaps above that as well.

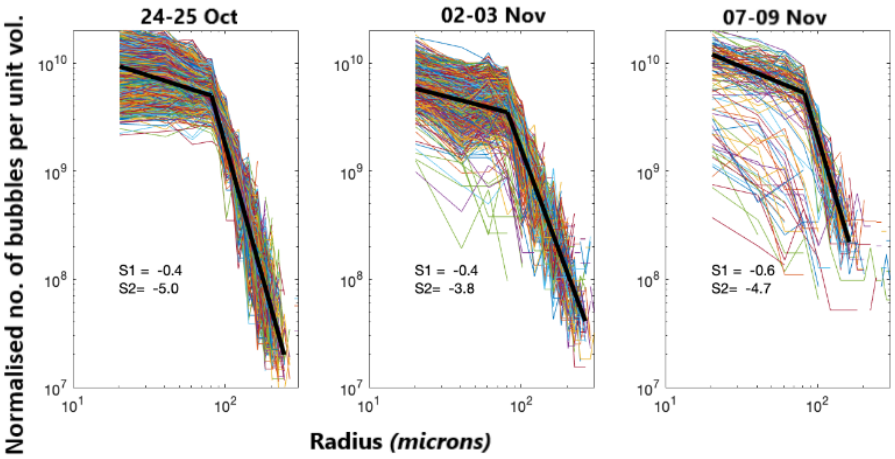

Figure 3.19: Bubble camera normalised fits of the number of bubbles (on the y-axis) with sizes ranging from about 20 μm up to 250 μm (on the x-axis). These normalised *BSD* patterns were obtained from individual distributions measured over 1 second for each storm. The shapes of most of these distributions collapse into a highly uniform pattern, which is characterised by two different slopes, S1 and S2. These bubble size distributions were obtained by Helen Czerski. The radius uncertainty (which mostly arises from the processing of bubble images) is ± 10 μm (see more details in the paper from Al-Lashi et al. (2016)).

Since the Hinze scale in typical active breaking waves is about 1 mm, and that no bubbles even of that size were seen in the far calmer conditions 2 m below the surface, there is strong reason to believe that there is no bubble fragmentation occurring at 2 m or below. The bubbles

we detected were formed a long time before they reached the camera or the resonator.

An inverse method was applied to extract the *BSD* by multiplying the scaled bubble size distribution BSD_s by void fraction V_f,

$$BSD = BSD_s \times V_f. \tag{3.7}$$

This result at $2\ m$ is limited in direct usefulness because we do not know what the bubble size distributions at other depths were. However, these normalised bubble size distributions were observed throughout the expedition, demonstrating that this scaling method is reasonable. The *BSD* in Figure 3.19 shows the total number of bubbles ranging from about 2.5×10^5 to 47 bubbles for the associated radii varying between about $20\ \mu m$ and $243\ \mu m$. At 2 meters depth, no bubble void fraction greater than 3.75×10^{-5} has been observed even in winds of up to $30\ m/s$.

These *BSD* patterns occur for almost all cases where the void fraction is greater than 10^{-6}, and a similar distribution is seen for lower void fractions. Note that this analysis is still being written up, and preliminary results are used to investigate various consequences in this thesis.

As it can be seen in Figure 3.19, the number of bubbles per unit volume per radius, N, shows two types of power law variations with radius a on a log-log scale as following:

- During the 24-25 Oct storm, N decreases with radius from $20\ \mu m$ to about $88\ \mu m$ at a rate equal to a slope of -0.4 ($N \simeq a^{-0.4}$), and from $88\ \mu m$ to $243\ \mu m$ at a rate described by a slope of -5 ($N \simeq a^{-5}$), indicated by $S1$ and $S2$, respectively, in the left hand-side panel from Figure 3.19.

- During the 02-03 Nov storm, N decreases with radius from $20\ \mu m$ to about $88\ \mu m$ at a rate equal to a slope of -0.4 ($N \simeq a^{-0.4}$), and from $88\ \mu m$ to about $250\ \mu m$ at a rate described by a slope of -3.8 ($N \simeq a^{-3.8}$), indicated by $S1$ and $S2$, respectively, in the middle panel from Figure 3.19.

- During the 07-09 Nov storm, N decreases with radius from $20\ \mu m$ to about $88\ \mu m$ at a rate equal to a slope of -0.6 ($N \simeq a^{-0.6}$), and from $88\ \mu m$ to only about $200\ \mu m$ at a rate described by a slope of -4.7 ($N \simeq a^{-4.7}$), indicated by $S1$ and $S2$, respectively, in the right hand-side from Figure 3.19.

The bubble size distributions are the most similar especially during 24-25 Oct and 02-03

Nov storms, and the distribution measured during the 07-09 Nov storm showing a less uniform pattern (Figure 3.19). The larger scatter of some of the distribution curves during the 07-09 Nov storm could imply that the dominant processes were affected when the wind-sea and swell dominated sea states are clearly separated.

3.6.2 Bubble backscattering cross-section per unit volume

To estimate the backscatter contribution from individual bubbles, the expression from Equation (2.67) in Section 2.4.2 was used to calculate the scattering cross-section per bubble of a given radius a across all measured radii,

$$\sigma_s = \frac{4\pi a^2}{[(f_R/f)^2 - 1]^2 + \delta^2}, \tag{3.8}$$

where $f = 260$ *kHz* is the sonar operating frequency, and δ is the total damping coefficient and was derived in Equation (2.69), Equation (2.70) and Equation (2.71) from Section 2.4.2. The resonance frequency of each bubble with radius a used in the equation above was calculated using an empirical expression (Dahl and Jessup, 1995; Medwin, 1977*a*),

$$f_R = \frac{3.25\sqrt{1 + 0.1z}}{a}, \tag{3.9}$$

which shows that the bubble resonance frequency varies with depth z; here $z = 0$ is considered at the mean sea level where the resonant bubble radius at 260 *kHz* sonar frequency is 13 μm. To obtain the backscattering cross-section σ_{bs} (the part of the bubble scattering that arrives at the sonar), the form in Equation (2.68) from Section 2.4.2 was used, and σ_s was divided by 4π,

$$\sigma_{bs} = \sigma_s/4\pi. \tag{3.10}$$

The above expression of backscatter cross-section is valid for $ka < 1$ (isotropic conditions; this property was discussed in more detail in Section 2.4.2) – with wave number $k = 2\pi/\lambda$ – where the scattering is assumed to be produced by spherical and small to medium size bubbles. According to Deane (2016) and Medwin (1977*a*), the scattering cross-section is much larger than geometrical cross-section at around $ka = 0.015$, where the resonant effects dominate.

Deane (2016) proposes a version of backscattering cross-section which contains the above isotropic model and also the Anderson's anisotropic model ($ka > 1$), where the geometrical scattering becomes important and it is especially useful for high frequency sonars and

non-spherical millimetre scale bubbles found in breaking crests; in this situation, the resonant effects are not significant, leading to this expression for backscatter cross-section:

$$\sigma_{bs,full} = \sigma_{bs} + \frac{(ka)^{\alpha_{bs}}}{\beta_{bs} + (ka)^{\alpha_{bs}}} \frac{a^2}{4}, \tag{3.11}$$

where $\alpha_{bs} = 4.2$ and $\beta_{bs} = 28$ are coefficients obtained from the least mean squares difference fit to the anisotropic theory of Anderson over the full range from resonant to geometrical scattering, $0.1 \leq ka \leq 10$ (Deane, 2016).

In this study, $\sigma_{bs,full} \simeq \sigma_{bs}$ because ka ranges from 0.02 to 0.26, which shows that the isotropic approximation ($ka < 1$) can be used. Moreover, given these ka values, our *BSD* does not contain bubbles which are resonant at the Delta T sonar frequency (260 kHz).

There is a specific number of bubble scattering cross-sections given by the number of bubbles per unit volume for each bubble radius. To obtain the total backscattering cross-section per unit volume in m^{-1}, all the backscattering cross-sections are integrated for each bubble radius with a 1 μm increment present in one unit volume as following:

$$S_{vb} = \int_{a_{min}}^{a_{max}} \sigma_{bs}(a) N(a) da, \tag{3.12}$$

where $a_{min} = 20$ μm and $a_{max} = 243$ μm, $N(a)$ is the derived bubble size distribution which varies with radius increment $da = 1$ μm. This yields the backscatter estimate based on an assumed bubble size distribution discussed in the previous section.

3.6.3 Plume-scale backscattering cross-section

Using the calibration results, Scandella et al. (2016) obtained the directional dependent beam pattern, $B_p(\theta)$ (shown in Figure 3.13), and a calibration parameter, X_0. Combining $B_p(\theta)$ and X_0, Scandella et al. (2016) found a source amplitude, a_{src}, expressed as

$$a_{src} = X_0 B_p(\theta), \tag{3.13}$$

where B_p was averaged over $\theta = 10^\circ$ for the $25 - 35$ sonar beams. A value of $(3.2 \pm 0.7) \times 10^5$ was estimated for X_0. The user-defined gain coefficient, G_u, depends on the hardware start gain, G_s, and the software display gain, G_d, where $G_s = 20$ dB and $G_d = 3$, yielding $G_u = 0.3$ (Scandella et al., 2016). Consequently, the backscattering cross-section in a Delta T sonar voxel can be obtained by combining the total echo intensity in a voxel E_v (resulted from

summing over all 25–35 beams), the bin range L_{bin}, the source amplitude a_{src} and the gain coefficient G_u as following (Scandella et al., 2016):

$$\sigma_{bs}(sonar) = \left(\frac{E_v L_{bin}}{a_{src} G_u} \right)^2, \tag{3.14}$$

where $\sigma_{bs}(sonar)$ is the backscattering cross-section in m^2 in a sonar depth bin. Finally, $\sigma_{bs}(sonar)$ was divided by the sample (insonified) volume V_{voxel} of a voxel to finally obtain the backscattering cross-section per unit volume in m^{-1} in a sonar voxel,

$$S_v = \frac{\sigma_{bs}(sonar)}{V_{voxel}}, \tag{3.15}$$

which can be converted in decibels (dB) as $10\ \log_{10}(S_v)$. The transformed S_v in decibels will be used in this thesis to show the backscatter distribution with depth and in time.

3.6.4 The base of the bubble layer

The generally accepted threshold for breaking-wave activity is a wind speed of roughly $5\ m/s$ (Dahl, 2003; Dahl and Jessup, 1995; Dahl et al., 1997; Trevorrow, 2003). During the HiWinGS cruise we often observed a far greater wind speed ($\sim$15 m/s on average) and we observed a constant bubble layer was below the sea surface. This bubble layer can be very shallow in calmer wind speed conditions ($9 - 10\ m/s$), confined in the uppermost 1–2 metres and oscillating with the wave period (Dahl and Jessup, 1995), or it can be significantly aerated in more intense wind speed conditions ($> 15\ m/s$) when deeper bubble plumes penetrate.

An example of the bubble layer structure is shown in Figure 3.20. The base of the bubble layer can be detected by tracing the backscatter signal present at the deepest position within the sonar matrix at each ping in time. Using this bubble layer base tracing technique, the contour of the bubble layer edge has been obtained, which highlights the maximum penetration depth of the bubble layer, z_{bl}, as shown by the smoothed thick red line and the non-smoothed thinner black line in Figure 3.20. The smoothed red contour was obtained using a moving average 9-second filtering window along the time-series.

The acoustic background noise can affect the desired retrieval of the bubble layer base. The backscatter noise (represented by very low backscatter values) present in the background of the sonar matrix from Figure 3.20a has been removed by applying a $S_v < -28\ dB$ filtering threshold, so that all backscatter values smaller than $-28\ dB$ are discarded from the sonar

profile. The backscatter, in the unfiltered (without S_v threshold) and filtered (with S_v threshold) sonar matrix, ranges from $-48\ dB$ to $-3\ dB$ and from $-28\ dB$ to $-3\ dB$, respectively. The unfiltered sonar matrix in Figure 3.20a contains backscatter background noise from probably very small and sparse bubbles, at very low void fractions.

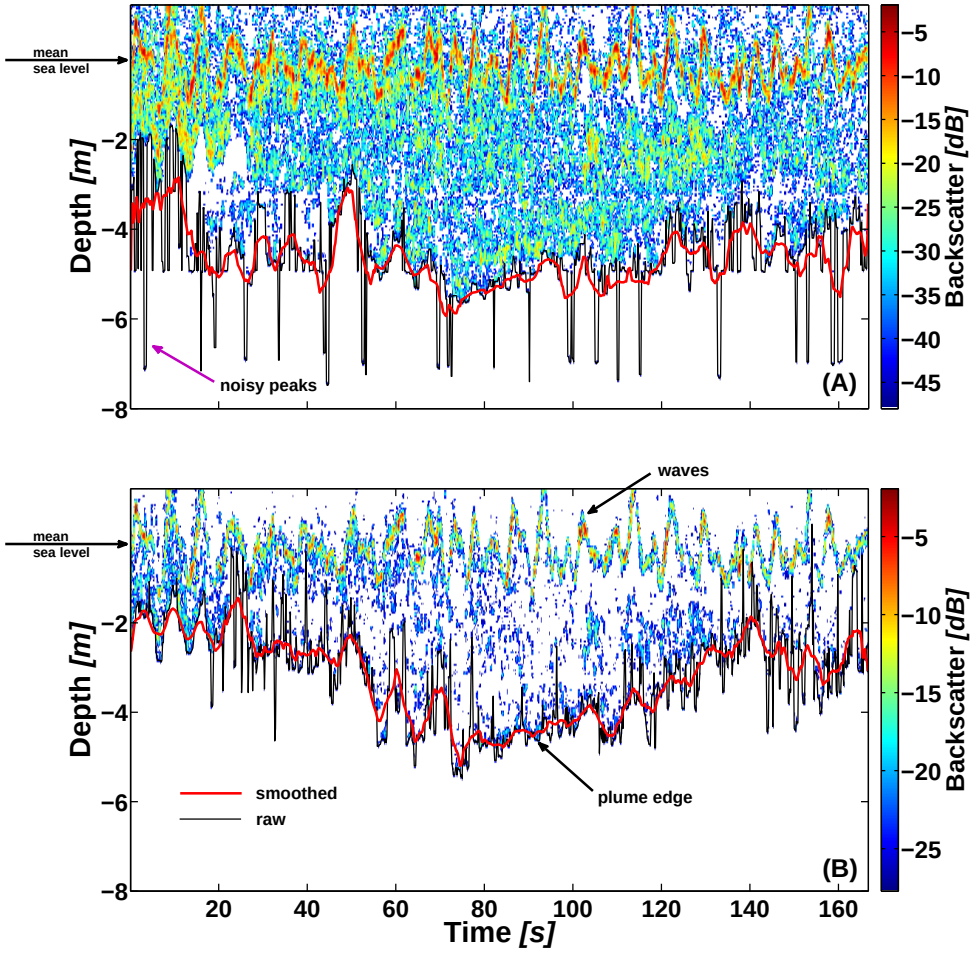

Figure 3.20: The visualisation of bubble layer bottom in the vertical cross-section of a 170 seconds persisting plume sampled during Nov 02-03 storm. (A) Non-filtered bubble layer base (no S_v threshold was used), so the sonar matrix contains background noise from very small bubbles and acoustical reverberation. (B) Filtered bubble layer base (the S_v threshold was used); here the waves, oscillating about the mean sea level and the plume edge, can be clearly observed. The red and chartreuse contours represent the smoothed (using a moving average filter) and non-smoothed (raw) signals, respectively, of the bubble layer base. The cyan, yellow and red colours represent larger backscatter values usually present closer to the sea surface; the lower backscatter, shown dark blue colour, is usually associated with the main plume. During the presence of this bubble plume event, wind speed was moderate to high, reaching up to 15 m/s.

This noise signal is particularly visible above the surface waves, where there is only air and

no oceanic bubbles (Figure 3.20a), but this noise signal can generally be removed by applying the S_v threshold, so the surface waves can then be clearly distinguished (Figure 3.20b). Consequently, choosing the $S_v < -28\ dB$ threshold is a convenient option. The criteria for choosing the $S_v < -28\ dB$ threshold refers to the mean amplitude of the noisy non-smoothed signal that should not exceed 1 standard deviation (SD) of the smoothed signal in the sonar matrix. Given that the base of the bubble layer is extremely inhomogeneous, thus inducing noise in the backscatter measurements, this filtering technique allows to obtain a more smoothed bubble layer base, which allows to examine the large features (such as averaged backscatter profiles and individual bubble plumes), not the smallest ones.

The bubble layer base tracking method shows the raw (non-smoothed) bubble layer depth, which presents noisy peaks with large uniform amplitudes (black curve in Figure 3.20a). The moving average filter dampens the raw signal and yields a smoothed curve, which describes a relatively uniform bubble plume base with a steady penetration (red curve in Figure 3.20a). To assess a level of noise in the extraction of the bubble layer bottom, the noisy peaks from the non-smoothed signal (black curve) have been compared to the smoothed signal (red curve). Therefore, the local maxima (largest peaks) from the non-smoothed signal, in both filtered and unfiltered sonar matrices, are depicted through a function specialized in finding peaks ($\mathrm{findpeaks}$) in MATLAB. In the unfiltered sonar matrix, the amplitude of the noisy peaks in the non-smoothed signal exceeded, on average, 1 standard deviation of the smoothed signal in a proportion of about 87% (Table 3.4). Conversely, the amplitude of the non-smoothed signal peaks in the filtered sonar matrix is on average about 50% lower than 1 standard deviation of the associated smoothed signal (Table 3.4).

Table 3.4: The proportion of average amplitude of noisy peaks a_{noise} of both filtered and non-filtered signals, and the associated minimum void fraction V_f (void fraction level at the edge of the bubble layer) in both filtered and non-filtered sonar profiles.

Parameters	Filtered	Non-filtered
a_{noise}	$50\% < 1\ SD$	$87\% > 1\ SD$
Minimum V_f	5.38×10^{-7}	5.04×10^{-9}

At high enough sampling frequency (6 Hz), a discrete structure of the bubble layer is re-

vealed in Figure 3.20. This leads to a non-continuous distribution of backscatter signal with depth and in time. Note that the blank space between the backscatter patches does not represent $0\ dB$ values, but a non-backscatter (a lack of backscatter signal) background field. In subsurface and near-surface sonar measurements, the $0\ dB$ values represent a high backscatter level (e.g. most of the times, the Delta T sonar measured a backscatter level lower than $0\ dB$ even close to the sea surface, where the reflectivity is the highest).

3.6.5 Comparison between the bubble layer and void fraction

The void fraction, calculated from the measured bubble populations, can be measured in the sampling volume of both the bubble camera and resonator as the bubble layer deepens.

Figures 3.21a, 3.21b and 3.21d show that the void fraction increases in the sampling volume of both the bubble camera and resonator as bubble plume events develop and deepen. Note that the region in the water column where the 25–35 sonar beams were recording the plumes does not exactly overlap the sampling volume of both the camera and resonator; the horizontal distance of the sonar beams from the spar buoy, at the resonator and camera depth levels, is in the 0.7–1 metres range, which might not exactly capture the signal present in the sampling volumes of the camera and resonator. However, the sonar, camera and resonator were exactly vertically aligned and the signal events are detected almost simultaneously by these instruments, indicating that they detected the same plume events.

However, the sampling volumes of the bubble camera and resonator cover only a fraction of the entire bubble plume, so the bubble camera and resonator cannot measure a descending plume from an actively breaking wave. As previously shown, the only instrument that can measure full-scale plumes is the sonar. However, given its acoustical limitations, the sonar cannot detect the shallow and high density bubble plumes usually present below active breaking waves.

The most significant event of bubble presence shown in Figure 3.21, in terms of penetration depth and void fraction magnitude, approximately occurred in the time interval 0624–0627 on Nov 02.

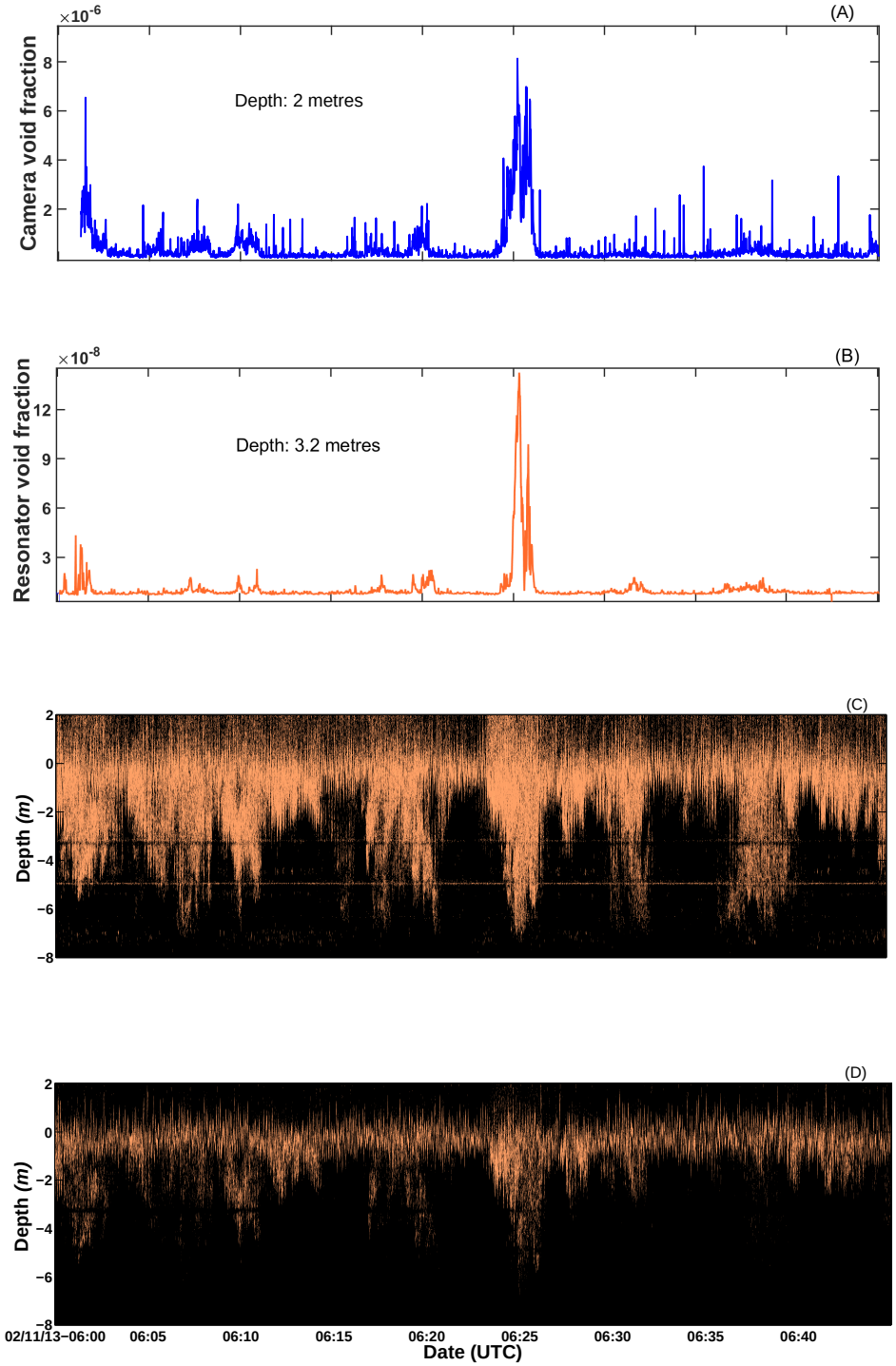

Figure 3.21: Simultaneous time-series of void fraction recorded by (A) bubble camera (B) resonator, and bubble layer evolution shown in the unfiltered (C) and filtered (D) sonar matrices. The image intensity of the filtered and unfiltered sonar matrices is related to the insonified sonar voxel density, so even a very weak signal is represented by an insonified (non-zero echo intensity) sonar voxel; this leads to a bubble layer with a much higher density of insonified voxels in the unfiltered sonar matrix, even though most of the signal is noise (C). A wind speed of about 15 m/s was present during these measurements.

During this time, the filtered sonar matrix shows a bubble plume event penetrating at a depth of 5.36 m below the mean sea level, while the resonator and the bubble camera recorded bubbles producing void fractions of 1.43×10^{-7} at 3.2 m depth (Figure 3.21b) and 8.13×10^{-6} at 2 m depth (Figure 3.21a), respectively.

Note that the 0 depth level in both filtered and unfiltered sonar matrices (Figure 3.21c and Figure 3.21d) represents the mean sea level computed from the surface displacement measured by the capacitance wires. Generally, the void fraction within the plume events decreases with depth (from 2 to 3.2 metres) by about half an order of magnitude (Figures 3.21a and 3.21b).

Since it contains background noise, the unfiltered sonar matrix is more sensitive to the signal generated by small and sparse bubbles or other noise sources which amplify the depth of the plumes. Therefore, the unfiltered sonar matrix shows background noise constantly present below the main bubble layer, down to 7 metres depth (Figure 3.21c). Note, however, that this means there are bubbles present in the water column, but these plume remnants haven been discarded. Patterns of weak signal, which generally disappear when the noise threshold is applied, are present in the sonar matrix. Such signal pattern can likely explain the two horizontal noise bands constantly present in the unfiltered sonar matrix, at 3.2 and 5 metres depth (Figure 3.21c). There are many plume events, present in the unfiltered sonar matrix, which are poorly matched with the bubble camera and resonator void fraction records, because it is assumed that most of these plumes contain very low void fractions (Figures 3.21a to 3.21c). This plume-void fraction comparison highlights the limitations of sonar data, because the definition of ”plume” is arbitrary in this case.

When background noise is removed from the sonar matrix, the deep level noise and noise bands disappear, and mostly plume events that contain a more significant void fraction are considered. Therefore, by removing the background noise, it can be shown, more clearly, that the void fraction enters both the bubble camera and resonator sampling volumes as the bubble layer penetrates deeper (Figures 3.21a, 3.21b and 3.21d). However, even after the noise removal, the bubble layer evolution, shown in the filtered sonar matrix, does not exactly match the void fraction records, indicating that there are still some deep plumes, which are associated with low void fractions (lower than fractions found in the sampling volumes of the bubble camera and resonator).

3.6.6 The bubble layer relative to the instantaneous sea surface

For a more detailed understanding of plume presence within the water column, the bubble layer must be represented with respect to the instantaneous sea surface. The algorithm used to accomplish this can be summarised in three steps: a) detection of the outer boundary of the wave envelope; b) removal of the wave envelope (with intermediary steps of signal filtering and assumption of wave envelope thickness); c) shifting the bubble layer with depth in each column of the sonar matrix.

The sea surface is a very efficient sound scattering source (as previously stated, it almost acts like a mirror), with a very large proportion of the incident acoustic signal being reflected back to the sonar. Therefore, an envelope with large backscatter signal (generally larger than the bulk backscatter) is constantly present at the sea surface, which, henceforth, will be referred to as the wave envelope. There is often a sparse low backscatter signal usually present in the voxels above the wave envelope. After visual inspection, an arbitrary chosen backscatter filter, $S_v < -16\ dB$, has been used to remove this backscatter noise. This allows for the detection of the outer boundary of the wave envelope by locating the non-zero backscatter signal in the depth bins with the highest row index in each column within the sonar matrix. At a 6 *Hz* sampling resolution, the sonar matrix is fairly sparse, hence some missing values can be present even in the wave envelope.

The missing values in the outer boundary of the wave envelope were replaced by interpolating the non-missing elements, permitting the tracking of the outer boundary (black contour in Figure 3.22a). This interpolation has been accomplished using the MATLAB function, $\mathrm{inpaintn}$, which uses an iterative process that converges toward a solution (for this task, it used 100 iterations, which is the default setting).

The thickness of the envelope was assumed to be 0.6 metres (using a visual approximation), although the thickness, especially at large sampling frequency, is not constant at every step in time (however, on average, the wave envelope thickness would be around this value). Consequently, the signal found between the outer wave envelope boundary and the depth bins located 0.6 metres below has been removed from the sonar matrix. Since the retrieved outer boundary does not track the wave envelope oscillations perfectly and the wave envelope thickness is not constant, there are still some post-filtering remnants of the wave envelope.

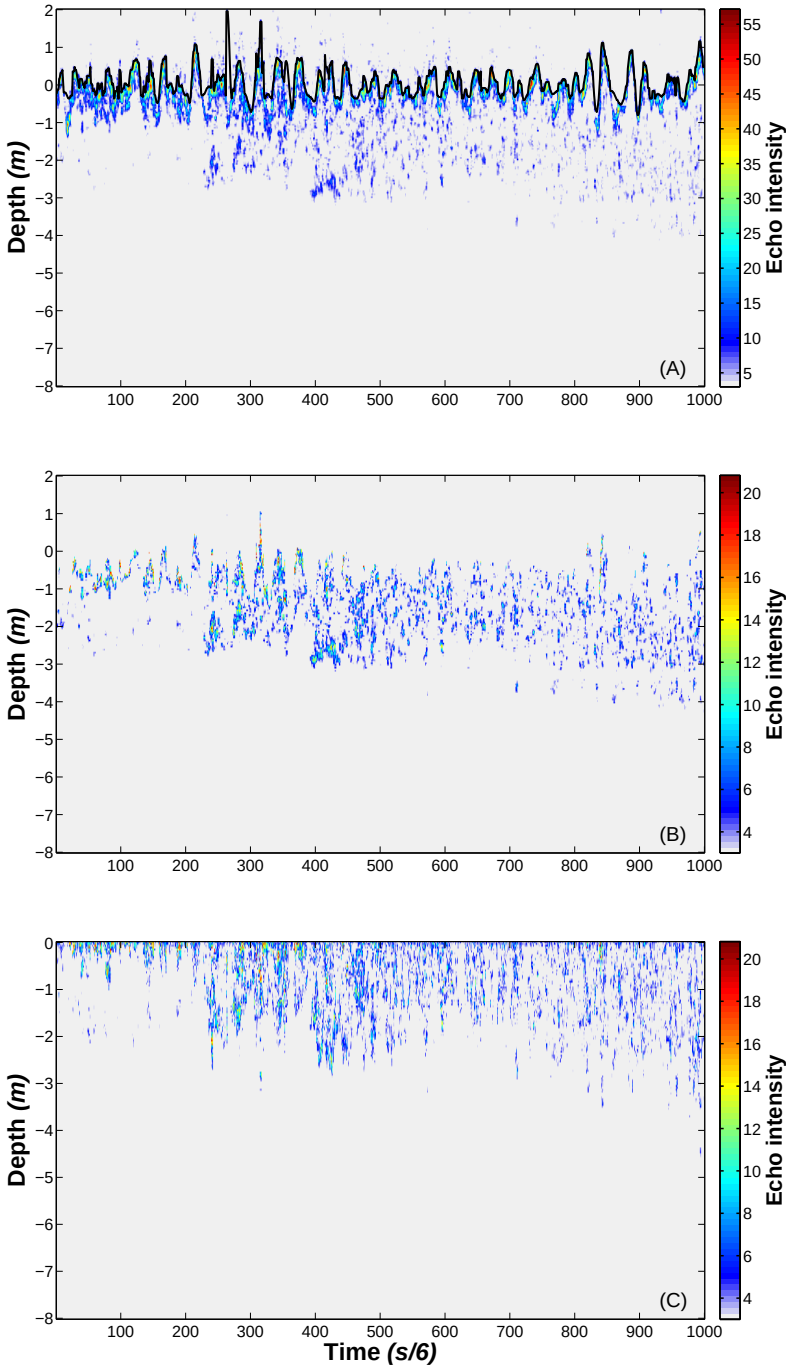

Figure 3.22: The result at each of the three-step algorithm for calculating the bubble layer relative to the instantaneous sea surface. (A) The sonar matrix with the overlaying outer boundary of the wave envelope (black contour). (B) The same sonar matrix, but with the wave envelope removed. (C) The sonar matrix representing the bubble layer with respect to the instantaneous sea surface. Each vertical line has been shifted so that the sonar matrix in (C) show its actual distance below the instantaneous surface, not its position relative to the buoy. The echo intensity is shown in the colour bars, transitioning from low (blue) to large (orange and red) values.

To remove the effect of these remnants, any potential large backscatter signal ($S_v >$

$-10\ dB$) located within the range of wave oscillations about the 0-metre depth bin level (zero-crossing level) has been removed. Oceanic waves generally have random amplitudes and phases, so they show a Gaussian variation about the zero-crossing level (see Section 2.2). In the sonar matrix, the zero-crossing level is at 8 metres above the depth level of the sonar, and it was calculated relative to the spar buoy using the capacitance wave wires (see Section 3.4.2). In the sonar matrix, the wave oscillations about the zero-crossing level have been assumed within an average amplitude of 1 metre (average troughs and peaks are 1 metre below and above the zero-crossing level, respectively). The filtering of the remnant signal ensures a higher confidence that the remaining backscatter signal is generally produced by subsurface bubbles. Figure 3.22b shows the sonar matrix with the filtered wave envelope and the backscatter generated by the bubble layer.

The S_v signal generated by the bubble layer can be often sparse (sonar voxels are not uniformly insonified), and it is known as the bulk bubble backscatter (which is equivalent to the bubble layer thickness that can be observed in the sonar matrix). To represent the bubble layer with respect to the instantaneous sea surface, the bulk bubble backscatter has been shifted over a number of rows (depth bins) in the sonar matrix proportional to a shifting index. This shifting index is calculated as the difference between the zero-crossing level and the non-zero S_v values located at the highest row index within the bulk bubble backscatter (upper bound of the bubble layer). This operation shifts upward or downward (depending on the shifting index given for each column in the sonar matrix) the bulk bubble backscatter. Consequently, the bulk bubble backscatter, in each column, will never be positioned above the zero-crossing level, but only below or at the same level (the zero-crossing level serves as a fixed cap within the water column), as shown in Figure 3.22. This allows for a correct localization of the bubble layer relative to the instantaneous (real) sea surface. Using the sonar matrix representation of the bubble layer relative to the instantaneous sea surface, given in Figure 3.22c, the bubble backscatter vertical profiles can be calculated.

There are periods, especially in the extreme environmental conditions during the Oct 24-25 storm, when there is a lack of backscatter signal in the more shallow (upper $2-3$ metres) region of the water column (including the sea surface) due to the possible presence of dense bubble plumes which entirely scatter and absorb the incident signal (see **??**). In these conditions, there is only a weak backscatter signal which is generated by close-range (relative to the sonar)

bubbles present deeper within the water column. This can notably diminish the thickness of the bulk bubble backscatter, underestimating the row index of the upper boundary of the bubble layer within the sonar matrix. Consequently, in a column where there is no backscatter signal even in the first $2-3$ metres below the sea surface (there are many 'empty' rows), the bulk bubble backscatter will be shifted over too many 'empty' rows, giving the appearance of a much shallower bubble layer than it would normally be. To avoid this effect, the bulk bubble backscatter located in a column with no backscatter signal for at least 2 metres below the sea level has not been shifted upward for more than 0.6 metres (value equivalent to the wave envelope thickness). Since it is not affected by acoustical attenuation, the bubble camera recorded the bubbles within the shallower region of the bubble layer (at 2 metres depth) that is not visible in the sonar matrix. Therefore, the assumption that there should be bubbles present at least at 2 metres depth in the extreme environmental conditions during which the sonar could not detect them is reasonable.

The shifted sonar matrix will be used throughout chapter 4 for the analysis of backscatter distribution and backscatter decay with depth varying with environmental conditions.

3.6.7 Backscatter decay with depth

The backscatter signal is generally stronger close to the surface (in the shallow region of the bubble layer), and it gradually declines as depth increases. This backscatter decay generally has an exponential variation, and is usually described by a coefficient with an e-folding scale. This exponential decay, from the sea surface to the plume bottom, has been generally reported in the literature. Therefore, an exponential function is used to fit the backscatter vertical profiles, implemented as (Thorpe, 1982; Trevorrow, 2003; Vagle et al., 2010; Wang et al., 2011)

$$S_v = S_v(0)\exp(-z/d), \tag{3.16}$$

where S_v is the backscatter strength decaying with depth z (positive downward) from the surface backscatter level $S_v(0)$. The rate of exponential decay is quantified by the e-folding depth coefficient d, which is the depth increment (in m) for which the backscattering decays by a factor of $e \sim 2.72$. Since the backscatter S_v is given in units of decibels (on logarithmic scale) within the depth profiles, the exponential backscatter decay is equivalent to a linear decay in

decibels.

Using the above definition, e-folding depth will be calculated and used in the depth-varying backscatter decay analysis from Sections 4.2 and 4.3.

3.7 The detection of individual bubble plumes

In this section a technique is developed to detect individual bubble plume events from the continuous bubble layer depth signal. This is a quantitative method based on the comparison between sonar (bubble layer depth) and resonator (void fraction) signals, which will be discussed in detail here. The steps of the algorithm will be set out in this section. Working with real oceanographic data, limitations apply to this method, as will be seen in this section.

The aim of constructing this algorithm is to delineate bubble plumes so that their persistence and frequency can be assessed in different ocean conditions. This plume detection algorithm is designed to be used specifically for the sonar record (bubble layer depth) to extract occurrences of individual bubble plumes. The steps covered to create the algorithm and compute the statistics of individual plumes are summarised in the following pseudo-code:

- Define a time-series of bubble layer depth (z_{bl}). Records from entire deployments can be used.
- Define the 5-second gap length and the 3.2-metre depth threshold (at the resonator depth level). The choice of the 5-second gap length is arbitrary, and it is based on the assumption that a plume must persist for at least 5 seconds.
- Convert the instances for which $z_{bl} \leq 3.2\ m$ to a boolean string (zeros $=$ above depth threshold; ones $=$ below depth threshold). The sequences of ones represent the detected events, while the zeros indicate that no events were detected.
- Using a regular expression that includes the gap length, the pattern showing the position indices (in the time-series) of the starts and ends of the detected events has been extracted. The MATLAB *regexp* function has been used to retrieve this pattern; this function uses four arguments: the boolean string obtained at step 3, the defined gap length, and the two strings 'start' and 'end' used to define the type of pattern to be retrieved.
- A boolean array that represents the detected pattern is obtained.

- Using the *regexp* function, the plume pattern represented by boolean strings, each being associated with a plume event, were split and stored in a cell array. The length (number of characters) of each element (boolean string) in the cell array was extracted, thus obtaining the duration of individual plume events.
- The maximum plume depth was obtained by extracting the maximum z_{bl} value in between the position indices of the plume detection pattern (starts and ends of each event).
- The plume frequency was obtained by counting the individual events from the plume detection pattern.

The development of the algorithm will be discussed in more detail in the following subsections. The accuracy of the algorithm will be assessed by applying the algorithm on both the sonar and resonator recorded samples, so that the detected events and gaps (from both sonar and resonator) can be matched.

A number of previous studies focused on bubble plumes measured in the ocean (Crawford and Farmer, 1987; Dahl and Jessup, 1995; Graham et al., 2004; Thorpe, 1982, 1986; Thorpe and Hall, 1983; Trevorrow, 2003; Vagle et al., 2010; Wang et al., 2011) and in the laboratory water tanks (Anguelova and Huq, 2012; Deane and Stokes, 2002; Leifer et al., 2007), which also discuss changes in plume characteristics with environmental conditions. Some of these authors identified individual oceanic bubble plumes as those events where the bubble penetration depth exceeds the mean plus 1 standard deviation (Trevorrow, 2003; Vagle et al., 2010) and a bubble plume event in a water tank was photographically detected as the distance from the highest to the lowest edges of the plume (Anguelova and Huq, 2012).

3.7.1 Events and gaps

To compare the signals from different subsurface bubble records, the bubble layer depth, z_{bl}, and void fraction, V_f, measurements have been used from independent sonar and resonator instruments, respectively.

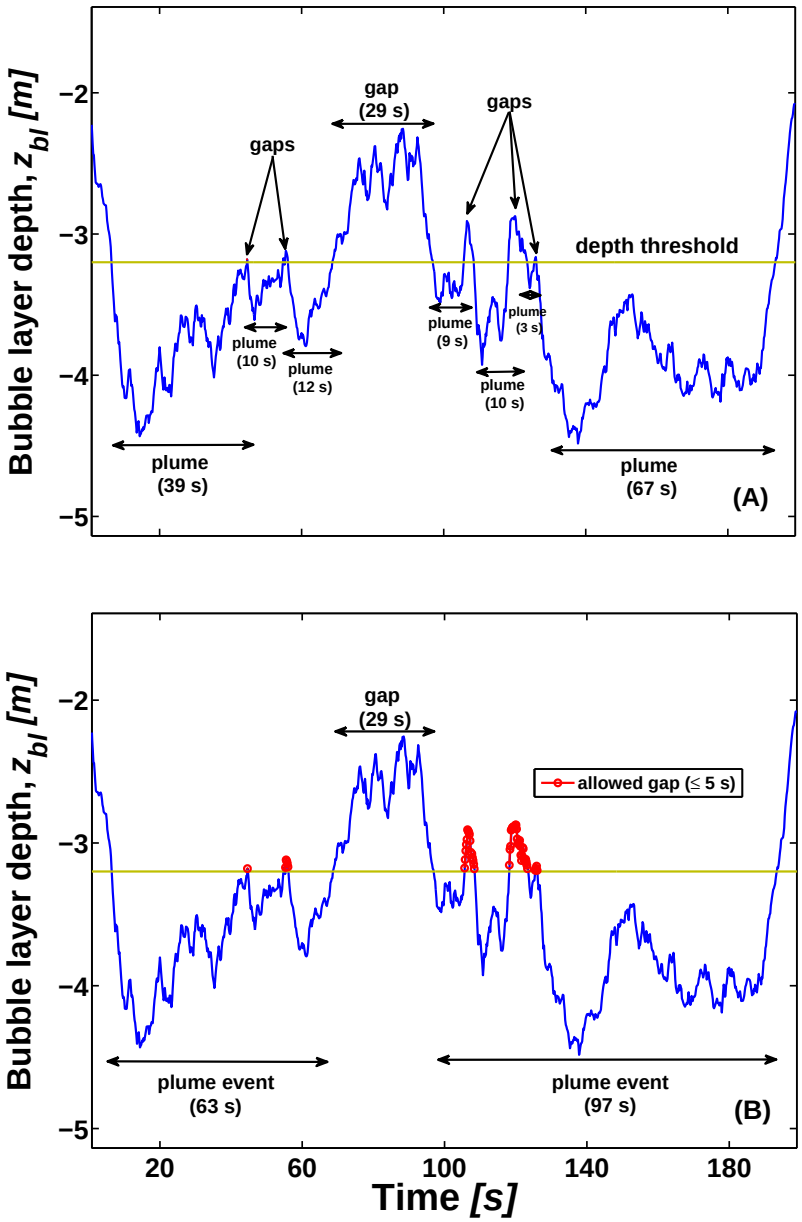

Figure 3.23: Time-series of bubble layer depth showing the plume detection process when applying the depth threshold when (A) no allowed gap was used, where there is a highly sensitive plume detection, with 7 events detected, and (B) an allowed gap was used, where the plume detection is much less sensitive, with only two main events detected.

The time evolution of the bubble plume bottom is often subject to very short but steep vertical oscillations, which is caused by the discrete patchy structure of the bubble plume that arises when the plumes are recorded with high resolution (at 6 *Hz* sampling frequency). This is shown in an example of a time-series of bubble layer bottom, sampled for about 200 seconds from the sonar records.

There are rapid variations about the 3.2 *m* depth location of the resonator, so a high num-

ber of individual plume events arises, inducing overestimation in the plume detection (Figure 3.23a). Some of the events are just small signal variations within the main plume event, with durations even as small as 3 seconds (Figure 3.23a). Plume events, at resonator depth, must be separated by an allowed gap of 5 seconds or more. Consequently, only two main bubble plume events were depicted by including the 5-second allowed gap (red lines with circles in Figure 3.23b). This shows that the allowed gap is very useful in determining the properties of individual plume events, such as frequency (production rate) and duration, which will be extensively used in the bubble plume statistical analysis from Section 5.2.2 here.

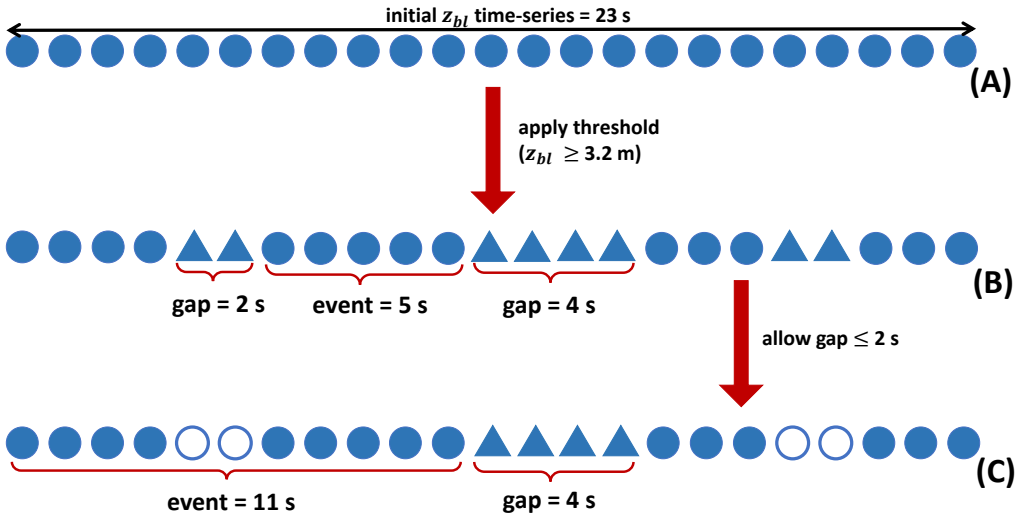

Figure 3.24: Schematic representation of the event detection algorithm, with (A) initial artificially generated bubble layer depth time-series, (B) pattern of gaps (triangles) and events (filled circles) sequences resulted from applying a depth thresholding, and (C) result of allowing a gap in the pattern from (B) (empty circles).

Let us consider a schematic representation of the plume detection algorithm. For simplicity, an initial artificial bubble layer depth (named z_{bl}) time-series, which contains discrete elements given at every second, has been considered; therefore, a 23 s long z_{bl} time-series is obtained shown in Figure 3.24a. The aim here is to distinguish between periods with a valid event detection and gaps (periods with no event detection).

To select individual events from this time-series, a 3.2 m depth threshold has been applied in the artificial z_{bl} signal, which corresponds to the depth at which the resonator was located during the measurements. By imposing this threshold, an individual bubble plume is depicted

only if $z_{bl} \geq 3.2\ m$, while the sequences with $z_{bl} < 3.2\ m$ are gaps. The maximum allowed gap length discussed above was also used in the artificial z_{bl} from Figure 3.24c, where an allowed gap of, for example, maximum 2 seconds ($\leq 2\ s$) was chosen, represented by the empty circles. As shown in Figure 3.24b, this thresholding technique generated sequences of events (filled circles, with $z_{bl} \geq 3.2\ m$) and gaps (triangles, with $z_{bl} < 3.2\ m$).

By depicting these individual events in time, their starting and ending points can be found at specific time instants. This has been accomplished by splitting the events as a function of the gaps using a regular expression described by the MATLAB function *regexp*. Counting the elements from the starting to ending points of an event yields the duration of that event, which is a property that will be included in the bubble plume statistics. The sequences of events separated by gaps – with their specific durations – are highlighted in Figures 3.24b to 3.24c.

This detection algorithm was applied using an identical approach as above in the resonator void fraction signal as well. In this case, there is a void fraction threshold imposed as $V_f \leq 6 \times 10^{-8}$, which is equal to one standard deviation void fraction. This ensured that even the smallest void fraction signals in the events are separated from the background flat signal. This threshold also represents the minimum void fraction level contained in a bubble plume, usually found at the plume edge, detected by both sonar and resonator. However, there are cases when a bubble plume is detected, but the associated void fraction lies below the threshold. The condition for an allowed gap $\leq 5\ s$ was also used for the detection of events in the void fraction data measured by the resonator.

3.7.2 Accuracy of the plume detection algorithm

To compare the two records in detecting a bubble plume, an accuracy test was conducted by computing the sum of true positives (*TP*) and true negatives (*TN*) rated to the presence of false positives (*FP*) and false negatives (*FN*),

$$Accuracy = \frac{TP + TN}{TP + FP + FN + TN}. \tag{3.17}$$

Here *TP* counts the time instants (in this case seconds) at which all the events are simultaneously detected by both the sonar at the resonator depth and resonator; *TN* counts the time instants at which neither the sonar or resonator detected any events; *FP* counts the time instants of all events detected by the sonar while the resonator fails to detect them; *FN* counts

the time instants at which the sonar fails to detect the events, but which are detected by the resonator. Consequently, all *TP*, *TN*, *FP* and *FN* have been computed by matching all the time instants of events measured by sonar and resonator in the real ocean.

The accuracy increases if more true positives and true negatives along with fewer false positives and false negatives are detected in a time-series. An example showing how the accuracy test works for a pattern of sonar against resonator artificial detection can be visualized in the scheme from Figure 3.25. Here a circle corresponds to a detection instant, while a triangle represents a gap instant.

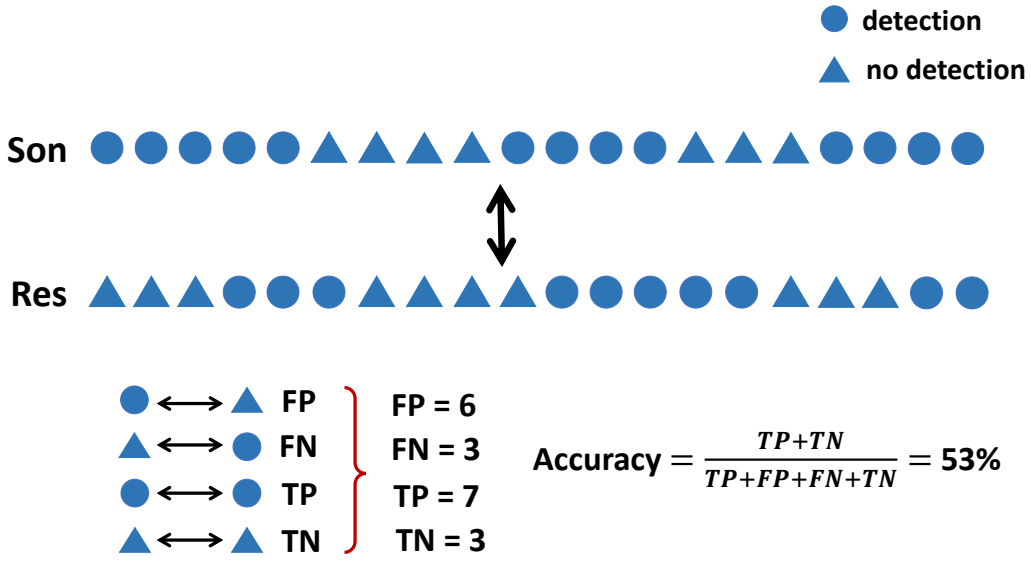

Figure 3.25: A schematic representation of artificially generated sonar and resonator matching patterns, using boolean expressions (false positives *FP*, false negatives *FN*, true positives *TP* and true negatives *TN*) with circles (ones) and triangles (zeros) to compute the accuracy of the plume detection algorithm.

The correlation between two circles yields a true positive and the correlation between two triangles generates a true negative (Figure 3.25). Any combination between circles and triangles yields false positives and false negatives as indicated in Figure 3.25. In this simple test from Figure 3.25 all the values from these combinations were introduced into the expression of Equation (2.17) and a detection accuracy of 53% was obtained.

3.7.2.1 Algorithm testing on observed time-series

To test the plume detection algorithm using data measured in the real ocean, the z_{bl} and V_f records have been compared to each other, sampled between 17:59:02 to 20:42:24 on Nov 02

2013, with the included allowed gap $\leq 5\ s$ condition. Using these two records, the detection accuracy has been computed (Figure 3.26). The 3.2 m and 6×10^{-8} depth and void fraction thresholds, respectively, are indicated by the two horizontal continuous lines present in both z_{bl} and V_f time-series from Figure 3.26. The void fraction threshold indicates that a bubble plume that penetrates down to the critical depth of 3.2 m contains a minimum void fraction of 6×10^{-8}. To perform the matching between the sonar and resonator signals, a detection pattern has been generated for each dataset, as illustrated by the horizontal sequences of dots (green nuances and magenta in the middle plot from Figure 3.26).

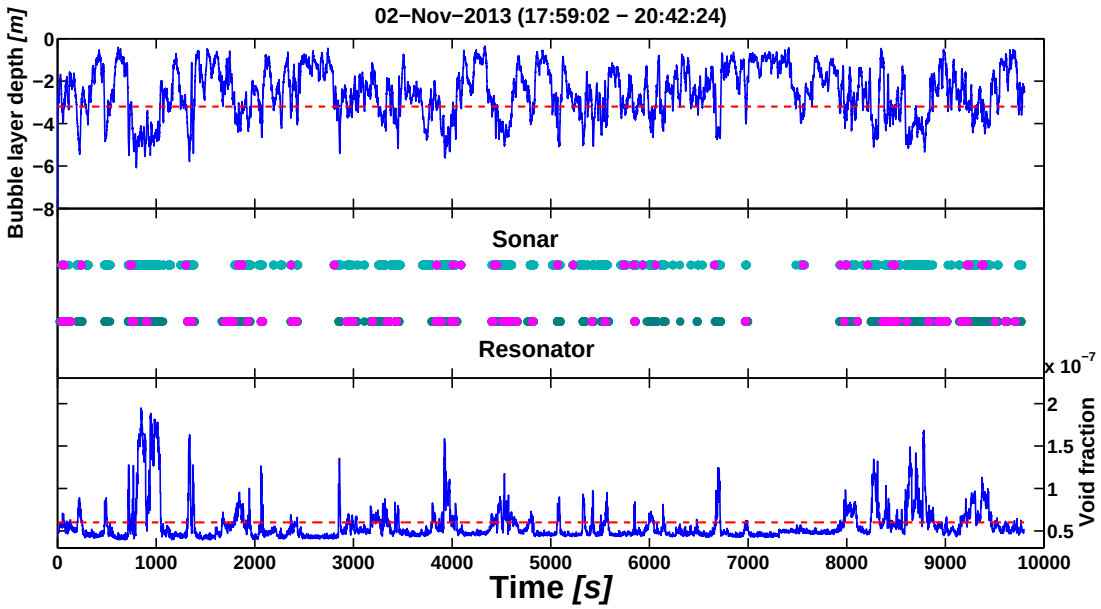

Figure 3.26: Time-series of sonar bubble layer depth and resonator void fraction signals, sampled from the real ocean, used to test the plume detection algorithm and show the detection patterns (sequences in green nuances are purely detected events; sequences in purple are the allowed gaps; blank spaces in between are not associated with plume events). The depth and void fraction thresholds are indicated by the horizontal red broken lines.

Each dot represents a detection instant of 1 second. The dots in the green nuances correspond to pure detection (no allowed gap condition needed), and the magenta dots show the allowed gaps. Consecutively aligned green and magenta dots group together in single events while being separated by large gaps indicated by the blank spaces (middle plot from Figure 3.26).

The events (green and magenta dots) and the large gaps in between (blank spaces) are stored as logical arrays (composed of zeros $=$ gaps and ones $=$ events). Gaps (zeros) are

present for about 69% of the total time interval in both sonar and resonator records. Therefore, only 31% of the data are actually detected events (ones), but this is not unusual. A period with moderate to relatively high plume activity was chosen, where wind speed reached top recorded values (during the Nov 02-03 storm) of $17 - 18\ m/s$, so for periods with low plume occurrence, the ones/zeros proportion in the plume detection algorithm would be even smaller.

By comparing the z_{bl} and V_f detection patterns, the true positives and true negatives are predominantly found for most of the time period. Using Equation (3.17), an accuracy of 81% has been obtained for the plume detection algorithm with the allowed gap $\leq 5\ s$, which means that in 81% of the time the plume detection algorithm successfully matched the sonar and resonator records.

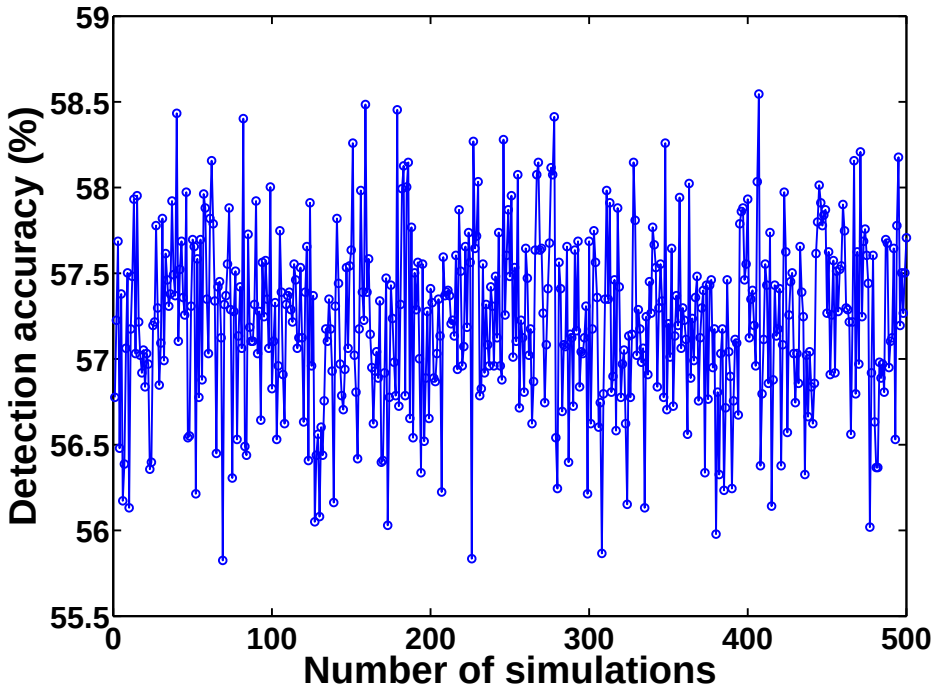

Figure 3.27: Simulated randomized sonar-resonator matchings with the associated detection accuracy for all 500 simulations.

To evaluate the significance of the above accuracy, I randomly generated 1000 sequences (artificial sequences with zeros and ones), with one half (500 random sequences) simulating the sonar detection and the other half (the rest 500 sequences) simulating the resonator detection. These simulated sequences have the same time length and they also contain the same proportion of zeros (69%) and ones (31%) as the original sonar and resonator detection patterns. Therefore, 500 matches have been simulated between these random sequences and

Equation (3.17) was used to compute the matching accuracy.

Figure 3.27 shows 500 values of accuracy resulted from the matches, ranging from about 56% to 58.5%. This means that if the detection is successful for about 57% of the time (on average) or less, then that particular detection algorithm does not perform better than chance. A higher accuracy (of 81%) is associated with the plume detection algorithm implemented here, thus the algorithm performs clearly better than chance, indicating that the patterns detected by both instruments are not randomly generated. However, it must be acknowledged that there is still a proportion of falsely detected plume signals. This may be caused by the fact that both instruments used quite different measuring techniques, with a smaller resonator sample size compared to the sonar beam sampling volume. The limited accuracy may also be caused by the presence of old and more diffuse plumes, which usually contain small and sparse bubbles (Leifer et al., 2007) that are associated with very low void fractions ($< 6 \times 10^{-8}$).

3.8 Summary and conclusions

Most of the datasets used in this thesis are collected from a multibeam Delta T sonar, allowing the construction of the sonar matrix of the subsurface bubble layer evolution in time and with depth. From the sonar matrix, the bubble layer structure and complex bubble plume statistics will be presented and analysed in chapters 4 and 5, respectively.

Using the data collected from wind sensors mounted on the R/V Knorr and from the Waverider buoy allows the investigation of the complex effects of wind speed and sea state on plume statistics and structure.

The bubble size distribution scaled by void fraction was obtained for each storm. The shape of the distributions provide insight on the uniformity in time and between storms, suggesting that the bubbles measured by the camera are contained in fully developed plumes, and no bubbles from active breaking penetrate to the camera depth level.

The bubble layer relative to the instantaneous sea surface, rather than the mean sea surface, was calculated using an algorithm based on the retrieval of the wave envelope and the manipulation of backscatter signal within the sonar matrix. This showed the true penetration depth of the bubble layer, and the true localisation of the backscatter signal within the water column. The e-folding depth coefficient was computed using the backscatter profiles with re-

spect to the instantaneous sea surface. Note that the plume detection algorithm was not used with respect to the instantaneous sea surface (by comparing sonar and resonator records) because the resonator position is fixed with respect to the sonar, so no shifting is needed to compare them.

Using simultaneous records from the sonar (bubble layer depth, z_{bl}), bubble camera and resonator (void fraction, V_f), a filtering technique that enabled the retrieval of the bubble layer base was employed. The bubble layer depth signal obtained using this technique will be later used in an algorithm for the detection of individual plumes.

A plume detection algorithm was developed and used to generate bubble plume statistics containing plume properties such as duration, maximum penetration depth and production rate (frequency). The method used simultaneous records of bubble layer depth z_{bl} and void fraction V_f from the sonar and resonator. A thresholding technique was used for both sonar (depth threshold) and resonator (void fraction threshold) records to detect and match the main events in both signals. To avoid the overestimation of the number of detected events, an allowed gap < 5 seconds technique was used in both z_{bl} and V_f signals. By matching the events detected in the z_{bl} and V_f signals using boolean expressions, an accuracy of 81% was found for the plume detection algorithm. Randomly simulating 500 artificial sonar-resonator matchings, with accuracies ranging between about 56% and 58% (which can be attributed to chance), ensured that the accuracy of the plume detection algorithm is clearly better than chance, so the successful matching of sonar and resonator signals is not randomly generated – it rather indicates the presence of bubble plume events at specific time intervals, especially that two independent instruments (sonar and resonator) were vertically aligned on the spar buoy to specifically measure injected bubbles from the same breaking-wave events. However, the limited accuracy indicates that there are some limitations in the plume detection algorithm, which could be attributed to the different sampling volume of the sonar and resonator, and to possible detected old deep plumes that have a low gas content from injected bubbles.

Chapter 4

Backscatter structure of the bubble layer

4.1 Introduction

The acoustical backscatter caused by the bubble layer and plumes in the upper $10 - 20\ m$ of the ocean has been the focus of a number of studies (Crawford and Farmer, 1987; Thorpe, 1982; Thorpe and Hall, 1983; Trevorrow, 2003; Vagle et al., 2010; Wang et al., 2011). As the oceans are so vast, the environmental and oceanic conditions can vary significantly from one region to another, so acoustic bubble measurements in the context of environmental factors are vital to better understand the large scale processes of bubble-plume structure. To quantify the bubble populations within the water column, the distribution of backscatter in the vertical bubble layer is studied here.

It has been noted by most authors mentioned above and others (Graham et al., 2004) that bubble density, associated with backscatter signal within the water column in the open ocean, decreases exponentially with depth. The backscatter exponential decay rate has been quantified using an e-folding depth coefficient (see Section 3.6.7). The aim in this chapter was to construct a set of e-folding depth statistics, which is then used to assess their relationship to wind speed, sea state and wave physics.

Given the lack of more complex measurements, the majority of these authors present wind speed as the only controlling factor for the change in the exponential decay rate. Only a

small number of studies show the effect of swell and wind-sea significant wave height on the backscatter change with depth in the bubble layer (Graham et al., 2004; Wang et al., 2011), and almost none show the influence of wave development and wind-sea wave Reynolds number on backscatter decay rate in a complex wave field. Only few authors reported backscatter observations at winds $\geq 20\ m/s$ (Vagle et al., 2010; Wang et al., 2011). Most studies report backscatter observations at low to medium wind speeds ($5-13\ m/s$) and also in less complex sea states (little or no mixture between wind-waves and swell).

In this chapter, the vertical backscatter structure and pattern of the 30-minute averaged bubble layer is examined. The backscatter decay with depth, due to bubble entrainment, is quantified by the e-folding depth coefficient. In the field data collected during HiWinGS cruise, the backscatter signal was observed to decay exponentially. This exponential decay is tested in each backscatter profile and, using a threshold based on the correlation coefficient of the best-fit lines, a backscatter threshold/filter (acting to filter the backscatter noise from the profiles as an effect of averaging) was employed. Applying this exponential decay function allowed the generation of the e-folding depth statistics from all three storms.

4.2 The structure of the backscatter distribution with depth

The environmental parameters, wind speed (U_{10}), inverse wave age (u_*/c_p), wave Reynolds number (R_H) and significant wave height of wind-sea (H_{sw}), are expected to have an effect on the structure of the backscatter (S_v) vertical profile. It is important to note that the analysis that will be laid out in this chapter focuses on the averaged bubble field, not on individual plumes.

To be comparable with the environmental parameters, which were averaged over 30 minutes, the backscatter sonar matrix was also averaged over 30 minutes. Therefore, 30-minute averaged backscatter profiles, distributed with depth and in time, were obtained and combined to generate an average backscatter sonar matrix for each storm among the 24-25 Oct, 02-03 Nov and 07-09 Nov storms. Each backscatter profile/column encompasses a record of the bubble layer relative to the instantaneous sea surface averaged over 30 minutes (see in Section 3.6.6 the method used to calculate the bubble layer relative to the instantaneous sea surface).

One advantage of the profile averaging is the elimination of the patchy structure of the bub-

ble layer, so the intrinsic backscatter structure can be analysed. However, the original (high resolution) sonar matrix is sparse, so its row-wise averaging yields an output that contains a substantially lower S_v signal (S_v ranges from -65 to -24 dB) than the non-averaged sonar matrix (S_v ranges from -28 to -5 dB). The disadvantage of the averaging is thus the generation of this low S_v signal which introduces a noise that distorts the penetration pattern and structure of the bubble layer. This causes the exponential decay function to generally poorly describe the variation of the profiles that contain this noisy S_v signal. This would yield a low confidence in the usage of e-folding depth for the estimation of the backscatter decay with depth. Other models could be potentially employed to characterise the averaged backscatter profiles, but it is undesirable to fit any model to these noisy profiles that form an almost uniform penetration pattern.

Consequently, the S_v values are filtered here, which led to the trimming of the S_v profiles. The filtering has been done incrementally (at a step of 1 dB) to verify the average correlation coefficient (R^2) of the exponential best-fit lines relative to the S_v profiles at each filtering step.

The accuracy of an exponential variation of the backscatter decay increases (R^2 increases) with the incremental trimming of the S_v profiles. However, too much trimming is undesirable because it would remove the signal scattered by many of the bubbles forming the bubble layer. Therefore, a trade-off between the magnitude of trimming and the average R^2 value for the exponential backscatter decay of the profiles has been considered.

After a visual inspection of the effect of trimming on the S_v profiles, a cut-off of $R^2 = 0.8$ was used. The effect of the trimming has been visualised in terms of the shape of the averaged bubble layer – the shape and penetration depth could be clearly distinctive using the trimming at $R^2 = 0.8$. This cut-off indicates that the trimming of S_v profiles ceases when an average (over all S_v profiles) $R^2 = 0.8$ is reached. The $R^2 = 0.8$ level ensures that the exponential best fits represent the backscatter variation within the vast majority of the profiles. However, since the trimming was done in increments of 1 dB, an overshooting of the cut-off usually occurs, and when this occurs the overshooting R^2 value is considered as the final one. Table 4.1 shows the average R^2 for each dB level in the S_v profiles.

As it will be shown in the following paragraphs, a trimming at a different decibel level has been used for each storm. The different trimming levels are used as a compromise to retrieve the pattern of backscatter exponential decay, however these trimming levels are imposed by

the $R^2 = 0.8$ cut-off, which is generalised for all storms.

Table 4.1: The trimming of the backscatter profiles using an average R^2 at each dB level for each storm.

dB level	Average R^2 (Oct 24-25)	Average R^2 (Nov 02-03)	Average R^2 (Nov 07-09)
-65 dB	0.0144	0.7695	0.5886
-64 dB	0.1101	0.7803	0.5902
-63 dB	0.2073	0.7911	0.5946
-62 dB	0.2660	0.7927	0.5957
-61 dB	0.3256	0.7954	0.5971
-60 dB	0.3991	0.7976	0.5980
-59 dB	0.4447	0.7994	0.6073
-58 dB	0.4803	0.8067	0.6066
-57 dB	0.5150	–	0.6077
-56 dB	0.5450	–	0.6142
-55 dB	0.5885	–	0.6156
-54 dB	0.6299	–	0.6212
-53 dB	0.6523	–	0.6286
-52 dB	0.6784	–	0.6510
-51 dB	0.6965	–	0.6719
-50 dB	0.7061	–	0.6940
-49 dB	0.7174	–	0.7078
-48 dB	0.7325	–	0.7405
-47 dB	0.7442	–	0.7828
-46 dB	0.7552	–	0.8215
-45 dB	0.7643	–	–
-44 dB	0.7843	–	–
-43 dB	0.8096	–	–

For the Nov 07-09 storm, the S_v profiles are trimmed from -65 dB (non-trimmed profiles) to a -46 dB level. The non-trimmed profiles, in Nov 07-09 storm, have a relatively low average

R^2, and the -46 dB level reached the R^2 cut-off, overshooting at $R^2 = 0.8215$ (Table 4.1). This provides higher confidence that the e-folding depth can reasonably quantify the exponential backscatter decay within the profiles trimmed to the -46 dB level.

For the Oct 24-25 storm, the S_v profiles are trimmed from -65 to -43 decibels. The trimmed profiles at the -43-decibel level are characterised by an average R^2 slightly overshooting (the cut-off has just been exceeded) at 0.8096 (Table 4.1). The variation of the S_v profiles observed in Nov 02-03 storm is well described by the exponential decay function ($R^2 = 0.77$) even when the profiles are not trimmed (Table 4.1). Consequently, the R^2 cut-off has been reached after a trimming by only 7 dB (from -65 dB to -58 dB), so these profiles are characterised by a wider S_v signal range than that of the profiles observed in Oct 24-25 and Nov 07-09 storms.

The varying trimming levels employed above for each storm could be explained by the different penetration depth of the averaged bubble field under changing wind and sea state conditions. For instance, during the Nov 02-03 storm, the wind was relatively steady for most of the time period, so the bubble layer shows an almost constant penetration for a significant part of the storm, with a gradual evolution and no steep variability, as opposed to the strong variation of the bubble layer in both Oct 24-25 and Nov 07-09 storms. The near surface backscatter strength in the Nov 02-03 storm is also relatively constant throughout the storm while, particularly in the Oct 24-25 storm, the backscatter signal strongly varies as there was a rapid transition from the eye of the storm to top wind forcing.

Given the difficulty in conducting measurements during the extreme environmental conditions from 24-25 Oct storm, approximately 53–70% of the values in the wave record are missing. Consequently, 70% and 53% of the R_H (and H_{sw} which is used to compute R_H) and u_*/c_p values, respectively, are missing from the records during the 24-25 Oct storm, so only the remaining data can be used for quantitative analysis. There is only about 20% and 10% of the R_H (and H_{sw}) and u_*/c_p missing data, respectively, in the 07-09 Nov storm.

4.2.1 The evolution of depth-varying backscatter during Oct 24-25 storm

As shown in Figures 4.1a and 4.1d, the backscatter distribution with depth has a similar evolution to that of wind speed. The 30-minute averaged backscatter (S_v) profiles generally show a greater penetration depth as U_{10} increases (Figures 4.1a and 4.1d). The e-folding depth (red

line with circles in Figure 4.1d) shows a similar pattern to the averaged bubble layer, indicating a less steep backscatter decay under a higher wind stress. The e-folding depth significantly decreases when a low wind speed of about $8-9\ m/s$ is present (in the eye of the storm, at 0400–0600 on Oct 25) and the backscatter profiles reach the lowest penetration depth (Figures 4.1a and 4.1d). This implies that most bubbles are confined in the upper shallow metre, so there is a steep change in the backscatter within the water column. This effect is similar to the observations of a larger bubble density near the surface associated with low e-folding scales recorded by Trevorrow (2003).

The backscatter profiles show that the bubble concentrations reached up to $-17\ dB$ close to the surface, particularly in the 1715–1815 (Oct 25) time interval (in the second part of the storm).

This is associated with a rapid wind speed transition from $8-9\ m/s$ to $27-28\ m/s$, while the detected bubbles reached maximum penetration of about $5-5.5\ m$. At the same time, although a large S_v signal (of -23 to $-20\ dB$) was found down to $2-3$ metres depth within the water column (an indication of dense bubble populations spreading down the water column), a lower e-folding depth ($d = 0.9\ m$) characterises a relatively steep backscatter decay within the profiles observed in the 1715–1815 (Oct 25) time interval (Figure 4.1d); this backscatter variation is probably characterised by a strong contrast in the S_v signal still present between the upper $2-3\ m$ and the deeper regions in the profiles. Although some dense bubble populations developed under this rapidly transitioning wind, these bubble structures did not probably have enough time to increase even further in density. However, in the last about 3 hours of the recorded storm and after about 6 hours of wind blowing steady at $26-27\ m/s$, more bubbles appeared to be accumulating in the upper ocean, gradually increasing the density of the bubble layer. This is indicated by a strongly increasing trend of e-folding depth (eventually reaching up to about $3\ m$) that is associated with a significantly attenuated S_v signal (by about $12-14\ dB$).

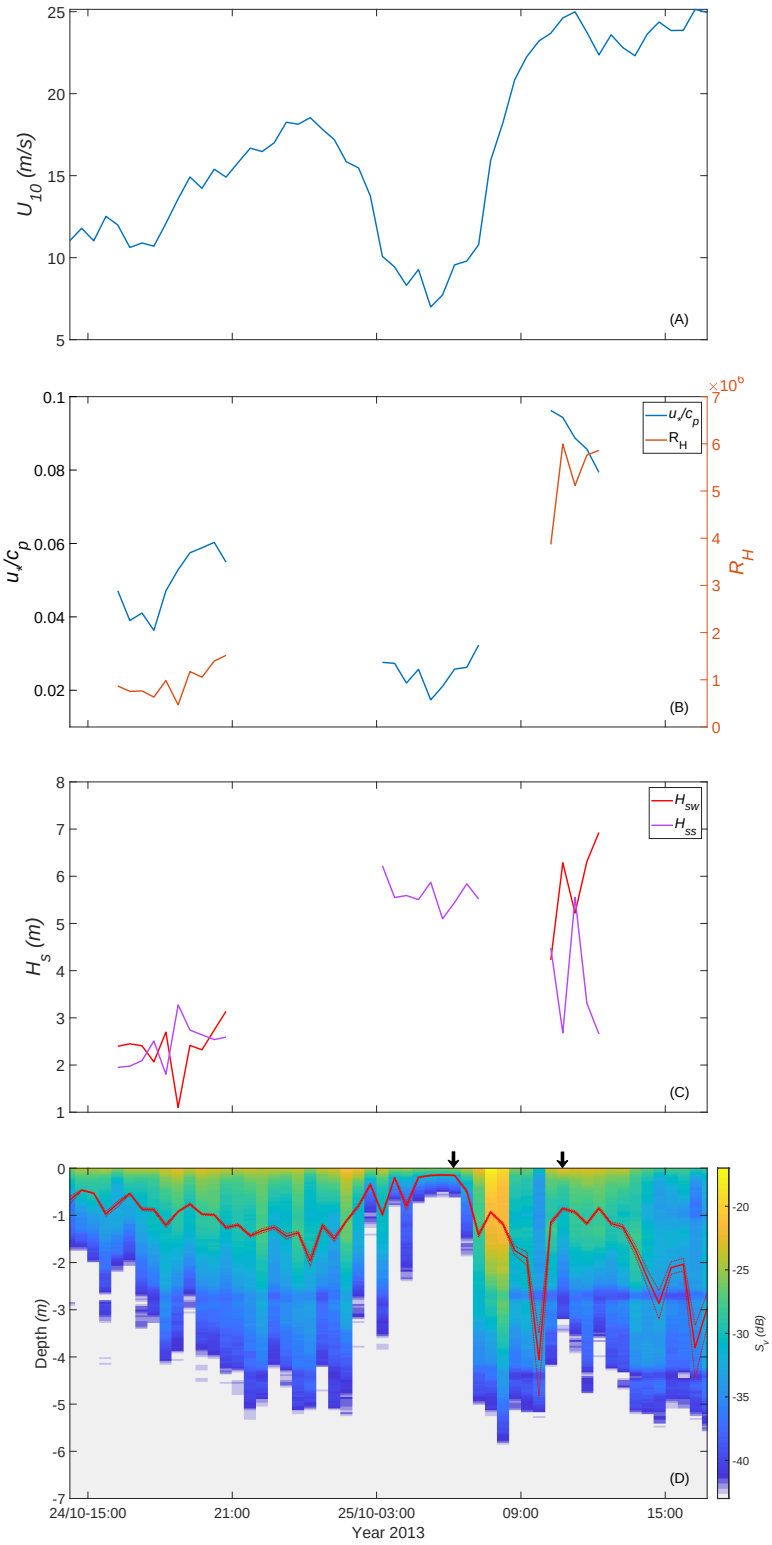

Figure 4.1: Time-series of environmental parameters, backscatter depth distribution and e-folding depth during Oct 24-25 storm. The evolution of U_{10} (A), R_H superimposed on u_*/c_p (B), significant wave height, H_s, broken down in wind-sea (red) and swell (magenta) (C) and e-folding depth, d (red solid line) superimposed on the 30-minute averaged sonar matrix (D). The dotted red lines in (D) represent the upper and lower 95% confidence bounds of e-folding depth. The S_v values in (D) range from -43 dB (the backscatter trimming level) to about -14 dB. The values on vertical axis in (D) are negative because they show the depth below the instantaneous sea surface. The thick black arrows above the sonar matrix indicate the sampling periods of the directional wave spectra shown in Figure 4.2.

The lowest e-folding depth and shallowest S_v profile, present in the 0400–0600 time interval, are associated with the least developed waves (shown by the low u_*/c_p values in Figure 4.1b). A possible explanation of this effect is that when wind exerts lower shear stress over the surface waves (thus transferring less momentum), there might be a lower energy dissipation via white-capping, and thus a reduced transfer of vertical momentum to entrain subsurface bubbles in the water column. However, there is no available information in this thesis about bubble entrainment and its connection to energy dissipation via white-capping. Measurements of bubbles, turbulent diffusion and underwater currents would potentially reveal the bubble entrainment, which could be then related to the vertical momentum transfer by breaking waves.

Observations during HiWinGS, conducted by Brumer et al. (2017), show a reduction of whitecap fraction for less developed waves (low inverse wave age), but the relationship is weak ($R^2 = 0.24$), with a significant variability being left unexplained by inverse wave age. Although U_{10} exerted steady high shear stress at $23 - 24\ m/s$, the profiles observed in the 1015-1315 (Oct 25) interval show a lower both bubble penetration (of about $3.5 - 4\ m$) and e-folding depth ($d \sim 0.8 - 0.9\ m$). In this time period, the sea state is characterised by highly developed waves and high energy wind-sea waves (both inverse wave age and R_H were possibly close to their maximum peak). A relatively mixed sea state was prevailing at that time, with wind-sea waves ($H_{sw} = 6 - 7\ m$) superimposed on slightly smaller swell ($H_{ss} = 4 - 5\ m$). However, using a wave record with so many missing elements does not provide a clear picture on a possible wave mechanism causing the steeper backscatter decay with depth.

Although the wind stress over the surface waves increases in the 1615–2045 (Oct 24) time interval, wind-sea waves with steady low energy are present (indicated by low R_H and H_{sw} values). This might be caused by a delayed response of wind-sea waves to the wind input, but, in this case, no clear trend can be observed due to significant missing wave data during the Oct 24-25 storm. At this time, the pattern of bubble penetration and e-folding depth appears to follow more closely that of wind stress (Figure 4.1).

4.2.1.1 The local wave field variability

The directional wave spectrum record, sampled at 0615 on Oct 25 (during the passage of the eye of storm; indicated by a thick black arrow in Figure 4.1d), shows that the wave field is dominated by swell. A wide (with direction) and large spectral peak, almost entirely present

in the gray shaded area (swell partition is shaded and wind-sea is not shaded) of the polar plot in Figure 4.2 (upper panel), suggests that high energy swell waves ($S(f_{wave}, \theta_{wave}) > 0.09\ m^2/Hz\ deg^{-1}$) were propagating from multiple directions (generally north-west to south-west).

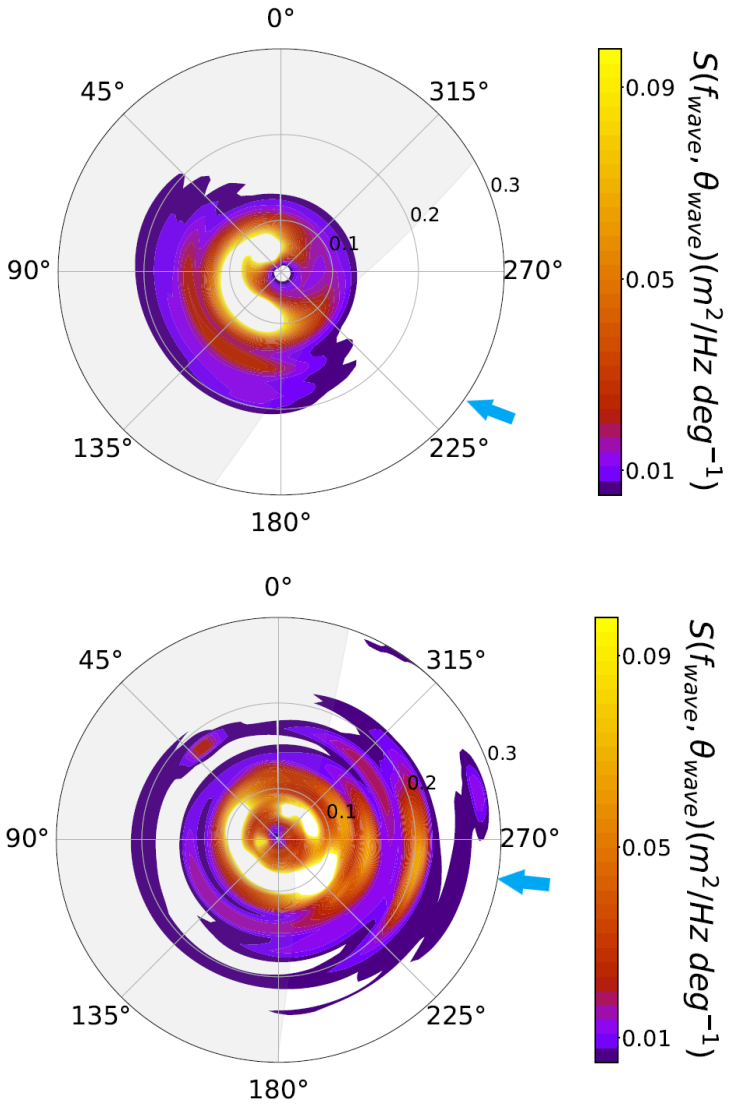

Figure 4.2: Two records of directional wave spectrum sampled at 0615 on Oct 25 (upper panel) and 1045 on Oct 25 (bottom panel). The contours show different levels of $S(f_{wave}, \theta_{wave})$, the 0° angle represents the north coordinate, the radial ticks indicate different f_{wave} values. The wave components are partitioned in swell (gray shading) and wind-sea (no shading). The colorbar is on logarithmic scale. (Upper panel) The presence of a high energy dominating swell. (Bottom panel) The presence of a mixed wave field. The wind directions were 232° and 265° on Oct 25 at 0615 and 1045 respectively (indicated by the cyan arrows).

Most of the energy in the swell spectral peak is concentrated at a $f_{wave} < 0.1\ Hz$, but

with an important part of the energy distributed to higher frequencies as well (upper panel in Figure 4.2). This high energy swell may be associated with steep backscatter decay with depth (e-folding depth $d = 0.4\ m$) because the wind-sea waves (which are more likely responsible for breaking waves and bubble injection), at this time, had a low energy (with $S(f_{wave}, \theta_{wave})$ not exceeding about $0.02\ m^2/Hz\ deg^{-1}$), so they were suppressed by the large swell (Figure 4.1d and upper panel in Figure 4.2).

The directional spectrum, sampled at 1045 on Oct 25, was recorded just after the passage of the eye of the storm in the time period when a lower bubble concentration (but still significantly higher than that during the passage of the eye of the storm) was recorded within the water column in steady high winds blowing at $23 - 24\ m/s$. The wave spectrum shows that the energy in the spectral peak is distributed to both swell (gray shading) and wind-sea (no shading) waves (bottom panel in Figure 4.2). However, most of the energy distribution is contained in the wind-sea waves at a $f_{wave} > 0.1\ Hz$, especially for those waves propagating from east/south-east (bottom panel in Figure 4.2). This suggests that there was a mixed sea state (coexistence of wind-sea and swell), but with a dominant wind-sea (propagating from east to south), present at that time. It has been shown that, at least locally, the reduced bubble concentration and penetration depth have an approximately simultaneous occurrence with the mixed wave field that contains high energy wind-sea waves superimposed on swell (Figure 4.1d and bottom panel in Figure 4.2).

4.2.2 The evolution of depth-varying backscatter during Nov 02-03 storm

During the Nov 02-03 storm, the environmental conditions are milder and bubble concentration is lower, so the sonar beam was never completely absorbed or scattered. This allows the sonar to more frequently detect higher backscatter signal at deeper positions in water column. During most of the time period, between 0600 (Nov 02) and 0600 (Nov 03), there is a relatively constant high bubble concentration (with a S_v signal of up to about $-22\ dB$) present close to the surface.

In many profiles, a large S_v signal ranging from about $-33\ dB$ to $-30\ dB$ is present at deeper levels of $2 - 3\ m$ (Figure 4.3d) compared to the profiles observed in Nov 07-09 storm where such large S_v signals were mostly confined in the upper 1-metre layer.

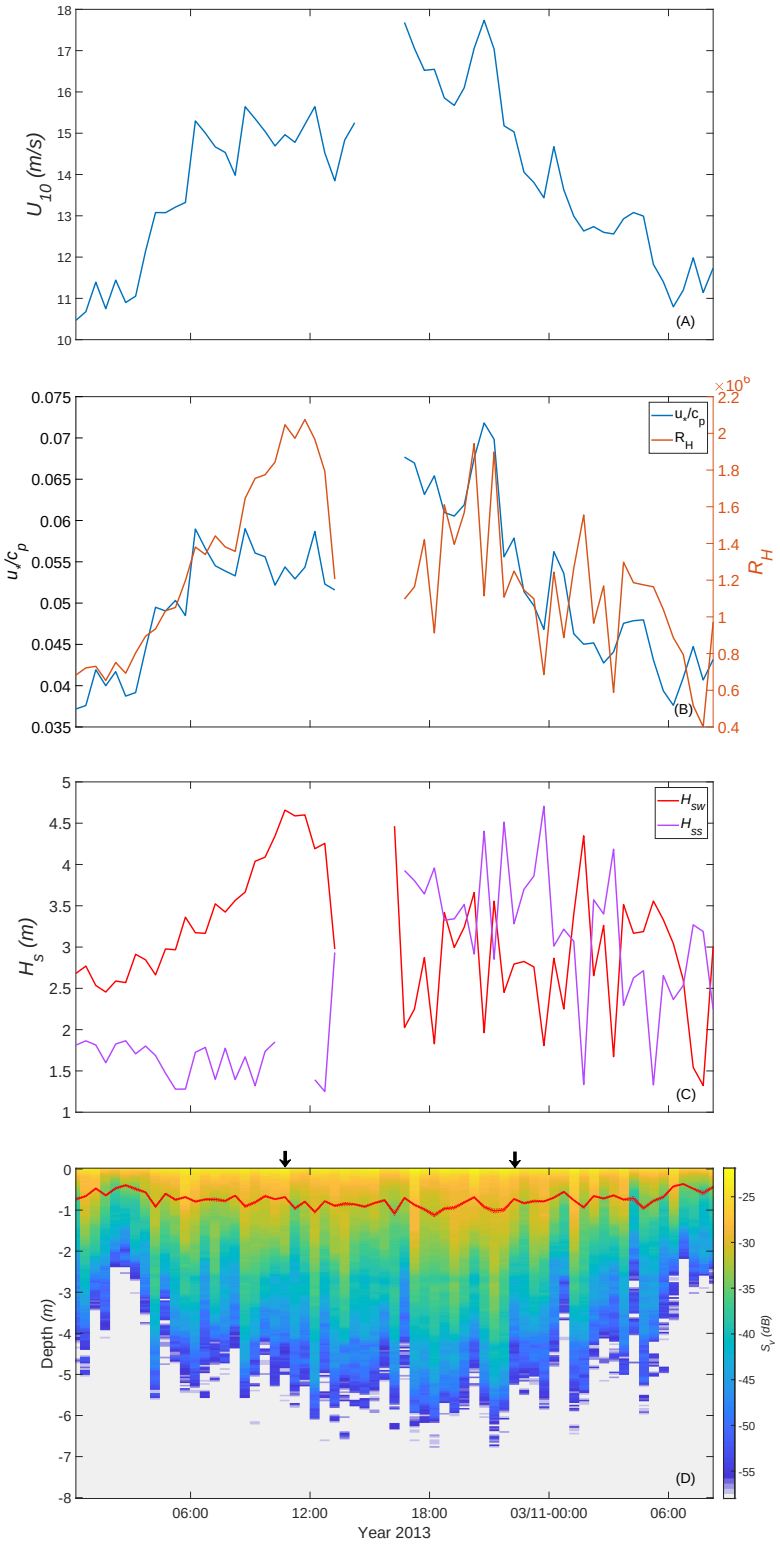

Figure 4.3: Time-series of environmental parameters, backscatter depth distribution and e-folding depth during Nov 02-03 storm. The S_v values in (D) range from -58 *dB* (the backscatter trimming level) to about -20 *dB*. The red solid line in (D) represents the evolution of e-folding depth superimposed on the backscatter profiles. The dotted red lines in (D) represent the upper and lower 95% confidence bounds of e-folding depth. The thick black arrows above the sonar matrix indicate the sampling periods of the directional wave spectra shown in Figure 4.4.

In general, a less steep backscatter decay with depth (e-folding depth maintained steady at around $1 - 1.1\ m$) was forced by a steady high wind stress and large wind-sea waves during most of this storm.

The e-folding depth is significantly shallower in the Nov 02-03 storm than in the previous storm, and the e-folding depth does not exceed $1\ m$ very often (Nov 02-03 storm), while the e-folding depth can even exceed $3\ m$. For example, at $15\ m/s$ wind speed, the e-folding depth in the Nov 02-03 storm is below $1\ m$ (about $0.8\ m$), compared to an e-folding depth of approximately $1.5\ m$ recorded during the Oct 24-25 storm.

The S_v profiles penetrate deeper and e-folding depth grows (however, showing relatively large variability) as U_{10} increases up to about $15\ m/s$. Although U_{10} continues to increase to about $18\ m/s$, the bubble concentration only shows a small increase. Similarly to wind speed, the trend of inverse wave age reaches a relative plateau (varying about a value of 0.055) during the 0615–1245 (on Nov 02) time interval (Figure 4.3b). The wave field at that time is mostly dominated by the largest wind-sea waves ($H_{sw} = 4.5\ m$) recorded here (Figure 4.3c). After this time interval, the waves continue to grow under a higher wind stress, reaching maximum development at 1615–2115 (on Nov 02), when the trend of backscatter decay and bubble penetration depth remained relatively steady (Figures 4.3b and 4.3d). The sea state is characterised by a strong contrast in H_{sw} variability between the first half (relatively smooth H_{sw}) and second half (highly variable H_{sw}) time interval (Figure 4.3c). The large H_{sw} variability in the second half of the storm (from about 1800 on Nov 02 to 0800 on Nov 03) is coincident with the presence of a large swell (also with highly variable H_{ss}) that appears to dominate the wind-sea. In this relatively mixed wave field, the bubble penetration and e-folding depth are on a falling trend, while the wave development and R_H are also in a declining phase.

The evolution of backscatter profiles is more similar to that of R_H because R_H encompasses the effect of a relative equilibrium between wind-sea wave energy and surface shear stress. The time periods with the largest H_{sw} and shear stress values do not match, inducing a relatively steady evolution of R_H in the time interval 0945–2115 on Nov 02 (with notable variability, especially in the last 4 hours of this time interval; since there are missing data during this time interval, a complete account for this trend cannot be made) when the bubble concentration level and penetration depth also maintain steady.

4.2.2.1 The local wave field variability

The directional wave spectrum, measured at 1045 (on Nov 02), shows that most of the energy in the wave field is contained by wind-sea waves (upper panel in Figure 4.4). These dominant wind-sea waves generally propagate from south/south-east, and their spectral peak is mostly distributed at a frequency $f_{wave} > 0.1$ *Hz* (upper panel in Figure 4.4).

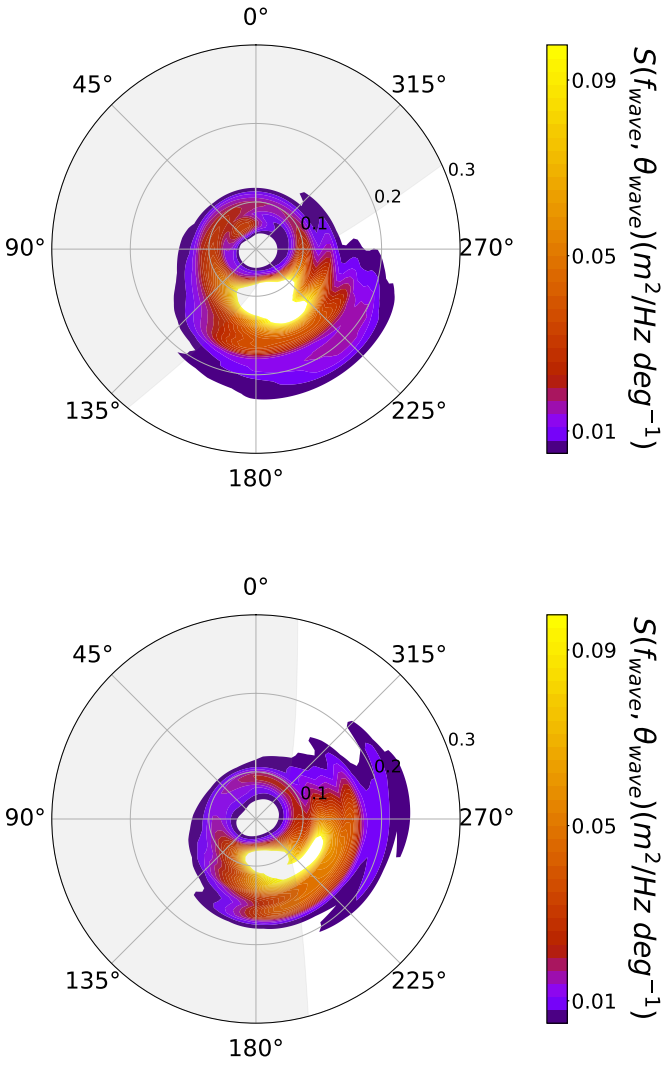

Figure 4.4: Two records of directional wave spectrum sampled at 1045 on Nov 02 (upper panel) and 2215 on Nov 02 (bottom panel). The contours show different levels of $S(f_{wave}, \theta_{wave})$, the 0° angle represents the north coordinate, the radial ticks indicate different f_{wave} values. The wave components are partitioned in swell (gray shading) and wind-sea (no shading) components. The colorbar is on logarithmic scale. (Upper panel) The presence of a dominating wind-sea. (Bottom panel) The presence of a mixed wave field.

Only a small part of the spectral peak distribution is contained by a swell propagating from

south-west, but overall swell is strongly dominated by wind-sea. In these wind driven sea state conditions, the bubble layer is in a deepening phase associated with an increasing trend of e-folding depth (Figure 4.3d). This wave spectrum was sampled at the peak-time of wind-sea dominance, as it is also shown by the largest H_{sw} recorded in this period (Figure 4.3c). As shown in the backscatter profile from Figure 4.3d, the bubbles reach close to maximum penetration and concentration after this dominant wind-sea period.

A mixed sea state (coexistence of swell and wind-sea) was recorded at 2215 (on Nov 02), with the spectral peak's energy being distributed slightly more to the swell component (bottom panel in Figure 4.4). The spectral peak, for both swell and wind-sea, is not as clearly separated as previously in the frequency domain because an important part of the energy of swell is distributed in the same frequency band as that of wind-sea, $0.1\ Hz < f_{wave} < 0.2\ Hz$ (bottom panel in Figure 4.4). However, swell waves contain most of their energy at lower frequencies ($f_{wave} < 0.1\ Hz$), while wind-sea waves contain theirs at $f_{wave} > 0.1\ Hz$ (bottom panel in Figure 4.4). At that time, swell and wind-sea waves were propagating from similar directions, respectively from south and south-east. These overlapping wind-sea and swell waves are associated with fairly strong bubble activity, but both penetration and e-folding depth are in a declining phase (Figure 4.3d).

4.2.3 The evolution of depth-varying backscatter during Nov 07-09 storm

This storm is characterised by a mostly separated sea state where there is a sharp transition between wind-sea and swell conditions – wind-sea and swell each dominate over separate time intervals (Figure 4.5c).

In the first part of this storm there were two peaks, similar in magnitude, in the sea state development (with $u_*/c_p \sim 0.05 - 0.06$), occurring from 1600 to 2200 on Nov 07 and from 0100 to 0500 on Nov 08, indicating the presence of young waves which were mostly dominating the wave field (Figure 4.5b). These young waves are the largest wind-driven waves recorded during this storm (in the 0100–0500 on Nov 08 time interval), with H_{sw} reaching up to $4.2\ m$ (Figure 4.5c). Under these large young waves, the averaged bubble layer showed the greatest depth, reaching down to 4–4.5 m.

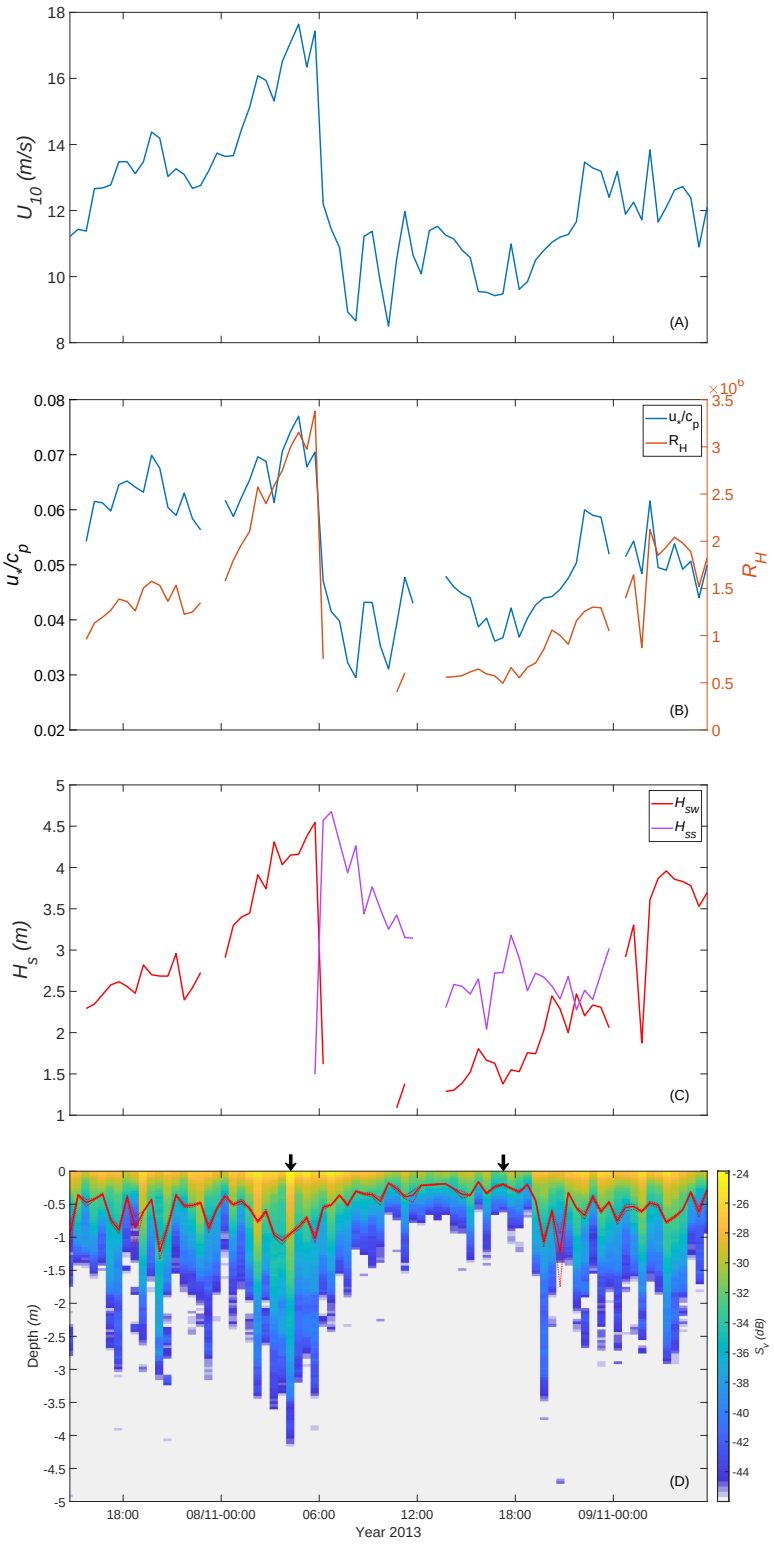

Figure 4.5: Time-series of environmental parameters, backscatter depth distribution and e-folding depth during Nov 07-09 storm. The S_v values in (D) range from -46 *dB* (the backscatter trimming level) to about -23 *dB*. The red solid line in (D) represents the evolution of e-folding depth superimposed on the backscatter profiles. The dotted red lines in (D) represent the upper and lower 95% confidence bounds of e-folding depth. The thick black arrows above the sonar matrix indicate the sampling periods of the directional wave spectra shown in Figure 4.6.

The water column also contained a higher backscattering level due to the presence of bubble scatterers in higher densities at deeper levels (S_v values of about $-35\ dB$ can be found at a depth of 3 metres).

This larger bubble concentration in the water column is indicated by a maximum in e-folding depth (varying around 1 metre) present in the 0100–0500 on Nov 08 time interval (Figure 4.5d). The shallowest averaged bubble layer and lowest e-folding depth are associated with the least developed and smallest wind-sea waves present in the 1015–1845 on Nov 08 time interval when a large swell ($H_{ss} = 4 - 4.5\ m$) was dominating (Figures 4.5c and 4.5d).

In this storm, the peak in wind speed is very well matched, in time, with wind-sea waves reaching maximum energy (largest R_H). During this time interval (0100–0500 on Nov 08) with waves characterised by large R_H, the large bubble concentration and entrainment may be associated with a larger wave energy dissipation via wave breaking (with the presence of whitecaps as an effect).

There is some evidence for this effect provided by Brumer et al. (2017) who explored the relationship between whitecap fraction and R_H (also computed based on H_{sw}) during the Hi-WinGS cruise. They found that whitecap fraction generally increases with R_H, but the relationship is characterised by a large variability (only about 30–40% of the whitecap fraction variability could be explained by R_H). However, compared to other sea state parameters, Brumer et al. (2017) found R_H to be the one with the closest relationship to whitecap fraction.

4.2.3.1 The local wave field variability

During periods of maximum bubble penetration and weakest exponential backscatter decay (e-folding depth maximum), wind-sea waves were propagating from south/south-east on Nov 08 at 0415 (Figure 4.5d and upper panel in Figure 4.6). The wide spectral peak (which covered a wide segment of direction) is almost entirely found in the wind-sea partition, with almost no wave energy at frequencies below $0.1\ Hz$ (upper panel in Figure 4.6). In this developed sea state and high wind stress with strongly dominating wind-sea, there were only some very low energy swell components propagating from west/south-west and east/north-east (upper panel in Figure 4.6).

The shallowest bubble penetration and lowest e-folding depth (steep exponential backscatter decay) are associated with a high energy swell propagating from south/south-east on Nov

08, at 1715 (Figure 4.5d and bottom panel in Figure 4.6). The swell component contains almost the entire energy observed in the wave spectrum at that time. The wind-sea waves are almost entirely suppressed by the propagating swell, and only a very low energy wind-sea (with $S(f_{wave}, \theta_{wave}$ of about $0.01\ m^2/Hz\ deg^{-1}$) was propagating from east/north-east (Figure 4.6).

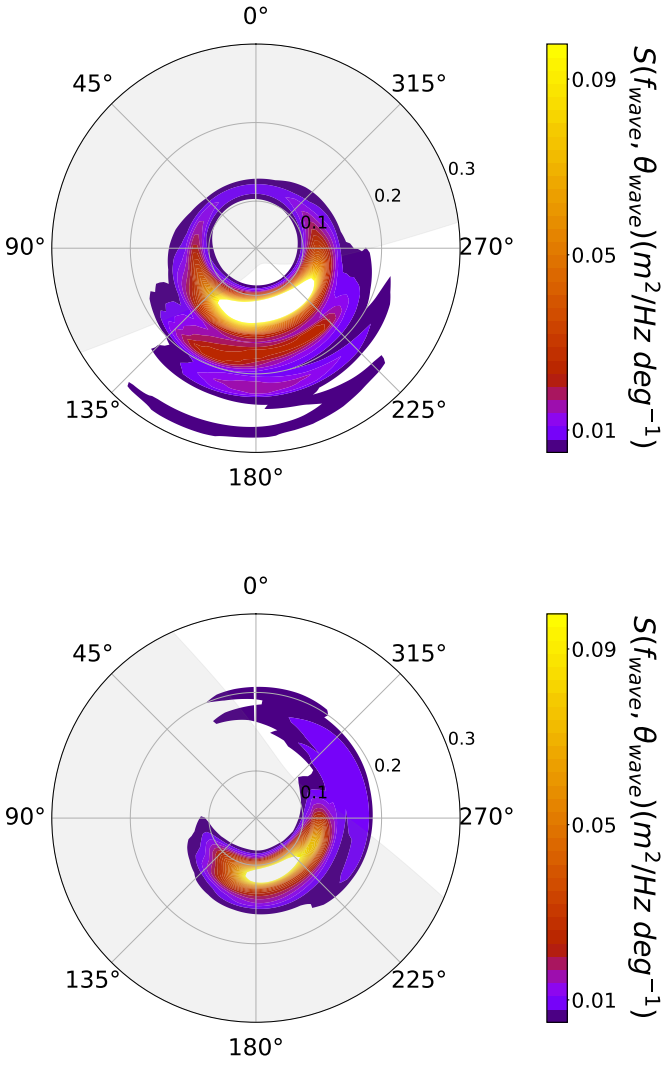

Figure 4.6: Two records of directional wave spectrum sampled at 0415 on Nov 08 (upper panel) and 1715 on Nov 08 (bottom panel). The contours show different levels of $S(f_{wave}, \theta_{wave})$, the 0° angle represents the north coordinate, the radial ticks indicate different f_{wave} values. The wave components are partitioned in swell (gray shading) and wind-sea (no shading). The colorbar is on logarithmic scale. The presence of a dominant wind-sea (upper panel) and dominant swell (bottom panel).

Most of the energy of these swell waves (the spectral peak) is distributed at a $f_{wave} > 0.1\ Hz$. Compared to the previously observed spectra, this higher frequency swell is distinctive because such wave energy distribution with frequency is more typical for wind-sea waves.

However, all wind-sea wave peaks shown here and in previous sections do not exceed $0.2\ Hz$ in the frequency domain.

4.3 The effect of environmental conditions on backscatter decay

Wind speed is a quantity generally used by many authors in the parameterisation of whitecaps (Asher and Wanninkhof, 1998; Zhao and Toba, 2001), which are caused by wave breaking (Callaghan et al., 2012) and subsurface bubble injection via bubble rising (Deane and Stokes, 2002; Leifer et al., 2007). However, wind speed alone does not provide a direct physical mechanism for changes in bubble concentration with depth (Woolf, 1993), especially in high winds (McNeil and D'Asaro, 2007), but rather drives the sea state that induces wave breaking and subsequent bubble entrainment. The influence of both wind speed and sea state on backscatter exponential decay, via e-folding depth, are explored in this section.

The Oct 24-25, Nov 02-03 and Nov 07-09 storms, each showing the evolution of e-folding depth and environmental parameters, are directly compared to better understand the scale and complexity of environmental forcing of e-folding depth. The relationships of e-folding depth with wind speed and sea state are examined via least square statistical analysis. Given that wave breaking is associated to wind-driven waves, the dependence of e-folding depth on wind-sea significant wave height in a complex wave field is also investigated here.

4.3.1 Wind speed and sea state dependence of e-folding depth

A period from about 0700 to 1600 on Oct 25 with a rapid intensification of U_{10} (up to $25\ m/s$) and bubble entrainment (d peaked at about $4\ m$) is depicted in Figure 4.7. These wind speed conditions favoured a rapid development of very young sea ($u_*/c_p \sim 0.09$) which consists of high energy wind-sea waves with a larger R_H reaching up to 6×10^6 during this period.

There was a period of about three hours during Oct 24-25 storm when a below average e-folding depth ($0.8\ m$) was present, while wind speed and sea state variables showed above average values. This indicates a shallower backscattering under the forcing of high wind stress ($U_{10} > 22\ m/s$) and high energy young wind-sea waves. During this anomalously low bubble

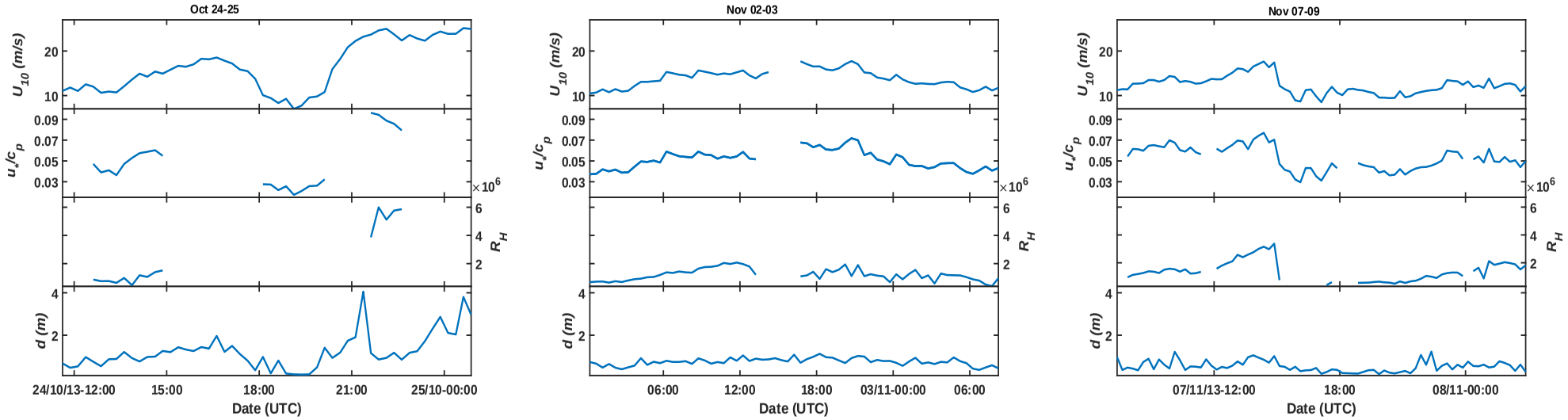

Figure 4.7: Comparison of time evolution of e-folding depth (d) with variation of wind speed and wave parameters for all three storms. The patterns of these parameters in each column with box plots correspond to each storm. All parameters in these box plots are on the same scale for a direct comparison.

presence, the e-folding depth showed a similar level to that present during notably lower winds ($12-14\ m/s$). Given the limited wave data, it is difficult to infer any air-sea interaction mechanisms that could cause this anomalously low e-folding depth. A reduction of drag and subsequent sea surface roughness in high wind stress (Bye and Jenkins, 2006; Powell et al., 2003) could possibly explain the decline of bubble entrainment. However, for this to be a potentially viable explanation, the proportion of older waves should increase at higher winds, but very young waves (which act to increase the surface roughness) were observed at $U_{10} > 22\ m/s$ during HiWinGS.

During the Nov 02-03 and Nov 07-09 storms, the presence of milder environmental conditions led to a lower magnitude of backscatter exponential decay (average e-folding depth of about $0.6\ m$) compared to Oct 24-25 storm (average e-folding depth of about $1.2\ m$). The highest wind speed of almost $17\ m/s$ in the Nov 02-03 storm corresponded to younger waves ($u_*/c_p \sim 0.06-0.07$) as shown in Figure 4.7 (middle panels). Here, a similar wave development to Oct 24-25 storm appears to be a favourable environment for larger bubble concentrations (e-folding depth reaches a peak of $1-1.1\ m$). At this stage, wind-sea waves (mixed with swell), characterised by a $R_H \sim 1.8 \times 10^6$, were recorded, compared to wind-sea waves (separated from swell) corresponding to a larger R_H (exceeding 2×10^6) that were observed during the Nov 07-09 storm.

In the Nov 07-09 storm, as soon as the wind speed reaches about $17\ m/s$ and waves become younger (at $u_*/c_p \sim 0.07$), the e-folding depth rapidly increases (panels on the right in Figure 4.7). On the other hand, the pattern of e-folding depth does not match the wind-sea wave field variation, and R_H is also characterised by large variability, so the magnitude of R_H is generally closer to that of d. A time period (from 0345 to 0545 on Nov 08) with an even more poorly matched d with R_H is associated with the peak in the wind-sea wave energy, when R_H shows a 40–50% higher variability than that of d.

In the 1445–2115 (on Nov 07) time interval, neither wind speed, inverse wave age or wave Reynolds number appear to show any relationship with the e-folding depth, and the e-folding depth does not have a clear trend (it appears to show an almost random variation, varying fairly symmetrical about its mean). The details showing the association of e-folding depth with the environmental parameters are discussed in the following sections.

4.3.1.1 Relationship of e-folding depth with wind speed and sea state

The observations in the Oct 24-25 storm show a close to linear growth of e-folding depth with increasing U_{10} (Figure 4.8). This relationship can be approximated by using a power-law of the form $y = ax^b$, with the best-fit described by the following expression:

$$d = (2.2 \pm 3.2) \times 10^{-2} U_{10}^{1.1 \pm 0.3}, \tag{4.1}$$

where the coefficients with the 95% confidence bounds are present to quantify the uncertainty of the regression fitting line (Figure 4.8). The relationship estimated by the power-law best-fit is characterised by the correlation coefficient, $R^2 = 0.49$. Up to $U_{10} = 18 - 20\ m/s$, the power-law fits the data reasonably well, with a relatively low magnitude of the residuals, RM (on average, $RM \sim 0.5\ m$), and the residuals are characterised by a more random variation.

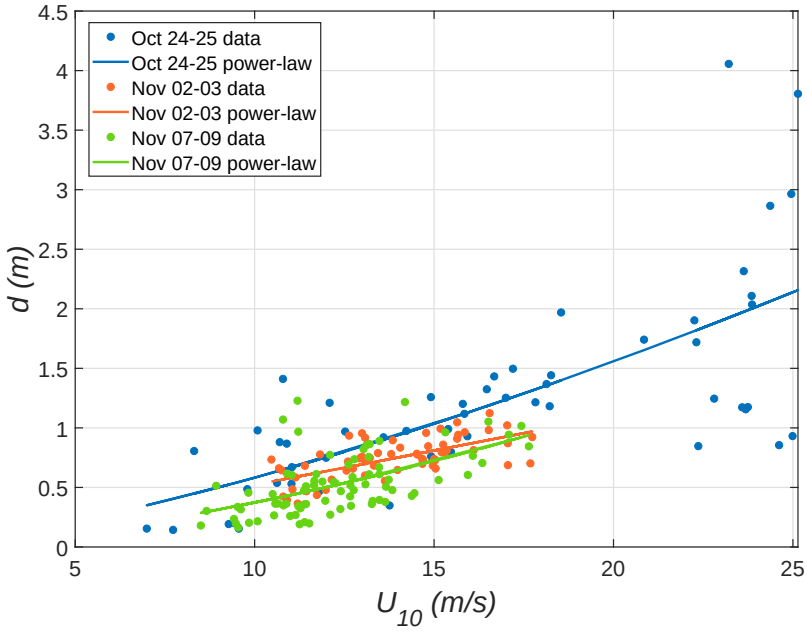

Figure 4.8: Relationship between e-folding depth, d, and wind speed, U_{10}, fitted by power-law models for each storm. The data points are averaged over 30 minutes.

There is considerable scatter at $U_{10} > 20\ m/s$, with a poor fit (average RM is around $2\ m$), and the residuals are not homogeneously distributed about the fitting line. This indicates a strong variation in the bubble concentration under steady wind forcing, but, due to the lack of more wave data, no clear physical wave mechanism can be inferred that might explain the large scatter in the relationship. More coincident subsurface bubble and wave observations taken at $U_{10} > 20\ m/s$ would be needed to explain the scatter.

In the Nov 02-03 storm, an approximately linear relationship characterises the increase of d with growing U_{10}, which is described by the following power-law:

$$d = (4.4 \pm 3.8) \times 10^{-2} U_{10}^{1.4 \pm 0.5}, \tag{4.2}$$

with a correlation coefficient, $R^2 = 0.45$. Compared to the Oct 24-25 storm, the power-law in Equation (4.2) shows a lower rate of increase of d within the $10 - 18\ m/s$ wind speed range (which is the range measured during the Nov 02-03 storm). However, the power-law used to model the relationship from Nov 02-03 storm shows a substantially lower fitting error (see the values of root mean square error, *RMSE*, in Table 4.2), also indicated by a relatively random variation of the residuals.

A more than linear relationship defines the increase of d with growing U_{10} in the Nov 07-09 storm. The power-law describing this relationship has the following expression:

$$d = (0.9 \pm 1.1) \times 10^{-2} U_{10}^{1.6 \pm 0.5}, \tag{4.3}$$

for which the correlation coefficient is $R^2 = 0.33$. The Nov 07-09 storm is described by a similar rate of increase of d (by $0.8 - 0.9\ m$) to that observed in the Oct 24-25 storm within a wind speed ranging from 8 to $18\ m/s$. Despite the weaker correlation, a clear pattern in the relationship between d and U_{10} exists, as the power-law model fits the relationship with a notably lower *RMSE* than that used for the Oct 24-25 storm (see Table 4.2). The 95% confidence bonds in the e-folding depth relationship with wind speed observed in all three storms do not significantly vary, indicating that all exponents of wind speed are statistically similar.

Using the power-law models shown in Figure 4.8, wind speed generally accounts for less than half of the e-folding depth variance in any of the storms (with the Oct 24-25 storm being the most important contributor to the variance). More of this variance might be physically explained by breaking-wave statistics, subsurface turbulence and gas saturation level (which are not available in this thesis) that might affect the injection and entrainment of bubbles. It is also likely that the backscatter trimming magnitude would have a contribution on changing the variation of e-folding depth but, as long as there is not a substantial change in the trimming, the impact on the variance of the relationship above would be minor.

Table 4.2: Comparison between the power-law best fits used for the Oct 24-25, Nov 02-03 and Nov 07-09 storms using wind speed and sea state parameters as predictors for e-folding depth. The parameters used to assess the predictor fitting are R^2 and root mean square error, *RMSE* (given in units of the dependent variable).

Predictor	Deployment	Best-fit	R^2	*RMSE*
U_{10}	Oct 24-25	$d = (2.2 \pm 3.2) \times 10^{-2} U_{10}^{1.1}$	0.49	0.58
U_{10}	Nov 02-03	$d = (4.4 \pm 3.8) \times 10^{-2} U_{10}^{1.4}$	0.45	0.13
U_{10}	Nov 07-09	$d = (0.9 \pm 1.1) \times 10^{-2} U_{10}^{1.6}$	0.33	0.21
u_*/c_p	Oct 24-25	$d = (4.1 \pm 4) \times u_*/c_p^{0.5}$	0.38	0.30
u_*/c_p	Nov 02-03	$d = (9.1 \pm 7.3) \times u_*/c_p^{0.8}$	0.41	0.13
u_*/c_p	Nov 07-09	$d = (19.2 \pm 25) \times u_*/c_p^{1.2}$	0.31	0.21
R_H	Oct 24-25	–	–	–
R_H	Nov 02-03	$d = (0.6 \pm 1.3) \times 10^{-2} R_H^{0.3}$	0.29	0.15
R_H	Nov 07-09	$d = (0.5 \pm 1.4) \times 10^{-3} R_H^{0.5}$	0.32	0.21

A linear fit was used by Vagle et al. (2010) to assess the relationship between e-folding depth and wind speed. This is similar to the approximately linear relationship also obtained in this thesis. Vagle et al. (2010) reported a similar correlation coefficient ($R^2 = 0.43$) to that obtained in this thesis for this relationship. A clear increase of e-folding depth with wind speed, in hurricane conditions, has been observed by Wang et al. (2011) (but no statistical model was used to assess the relationship). Less significant relationships have been noted by Crawford and Farmer (1987) and Thorpe (1982). Vagle et al. (2010) and Wang et al. (2011) conducted measurements at wind speeds $> 20\ m/s$, whereas Crawford and Farmer (1987) and Graham et al. (2004) measured e-folding depth in lower winds of only up to about 10 m/s. All authors, except Wang et al. (2011), used upward single beam sonars designed to offer point measurements of the subsurface bubble layer. Wang et al. (2011) used a high frequency 300 *kHz* acoustic Doppler current profiling sounder (ADCP) to vertically profile the bubble plumes under a category 4 hurricane. The data sampling ranges from 15-minute averages (Wang et al., 2011) to 2.25-hour averages (Vagle et al., 2010). The latter author used these larger sampling times because the measurements were collected over a 1-month period.

Most authors agree that e-folding depth increases with wind speed. As the values measured by Crawford and Farmer (1987) are sparse and show considerable scatter, a low-significance wind speed influence on the decay rate of bubble concentration with depth has been reported (Pearson coefficient $R = 0.6$, with p-value $= 0.09$ significance level). Graham et al. (2004) also reported an increasing e-folding depth with growing wind speed. Although Vagle et al. (2010) found that e-folding depth relates well to wind speed (Pearson coefficient $R = 0.8$, p-value $< 10^{-4}$), the relationship is characterized by a large scatter (as characterised by a mean standard deviation, $SD = 0.3\ m$). Vagle et al. (2010) notes that some of the scatter was observed because the collected reanalysis wind speed data did not include smaller scale local wind events. Graham et al. (2004) conducted the e-folding depth measurements at low wind speeds (in the $7-11\ m/s$ range) and they found the uncertainty of the measured e-folding depth to be much lower (with a mean $SD = 0.07\ m$).

This thesis presents a trend of e-folding depth with growing wind speed similar to the findings of Wang et al. (2011). This implies a similar variation in bubble entrainment under a similar wind speed input. The e-folding depth values, estimated by Vagle et al. (2010) at similar wind speeds, are larger than estimates from Wang et al. (2011), but similar to the values recorded in this thesis. These differences could arise because the backscatter profiles recorded by Vagle et al. (2010) were based on a depth reference with respect to the wave surface, which can induce a larger e-folding depth scale than when a depth reference relative to the mean sea level is used by authors such as Wang et al. (2011) and Thorpe (1982). Wang et al. (2011) observed the backscatter from bubble entrainment at a larger scale. Another possible cause for these differences in e-folding depth magnitude could be the different types of acoustical instruments used in the observations. For instance, single-beam sonars, like the one used by Vagle et al. (2010), do not have a built-in time varying gain, so they have a considerably higher starting gain, making them sensitive to a wide array of backscatter signals.

Although the trend and magnitude of the variation of e-folding depth with wind speed are similar to those recorded by Vagle et al. (2010), the uncertainty of the measured e-folding depth was found to be lower in this thesis (mean $SD = 0.2\ m$) than observations by Vagle et al. (2010). The relationship between e-folding depth and wind speed discussed here is also characterised by uncertainty, with the highest and lowest uncertainty characterised by $SD = 0.7\ m/s$ (for a $22 - 24\ m/s$ wind speed range covering only about 6% of the 30-minute

averaged data) and $SD = 0.5\ m/s$ (for a $11 - 13\ m/s$ wind speed range covering about 23% of the 30-minute averaged data).

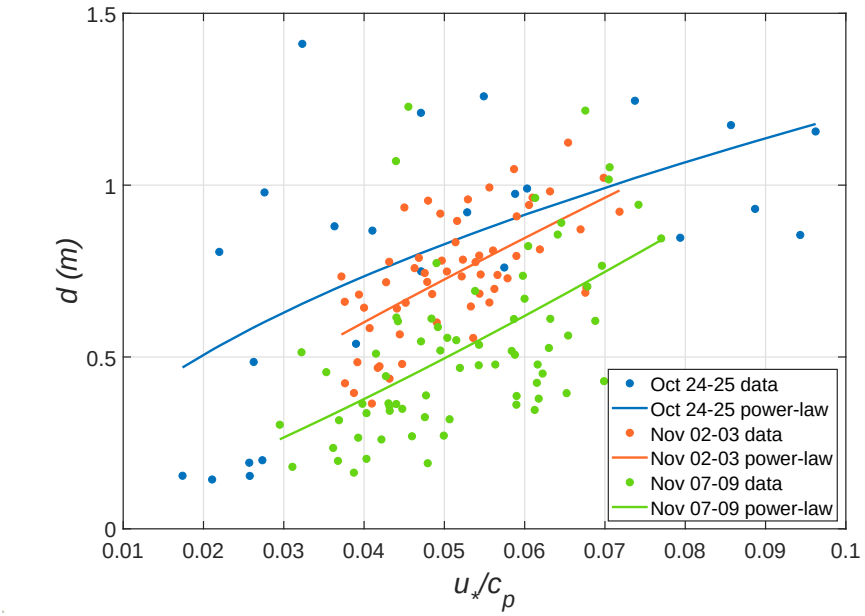

Figure 4.9: Relationship between e-folding depth, d, and wind speed, u_*/c_p, fitted by power-law models for each storm. The data points are averaged over 30 minutes. Although there exists a high level of scatter, with no strong relationship, approximate fits are still shown. The e-folding depth data is distributed over a similar inverse wave age range in the Nov 02-03 and Nov 07-09 storms, but over much wider one in the Oct 24-25 storm. The first two storms are similar (characterised by mixed sea state), but the third storm is significantly different (characterised by separated sea state).

Although slightly more than half of u_*/c_p data is missing from the records in the Oct 24-25 storm, the remaining data can still be used to estimate a trend of the dependence of e-folding depth on u_*/c_p. This data can be fitted by the following power-law:

$$d = (4.1 \pm 4) \times u_*/c_p^{0.5 \pm 0.3} \tag{4.4}$$

which is characterised by $R^2 = 0.38$ (Figure 4.9). The power-law describes an influence on d as the input from u_*/c_p increases, with $d < 1.5\ m$ even in the most developed wave field recorded in all three storms ($u_*/c_p \sim 0.09 - 0.1$). However, the only available u_*/c_p values larger than 0.07 are coincident with the anomalously low d, so there is no u_*/c_p data coincident with the largest d values recorded in all three storms. This obviously distorts the least square fitting, so the current power-law model cannot entirely explain the relationship. From Figure 4.9 (the Oct 24-25 data) it is currently unknown if there would be a significant number of d values

increasing rather than remaining constant as waves develop, so more data is evidently needed to fill this gap. Even so, Figure 4.9 shows a notable pattern, with normally distributed residuals about the fitting line, so the power-law fits the relationship reasonably well (see Table 4.2).

In the Nov 02-03 storm, d increases approximately linearly with growing u_*/c_p (Figure 4.9), which is a similar relationship to the wind speed dependence. This similarity is expected, since inverse wave age includes the friction velocity which is highly correlated with U_{10}. This approximately linear relationship is expressed by the following power-law:

$$d = (9.1 \pm 7.3) \times u_*/c_p^{0.8\pm0.3} \tag{4.5}$$

with the inverse wave age capturing less than half of the d variance ($R^2 = 0.41$). The sensitivity of d to the u_*/c_p input is higher than that from the Oct 24-25 storm, d showing an almost twice the rate of increase in the Nov 02-03 storm (Figure 4.9). A lower *RMSE* (driven by the lower d variance), by a factor of 2, is also associated with the power-law fit from the Nov 02-03 storm (Table 4.2). The scatter in the relationship between d and u_*/c_p, as the waves become younger, is relatively uniform, and the strongest bubble entrainment ($d > 0.9\ m$) occurs almost exclusively under younger waves ($u_*/c_p > 0.05$).

An approximately linear relationship characterises the increase of d with growing u_*/c_p in Nov 07-09 storm. This relationship is described by the power-law of the form,

$$d = (19.2 \pm 25) \times u_*/c_p^{1.2\pm0.5}, \tag{4.6}$$

with almost one third of the d variance being explained by u_*/c_p using this model ($R^2 = 0.31$). The rate of increase of bubble entrainment with the u_*/c_p input is similar to that during the Nov 02-03 storm. Compared to the Nov 02-03 storm, the magnitude of the d variation in the Nov 07-09 storm is lower by approximately $d = 0.2\ m$ (equivalent with the approximate gap between the two regression lines), with most of the data points (green dots) being found below the trend from the Nov 02-03 storm (Figure 4.9). This implies that even under the youngest waves ($u_*/c_p > 0.05$) the bubble backscatter decay within the water column is about $15 - 20\%$ steeper. This is possibly due to a less persistent wind shear stress during the Nov 07-09 storm (although the magnitude of the peak wind speed is similar to that during the Nov 02-03 storm), while, during the Nov 02-03 storm, wind speed blows steady for a longer time, so more energy is accumulated in the wave field.

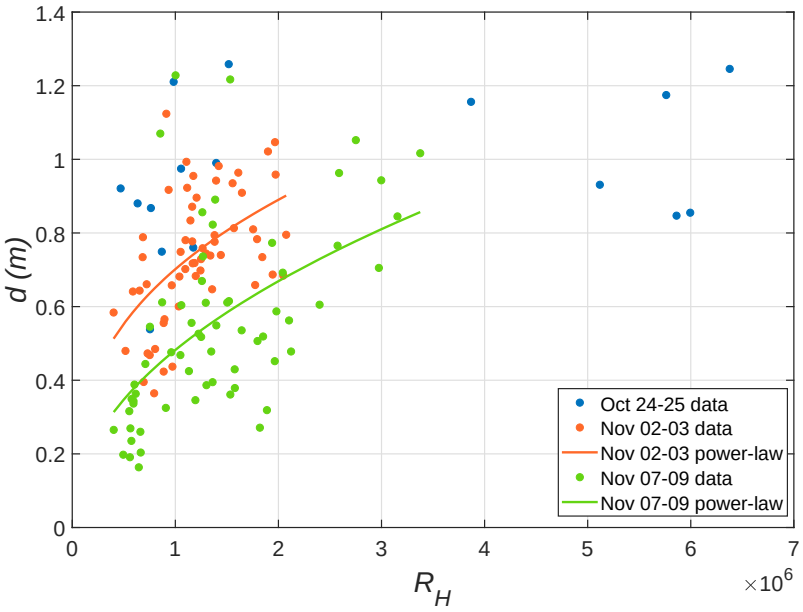

Figure 4.10: Relationship between e-folding depth, d, and wave Reynolds number, R_H, fitted by power-law models for each storm. The data points are averaged over 30 minutes. The e-folding depth data is distributed over a similar wave Reynolds number range in the Nov 02-03 and Nov 07-09 storms, but over much wider one in the Oct 24-25 storm. It it shown here that d reaches a maximum of about $1\ m$ even at the highest R_H.

The large number of missing R_H values in the Oct 24-25 storm led to sparsely distributed data points in Figure 4.10. Consequently, the variation of d with R_H does not show a clear trend that can be statistically modelled, so no least square regression was fitted. Figure 4.10 shows that d varies within the full range ($0.53\ m \leq d \leq 1.26\ m$) under waves with low R_H ($< 2 \times 10^6$), implying a very strong d variation with R_H in lower energy wind-sea. Figure 4.10 shows that the d values are capped at $1.26\ m$ even in a wave field with higher energy wind-sea waves ($R_H > 3 - 4 \times 10^6$). However, there are too few data points in such high R_H regime to generalize any capping effect. The d full recorded range, in Oct 24-25, expands much further than $1.26\ m$, but, given the limited information on R_H, the full trend of d at high R_H is not known from Figure 4.10.

In the Nov 02-03 storm, Figure 4.10 shows a more steep increase of d with growing R_H under lower energy wind-sea waves ($R_H < 1.2 \times 10^6$), and a milder increase of d at $R_H > 1.2 \times 10^6$. This relationship is fitted by this non-linear power-law:

$$d = (0.6 \pm 1.3) \times 10^{-2} R_H^{0.3 \pm 0.2}, \tag{4.7}$$

with R_H explaining about 30% of the d variance (Table 4.2). This model has a similar *RMSE* (reasonably low) to that of the models used to describe the relationships of wind speed and inverse wave age with d (Table 4.2).

Compared to Equation (4.7), a power-law with a slightly larger b parameter was fitted to capture the variation of d with R_H in the Nov 07-09 storm. This suggests a slightly lower variation in bubble backscatter decay under lower energy waves in the Nov 07-09 storm (d increases at a lower rate by less than a factor of 2 with R_H ranging from about 0.5×10^6 to 1.2×10^6). The power-law best fit for this relationship has the following form:

$$d = (0.5 \pm 1.4) \times 10^{-3} R_H^{0.5 \pm 0.2} \tag{4.8}$$

which is characterised by a correlation coefficient $R^2 = 0.32$, indicating a similar explanatory power of d variance with R_H to that recorded in the previous storm. In terms of model fitting confidence, it appears that the power-law inverse wave age and R_H dependencies of d, used in the Nov 07-09 storm, have similar *RMSE* values (Table 4.2), largely because the friction velocity, used in the definition of both sea state parameters, has a strong effect on these relationships.

From the analysis in this section, it is apparent that wind speed is a better predictor for the variation of d than both u_*/c_p and R_H given that wind speed has a relationship with both white-cap coverage (Brumer et al., 2017; Sugihara et al., 2007) and sea state. However, R_H and u_*/c_p also capture some of the variability of white-capping (Brumer et al., 2017). In particular, if the wave field statistics are fully available, Brumer et al. (2017) recommends that the R_H parameterisations of whitecap coverage should be used because they are in a closer agreement to previous studies than wind speed only parameterisations for air-sea gas transfer.

4.3.1.2 Wind-sea dependence of e-folding depth in a varying wave field

During the Oct 24-25 storm, wind-sea and swell H_s have similar magnitudes. At lower wind ($10 - 12\ m/s$), the wave field consists of the wind-driven and swell waves of about $2\ m$, while large wind-sea and swell waves (with $H_{sw} \sim 5 - 6\ m$ and $H_{ss} \sim 4 - 5\ m$) coexist at high winds ($> 20\ m/s$). For about 15 hours in the second part of Nov 02-03 storm, the sea state was also characterised by swell/wind-sea interaction, which is associated with an increase in the H_{sw} and H_{ss} variability. This wave interaction is characterised by both wind-sea and swell waves

with an average significant wave height of about $3-4\ m$ at relatively high winds ($17-18\ m/s$). The coexistence of wind-sea and swell yields a mixed sea state (Portilla et al., 2008; Wang and Hwang, 2001), which is expected because of a combination of high wind shear stress (usually driving wind-sea) and the presence of large swell. When wind-sea and swell do not coexist, but evolve separately over different time periods (their dominating periods, in terms of magnitude, do not overlap), a separated sea state is present. The first 12-hour time period and almost the entire period of the Nov 02-03 and Nov 07-09 storms, respectively, are characterised by a separated sea state.

In this section, the objective is to assess the change in the influence of H_{sw} (since wind-sea waves, rather than swell, are usually associated with wave breaking) on d during periods of mixed and separated sea state conditions. Figure 4.11a shows that d varies within its full range (from about $0.36\ m$ to $1.26\ m$) under waves with $H_{sw} < 4\ m$ in a mixed sea state. A relatively steady bubble backscatter signal (with d ranging from about $0.9\ m$ to $1.2\ m$) is associated with a wide range of H_{sw} (extending from $4\ m$ to almost $8\ m$). Although there is a steep variation of d for H_{sw} ranging from about $1\ m$ to almost $4\ m$ (Figure 4.11a), the overall relationship is characterised by a large scatter and no significant correlation exists, so no least square fit has been employed. The reason this relationship has been considered is to show the possibility of swell reducing breaking waves in mixed sea state, reducing the effect of wind-sea on bubble presence. As it has been observed in the previous sections, mixed sea state is often associated with much younger waves which, given their low development stage, are potentially associated with less significant wave breaking. In conclusion, this relationship is complex and needs further investigation, with more information needed about the effect of swell and wave development on wave breaking in particularly mixed sea state.

The contribution of wind-sea waves to the change of bubble backscatter decay rate becomes important when these wind waves are not superimposed on swell, so the situation approximates purely wind-driven waves in a separated sea state (Figure 4.11b). Therefore, the periods with the highest winds and largest H_{sw} are better matched in a separated wave field. The wind-sea dependence of bubble entrainment in a separated sea state is approximated by the relationship between e-folding depth d and H_{sw} expressed by the following power-law:

$$d = (0.29 \pm 0.08) H_{sw}^{0.68 \pm 0.23}, \tag{4.9}$$

where the best-fit uncertainty is quantified by the 95% confidence bounds, and the correlation coefficient is $R^2 = 0.33$.

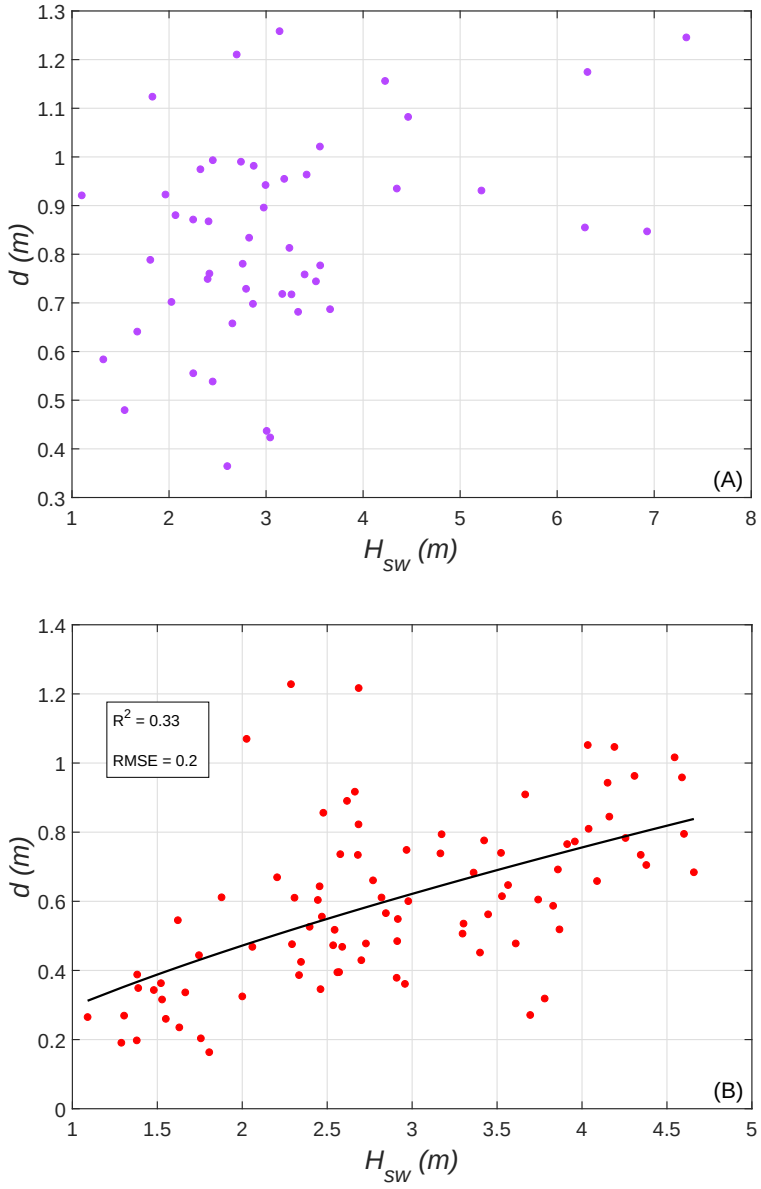

Figure 4.11: (A) Variation of e-folding depth, d, and wind sea significant wave height, H_w, during swell/wind sea interaction (mixed sea state) present in Oct 24-25 and periods during Nov 02-03 storms; due to the lack of a clear trend, no relationship between d and H_w could be fitted. (B) Variation of d with H_w during swell/wind sea separation (separated sea state) occurring in Nov 07-09 storm and periods during Nov 02-03 storm; in this case, a relationship is present, described by a power-law best-fit (solid black line).

The power-law model in Equation (4.9) generally shows a good fit (characterised by a relatively low fitting bias shown by $RMSE = 0.2\ m$), with a poorer fit at low H_{sw} ($< 2\ m$). Figure 4.11b shows that growing pure wind waves usually induce a lower backscatter decay

rate driven by a higher bubble concentration in the water column. The poorer fit at low H_{sw} is also partly influenced by some periods with the largest d variability as the wind-sea waves were growing larger, affecting the correlation and skewing the regression line.

4.4 Summary and conclusions

A backscatter threshold varying from $S_v = -58\ dB$ to $-43\ dB$ was used to quantify the shape and penetration depth of the 30-minute averaged bubble layer. This threshold permitted the filtering of the backscatter contributions from the low bubble concentrations, and is based on the correlation coefficient threshold ($R^2 = 0.8$) that delimited the best-fit of the S_v exponential decay function at each dB level. The backscatter decaying exponentially with depth in bubble plumes was previously observed in the literature, so the aim here was to test if the same variation applies in this study. Indeed, the backscatter signal in the 30-minute profiles from all three storms was shown to decrease approximately exponentially with depth, as confirmed by the average $R^2 = 0.8$ characterising the exponential decay best-fits for all profiles. This variation was quantified by a decay coefficient known as e-folding depth, which typically estimates the spatial distribution of the backscatter signal that follows an exponential trend. A low e-folding depth indicates a steep backscatter decay rate with depth. The depth range of the backscatter profiles was significantly lower in this study than in most other observations from the literature because the Delta T sonar used in this study was located at a depth of 8 metres below mean sea level. A generally lower average bubble layer penetration depth has been observed in this thesis than in previous studies from the literature. This is likely because the mooring of acoustical devices used in other studies at larger depth levels may permit a more accurate measurement of the smaller e-folding depth values during low bubble activity periods. As bubble entrainment likely increases with increasing wind speed, an increase of e-folding depth scale was also observed in the individual backscatter profiles sampled at higher wind speeds.

The averaged backscatter depth distributions were compared with averaged wind speed, inverse wave age and wave Reynolds number records in Oct 24-25, Nov 02-03 and Nov 07-09 storms. The patchy structure of the backscatter signal from the bubble layer beneath is averaged out, and the signal is continuously distributed with depth. At high winds ($> 22\ m/s$), bubble populations are injected deeper along the water column, the S_v signal in the bubble

layer was affected by strong acoustical attenuation, and the near surface bubble region (usually characterised by a stronger S_v signal due to higher bubble concentration confined in the upper metre of the ocean) could not be acoustically distinguished from the bulk bubble layer. In these extreme environmental conditions, the averaged backscatter signal from the bubble layer extends to the maximum depth recorded here of about 6 metres.

Generally, wind speed, inverse wave age and wave Reynolds number show a weak relationship with e-folding depth. However, all these environmental parameters explain less than 50% of the d variance. Although it does not provide a direct mechanism for bubble entrainment, wind speed shows the closest relationship to e-folding depth. This implies that bubble entrainment is fairly sensitive to the vertical transfer of horizontal momentum by wind shear stress. The sea state (particularly R_H) control of d is partly affected by wind-sea/swell interaction, which influences the wind-sea energy content transferred by wind, so the trend of H_{sw} changes in mixed sea state conditions. The poor correlation of H_{sw} with the variation of d in a mixed sea state is also statistically quantified, confirming the poor relationship between R_H and d in such conditions. Particularly in the Nov 02-03 storm, H_{sw} exhibits significant variation with no clear pattern during the relatively long time interval characterised by mixed sea state conditions. This indicates that there is a strong contrast between the smooth trend and high variability of H_{sw} in relatively pure wind-sea and mixed sea state conditions, respectively. The e-folding depth still shows an increasing trend (although associated with large scatter) even in a mixed wave field, indicating that a strong transfer of momentum from shear stress to a more chaotic wave field still occurs. To have a complete picture of the backscatter variability in the bubble layer, simultaneous measurements related to white-capping (breaking-wave characteristics), sea state and underwater flow fields are needed.

Although measured at similar wind speeds, the e-folding depth coefficients obtained by Vagle et al. (2010), Graham et al. (2004) and Crawford and Farmer (1987) are larger than the e-folding depth values presented in this chapter. This difference in the measurements may arise because the other authors used single-beam profiling echo-sounders, unlike the Delta T imaging multibeam sonar used here, which is a device designed for lower gain applications (targets with stronger backscatter signal), so it has a configuration with a low start gain, as opposed to the single-beam sonars. On another hand, the magnitude of e-folding depth observed by Wang et al. (2011) is closely comparable to the e-folding depth measured in this

study at similar wind speeds; Wang et al. (2011) used an acoustic Doppler current profiling sounder (ADCP), which is also characterized by a configuration with a lower start gain (similar to the Delta T sonar), so it is not designed to detect weaker backscatter signals in the water column, retrieving a steeper backscatter gradient along the water column. Other factors, not reported in the other studies, may also have a significant influence on the differences in the bubble measurements.

Chapter 5

Dynamics of individual bubble plumes

5.1 Introduction

Individual bubble plume events were extracted from the main sonar bubble layer depth signal using the plume detection algorithm described in detail in Section 3.7. The detected individual plumes have different features, such as maximum penetration depth, duration and production rate, which were used to build a plume statistics database. The change in the plume statistics under varying environmental conditions is only scarcely studied in the literature. For example, the plume production rate as a function of wind speed only was previously investigated by Anguelova and Huq (2012). Wave breaking rate in open ocean was previously observed by Kleiss and Melville (2010, 2011).

In addition to the wind speed dependence of plume production rate, the effects of sea state and wind stress on plume production rate are presented in the second part of this chapter. The influence of complex wind/wave conditions on other plume parameters, such as plume duration and maximum penetration depth, complete the statistical analysis in this chapter.

5.2 The effect of environmental conditions on bubble plume statistics

In this section, three major parameters are presented: plume maximum penetration depth, plume duration and number of plume events per hour (plume frequency), which we term the plume production rate. This plume statistics will be used to better understand the complex plume behaviour in response to changes in environmental forcing. As a reminder, the void fraction that the threshold for plume detection corresponds to is 6×10^{-8}, so plumes associated with lower values than this void fraction level are discarded.

In the first part of this section, the change of bubble plume properties is quantitatively investigated in relation to the input from wind speed and sea state. Relationships between plume statistics and environmental parameters are statistically quantified in the second part of this section.

5.2.1 Evolution of individual plumes in different environmental conditions

One of the main properties of an individual plume is its duration recorded as the time of plume presence in the sonar 10-beam field of view. The bubble plumes are injected or advected into the 10-beam sampling volume, and decay away via bubble dissolution or by being advected outside the sonar sampling volume. The plume presence in the 10-beam sampling volume can also be the result of lateral advection from neighbouring locations (Dahl and Jessup, 1995), which can affect the investigation of the local breaking-wave mechanism as a source for plume injection (see the case studies in Chapter 6). As environmental conditions become more extreme, individual plumes also penetrate to greater depths. The maximum plume depth is a point measurement of the largest depth at which an individual bubble plume penetrates. To get more meaningful plume statistics, the occurrence of plumes, together with their duration and maximum penetration depth, have been aggregated into hourly averages. Consequently, to compare against plume statistics, U_{10}, inverse wave age and R_H have been hourly averaged as well.

The highest number of plume events (487) was observed in the more extreme conditions of

Oct 24-25 storm, and significantly fewer plume events (198) were recorded during the milder conditions from Nov 07-09 storm. Also, relatively many individual plumes ($= 403$) were observed during the Nov 02-03 storm, although wind and wave peaks were only slightly higher than in the Nov 07-09 storm. However, a high wind speed and developed sea state were constantly present throughout Nov 02-03 storm. Since the plume detection algorithm could not resolve the very short plume events separated by gaps larger than the maximum allowed gap ($= 5\ s$), some events persisting for as short as $1\ s$ were found throughout all three storms. These events persist even less than the maximum allowed gap used in the plume detection, so the decision to discard events with a duration $< 5\ s$ was taken. Consequently, 85, 76 and 22 events were removed from the plume statistics corresponding the Oct 24-25, Nov 02-03 and Nov 07-09 storms, respectively. As a result, 402, 327 and 187 individual plumes are obtained for Oct 24-25, Nov 02-03 and Nov 07-09 storms, respectively. The missing wave data, discussed in Section 4.2, also reflect the gaps in the time-series of u_*/c_p and R_H shown in Figure 5.1.

The bottom plots (left to right) from Figure 5.1 show the hourly variation of all recorded individual plumes (triangles) with the associated maximum penetration depths (colour-coded) distributed on the y-axis as a function of their duration. In the first part of Oct 24-25 storm, the wind speed was moderate to high (up to about $20\ m/s$) and the reasonably well developed sea state ($u_*/c_p \sim 0.05 - 0.06$; however, only 5 hours of wave data collected in this time interval) were associated with more bubble plumes penetrating at $5-6\ m$ depths (yellow triangles in the left bottom plot from Figure 5.1), and only a few (~ 5 plumes) persisted for more than $300\ s$. At this time, a number of 31 plumes per hour has been observed. There was also a period with a lack of plume presence when the eye of the storm was present, indicated by the arrow in the bottom plot from Figure 5.1a, when the wind was lowest (down to 8 m/s), but with no information about wave development.

In Oct 24-25 storm, the rapid sea state transition (in only about two hours) from swell to highly developed young wind waves (inverse wave age increased from ~ 0.02 to 0.09), under a steeply rising wind (to $\sim 23\ m/s$), initiated a very rapid formation of longer lasting bubble plumes, at a rate increasing from 0 to 29 plume events per hour, which penetrated down to a depth of $6 - 7\ m$ (blue triangles in the left bottom plot from Figure 5.1). There was a relatively sharp decline in plume number while there was an indication of developed waves

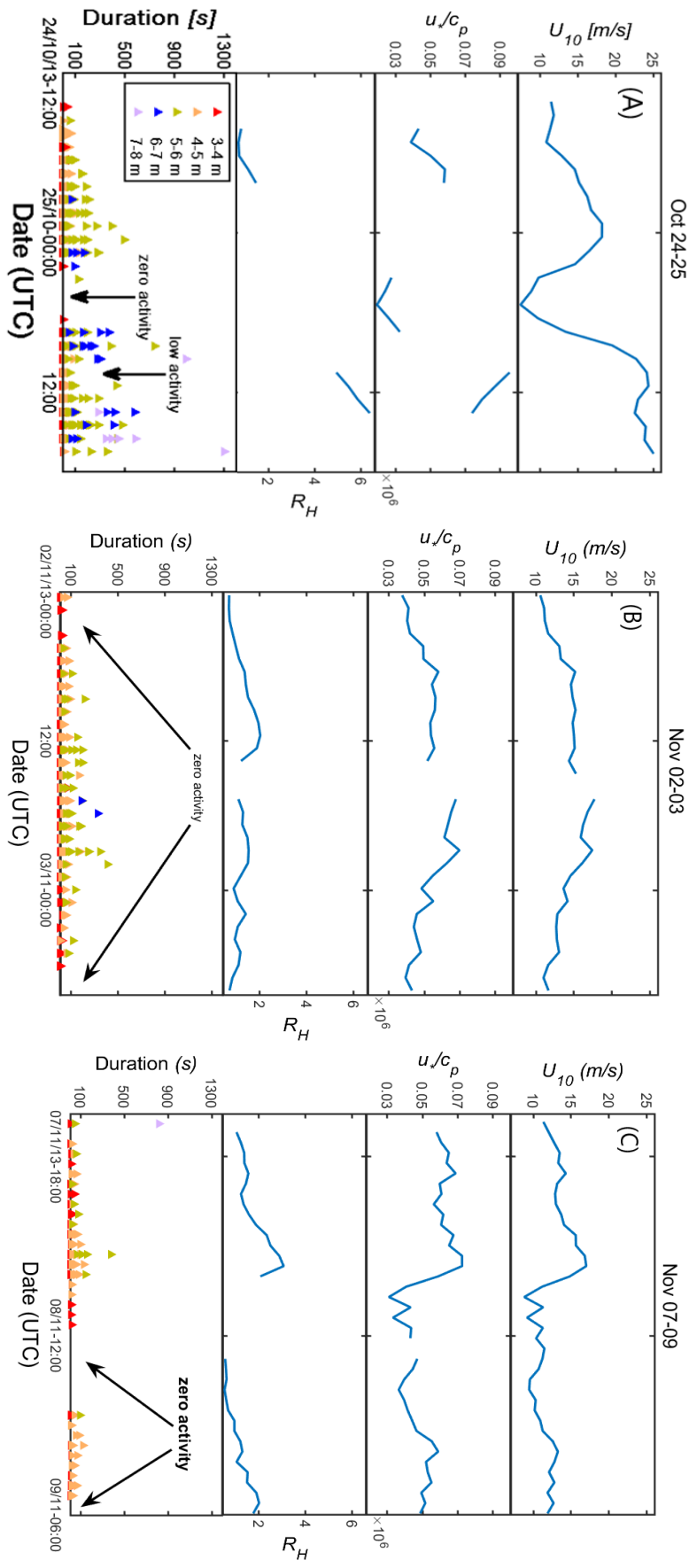

Figure 5.1: Time evolution of individual plumes with the variation of wind speed and wave parameters for all three storms; each triangle in the bottom plot represent a single plume, described by its duration (on the *y*-axis) and colour-coded by its maximum penetration depth; a larger number of triangles is linked to the production of more plumes.

($u_*/c_p \sim 0.07 - 0.08$) and the winds also remained very high (left bottom plot from Figure 5.1), but the data is only available for about two hours. In these conditions, the bubble plumes were shallower (not exceeding more than about $5\ m$), and they did not usually persist for more than $\sim 100\ s$.

Similarly to the bubble layer depth and e-folding depth, frequent bubble plumes systematically penetrating at largest depths of $6 - 8\ m$ were also observed during a period with a slightly declining sea state (u_*/c_p decreased down to about 0.07), so not in the youngest waves (note, however, that this declining trend in sea state only covers a time interval of about 3 hours, with many gaps in its evolution because of the incomplete dataset, so it is difficult to draw any clear conclusion about plume behaviour being associated with any systematic sea state decay). The values for the duration of individual plumes fall within a broader spectrum in this period, with some of the plumes persisting for more than $600\ s$, and one event was observed to persist for about $1300\ s$. Most deeper plumes tend to last longer as they probably contain smaller degassing bubbles that do not rise back at the sea surface, but remain in the water column for a longer time until they are dissolved or advected outside the sampling volume.

The milder wind speed and sea state conditions during Nov 02-03 storm generated a more uniform plume production throughout the entire period (middle bottom plot from Figure 5.1). More bubble plumes (up to $28 - 32$ per hour) gradually formed under the youngest waves observed in Nov 02-03 storm ($u_*/c_p \sim 0.05 - 0.06$), but these waves did not reach their peak energy content, being characterised by a 30% lower R_H compared to the maximum. Similarly to the Oct 24-25 storm, the variability of plume duration appears to be largest at highest winds ($17 - 18\ m/s$) and under mixing swell/wind sea waves, ranging from about $5\ s$ to a maximum of $408\ s$ per plume (reached by one plume) as shown in the middle bottom plot from Figure 5.1.

In the Nov 02-03 storm, an increased plume production occurs even under waves that show a weaker development. Likewise, the plume production can rapidly cease as the waves decay more slowly.

The Nov 07-09 storm is characterised by young waves induced by approximately pure wind-sea, which were associated with a large shear stress induced energy content (R_H reached the maximum measured here), and very low energy swell waves, so plume occurrence varied in accordance to these wave conditions. The plume production increased to $15 - 20$ plumes per hour under the young waves ($u_*/c_p \sim 0.05 - 0.06$), as shown in the right bottom plot from

Figure 5.1. In this period, the maximum depth of individual plumes was in the range of $3-5\ m$, with only a few plumes propagating deeper than $5\ m$ (right bottom plot from Figure 5.1). The plume production is very sparse in the generally less active environmental conditions from the Nov 07-09 storm. However, plume production was more than three times larger than the variation for both wind speed and wave development.

Although qualitatively the plume patterns appear to generally match environmental forcing in all three recorded storms, the large excursions of plume frequency relative to the environmental parameters show that wind speed and sea state are not the only controlling factors for the production of bubble plumes. A better understanding of the relationship between plume frequency and wave breaking characteristics, by tracing the breaking-wave source of individual plume injections, might provide further insight on plume production rate in complex environmental conditions.

5.2.2 Relationship between plume features and environmental parameters

In this section, the influence of wind speed, inverse wave age and wave Reynolds number on bubble plume statistics is investigated through statistical analysis. This consists of finding the relationship between plume properties and wind speed below waves with varying energy content (particularly wind-sea waves) and at different stages of development. The duration of plumes is important for acknowledging how much time can bubbles persist in plumes before degassing, dissolving or advecting. Therefore, the variation of plume duration with environmental parameters for different coefficients of maximum plume penetration depth has been statistically evaluated.

To conduct the statistical analysis of these interactions, the wind speed, inverse wave age, wave Reynolds number and plume parameters (maximum depth, duration and frequency) data was extracted for every event in a 1-hour period, then the data was averaged, and the hourly averaged parameters across all three recorded storms were obtained. It is important to note that any bubble plumes that are produced directly above the sampling volume and also those advected into the sampling volume are considered in the statistics, since the sonar cannot differentiate between the two types of plume occurrences.

5.2.2.1 Plume frequency dependence on wind speed and sea state

The relationship between number of plumes per hour (plume frequency, P_f) and wind speed yields a steep growth of plume production from 0 to the maximum recorded of 32 plumes/hour across a relatively narrow wind speed interval (ranging from 8.5 to 19.5 m/s) as shown by the circles in Figure 5.2.

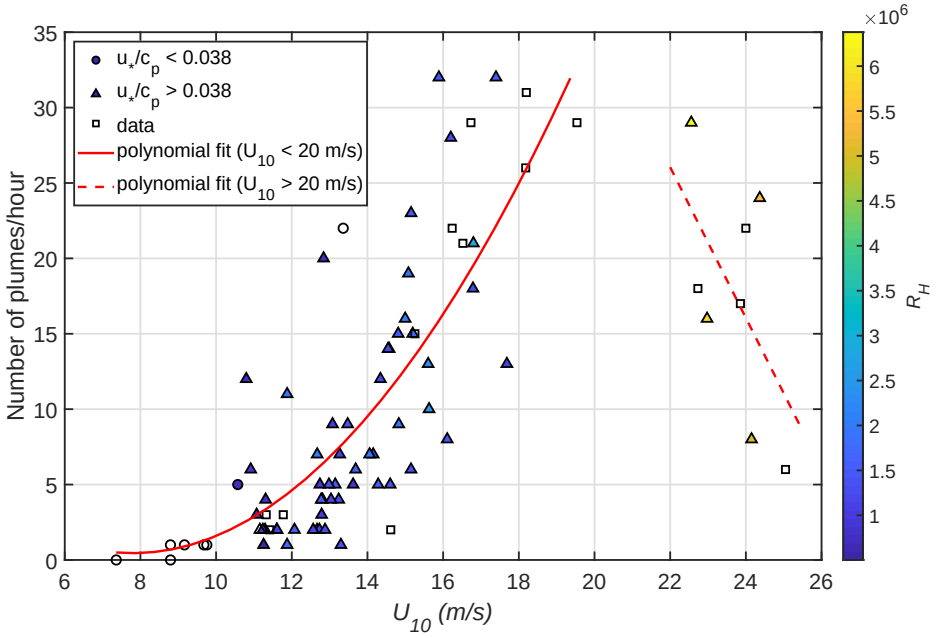

Figure 5.2: Relationship between plume production rate and wind speed, with the dots and triangles representing measurements during decaying and developing sea states, respectively; these symbols are colour-coded by values of wave Reynolds number. The red solid line is the best-fit for an increasing trend in plume production at $U_{10} < 20\ m/s$, whereas the red dashed line is the best-fit for an anomalously decreasing trend in plume production at $U_{10} > 20\ m/s$.

A wind-wave equilibrium threshold of $u_*/c_p = 0.038$ has been employed in this analysis. This threshold was suggested by Blomquist et al. (2017) for the HiWinGS campaign, and it indicates the equilibrium between wave growth and momentum transfer from wind stress. Consequently, a separation between less developed waves with $u_*/c_p < 0.038$ (below wind-wave equilibrium shown by the circles in Figure 5.2) and more developed waves with $u_*/c_p > 0.038$ is shown in Figure 5.2.

The data points which do not contain any inverse wave age information (because of missing elements in the recorded time-series) are represented by the squares in Figure 5.2. To show the influence of both u_*/c_p and R_H on plume frequency as it varies with wind speed, the data

points in Figure 5.2 are colour-coded as a function of R_H. However, because of missing R_H elements from the data set, a number of about 20 hourly data points (out of a total of 98) have not been colour-coded in Figure 5.2.

The relationship between plume frequency, P_f, and 10-metre wind speed, U_{10}, at $U_{10} < 20\ m/s$, is fitted with a quadratic polynomial (red solid line in Figure 5.2) of the form

$$P_f = 0.24\ U_{10}^2 - 3.7\ U_{10} + 15, \tag{5.1}$$

with the correlation coefficient $R^2 = 0.58$ and the uncertainty of the regression model indicated by the $RMS = 5.76$. As wind speed increases, the plume production rate has been observed to increase with higher breaking-wave frequency (Farmer et al., 1993), but clearly more information is needed to generalise the breaking-wave induced plume production since Farmer et al. (1993) retrieved a very limited number of breaking-wave frequency records. The above wind speed dependency of plume frequency is in agreement with the findings of Anguelova and Huq (2012); the only difference is the scale of plume formation. Anguelova and Huq (2012) reported that, for a time interval of 10 minutes, about 100 events occur at $10\ m/s$ wind and more than 300 at $16\ m/s$ in a long and relatively narrow water-body section (within wind-wave tank) of $120\ cm \times 70\ cm$. The very pronounced difference between the very large plume frequencies observed by Anguelova and Huq (2012) and the findings in this study could be explained by the physical scale of the detected plumes. These authors measured plumes in the wind-wave tank laboratory environment. In ocean field observations, the recorded plumes are generated by spatially larger breaking waves induced by higher winds. Also, the sea state in the real ocean is much more complex, with the frequent presence of mixed wind waves and swell, which can maintain conditions under which larger subsurface bubble populations are entrained in the upper ocean. Another possible cause could be the greater gas saturation in large storms (measured during HiWinGS campaign) that can slow the dissolution in plumes. The different measurement techniques used by these authors (they used photographic methods) could also influence the outcome. However, the range of plume frequency values obtained here is in general agreement with other field observations which revealed a similar plume production ranging between 10 and 40 plumes per hour (Trevorrow, 2003; Vagle et al., 2010).

For most of the observation period a lower plume frequency ($P_f < 10$ plumes/hour) was observed under the less developed waves ($u_*/c_p < 0.038$, circles in Figure 5.2). However,

the overall plume frequency showed a strong variation in these mature waves (from 0 to a maximum of 32 plumes/hour) at $U_{10} < 20\ m/s$. The largest plume production of $> 25 - 32$ plumes/hour was almost exclusively observed in young developing waves ($u_*/c_p > 0.038$) as shown by the triangles in Figure 5.2, taking into consideration that a notable number of high P_d records are also associated with missing inverse wave age values (empty squares in Figure 5.2). However, similarly to the mature waves, these younger waves were generally associated with a wide range of plume frequencies. Consequently, only a fairly weak inverse wave age dependence of P_f has been found for $U_{10} < 20\ m/s$ (with Pearson correlation $R = 0.54$, p-value = 10^{-4}).

The opposite trend is seen for winds $> 20\ m/s$, which corresponds to a strong decline in plume production over a wind speed range of $23 - 25\ m/s$. The plume production decayed from about 29 to only 6 events/hour over a short wind speed interval. As will be shown in one of the case studies from Section 6.2, plumes tend to merge together to become a constant background bubble field as the upper ocean begins to supersaturate under high wind stress. This plume merging could also have caused the low plume frequency at such high winds. However, no clear connection between plume duration and plume frequency was observed here (although not shown), with a Pearson correlation coefficient $R = -0.08$, indicating that plume frequency was not necessarily underestimated due to long lasting plumes or background bubble field, so the cause for this decline of plume frequency at such high winds still remains unclear. There is a negative correlation (with p-value = 0.02 significance level) between P_f and U_{10}, here fitted by a linear polynomial best-fit line (with $R^2 = 0.32$) as shown by the dashed red line in Figure 5.2,

$$P_f = -5\ U_{10} + 1.4 \times 10^2. \tag{5.2}$$

Figure 5.2 shows that, at high winds ($> 20\ m/s$), the decreasing number of plumes is associated with a young sea state ($u_*/c_p > 0.038$), at least for the time period of 4 hours during which there was available u_*/c_p information. Moreover, this steep decline of plume frequency at $U_{10} > 20\ m/s$ is also associated with a wave field containing most of the energy as shown by the highest R_H computed for this period (yellow-orange to red triangles, Figure 5.2). In the presence of waves associated with a lower R_H ($R_H < 3 \times 10^6$), there is a steady increase of plume production with growing wind speed (symbols colour-coded by shades of blue, Figure 5.2).

5.2.2.2 Plume development dependence on wind speed and sea state

In this study, the increase in wind speed is correlated with the extension of the lifetime of individual plumes (Figure 5.3). The increase of plume duration P_d with growing wind speed U_{10} is described by a linear polynomial best-fit (with $R^2 = 0.34$), which has a non-linear appearance (concave shape) on the log-log scale that is used in Figure 5.3,

$$P_d = 4.3\ U_{10} - 26, \tag{5.3}$$

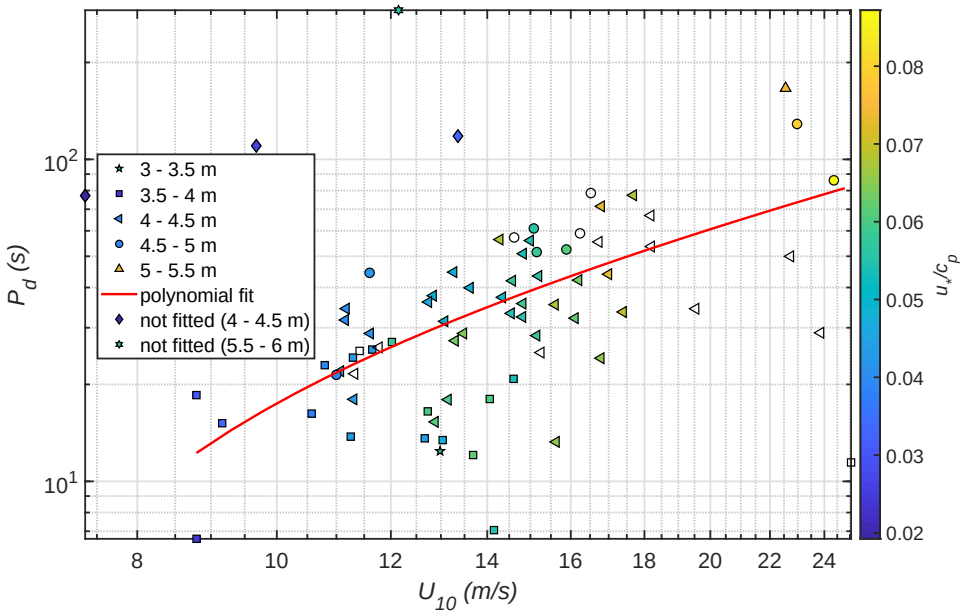

Figure 5.3: Relationship between hourly averaged P_d and U_{10}, with the different symbols in scatter plot accounting for specific maximum penetration depth intervals; these symbols are colour-coded by values of inverse wave age. The symbols that are not colour-coded indicate the lack of inverse wave age data. The red solid line is the best-fit for this data, and it is curved on a log-log scale. Four squares and one hexagram symbol are considered outliers, so they are not included in the fit. P_d shows a large variation at $U_{10} > 22\ m/s$, with strongly diverging values (these data points are split to show partly an increasing and decreasing trend).

The log-log scale is used to accommodate the large observed variation in P_d. The uncertainty of the best-fit is indicated by a $RMS = 21.12\ s$ whose magnitude is particularly influenced by the large P_d variation (from $11\ s$ to $166\ s$) at $U_{10} > 22\ m/s$, thus decreasing the overall fitting performance. There were four larger P_d values (squares and hexagram in Figure 5.3), separated from the main variation, which were treated as outliers, so they were not included in the fitting. The symbols which do not contain any inverse wave age information (because of

missing elements in the recorded time-series) are not colour-coded in Figure 5.3.

The cause for the variation in P_d values (including the outliers) could be explained by some limitations in the plume detection algorithm which may have not been able to accurately resolve some of the large variation of the duration of the bubble plumes present at the time. Another cause that could have influenced these strongly varying plume durations is the uncertainty regarding the alternating plume occurrence in the sampling volume, which can be associated with lateral advection (previously discussed in this section) of, on one hand, short, shallow bubble penetrations (close to the depth threshold) and, on the other hand, deep bubble plumes organised as a bubble field constantly present in the 10-beam sonar sample volume, but also with bubble dissolution and dissolving.

The deeper bubble plumes are more likely to last longer because they contain more smaller bubbles which may live long enough to penetrate deeper within the plume (Anguelova and Huq, 2012). They may be evolving under the influence of hydrostatic pressure and slow de-gassing and dissolution (Deane and Stokes, 2002), and they can also stabilize against further dissolution when fully coated by surface-active materials (Anguelova and Huq, 2012; Czerski, Twardowski, Zhang and Vagle, 2011). These long lasting plumes may also probably be in highly saturated seas, so they are not going to dissolve quickly. This effect may also influence some of the large plume durations present even at lower wind speeds, indicating a separated dynamics of plumes relative to the sea surface forced by wind stress.

The effect of the above mechanism is the deepening of bubble plumes as their duration increases under the influence of stronger winds. The transition from shallower (squares) to deeper (circles and triangles) plume penetration with increasing plume duration and wind speed can be observed in Figure 5.4. Trevorrow (2003) did not find a correlation between plume duration and plume depth. Trevorrow (2003) speculates that the major cause of the lack of correlation is the variation of near-surface current which can influence the advection and motion of plumes. During the HiWinGS cruise, we had the advantage of directly intercepting breaking waves upwind, thus most of the plumes were forming in the measuring range of our instruments. However, the extreme conditions at sea can generate a complex wind/wave dynamics, making the sonar observations susceptible to lateral plume advection, which could not be resolved by a very narrow horizontal sonar field of view (see more details in Section 6.2).

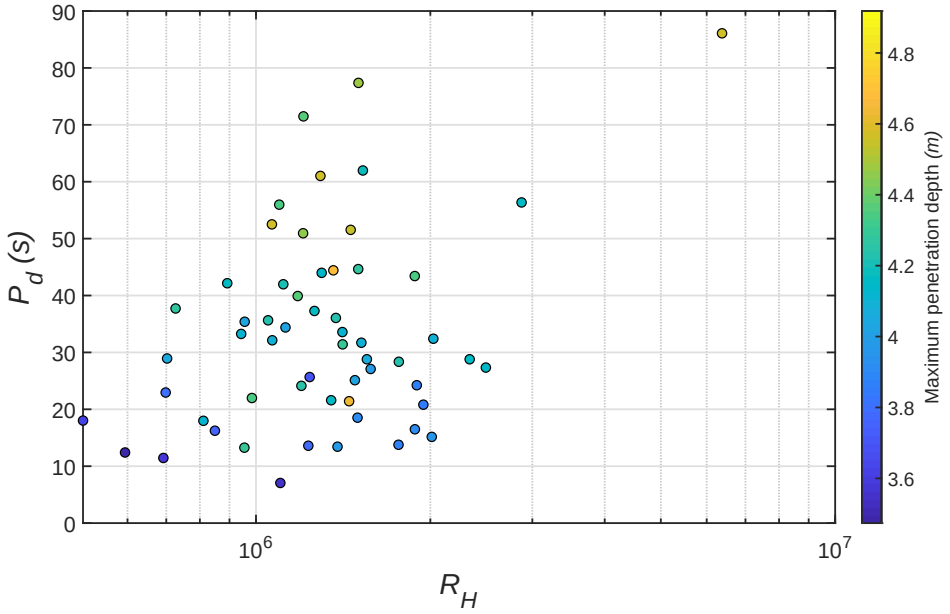

Figure 5.4: The variation of P_d with R_H colour coded by maximum plume penetration depth. The large scatter and no clear trend led to the absence of any regression model to fit this variation.

The results of increasing maximum plume depth with wind speed found here generally agree with findings reported by Thorpe (1982) and Vagle et al. (2010), who both also observed a positive relationship between wind speed and plume depth. The most persistent bubble plumes (with hourly mean durations of $\sim 86-166$ s) were encountered in young waves (yellow and orange symbols) during the Oct 24-25 storm. These young seas are associated with waves that are far from wind-wave equilibrium, with wind stress strongly forcing the waves.

The waves here, associated with longer-lasting plumes, were developing into large pure wind waves with heights of up to $5-6$ m. Also, the shallower plumes (squares in Figure 5.3, with maximum plume depth of $3.5-4$ m) are generally found under more mature waves ($u_*/c_p < 0.05$), and did not persist for more than $25-26$ s in winds below $14-15$ m/s. However, generally at winds < 20 m/s, bubble plumes penetrating deeper than $4-4.5$ m show a strong variation in duration and penetration depth with no clear dependence on wave age. This indicates that, as wind and waves tend to balance each other, wave age does not appear to have a clear control over plume development.

As shown by the large scatter in Figure 5.4, there is no significant influence of the change in R_H on P_d. Therefore, no regression model has been employed to assess the relationship between R_H and P_d. Even so, a weak increasing trend of P_d as wind-sea waves acquire more

energy can be observed in Figure 5.4, but accompanied by a highly variable P_d (ranging from about 7 s to 86 s) over a relatively narrow R_H range. Given the missing R_H elements (particularly the large values usually present at $U_{10} > 20$ m/s), the P_d variation under high-energy wind-sea waves cannot be assessed.

No clear change in maximum depth of plumes with varying R_H was observed (Figure 5.4). The large variability of both plume duration and maximum depth with varying R_H is partly caused by a lack of continuous (in time) R_H data available. Since R_H generally characterises the energy/variance of waves (wind-sea) as a response to wind stress forcing, which is a process usually occurring at the surface/near-surface level, it could be speculated plumes could be influenced by various bubble stabilising effects and subsurface deeper turbulence/currents, which are phenomena occurring separately from the surface/near-surface processes. The stronger relationship of P_d with wind speed may be influenced by both surface and deeper processes (e.g. Langmuir circulation), however the effect of the possibly coupled wind/upper ocean processes on plume dynamics has not been assessed here.

5.3 Summary and conclusions

The objective in this chapter was to assess the impact of environmental parameters on bubble plume statistics. This was achieved by examining the dependence of plume duration, maximum penetration depth and frequency on wind speed, sea state and wave-induced subsurface turbulence. At wind speed < 20 m/s, the plume frequency increases non-linearly with wind speed; a much smaller change in wind speed above the mean (with 10% to 20%) is required to induce a very steep growth from 0 to a maximum of 32 plumes/hour, so clearly wind speed only cannot explain the variability of plume occurrence. Although plume frequency showed a strong variation (from 0 to 22 plumes/hour) with inverse wave age, the largest number of plume events was exclusively recorded in young developing waves ($u_*/c_p > 0.038$) at a wind speed close to 20 m/s. At a wind speed > 22 m/s, a notable decline in plume production rate to only 8 plumes/hour was observed while wind speed had a relatively steady evolution. As in the case of a shallower bubble penetration, this less frequent plume production at high winds is associated with the presence of the youngest waves recorded here ($u_*/c_p \sim 0.07 - 0.08$).

As individual plumes develop and become more mature, they may also contain relatively

more smaller bubbles which tend to live long enough to penetrate deeper, so it was found here that the maximum penetration depth of plumes gradually increases with plume duration. The wind-sea wave energy as a response to wind stress, represented by R_H, was not found to be connected to the varying persistence of bubble plumes. Plume duration was also likely affected by nearby bubble populations advecting into the sonar sampling volume over pre-existing plumes, as some more persisting plumes were observed here. Among all wind/wave parameters, generally the wind speed dependence of plume development (duration and maximum penetration depth) and production rate is the most significant, although even wind speed can only explain about half of the variation in plume dynamics.

Chapter 6

Individual breaking waves and bubble plumes

6.1 Introduction

The main aim of this chapter is a comparison between individual breaking waves and subsequent bubble-plume formation. A potential relationship of whitecap fraction with hourly-averaged backscatter signal variation in the uppermost metre of the ocean and within the full water column (exponential variation of the backscatter signal estimated by e-folding depth) is investigated. It combines observations of individual local breaking waves at the sea surface recorded by the foam camera with the bubble properties detected by the sonar. The difficulty in quantifying the initiation of a bubble plume when a breaking wave occurs above a pre-existing bubble plume is also discussed.

The breaking waves capture by the foam camera at a distance of approximately 2–3 meters away. This is within the range that includes the footprint of the sonar 10-beam subdomain, so the sonar sampling volume was approximately below the breaking waves. This permits a direct comparison between the breaking wave and subsurface bubbles. The foam camera has an estimated field of view of approximately $4 - 5\ m^2$. Yet the horizontal range of the 10-beam subdomain is only about $1.4\ m$, so it only covers a fraction of the observed wave-breaking area (also depends on the size of breaking). The goal in this chapter is to investigate the subsequent generation of plumes by breaking waves, not necessarily during active breaking.

Breaking waves are a transient phenomena. For a direct comparison, high temporal resolution subsurface bubble measurements are needed to track the evolution of a bubble plume from a local breaking wave. Consequently, the bubble plumes in the sonar vertical sections here were sampled at the maximum temporal resolution (6 *Hz* ping rate). At this high sampling frequency, the backscatter signal reveals that the subsurface bubbles are organized in discrete patches, as will be shown in the case studies to follow in Section 6.2. The appearance of this feature in the sonar matrix was also discussed in chapter 3.

The approach of Callaghan et al. (2013) can be to extract active breaking wave from foam camera images, and avoid contamination with transient glint (the specular reflection of light from the water surface). After the glint removal procedure, the wave-breaking crest exceeds a pixel intensity (brightness) threshold (Callaghan et al., 2013). This signal extraction allows the construction of various breaking crest statistics by tracking the crest from one image to the next. More specifically, the intersection of the leading edge of the intensity signal with the threshold (and not the leading peak) is tracked to determine the speed and direction of the breaker (Callaghan et al., 2013). Unfortunately, this intensity thresholding technique could not be applied in this research because the raw images of the breaking-wave events in the foam camera were contaminated by strong brightness from the sky.

In Section 6.4, the hourly averaged uppermost metre S_v signal and e-folding depth were compared with the hourly averaged total whitecap fraction. From these comparisons, the influence of whitecap fraction on bubble scattering and entrainment in the shallow and full water column can be assessed. The whitecap fraction was extracted by our collaborators from Lamont Doherty Earth Observatory (Columbia University) through video analysis using an imaging system which consisted of two obliquely angled Imperx model Lynx 1M48 digital video cameras, with a sensing array of 1000×1000 elements of 7.4 μm in size (Brumer et al., 2017). These cameras were mounted on the flying bridge of the R/V Knorr ship at a height of 14.7 meters above the water line. For these measurements lenses with a wide field of view (68.7°) were used with a 6-*mm* focal length (Brumer et al., 2017).

6.2 Individual breaking waves and subsurface bubbles

Four case studies of breaking waves/foam patches were selected to represent a range of situations where subsurface bubbles are present simultaneously in the water column. The wind speed and wave state conditions for all four case studies are summarised in Table 6.1.

Case study 1 is the simplest case, where a shallow bubble plume develops from a local breaking wave. During the event from this case study, the wave field was characterized by 3-metre wind sea waves superimposed on a 3.2-metre swell. These wave conditions were accompanied by a steady wind speed of about 18 m/s.

Case study 2 presents a breaking wave event that is thought to form a deep bubble plume. The initial evolution is similar to that of case study 1, yet the bubble layer penetrates deeper to form a fully-developed plume. The breaking-wave and subsequent bubble injection conditions from this case study were driven by a mixed sea state with large wind sea waves $3.5\ m$ superimposed on a large swell $4\ m$. The wind speed during this event was steady and close to the maximum recorded value during the Nov 02-03 storm of about $15-16\ m/s$.

Case study 3 describes the evolution of a persistent bubble plume initiated by a large breaking wave (its foam patch area covers almost the camera's entire field of view). The impact of three following breaking waves occurring above the already formed bubble plume are also investigated. During the time interval from this case study, large wind-driven waves with a height of about 5.5 metres were riding on swell waves of about 5 metres in height. Steady winds dominated here, reaching the maximum value recorded during the cruise (about 27 m/s).

Case study 4 describes a local breaking wave occurring above a preexisting bubble plume. The plume was likely triggered by nearby wave breaking (not detected by the foam camera) and advected into the sonar sample volume. The sea state during the time interval of this case study was dominated by wind-sea waves with an amplitude of about 3.7 metres and superimposed on a 2-metre swell. The wind speed driving the surface short waves was quite high, reaching about 17 m/s, in a steady phase.

Table 6.1: Conditions of wind speed U_{10} (rising, falling or steady), wind sea significant wave height H_{sw} and swell significant wave height H_{ss} for all four case studies.

Case study	U_{10} (m/s)	H_{sw} (m)	H_{ss} (m)
1	18	3	3.2
2	15	3.5	4
3	27	5.5	5
4	17	4	2

6.2.1 Case study 1: bubble plume evolution from a local wave breaking wave

The breaking wave event described here was recorded from 18:10:22 to 18:10:29 on Nov 02. This event is presented as a sequence of seven foam camera images that show the evolution of the breaking wave for seven seconds (Figure 6.1). The first image presents the moment of breaking, which occurs in the first second or so, and the following images show the post-breaking stage of the generated foam patch.

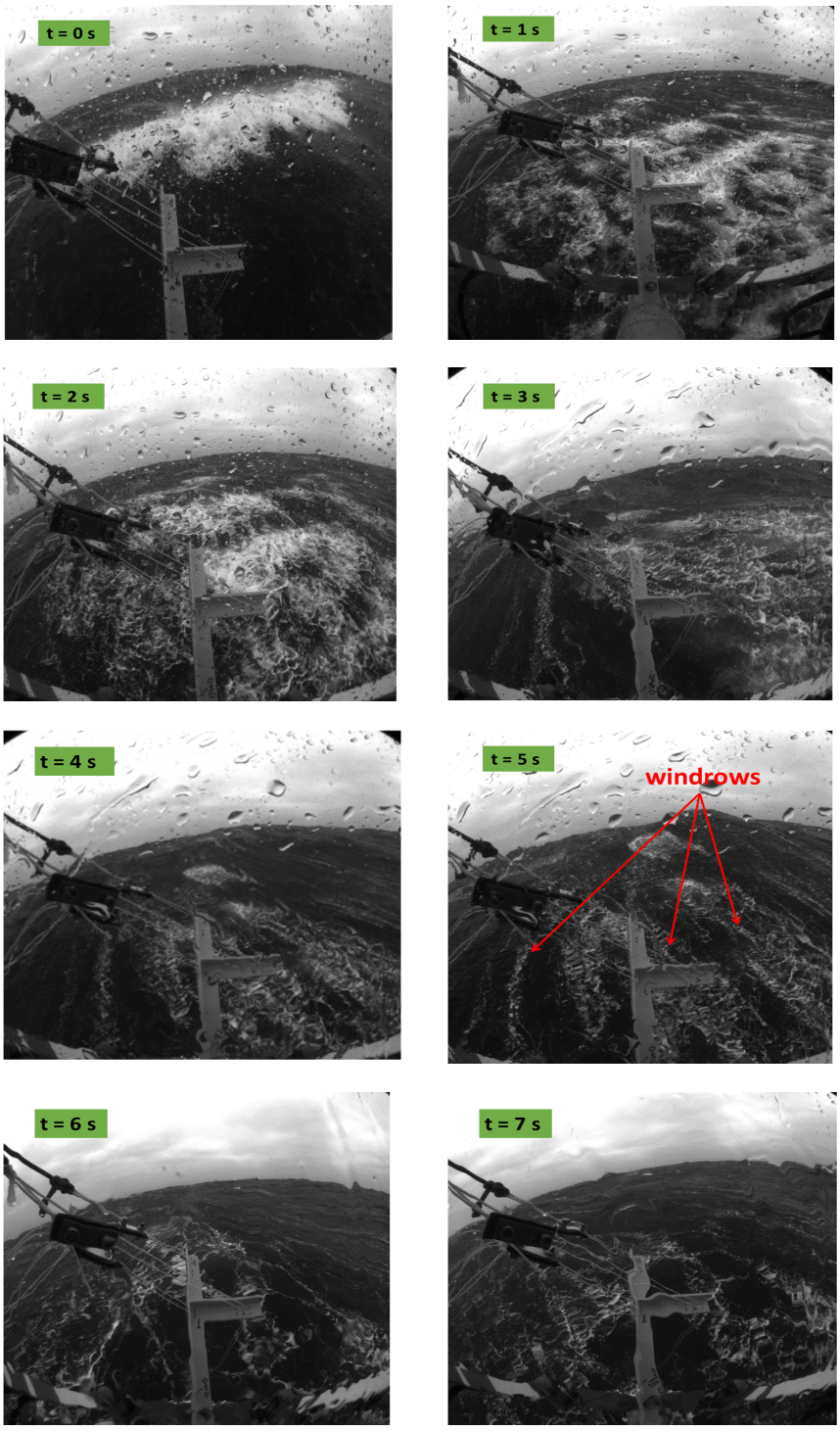

Figure 6.1: Sequence of images of a breaking wave event recorded for seven seconds in case study 1. The time step between the images is one second. Windrows are identified by the red arrows.

Wave breaking induces dissipation of turbulent kinetic energy (Lamarre and Melville, 1991; Melville, 1993; Terray et al., 1995). Up to 40% of the pre-breaking wave energy can be lost through breaking, and 30–50% of this energy is used to entrain the highly dense initial shallow bubble plume (Lamarre and Melville, 1991). However, in this case study no dense plumes

have been tracked.

Shown in this chapter are local observations of plumes evolving from the breaking onset to a stage where they are fully-developed/mature. This provides insight on the larger scale dynamics of bubble plumes, which is compared to the evolution of concomitant breaking waves, since bubbles contained in these fully-developed plumes are in general remnants of the initially injected dense bubble plumes during strong wave-breaking induced turbulence.

The sonar matrix for case study 1 is shown as Figure 6.2. The onset of the breaking wave event is indicated in the sonar matrix by the red dashed vertical line (Figure 6.2), and corresponds to the image at $t = 0\ s$ (Figure 6.1). The sonar matrix during a time period of about 17 seconds prior to the breaking point shows that there was no deep bubble entrainment in the water column, so the development of a bubble plume after the breaking point is the result of a local breaking wave.

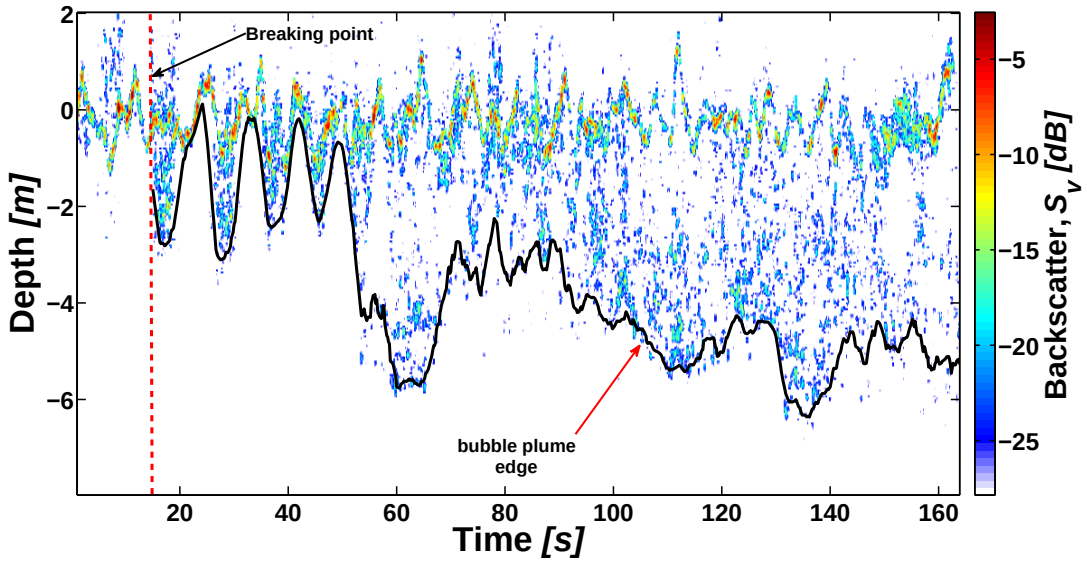

Figure 6.2: A sonar time-series showing the evolution of a bubble plume from a local breaking wave (indicated by the dashed vertical red line). The vertical axis shows the depth distribution, relative to the mean sea level, of the backscatter signal from the waves and subsurface bubbles; the zero value indicates the mean sea level, the negative values are the depths below mean sea level, and the positive values are the amplitude of the waves above mean sea level.The base of the plume is indicated by the black contour line.

The sonar matrix from this event shows the gradual development of a bubble plume with time after the onset of the wave breaking (Figure 6.2). This bubble plume likely formed as a

result of this breaking wave, considering that the plume is actually initiated at a relatively short time after the breaking point (Figure 6.2). There is some uncertainty involved, because the plume could have also advected into the sampling volume from surroundings. However as the plume shows a clear development from a shallow to a deep phase, so an initiation at the breaking point appears as a logical proposition.

The shallow bubble layer appears to oscillate with the surface waves before it starts deepening Figure 6.2. This means that the kinematics of the shallow bubble layer might be dominated by orbital motion of surface gravity waves. A similar observation of a shallow bubble layer controlled by wave orbital motion is reported by Dahl and Jessup (1995), where a downward bubble entrainment velocity of $\sim 1\ m/s$ was estimated from a sonar using a Doppler technique. The largest oscillations from wave orbital motion are close to the sea surface, and they become smaller with depth. It can be observed that the penetration of these bubbles within the shallow bubble layer is double that of the oscillating waves (as shown by the sea surface displacements relative to the spar buoy), reaching down to about 2.6 meters on average (Figure 6.2a).

In the study of Dahl and Jessup (1995), the bubbles entrained downward by wave orbital motion have a penetration depth approximately equal to the wave amplitude. The oscillatory bubble layer during the first 30 seconds in case study 1 (Figure 6.2) has the appearance of an alternating existence followed by disappearance of bubbles after wave breaking (the bubble layer is present approximately below wave troughs, but apparently disappears below wave crests). This effect may be a sampling artefact or could be explained by a combination between wave orbital motion and advection. More specifically, lateral advection could have occurred during the wave orbital cycle below wave crests, or stronger surface currents could have affected (via directional shearing or shallow advection) the bubble kinematics below wave crests.

After about 28 seconds, the bubble plume starts to deepen with time, reaching two depth maxima of 5.7 and 6.3 metres, respectively, about 42 and 116 seconds after the start of the event (Figure 6.2). The plume evolution is described in this case study for 147 seconds, because the arrival of a new breaking wave may have interfered with the pre-existent plume. A similar case study of simultaneous images of a breaking wave event and a subsurface bubble plume was discussed by Dahl and Jessup (1995). In that instance the bubble plume also penetrated down to about 4 meters from an initial shallow bubble layer; the entire plume de-

velopment, following the breaking wave, was observed for 75 seconds.

As time progresses, the deep fully formed bubble plume becomes disconnected from the wave orbital motion. This plume is likely driven by turbulent water motions possibly associated with Langmuir circulation (Li et al., 2013; Zedel and Farmer, 1991). The axis of the Langmuir circulation is parallel to wind direction, whereas the axis of the wave orbital circulation is perpendicular to wind direction, and the Langmuir circulation can transport bubbles at deeper levels. The possible signature of Langmuir circulation during the event from case study 1 is highlighted by the presence of windrows (foam bands) at the sea surface, which are visible in the foam images from $t = 4\ s$ onwards (Figure 6.1). These windrows could be the result of convergent flow from subsurface counter-rotating eddies formed when wind constantly blows over the sea surface The Langmuir circulation was also associated with deeper penetrating bubble plumes in the open ocean in several studies, e.g. see the work of Farmer et al. (1993) and Zedel and Farmer (1991).

6.2.2 Case study 2: breaking wave associated with a more slowly developing deep plume

This section describes the time progression of a gradually deepening bubble plume in response to a breaking wave. The evolution of a large breaking wave for a time interval of 16 seconds is shown in Figure 6.3. The resulting foam patch takes over 14 seconds to decay (Figure 6.3).

The sonar matrix in Figure 6.4 shows the evolution of the bubble layer bottom (highlighted by the black contour) during the breaking wave event. The bubble layer evolves for about two and a half minutes as a deep, mature bubble plume is formed from an initial shallow bubble layer. The deepening evolution of the bubble layer is similar to the one in case study 1, as it also begins from an initial shallow bubble layer, progressively penetrating deeper in time. In this case, however, the shallow bubble layer is present even before the onset of breaking. This suggests that the bubbles initially present in the water column did not result from the breaking wave. Another difference from case study 1 is that here the initial shallow bubble layer is not characterised by large vertical oscillations below the wave troughs (Figure 6.4). In this case, the bubble layer shows a relatively weak variability, so it does not appear to be influenced by

the wave orbital motions/oscillations on the shallow bubble layer.

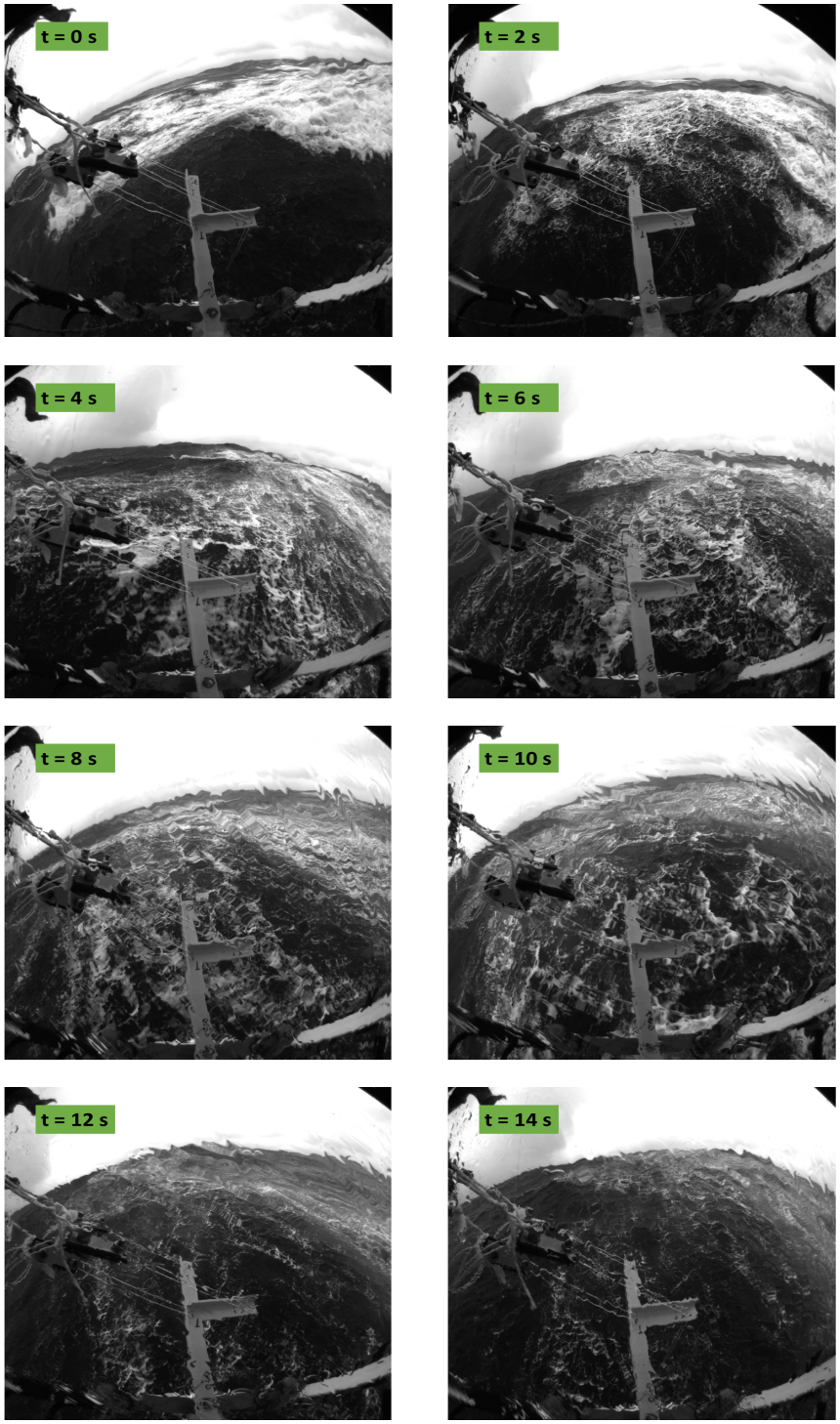

Figure 6.3: Sequence of images of a breaking wave event recorded for 14 seconds in case study 2. The time step between the images is 2 seconds. Note that most of the active breaking occurs before the wave crest reaches the sonar.

The deepening of the bubble layer begins approximately 15–20 seconds after the onset of breaking, and it penetrates down to about 5 metres (Figure 6.4). This first part of the deepening

process persists for about 70 seconds. In the next 85 seconds, the bubble layer penetration was characterised by a stronger variability, but eventually the bubbles penetrated down to a maximum depth of about 6 metres (Figure 6.4). A weaker and sparser backscatter signal can be observed in the last 85 seconds of the bubble deepening evolution (Figure 6.4), indicating that the bubble layer becomes less dense as it deepens.

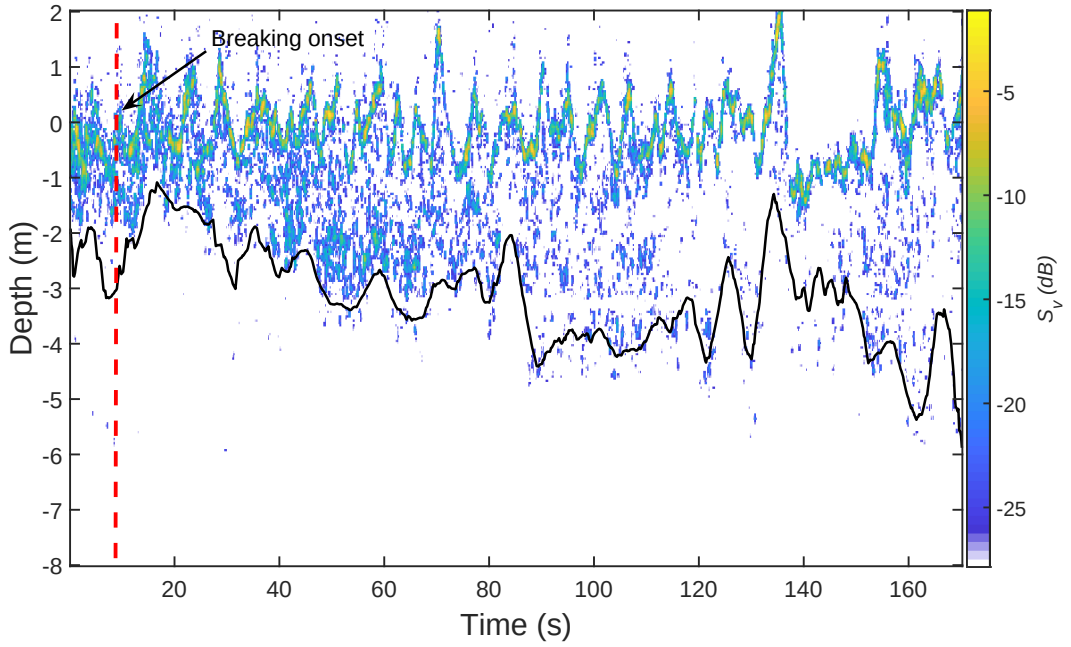

Figure 6.4: The sonar matrix from case study 2 showing a bubble plume progressing with respect to a local breaking wave (the breaking onset is indicated by the dashed vertical red line). The vertical axis shows the depth distribution, relative to the mean sea level, of the backscatter signal from the waves and subsurface bubbles; the zero value indicates the mean sea level, the negative values are the depths below mean sea level, and the positive values are the amplitude of the waves above mean sea level.

Given the cases of deep plume formation from an initial breaking wave discussed here, and other similar cases reported by Dahl and Jessup (1995); Farmer et al. (1993); Zedel and Farmer (1991), it appears that the breaking wave injects an initial high volume of bubbles/gas into the shallow ocean layer in the first metre or so (Deane, 2016). The deepening of plumes is driven by turbulence and bubble degassing (Deane and Stokes, 2002).

6.2.3 Case study 3: persistent bubble plume and multiple wave breaking

This section describes the evolution of a bubble plume with simultaneously occurring breaking waves.

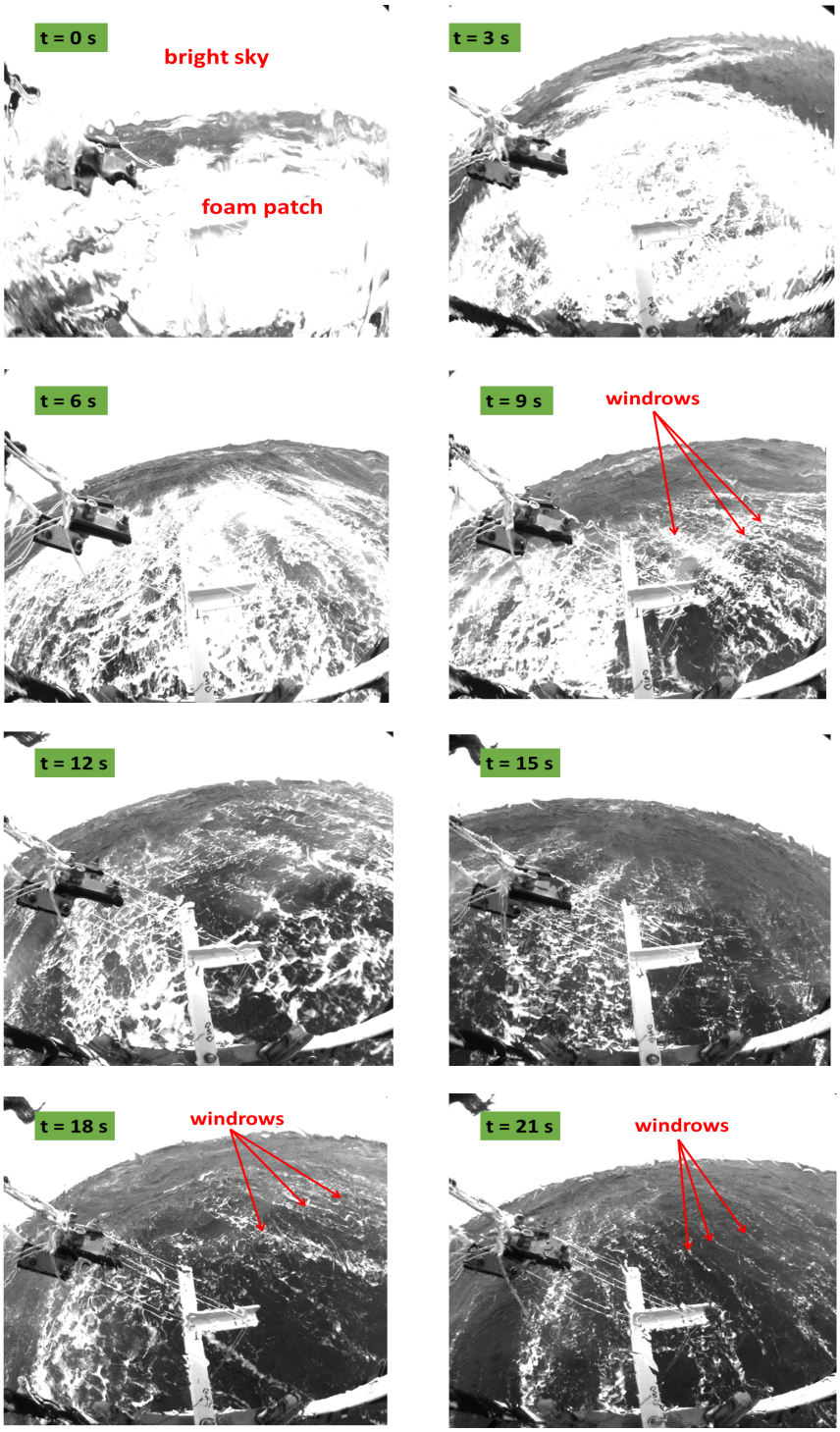

Figure 6.5: Foam camera images for case study 3 and separated by a time step of 3 seconds.

Comparing to case study 2, which was not entirely observed because of a secondary breaking wave occurrence, this bubble plume was recorded from its start to the end, despite three breaking waves following the initial breaker.

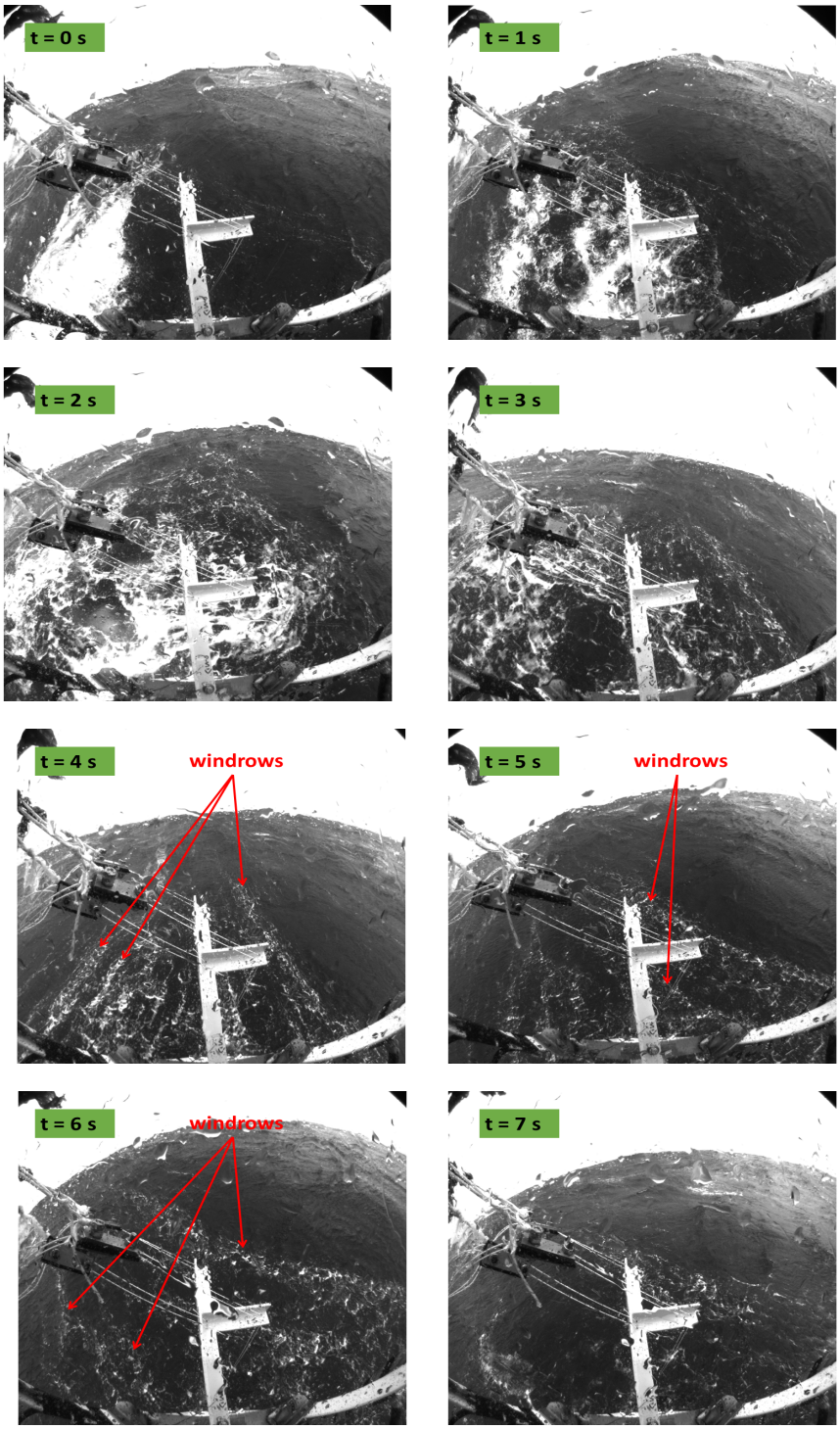

Figure 6.6: Breaker 2 for case study 3 recorded for 7 seconds as shown by the sequence of images separated by a time step of 1 second.

Each breaking wave is described by a sequence of images generated by the foam camera, starting with the first sequence that shows the evolution of the initial breaker (Figure 6.5). The second Figure 6.6, third Figure 6.7 and fourth Figure 6.8 breaking wave events occurred directly above the already formed bubble plume, as shown in the sonar matrix (Figure 6.9).

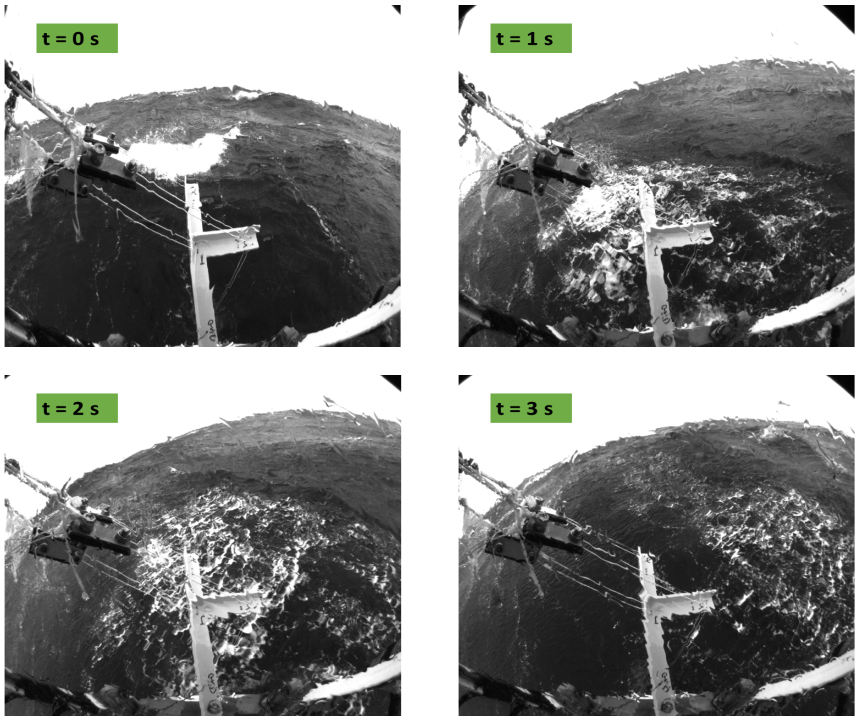

Figure 6.7: Breaker 3 from case study 3 recorded for 3 seconds as shown by the sequence of images separated by a time step of 1 second.

As it was difficult to visually depict the breaking initiation moment, the images were contaminated by a strong light from the bright sky and the foam patch from the breaking wave almost covered the entire foam camera's field of view. The image at $t = 0\ s$ represents the first frame in which foam patch is definitely identified and falls immediately after breaking. The time stamp of the rest of the images in each sequence is imprinted on the images.

No deep bubble plume was observed in the water column prior to the initial breaking wave (Figure 6.9). The subsequently formed breaking waves (breakers 2, 3 and 4) do not have a visible impact on the deep bubble plume below. These breakers are much smaller than the initial extensive breaker, with its foam patch covering almost the entire camera field of view (compare Figure 6.5 with Figures 6.6 and 6.8).

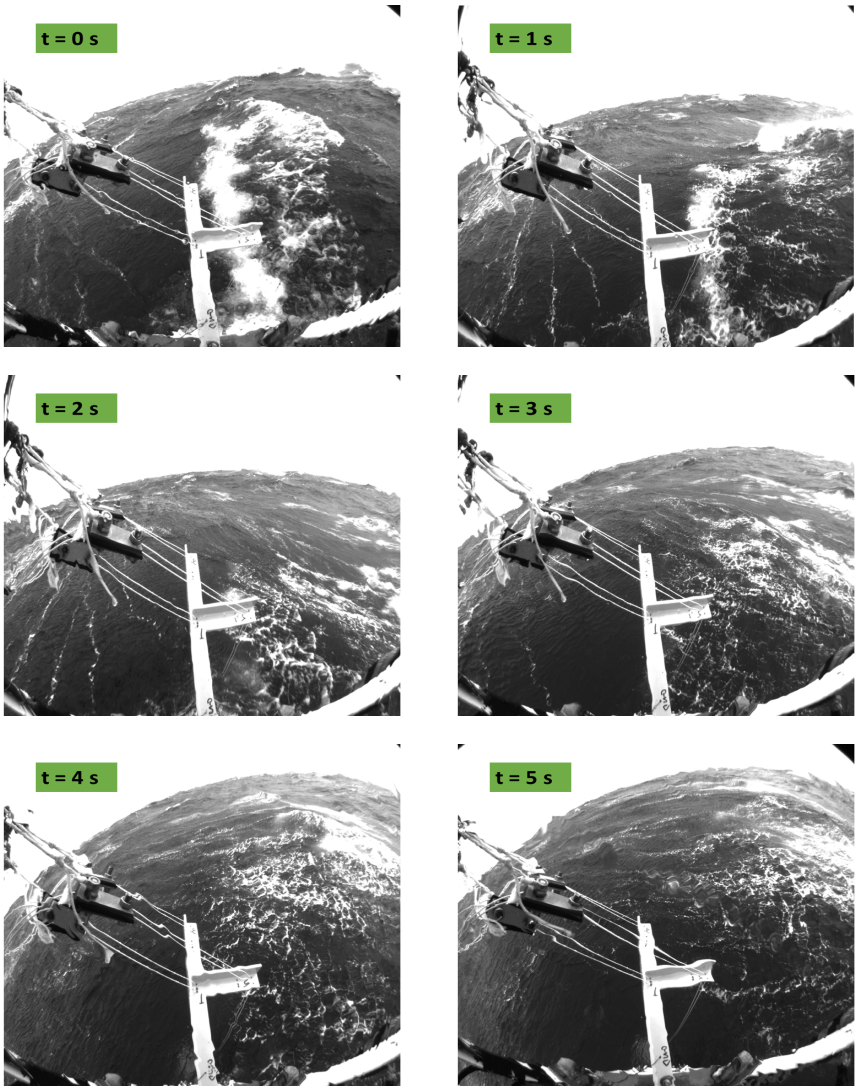

Figure 6.8: Breaker 4 for case study 3 recorded for 5 seconds as shown by the sequence of images separated by a time step of 1 second. Some windrows can be seen, particularly in the images at $t = 2\ s$.

Considering the large magnitude and persistence of breaker 1, the images in Figure 6.5 show the evolution of breaker 1 for 21 seconds. Breaker 2 was breaking from the lateral (from left to right relative to the camera field of view), and it occurred about 86 seconds after the onset of breaker 1, being observed for 7 seconds Figure 6.6.

Breaker 3 was a relatively small event, and it occurred about 117 seconds after the breaking point of breaker 1. It was recorded for only 3 seconds, as it was advected quite rapidly out of camera field of view (Figure 6.7). Breaker 4 propagates from the lateral, and occurs almost 260 seconds after the starting point of breaker 1 toward the end of the time interval. The foam patch from this breaker was mostly present in the lateral (on the right hand side of the Foam Camera images sampled at each second). Breaker 4 was observed for only 5 seconds as it

also was rapidly advected from the camera field of view (Figure 6.8).

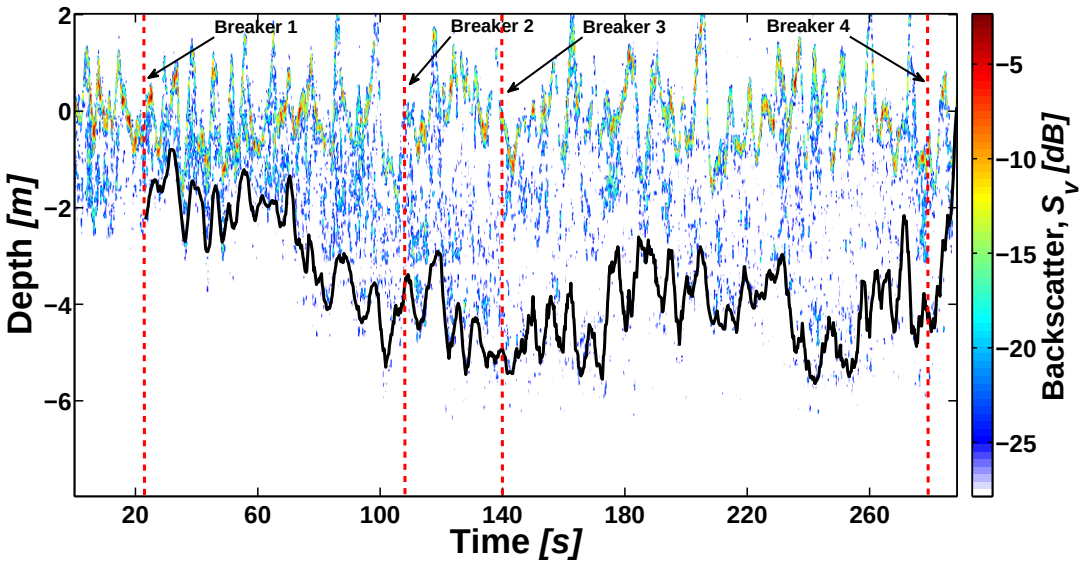

Figure 6.9: A sonar profile showing the evolution of a bubble plume from the very large breaker 1 (the foam patch formed immediately after breaking onset is indicated by a dashed red vertical line). The sonar matrix during a time period of about 23 seconds prior to the breaking point shows that there was no deep bubble entrainment in the water column, so the development of a bubble plume after breaker 1 is considered to be the result of a local breaking wave. Other 3 subsequent breaking waves are indicated by dashed red vertical lines, as breakers 2, 3 and 4 (shown in Figures 6.5 to 6.8). The vertical axis shows the depth distribution, relative to the mean sea level, of the backscatter signal from the waves and subsurface bubbles; the zero value indicates the mean sea level, the negative values are the depths below mean sea level, and the positive values are the amplitude of the waves above mean sea level. This event was sampled during the Oct 24-25 storm, at the highest recorded winds of 27 m/s.

The different directions these waves are travelling highlights the difficulty of recording in this kind of situation.

Immediately after the onset of breaker 1, a shallow bubble layer is present for just less than a minute. A bubble plume gradually develops over time from the shallow bubble layer, reaching to a maximum depth of 5.8 meters about 108 seconds after the start of the breaking wave event (Figure 6.9). This bubble plume takes longer to fully develop than the plume in case study 1–lasting for almost five minutes.

Prior to the development of the deep plume, the wave orbital circulation appears to control the depth variation of the shallow bubble layer, as seen in case study 1. As it oscillates with the surface waves, the shallow bubble layer penetrates to an average of 2.8 metres. This

is roughly double the wave amplitude (peak-to-peak) recorded by the sonar (note that differs from the significant wave height discussed earlier in this thesis, and this is just a relative sonar measurement of the spar buoy's position relative to the water line). The magnitude of these oscillations is about one metre larger on average than in case study 1 Figure 6.2. This is possibly caused by the large swell propagating during this event (see Table 6.1).

The depth of the fully formed bubble plume is not uniform in time, but decreases slightly in the time interval $150-220$ seconds (Figure 6.9). This may be caused by smaller scale turbulent eddies that do not advect bubbles so deeply.

In the last 60-second time interval of the event, the plume penetrated even deeper to about 5 metres depth, after which it gradually shoaled to less than 2 metre depth (Figure 6.9). It is not clear whether this is because of bubble dissolution and degassing or as an effect of plume advection out of the sonar sample volume. Breaker 4 also occurred at the end of this event, as the plume penetration was decreasing. However, this breaker rapidly passed across the sonar 10-beam footprint – with the associated whitecap shortly persisting quite far on the right hand-side of the camera field of view (see Foam Camera images in Figure 6.8) – so the possible effect of bubble injection likely did not have occurred in the water column within the sonar sample volume.

The secondary breaking events may reinforce the bubble plume, contributing to its persistence. This suggestion is motivated by observations of long periods with high bubble densities as an effect of multiple wave breaking conducted by Farmer et al. (2001), which continuously replenishes the bubble field, e.g. see the work of (Monahan, 1993) and Dahl and Jessup (1995).

6.2.4 Case study 4: local wave breaking above a pre-existing bubble plume

A single breaking wave occurring above a pre-existing bubble field is presented here, with four different stages of its evolution being captured along a time interval of 9 seconds (Figure 6.10) from 12:18:42 to 12:18:51 on Nov 02. The first stage describes the moment of wave breaking (at initial time $t = 0\ s$), which lasted about $1-2\ s$, followed by the post-breaking stages of the generated foam patch at $t = 2\ s$, $t = 4\ s$ and $t = 9\ s$ (Figure 6.10). The simultaneous presence

of a deep bubble plume was also observed, as shown in the sonar matrix from Figure 6.11. The bubble plume entered the sonar field of view about 53 seconds before the wave breaking started, and persisted for about 136 s (Figure 6.11) from 12:17:48 to 12:21:18 on Nov 02. The breaking wave occurs approximately above this pre-existing bubble plume. The initiation of this bubble plume is not connected to the breaking wave observed above, but it is likely the result of nearby wave breaking, and it is eventually advected into the beam sample volume.

The next stage is shown after two seconds at $t = 2\ s$ and it is described by a fully formed foam patch roughly delimited from the darker ocean by a red solid contour curve. The main foam patch does not appear like a continuous white coverage, but it has the appearance of discrete smaller foam patches (Figure 6.10). The plume below reached a depth of $5\ m$ (Figure 6.11). It is possible that the pre-existing bubble plume masks bubble injection from the breaking wave occurring above (Farmer et al., 2001).

A well defined foam patch continues to persist after 4 seconds Figure 6.10. The plume penetrated at about $4\ m$ relative to the instantaneous sea surface below the foam patch at that time. The foam patch finally lost definition and decayed after 9 seconds (at $t = 9\ s$).

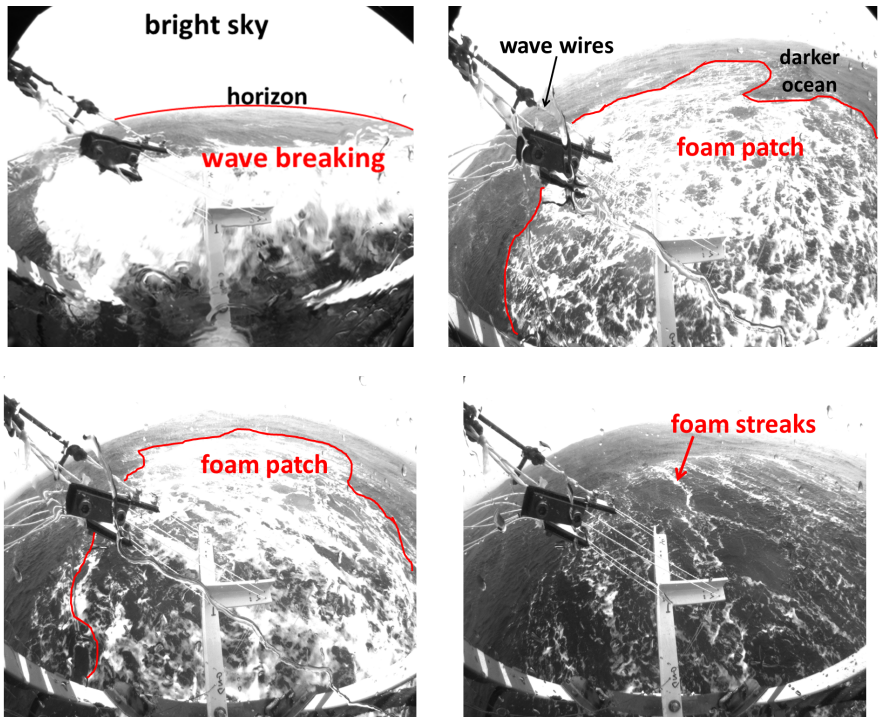

Figure 6.10: Case study 4 with a sequence of images of a breaking wave event recorded for 9 seconds. The time stamps on images are $t = 0\ s$, $t = 2\ s$, $t = 4\ s$ and $t = 9\ s$.

The advection of bubbles in and out of the sonar sample volume necessitates measure-

ments of both vertical and horizontal bubble velocities in the water column, which can be obtained using a Doppler echo-sounder – see the work of Dahl and Jessup (1995) and Wang et al. (2011). Unfortunately, one was not available during our research cruise. The plume eventually vanishes, and it is not clear whether through advection or bubble dissolution. Understanding the latter processes requires knowledge about bubble lifetime at different depths (bubbles of different sizes) and in different oceanic conditions in terms of the stabilizing surface-active material (surfactants) content.

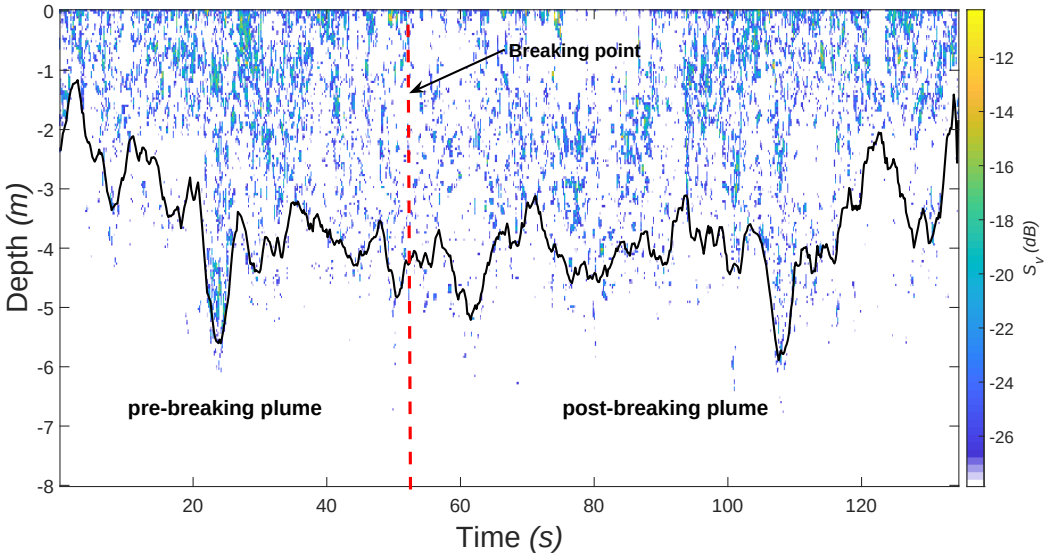

Figure 6.11: A sonar matrix showing an emerging persistent bubble plume relative to the instantaneous sea surface. This plume is not initiated by the breaking wave occurring above; the cause of initiation could not be detected from the present evidence. The local breaking wave, superimposed on the already formed plume, is indicated by the dashed vertical red line. The vertical axis shows the depth distribution of the backscatter signal from the waves and subsurface bubbles; the negative values are the depths below the instantaneous sea surface. This event was sampled during the Nov 02-03 storm, at winds of about 17 m/s.

The increase in the lifetime of bubbles at the air-sea interface as a result of soluble surfactant coating was reported by Modini et al. (2013), with bubble persistence ranging between 0.2 and 100 seconds. Moreover, the bubble-plume degassing times depend on the wave scale and breaking wave slope regardless if surfactants are present or not (Callaghan et al., 2013). Callaghan et al. (2013) made such observations in a controlled tank experiment where they could directly correlate a breaking wave with the subsequent plume production. Given the transient nature of breaking waves and the bubble-plume kinematics, it is very difficult to indicate

a particular breaking wave as a local source for plume injection.

As the bubble plume becomes fully-developed, its penetration is possibly driven by the larger scale Langmuir circulation, similarly to the other cases describing deep plume formation. The presence of Langmuir circulation could be indicated by the foam streaks present at the sea surface at the end of the recorded breaking wave event (Figure 6.10). The breaking wave above the pre-existing plume occurred when the plume was characterised by relatively sparse backscatter signal. This indicates that the newly injected bubbles may be confined just below the surface waves (in the uppermost metre of the ocean). Although the plume depth remains large and does not change significantly (mostly in the $4-5$ meters range), the patches in the sonar matrix become more densely packed and with a larger backscatter signal in the water column in the last part (about 70 seconds time interval) of the event (Figure 6.11). This may be caused by new bubbles replenishing the water column through feeding from the upper layer via larger scale turbulent mixing and Langmuir circulation. It is not possible to discount lateral advection being responsible for the larger backscatter signal within the water column.

6.3 Observed acoustical extinction and bubble size distribution

The sonar matrix in Figure 6.12a shows the evolution of a bubble plume for nearly five minutes. This bubble plume is fully developed throughout this event, so no initial deepening process can be observed. For the first 135 seconds (Part 1 in Figure 6.12a), the S_v signal was consistently present within the plume, and the surface waves were markedly defined by a strong S_v returning signal. Afterwards, the sonar matrix experiences a long period (more than 1 minute) with maximum loss of the S_v signal throughout the majority of the water column. A relatively steady wind speed of $> 20\ m/s$ maintained during the entire time interval.

Two bubble size distributions (*BSDs*), calculated from the camera records at 2 metres depth, have been each averaged over Part 1 and Part 2 time intervals (orange and light blue symbols and curves, respectively, in Figure 6.12b). Both *BSDs* are characterised by noticeably increasing slopes at a bubble radius $a \sim 81\ \mu m$ (Figure 6.12b). These slopes were represented by power-laws of the form:

- Part 1: $a^{-0.41\pm0.65}$ and $a^{-5.64\pm0.22}$ within bubble radius ranges $20-81\ \mu m$ and $81-240\ \mu m$, respectively.
- Part 2: $a^{-0.68\pm0.65}$ and $a^{-5.25\pm0.38}$ within bubble radius ranges $20-81\ \mu m$ and $81-180\ \mu m$, respectively.

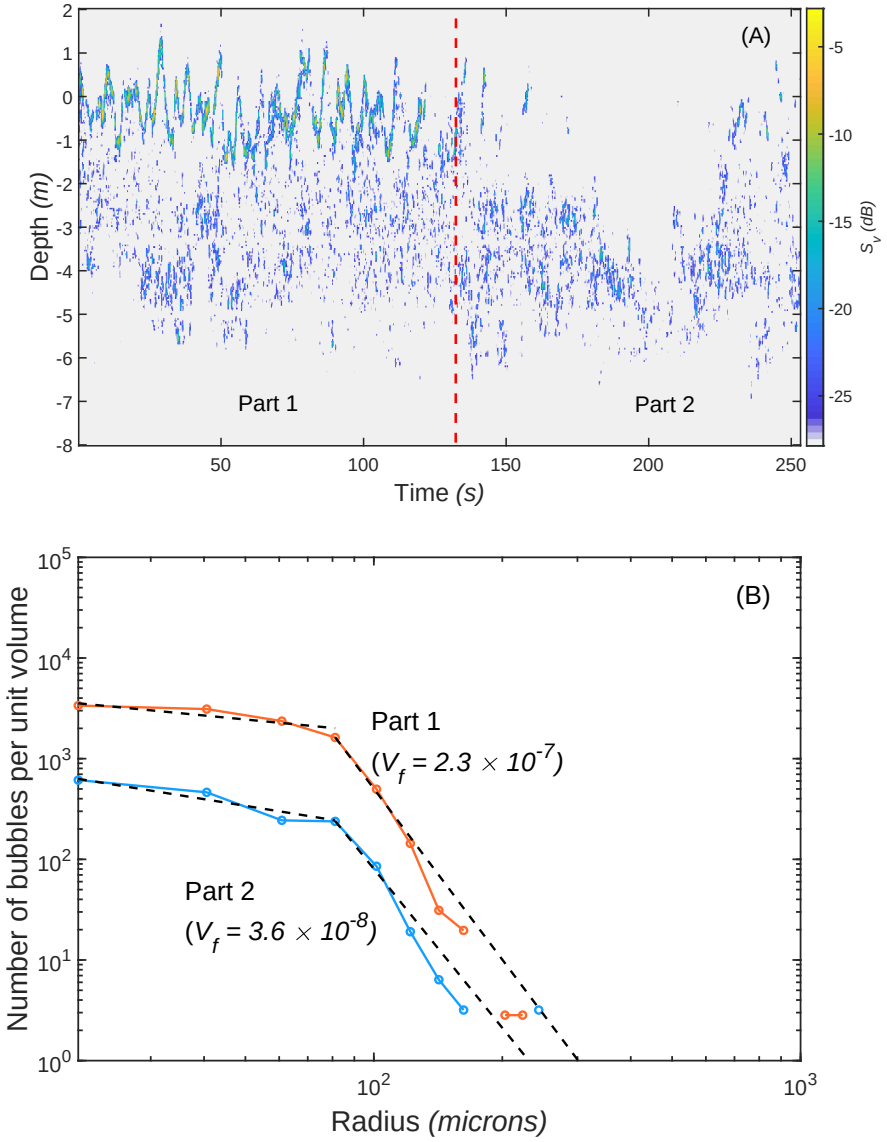

Figure 6.12: (B) Average bubble size distribution and void fraction records during a plume event split in Part 1 and Part 2 represented on a log-log scale. The light blue and orange curves with dots represent the *BSD* data, while the dotted lines, which denote a change in slope, are the power-law fits to the data (B). The sonar matrix in (A) shows the evolution of this plume event. The wind speed during this event was about 22 m/s.

The difference in the average number of bubbles between Part 1 and Part 2 is almost an order of magnitude. Compared to Part 1, the average size of bubbles present in Part 2 also

decreases with about $50 - 60\ \mu m$. The decline in bubble density during Part 2 is associated with a lack of S_v signal throughout most of the water column particularly between $160 - 230\ s$, when there are likely almost no bubbles whose scatter could be detected by the sonar.

This is indicated by the void fraction (V_f) calculated from the camera's bubble density records. The void fraction reaches a minimum during this time interval of $V_f \sim 5 \times 10^{-8}$ at 2 metres depth, which is lower than the V_f threshold at 3.2 metres depth used in the plume detection algorithm. There is a a substantial drop in average void fraction, between Part 1 and Part 2, V_f decreasing with almost an order of magnitude (Figure 6.12).

Total acoustical attenuation (extinction) is one possible explanation for the drop in S_v signal in Part 2, caused by the presence of highly dense bubble populations scattering all of the incident acoustical signal. Given the actual decline of bubble density associated with a very low average Vf (Figure 6.12b), this lack of S_v signal is likely not caused by total acoustical attenuation. The acoustical attenuation may, however, be the explanation for the wave envelope S_v signal also being lacking (Figure 6.12a). This is interesting as the return signal from the wave envelope should be strongest especially in a water column with few bubbles (there are no intermediary scatterers or obstacles on the trajectory of the incident signal).

Deane et al. (2013) calculated the change of bubble size distribution with depth and at different turbulence levels. The influence of wind speed on this change in bubble size and resonance frequency is assessed using a surface bubble layer (SBL) model. A SBL can efficiently absorb sound within a band of resonance frequencies of different-sized bubbles, increasing the return loss of sound incident on the surface. Deane et al. (2013) found that the surface return loss increases with wind speed at different rates as a function of bubble resonance frequency (e.g. for 10-kHz and 17-kHz resonance frequency, the surface return loss becomes significant at wind speeds of about $11 - 12\ m/s$ and $8 - 10\ m/s$, respectively). This indicates that, at very low wind speeds, the backscatter field, even in the uppermost metre layer, is dominated by scattering from very small bubbles at resonance. Since the Delta T sonar operates at much higher frequency than those mentioned by Deane et al. (2013), these very small resonance bubbles would be mostly responsible for the surface return loss at very low wind speeds. However, the sonar matrix shown in Figure 6.12a is sampled during winds $> 20\ m/s$, leading one to conclude that small bubbles are the explanation for the lack of surface signal.

It is not possible to detect the population of bubbles in the uppermost metre of the ocean

visually, as the bubble camera was deployed further down the buoy–predominantly for reasons of practicality.

6.4 The influence of whitecap fraction on subsurface bubbles

In this section, the relationship of whitecap fraction, W_f, with both top metre column-averaged backscatter signal (calculated for the bubble layer with respect to the instantaneous sea surface – see Section 3.6.6) and e-folding depth. Both these bubble parameters have been chosen to assess the influence of whitecap fraction on the bubble backscatter signal in the uppermost metre and in the entire water column via exponential decay (e-folding depth). The total whitecap fraction, shown here, is the average coverage of a whitecap emerging from a breaking wave along a time interval of one hour, and it includes both active and quiescent whitecaps. The whitecap data was collected and processed by collaborators from Lamont Doherty Observatory based at Columbia University – for details see the work of Brumer et al. (2017). For comparison against whitecap fraction, the top metre column-averaged backscatter signal and e-folding have been also averaged over one hour.

Although, as observed in the case studies from this chapter, there does not seem to exist a connection between local breaking waves and the kinematics of bubble plumes particularly as plumes become fully-developed (reach maximum penetration and their backscatter signal becomes weaker and sparser), the aim here is the investigation of the average bubble dynamics in relation to whitecap fraction. Naturally, the average relationships should converge more clearly than local ones, so, on average, whitecap variation might show an influence on bubble entrainment and backscatter variation.

The whitecap fraction data has been collated from all three storms (98 hours). However, this analysis is substantially limited by the large number of missing elements in the whitecap fraction data – of the total 98 hourly data points, about 76% are missing. Even so, there are still few data points available, which at least would help giving an approximate indication of the whitecap fraction influence on bubble entrainment and would also somehow inform the value of the effort to conduct future similar investigations using more complete datasets.

6.4.1 The whitecap fraction variation with backscatter signal

The S_v signal in the uppermost metre appears to overall increase in strength with the growing W_f. However, this relationship is characterised by large scatter, with few outlying hourly values (at $S_v < -36\ dB$) associated with strongly varying W_f (from about 0.017 to 0.041). The uppermost metre S_v also covers a wide range of values (from about $-35\ dB$ to $-27\ dB$) at $W_f < 0.01$ (Figure 6.13a). This overall positive trend is indicated by the generally larger S_v signal generated by more bubbles present in the uppermost metre as whitecap fraction increases. The uppermost S_v signal increases from about $-36\ dB$ to a maximum of $-26\ dB$ over a $0.001 - 0.06$ W_f range (Figure 6.13a). Given the large gaps in the W_f time-series, the correlation coefficient characterising this relationship is weak (R Pearson coefficient is 0.33) and has low significance at a 95% confidence interval (p-value $= 0.12$). This indicates that a least square model cannot be assigned with confidence to fit this trend, so the varying bubble population in the upper-metre water column cannot clearly be traced back to breaking waves and whitecap fraction.

The part of the variation during a period with $U_{10} > 20\ m/s$ is highlighted in Figure 6.13a (red diamonds). This shows that, for about 8 hours, there is a significant trend in the uppermost metre S_v variation with W_f at $U_{10} > 20\ m/s$. During this period, both the uppermost metre S_v and W_f show a decreasing trend while U_{10} maintains at a constant level of $23 - 24\ m/s$. The reason for this steep S_v decrease in the uppermost metre is probably the strong attenuation induced by the accumulation of more bubbles in the shallow water column. This induces strong signal scattering and absorption by these bubbles, so only remnant weak S_v signal reaches back to the sonar.

This increase of S_v signal attenuation at high winds, as an effect of stronger bubble entrainment in the top metre, is to be expected. However, a stronger S_v signal attenuation with decreasing W_f could be considered surprising because usually larger whitecap fractions are associated with higher winds (Asher and Wanninkhof, 1998; Brumer et al., 2017; Sugihara et al., 2007; Zhao and Toba, 2001) in which conditions there is the possibility of the occurrence of potentially more intense and frequent breakers which could lead to stronger bubble injections, hence stronger S_v signal attenuation in the uppermost metre. Given the small sample size (out of the full time-series for all 3 storms), this local trend might not be part of the

general trend, which could not be recorded because of large gaps in the W_f dataset.

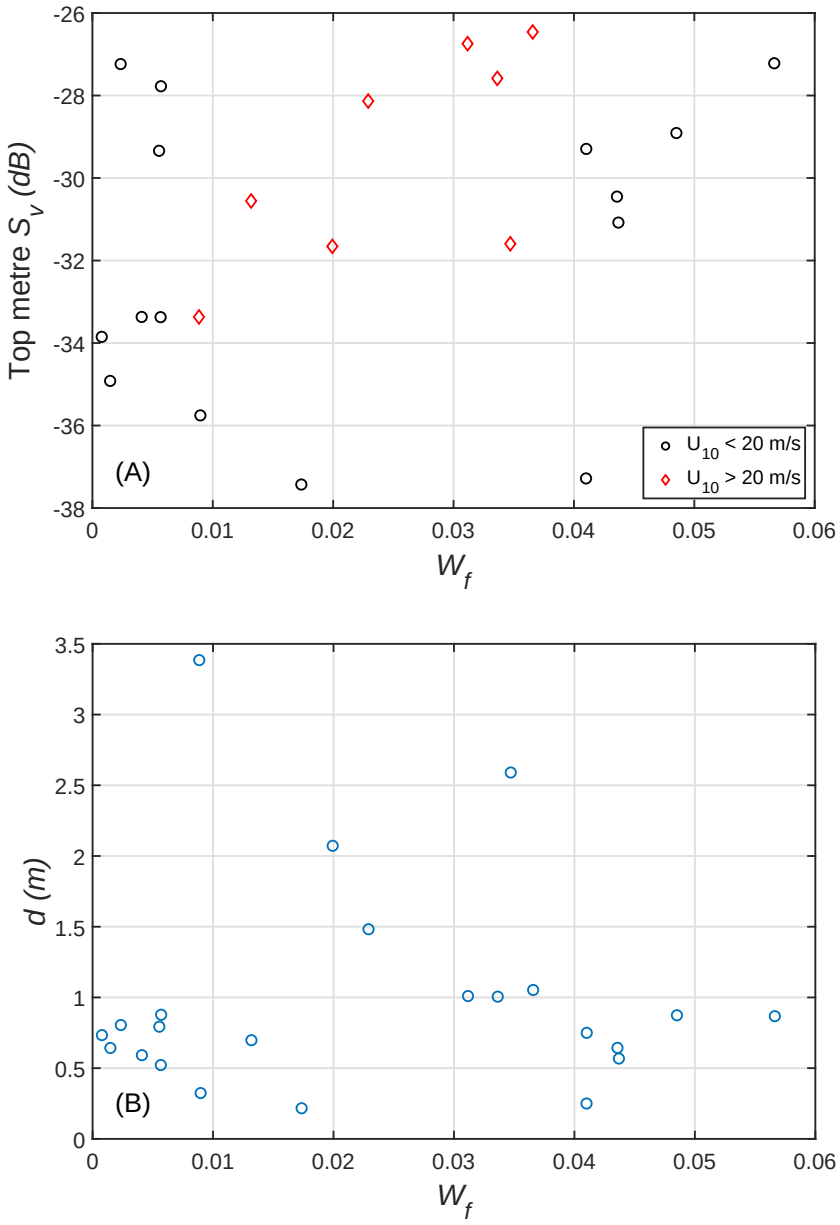

Figure 6.13: The variation of hourly averaged W_f with hourly averaged uppermost metre S_v signal (A) and d (B). The data points in (A) are colour-coded as a function of $U_{10} < 20\ m/s$ (black circles) and $U_{10} > 20\ m/s$ (red diamonds).

Figure 6.13b shows the variation of e-folding depth, d, with W_f. No relationship can be inferred from this variation described by an insignificant correlation (R Pearson coefficient is close to 0). During most of this recorded time period, d varies within a small range (from about $0.2\ m$ to $1\ m$) while W_f varies within its full range Figure 6.13b. This indicates that, even on average, W_f has no influence on the exponential S_v decay within the full water column (from the instantaneous sea level to about 8 metres depth). Since both d and W_f have a dependence

on U_{10}, a relationship between d and W_f would be expected. However, unlike W_f which is the direct effect (still with significant uncertainty at high winds) of wind stress forcing the sea surface, d is not directly driven by wind stress, but other underwater dynamical processes more directly influence the motion and transport of bubbles within the water column.

The bubbles entrained in the full water column are not usually characterised by strong enough buoyancy, so these bubbles do not probably contribute to a whitecap ”feeding” mechanism from below. Therefore, any variation of whitecap growth is not connected to these bubbles.

Further W_f measurements are needed to complete the dataset particularly to be used for a much more comprehensive investigation of the influence of W_f on the change in bubble scattering in the uppermost metre of the ocean. This further investigation may reveal a more complete overview of the general S_v signal trend with varying W_f, including the trend during periods with high winds and strong acoustical attenuation and how it fits in the more complete variation. The result in Figure 6.13a, although incomplete, shows that there is potential for a better understanding of the connection between the breaking surface processes and subsurface bubble dynamics (using even acoustical attenuation measurements) in the uppermost metre of the ocean. Moreover, in addition to more complete observations of W_f from active wave breaking, camera measurements of void fraction closer to the sea surface would offer a more clear explanation of any possible connection between the uppermost metre backscatter signal and void fraction.

6.5 Summary and conclusions

One of the aims in this chapter was to assess the process of bubble plume formation in relation to local wave breaking. To accomplish this, four case studies of individual breaking wave events, recorded by the Foam Camera, compared with simultaneous sonar profiles of subsurface bubbles were analysed. Each case study was chosen to highlight different situations. They include the development of a deep bubble plume from a single breaking wave, the occurrence of multiple breaking waves above a pre-existent deep plume formed from an initial large breaker, a single breaking wave occurring above a pre-existent fully formed plume that was advected into the sonar sample volume from nearby wave breaking. Case studies 1–3 describe

two stages in the evolution of a bubble plume from an initial breaking wave. In the first stage, a shallow bubble layer usually propagates for about 20 to 50 seconds after wave breaking, and its kinematics is driven by wave orbital motion and smaller scale turbulent mixing. In the second stage, the bubble layer gradually penetrates deeper until a plume is fully formed, mostly evolving probably under the influence of large scale turbulent mixing and Langmuir circulation. The presence of Langmuir circulation was assumed from the observation of windrows at the sea surface in the Foam Camera images, which could be indicative of Langmuir circulation. The comparison between the kinematics of shallow bubble layer and deep plume highlights that a larger scale turbulent mechanism is likely necessary for the formation of a deep plume.

The cause of S_v signal loss in almost the full water column of a plume event (from the surface waves to 8 metres depth) was explored using concomitant camera measurements of bubble size distribution. This signal loss is likely present because there are very few bubbles existing in the water column at 2 metres depth and below (very low void fraction which is associated with bubbles whose scatter signal is not detected by the sonar). However, since there was also a lack of S_v signal from the wave envelope, a very dense bubble layer was possibly present above 2 metres depth, outside the range of the bubble camera (probably in the uppermost metre or even shallower water column). This shallow dense bubble layer is supposed to scatter and absorb most or all of the incident acoustical signal, stopping it to reach the surface waves. Extended measurements, with multiple such events, of void fraction (bubble density) in the shallow water column, wave envelope S_v and white-capping are needed to reconcile acoustical and optical records as wave breaking induced bubble injection varies in time.

The final aim was to assess the change in bubble dynamics and entrainment in the uppermost metre and full water column in response to varying whitecap fraction. This was accomplished by comparing the hourly averaged uppermost metre S_v signal and d with hourly averaged W_f. This analysis revealed a trend in the uppermost metre S_v variation with W_f, indicating a possible connection of whitecaps with subsurface bubbles in the top metre layer. Given the many missing elements from the W_f dataset, there is some significant scattering, so there are more chances that a notable number of available data points to be the effect of noise present in the dataset. However, this result shows the need to extend the analysis using more complete datasets, and then more confidently confirm the existence of a trend which could

be generalised to construct relationships used in W_f parameterisations. This would help to better understand the direction of the influence – from the surface to the subsurface bubbles, vice-versa or both directions, leading to a possible explanation of a ”feeding” mechanism of whitecaps by the bubbles below (in the uppermost metre).

Chapter 7

Conclusions and future work

7.1 Summary of results

This thesis describes a set of observations of bubble properties taken during a research cruise in the North Atlantic. This cruise was notable for experiencing wind speeds up to 30 m/s. An upward-pointing sonar provided the primary source of data, and an algorithm was developed to identify individual bubble plumes (Section 3.7). The size distribution of bubbles during the research cruise was described, and relationships with the prevailing conditions explored in Chapter 4. The dynamics of individual bubble plumes was presented in Chapter 5 and the influence of the breaking wave upon them was investigated in Chapter 6.

A complex mechanism controls the structure and penetration depth of bubble plumes. High winds exert stress at the sea surface, thus the sea state becomes energetic (especially during strong and large-fetch storms) where surface waves locally generated by wind (wind-sea waves) and remotely generated waves (swell) can occur simultaneously and interact with each other, producing a mixed sea state. When swell does not propagate from large distances to interfere with wind-sea waves, a separated sea state predominates. A mixed sea state and pure (or predominant) wind-sea, accompanied by high winds, usually induce unstable surface waves (steep waves), as momentum and energy are transferred from the atmosphere to the ocean. These waves eventually break and generate strong turbulent kinetic energy at the sea surface and through the water column. During the wave breaking process, gas is injected from the atmosphere into the upper ocean in the form of subsurface bubbles via wave-induced

turbulent dissipation, which later gradually develop into deep bubble plumes.

A key transformation of the bubble acoustical signal, from echo intensity to volume backscatter strength, has been employed here. The depth varying backscatter strength was used throughout this thesis to quantify the dynamics and structure of the bubble layer. Using sonar calibration parameters generated by Scandella et al. (2016) and sonar depth bin size, the volume backscatter strength was converted from echo intensity.

The results obtained in this thesis that describe the influence of both wave development and wind-wave energy, via inverse wave age and R_H respectively, on bubble penetration and entrainment (Figures 4.1, 4.3 and 4.5) are aimed at the improvement of the current lack of understanding (because of the lack of open ocean observations) in the literature.

7.2 Contribution to the literature

The main contribution of the research presented in this thesis is to simultaneously highlight the difficulty of both taking high-quality measurements in challenging marine environments and highlight the potential of such measurements to increase our understanding of this complex situation. The individual insights are described below, but they combine to advance our understanding of the influence of atmospheric conditions and sea state on the bubble distribution and dynamics in extreme wind speed conditions (8–30 m/s) and interacting waves.

7.2.1 Averaged bubble layer and e-folding depth

Averaging the bubble layer represented an important step because the averaging shows the continuous bubble backscatter distribution with depth. Given it was calculated relative to the instantaneous free surface, the variation of the backscatter signal is more realistically localised within the water column. It was observed that backscatter is not varying homogeneously with depth. The backscatter decreases approximately exponentially with depth, as described by an exponential coefficient known as e-folding depth that was computed from the variation of each hourly backscatter vertical profiles. The exponential backscatter variation observed here is in agreement with Trevorrow (2003), Vagle et al. (2010) and Wang et al. (2011). Since e-folding depth assesses the backscatter decay rate, it provides a good estimation for the bubble entrainment rate along the water column. A relationship between average bubble layer depth

and e-folding depth has been observed in this thesis. The bubble penetration depth is notably larger when the bubble entrainment rate is higher, so the rate of backscatter decay becomes more damped.

From all wind/sea state parameters, wind speed was found to be the most efficient predictor for the variation of both bubble layer depth and e-folding depth, explaining a maximum of about 49% of their variation ($R^2 \sim 0.49$ during Oct 24-25 storm). Bubble penetration depth and entrainment increase with wind speed, as was also observed by Trevorrow (2003), Vagle et al. (2010) and Wang et al. (2011). Although wind speed alone does not explain the complex mechanism of bubble generation, entrainment and penetration depth, it does transfer energy and momentum to the sea, changing the sea state which can then influence bubble processes via wave breaking, wave development and locally driven wind-wave energy.

Wave development was classified in this thesis in two types of waves: swell-dominated waves (described by inverse wave age < 0.038) and developing/growing waves (described by inverse wave age > 0.038). Wave Reynolds number, R_H, is an estimate for the wind stress induced energy content of wind-sea waves. The deepest bubble penetrations and lowest backscatter decay rates were found at highest winds ($> 20\ m/s$) in exclusively developing waves (inverse wave age > 0.038) and in water with highest R_H. The largest variation of both bubble penetration depth and backscatter decay was also observed at highest winds and in developing sea state, but at low R_H. Anomalously low values of these bubble parameters were observed in these conditions, which can be associated with the presence of many very small bubbles within the bubble layer (perhaps due to strong turbulent bubble fragmentation rates), which were not detected by the sonar. Compared to wind speed, overall, inverse wave age and R_H explain less of the variation (only a maximum of about 41% and 32%, respectively) of both bubble layer depth and e-folding depth.

In the presence of swell (yielding mixed sea state), wind-sea waves (wind-sea significant wave height, H_{sw}) show a highly variable effect on bubble entrainment (backscatter decay rate) and penetration depth. From the information available in this thesis, the cause (or causes) for this variability is not clear. However, wave breaking characteristics (in terms of frequency and strength), associated with wind-sea waves, might change in mixed sea state conditions, thus affecting the bubble entrainment. These situations show that conditions are complex and no clear conclusion on the effect of bubble processes in a mixed wave field can be drawn,

but this can be further investigated using more information about wave breaking and wind-sea wave dynamics in a mixed sea state. On the other hand, a more clear influence of wind driven waves emerges when wind-sea is separated from swell (they each dominate at different time intervals). Growing pure (approximately) wind-sea waves can induce an approximately linear increase of e-folding depth and penetration depth. However, still only about 33% ($R^2 \sim 0.33$) of the variation of e-folding depth can be explained by pure wind wave dynamics.

Since there is still room for improving the understanding of the complex mechanisms influencing bubble entrainment and penetration depth, other factors (not only the physical factors investigated in this thesis), related to oceanic biology and chemistry, and bubble properties, may bring new insights on these mechanisms.

7.2.2 Non-averaged bubble layer and plume statistics

Since a Delta T sonar with high spatial and temporal resolution was used, the non-averaged (full resolution) bubble layer is useful to detect very sharp changes of the bubble penetration depth, and to observe the patchy, discrete structure of the bubble layer. The very sensitive penetration depth of the non-averaged bubble layer was used to find individual plume penetrations, which were classified as such only if they reached below a penetration depth threshold of 3.2 metres (this is the depth at which one of the working resonators was mounted) – the resonator was used to measure void fraction of bubbles present in the water column during plume events. The individual plumes were identified (with an 81% accuracy) by an algorithm developed in this thesis, which encompassed the matching between void fraction and non-averaged bubble layer depth signals generated by the resonator and sonar, respectively. This is a physical identification of plumes using signals from bubbles simultaneously measured by two independent sensors at different depths, compared to other methods of defining plumes in the open ocean, used by Trevorrow (2003) and Vagle et al. (2010), which are only based on basic statistics (such as standard deviation). The plume detection algorithm could be potentially improved in the future by not only considering fixed depth threshold and gap length (this is how the algorithm is currently implemented), but by varying these features. Eventually, a heat map of the accuracy of plume detection algorithm, as a function of many depth thresholds and gap lengths arbitrary chosen, could be generated, and the depth threshold and gap length

associated with the highest accuracy can be selected and used in the final plume detection algorithm.

The following properties of individual plumes were described in this thesis: plume frequency (number of plumes per hour), plume duration and maximum plume depth. The number of plumes increases sharply with wind speed to a maximum of 32 events per hour in a low R_H regime ($1 - 3 \times 10^6$) and in both mature and young seas. An opposite trend was observed in high winds ($> 20\ m/s$), when the number of plumes plummeted down to 6 events per hour in a high R_H regime ($4 - 6 \times 10^6$) and in mostly young seas (inverse wave age > 0.038, however there are missing elements at winds $> 20\ m/s$, limiting the overall classification of sea state) during the Oct 24-25 storm. Although large swell and wind waves were simultaneously present and interacting during Oct 24-25 storm, in such high winds the seas mostly consisted of young waves (note the limitation of such classification imposed by the missing elements mentioned above). The strong plume frequency decline at high winds ($> 20\ m/s$) may be caused by plumes merging together into continuously present bubble fields, so the plume detection algorithm could not individually identify plumes in these conditions any more. On the other hand, the variation of plume duration was split at winds $> 20\ m/s$ (strong plume duration variance). At such wind speeds, plume duration strongly varied from about $11\ s$ to $166\ s$, indicating the limited plume identification accuracy of the algorithm (which does not encompass other possible oceanic factors that can influence bubbles). Although plume frequency shows an evident dependence on wind speed, still only about 60% of plume frequency variation can be explained by wind speed.

Plume duration also generally increases with wind speed (with about 34% of the variation explained). This limited wind speed accountancy of plume duration variation is surely partly caused by the strong variation of plume duration at $U_{10} > 20\ m/s$. Even so, anomalously high and low plume durations have not been included in the analysis – these values were treated as outliers because their variance was even higher than the scattering of the other data points. A large variance of plume duration with inverse wave age suggests that plumes can persist over a wide range of time intervals in both mature and young seas – only a relatively weak wave age influence on plume duration variance was found. Given its large variation over a narrow R_H range, plume duration does not show a clear dependency on wind-sea wave energy content.

Bubbles within plumes recorded during HinWinGS do not dissolve quickly (also dependent

on surfactant concentrations and differential bubble pressure levels), so plumes which last longer usually have more time to penetrate deeper. This process can be demonstrated in this thesis by the observation of plume maximum depth increase with plume duration but only when a decoupling from physical processes is considered. However, Trevorrow (2003) did not find a clear relationship between these two plume parameters, possibly (the author states) as an effect of plume advection due to strong near-surface current.

7.2.3 Local plume structure and kinematics concomitant with wave breaking

The aim was to better understand plume structure and kinematics with respect to wave breaking onset and associated whitecap evolution. Comparing individual breaking waves with simultaneously occurring subsurface bubbles, the time evolution of plume structure has been represented in three case studies from the moment of wave breaking. The bubble plume gradually penetrates deeper after wave breaking, but the bubbles were probably affected, in the first 20–30 seconds, by circular motions induced by wave orbital dynamics. The bubble plume eventually becomes fully developed when it reaches maximum depth – at this stage, the plume is probably driven by large scale turbulent eddies. The process of plume development after breaking onset is similar to measurements taken by Dahl and Jessup (1995). However, a clear conclusion that these plumes were caused by the observed breaking waves cannot be drawn – it is also possible that these plumes were advected into the sonar sampling volume just after these breaking waves, but this effect cannot be validated because of the limited sampling volume and sonar beam geometry that do not allow the observation of lateral plume advection.

The long lasting plumes (particularly shown in the sonar matrix from case study 3) and plumes which exist before wave breaking (sonar matrix from case study 4) show that plumes can organise into a steady state bubble field where bubbles take a very long time to dissolve. Given that the bubbles within these bubble fields survive for a long time in the water column, they most likely contain oxygen and nitrogen, which are gases with low solubility, so these gases are contained in bubbles for longer times. Therefore, the presence of these bubble fields indicates that there is an imbalance of the transfer rate of these poorly soluble gases (oxygen and nitrogen) from the atmosphere to the ocean (Keeling, 1993; Woolf and Thorpe,

1991): more gas is taken by the ocean than it is released into the atmosphere. The gas saturation due to the continuous presence of bubble fields can suppress the gas transfer rate from the ocean to the atmosphere (McNeil and D'Asaro, 2007). Vagle et al. (2010) estimated the air injection flux using an inverse model, and observed that air injection increases with bubble penetration depth. However, the measured environmental conditions (wind speed and sea state) were milder than during HiWinGS cruise, and the gas volume levels in the full water column may have been lower, so gas saturation was probably not reached (there was still room for gas transfer).

7.2.4 Hourly averaged whitecap fraction influence on subsurface bubble dynamics

The hourly sampled total whitecap fraction, W_f (which encompasses the active and quiescent whitecaps), was measured during HiWinGS campaign by collaborators from Lamont Doherty Earth Observatory (Columbia University). The change of total whitecap fraction was not found to be connected to bubble dynamics in the full water column (extending from the instantaneous free surface to 8 metres depth at which the sonar was located) as shown by a lack relationship of W_f with the hourly averaged e-folding depth, d (which characterises the bubble entrainment via exponential backscatter decay in the full water column). However, a trend of uppermost metre S_v signal with W_f has been recorded, but accompanied by a notable scatter, which is larger than the actual trend. Many data points (76%) were missing from the W_f dataset, so it is difficult to generalise this trend as a W_f parameterisation of the uppermost metre bubble dynamics. The parameterisation could also work in the opposite direction as a dependency of whitecaps on the uppermost metre bubble dynamics, which could be described by a bubble 'feeding' mechanism of whitecaps from the below upper metre water column. This partial result shows the necessity of acquiring a more complete W_f dataset (and of other wave breaking statistics), which would permit the formulation of this bubble 'feeding' parameterisation. This would advance the understanding of the physical mechanism based on subsurface bubble dynamics that controls the change of whitecaps at the surface (a physical connection between subsurface and surface bubble processes).

Although based on only 8 hourly data points, a particular trend at high winds ($> 20\ m/s$)

emerges. This trend describes the decline of uppermost metre S_v signal with decreasing W_f. At such high wind stress over the ocean, a decline of S_v is to be expected because of the strong acoustical attenuation in the water column. However, a decreasing of W_f, which closely follows the trend of uppermost S_v, is surprising. A better assessment of W_f variation at winds $> 20\ m/s$, together with more records of uppermost metre S_v related to W_f, are needed to understand the nature of subsurface bubble influence on whitecaps and vice-versa particularly in high wind speeds where the whitecap variation is highly uncertain. In addition to a reduced number of W_f records available in this thesis, another limitation that might have impeded the connection between the sonar backscatter measurements and W_f is that the camera measuring the whitecaps was not spatially synchronized with the sonar, so the physical connection between whitecaps and subsurface bubbles cannot be assessed.

7.3 Future work

Sonar bubble measurements were conducted at a different sampling frequency than that of wind/sea state parameters, so 30-minute averages were used to assess their relationships. However, this limitation can obstruct the observation of finer details in the relationships, which could better explain the variance. An exact match, in time, between higher temporal resolution measurements – not a too high sampling frequency because it will reveal large scattering that could mask a more clear trend, especially if the data is noisy – of subsurface bubbles, sea state, wave spectra and wind speed may yield a better explanation of the variance in the relationship of subsurface bubbles with these complex parameters.

A limitation of the wave Reynolds number (R_H), used in this thesis, is that it does not distinguish among the energy content of other types waves which could potentially generate breaking waves, such as cross-swell (swell propagation intersecting the wind direction) and counter-swell (swell propagating against the wind). These types of swell could be incorporated into the definition of R_H to better assess the influence of wave energy on bubble processes in different swell conditions. An estimation of turbulent kinetic energy dissipation (and the size of turbulent eddies) in water can be obtained by using a combination of acoustic Doppler current profiler (ADCP) measurements and the large eddy method, as shown by Gargett (2017) and Gargett (1994). This technique would offer new insights on the types of turbulent eddies

(size and intensity) needed to mix the bubbles downward, leading to deep plume formation, irrespective of local wind sea surface processes, as it was assumed in this thesis.

The foam camera breaking-wave and whitecap images, used in this thesis, were not processed to obtain a whitecap fraction statistics. Whitecap fraction statistics from the Foam Camera would enable a quantitative vertical cross-sectional analysis of the relationship between wave breaking and subsurface bubble plumes. However, active and quiescent whitecap fractions could be used separately in order to reduce the variance in the relationship between wave breaking and subsurface bubble formation at different stages of evolution. This comparison would help to investigate the suggested bubble 'feeding' mechanism of whitecaps from the shallow bubble layer below. It has been observed in some of the case studies from chapter 6 that the plumes develop and penetrate deeper once wave breaking ceases. Given the early strong buoyant forces, the bubble feeding from below is assumed to be most intense during wave breaking, and it possibly gradually decreases as the whitecap transitions from active to quiescent, and also as the bubble plume below deepens. However, this process has never been assessed in the open ocean. Simultaneous measurements of subsurface bubbles, whitecaps (active and quiescent) and aerosol production would reveal a complete process of bubble feeding of whitecaps from below, followed by the bubble bursting inside whitecaps and the subsequent aerosol ejection into the atmosphere and its impact on the marine boundary layer. Note, however, that the bubbles observed during HiWinGS, by both camera and sonar, were likely not involved in the process of 'feeding' the whitecaps. The most relevant bubbles for this would be those found within high void fraction plumes near the sea surface (uppermost metre), which cannot be measured by any acoustical device, including the Delta T sonar used in this project.

Following observations in chapter 6, the process of deep plume formation after wave breaking could also be influenced by gradual plume advection from a side, and not necessarily as a result of the observed breaking wave. A complete 3-dimensional multibeam sonar imaging would be required to resolve the advection of plumes from any side, and the full 3-dimensional scale of the plume could be retrieved as well, allowing a much more clear comparison with the breaking-wave whitecap area above.

Given that it was measuring bubbles below the high void fraction region that characterises active breaking (uppermost metre), the underwater bubble camera retrieved a notably narrower

range of bubble sizes and densities. Using the camera to measure bubble size distribution in the high void fraction region (camera mounted on a spar buoy in the top 1-metre ocean layer) would yield a wide range of bubble sizes (up to the *mm*–scale bubbles). However, caution is needed because the buoy can be subject to large-amplitude vertical motions, so the camera may not always be submerged, and some of the images will only contain noise, not bubbles. Those bubble size distribution measurements close to the sea surface (in the top 1-metre) could be combined with sonar backscatter measurements of bubbles along the water column below 1 metre to compute the void fraction in the shallow water column. This would remove the risk of underestimating the high void fraction region. A representation of the newly obtained void fraction in plumes as they deepen after wave breaking would reveal if these these deep plumes actually evolve from a region with high bubble density within a shallow layer induced by a breaking wave, indicating a more clear connection between plume formation and wave breaking. A quantitative estimate of gas volume distribution (gas volume would also not be underestimated close to the sea surface any more) as bubble plumes develop in time could also be obtained, yielding more accurate estimates of gas saturation in the water column. Simultaneous measurements of gas fluxes (oxygen, nitrogen, carbon dioxide), from the atmosphere to the ocean and vice-versa, are needed to better understand the change of gas fluxes (and the ocean's capacity to uptake gas) as a function of gas saturation in the full water column and plume dynamics.

The effect of surfactants on bubble persistence (surface bubbles and plumes of bubbles) via bubble coating can be investigated by combining laboratory experiments and oceanic observations. According to Modini et al. (2013), a higher surfactant concentration (dependent on chemical and biological activity) in the water reduces the bubble cap film thickness. This reduction was explained by Modini et al. (2013) via an increase in bubble persistence with higher surfactant concentration, so the bubbles had more time to drain and thin out with the aid of marginal flows along the bubble surface. Since bubbles persist longer, they are gradually affected by stronger hydrostatic forces as they penetrate deeper. Therefore, higher surfactant concentrations may influence the deep plume formation. The effect of an increase in persistence of deeper plumes (with the associated uncertainty caused by the scatter present in the relationship) was already observed in this thesis, which could be directly compared against surfactant concentration measurements in a future research. Modini et al. (2013) also ob-

served a strong decline in aerosol production and a lower droplet ejection velocity at the sea surface as surfactant concentration increases, so surfactant type and concentration might link both aerosol production and deep plume formation – as the surfactant concentration is higher, plumes might tend to penetrate deeper and persist more time, suggesting that there is more surfactant material in the water column available for aerosol production.

7.4 Overall summary

Although there are uncertainties, approximations and important assumptions in the results presented in this thesis, these results have shown important relationships describing bubble dynamics influenced by wind and sea state processes. This thesis offers an exhaustive characterisation of the response of the upper ocean to sea state and atmospheric forcing. This was accomplished by attempting to connect subsurface bubbles to the wave field energy and breaking waves. Measurements of individual bubble plumes and local breaking waves were synchronised in time to compare their evolutions. This highlighted the lack of connection between local breaking and bubble presence due to the transient nature of wave breaking and stochastic upper ocean processes that influence bubble-plume kinematics.

Appendix A

Wave processes in the open ocean

A.1 Oceanic processes for the balance of the wave spectrum

In the open ocean, the fully-developed wave spectrum tends to be stabilised by wave-wave interaction, which is outlined in this section.

A.1.1 Wave-wave interactions

In deep water, the waves that interact with each other usually obey the resonance condition, and this type of interaction is known as the quadruplet wave-wave interaction (Holthuijsen, 2007). The resonance condition implies that two pairs of interacting wave components exist if their wave numbers (they have the same wavelengths and directions) and frequencies match, so the four waves resonate when they are superimposed (Holthuijsen, 2007). This matching of wave numbers, k_{wave} and frequencies, f_{wave}, with the correspondent resonance condition, can be expressed as (Holthuijsen, 2007; Phillips, 1985)

$$\begin{aligned} f_{wave,1} + f_{wave,2} &= f_{wave,3} + f_{wave,4} \\ k_{wave,1} + k_{wave,2} &= k_{wave,3} + k_{wave,4} \end{aligned} \tag{A.1}$$

Given that this matching is between waves with neighbouring wave numbers, the waves of different scales (long waves and short waves) do not interact, so this interaction only applies to short waves (Melville, 1996). The quadruplet wave-wave interaction has the capacity to stabilize the shape of the JONSWAP spectrum (Holthuijsen, 2007), e.g. when the tail of the

spectrum is deviated locally by wind from a smooth f_{wave}^{-4} shape (a bulge might be present at the tail), the wave-wave interaction tends to attenuate any bulge formation back to a smooth shape of the tail. The wave-wave interaction transfers a significant fraction of energy at higher and lower frequencies (Holthuijsen, 2007; Melville, 1996), while it subtracts the energy mostly at mid-range frequencies (Holthuijsen, 2007).

These wave-wave interactions can be expressed as an integration, over each wave component, of all wave numbers present in the quadruplet interaction (Holthuijsen, 2007; Phillips, 1985),

$$\begin{aligned} Q_{s,ww}(k_{wave,4}) = \iiint T_1(k_{wave,1}, k_{wave,2}, k_{wave,1} + k_{wave,2} - k_{wave,4}) \\ E(k_{wave,1})E(k_{wave,2})E(k_{wave,1} + k_{wave,2} - k_{wave,4})dk_{wave,1}k_{wave,2} - E(k_{wave,4}) \\ \iiint T_2(k_{wave,1}, k_{wave,2}, k_{wave,4})E(k_{wave,1})E(k_{wave,2})dk_{wave,1}k_{wave,2}, \end{aligned} \tag{A.2}$$

where the wave-wave interaction source term has now been expressed as a function of wave number (in particular $k_{wave,4}$), $k_{wave,1}$, $k_{wave,2}$ and $k_{wave,3} = k_{wave,1} + k_{wave,2} - k_{wave,4}$, with the latter wave number being derived from the resonant condition, T_1 and T_2 are transfer coefficients, which are complicated functions of these wave numbers, and $E(k_{wave,1})$, $E(k_{wave,2})$ and $E(k_{wave,4})$ are the energy densities of wave numbers $k_{wave,1}$, $k_{wave,2}$ and $k_{wave,4}$. The first and second integrals in Equation (A.2) represent the passive interactions (the integral does not depend on $E(k_{wave,4})$) and the active interactions (the integral depends on $E(k_{wave,4})$), respectively (Holthuijsen, 2007). The energy growth or decay of wave component $k_{wave,4}$ depends on the balance between these passive and active interactions (Holthuijsen, 2007).

A.2 Breaking waves

A.2.1 Spilling breakers and surfactants

The surfactant films act to reduce the surface tension, elasticity and viscosity (Liu and Duncan, 2003, 2006). At the highest surfactant concentration, the bulge still forms, but it no longer contains a sharp toe and the capillary waves are no longer present ahead of the toe (Liu and Duncan, 2003). The formation of the ripples between the toe and the crest diminishes during the spilling process (Liu and Duncan, 2003), as shown in Figure A.1a. Shortly after the bulge formation, some smooth ripples form along the bulge and a 2-dimensional jet (sheet) emerges

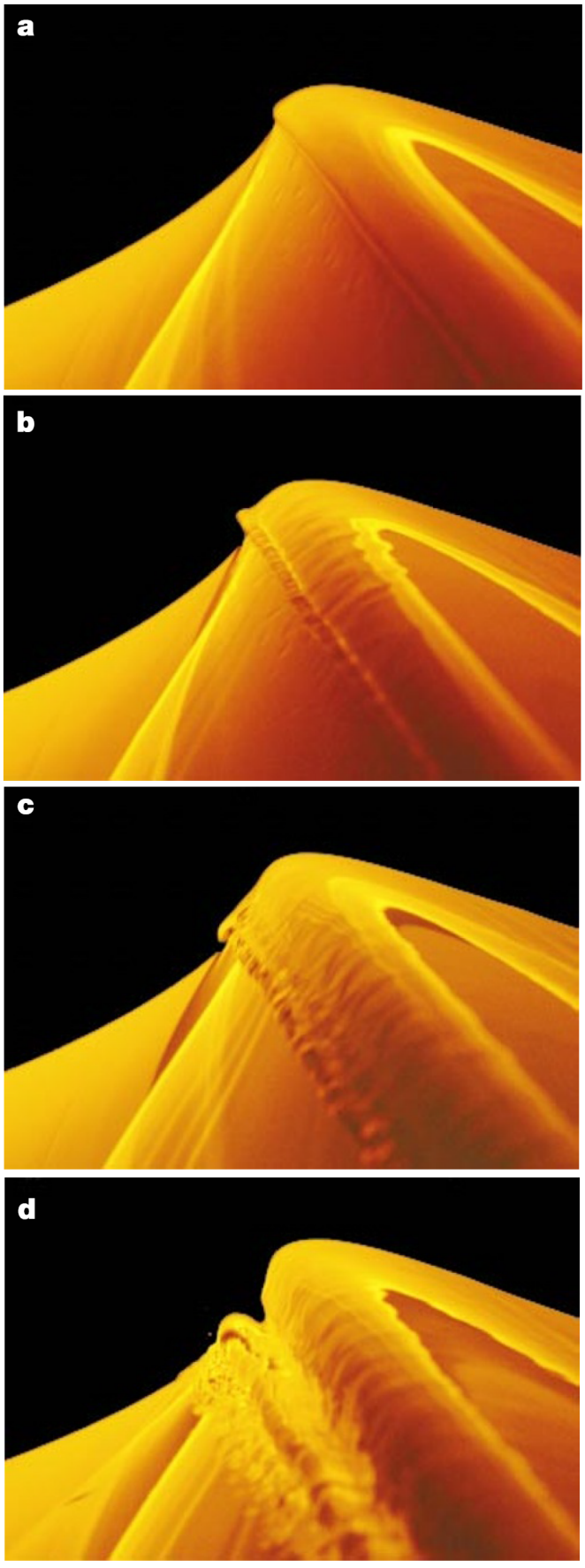

Figure A.1: The evolution of a spilling breaker in water with surfactants ("dirty" water). The width of all these images is about 12.5 *cm*. (a)–(d) Images collected by Liu and Duncan (2003).

from near the toe (Figure A.1b). The jet bends forward and then begins to slide down the wave face (Figure A.1c). Eventually, the jet impacts the front wave face, while entrapping a tube of air and producing a splash from the region of impact (Figure A.1d). These types of spilling breakers are usually responsible for white-capping and bubble generation in the open ocean.

The disruption of the surface and turbulence, caused by spilling breakers in contaminated water, are more intense than that in clean water (Liu and Duncan, 2003). Therefore, the bubble production and air-sea transfer are also likely more significant for oceanic spilling breakers than for those occurring in fresh water. Other observations that can confirm the influence of surfactants on the spilling breaking process are not currently present in the literature (to the best knowledge of the author). Although, the study of Liu and Duncan (2003) is exhaustive and conducted in very well controlled laboratory conditions, more observations are obviously needed to understand more aspects of this process in the ocean.

The results of the spilling breaking processes, reported by the above authors, come from experiments conducted in similar conditions (in terms of mechanics and frequency range), where the breakers were mechanically generated by a similar wave maker. These breakers were generated in wave tanks, not in wind tunnels, so the interaction between the wind and waves could no be assessed. The scale of the breaking process, during these experiments, is much lower than that in the real ocean (width and depth of wave tanks are in range of tens or hundreds of centimetres only, so the size of breaking waves is quite small). Using only these experimental results will likely impose some important limitations on the understanding of the complexity of the breaking wave process in the open ocean. However, these experiments are important to evaluate the effect of surfactants on breaking, which can be studied in more controlled environment, such as a wave tank.

A.2.2 Whitecap fraction dependence on wind speed and sea state

A range of several parameterizations for whitecap fraction have been proposed over time. Whitecap fraction W_f, as a function of wind speed at 10 meters elevation, U_{10}, is the most commonly used, and it takes the form of a power-law relation (Monahan, 1971; Toba and Chaen, 1973),

$$W_f = aU_{10}^b \tag{A.3}$$

with a and b derived from a set of observations. Empirically, whitecap fraction is assumed to vary non-linearly with wind speed. Following observations of whitecaps in the open ocean , the whitecap fraction was linked with the cubed wind speed (so the power-law coefficient is $b = 3$) by using $1/3$ as the power of whitecap fraction ($W_f^{1/3}$), so a linear regression approximation for the relationship between wind speed and $W_f^{1/3}$ is obtained (Asher and Wanninkhof, 1998; Sugihara et al., 2007). Asher and Wanninkhof (1998) and Sugihara et al. (2007) show a generally significant increase of whitecap fraction with wind speed. The number of samples collected by Asher and Wanninkhof (1998) is scarcer than in the study conducted by Sugihara et al. (2007), and the whitecap fraction dependence on wind speed is also weaker in the study of Asher and Wanninkhof (1998). Open ocean measurements of whitecaps conducted by Monahan (1971) and Toba and Chaen (1973) reveal that whitecap fractions shows a more than cubic increase with wind speed as described by a power-law coefficient $b \sim 3.5$. Whitecap fraction, observed by Toba and Chaen (1973), shows a more rapid variation with wind speed than in the measurements of Monahan (1971).

Larger whitecap fractions (between about 1% and 10%) were observed in the open ocean by Ross and Cardone (1974), but the collected samples are quite scarce. These larger whitecap fractions were measured at wind speeds ranging between about 10 and 20 m/s. At a similar wind speed range, Toba (1972) observed notably lower whitecap fractions (ranging between 0.02% and 1%). Much larger variance and bias in the whitecap fractions dependence on sea state (wave age) were observed by Monahan (1971), Toba (1972), Toba and Chaen (1973) and Ross and Cardone (1974), indicating that wave age is a worse predictor for whitecap fraction than wind speed. The large uncertainty in the wave age dependence may be caused by different measuring techniques of wave age and varying whitecap fraction separation criteria, along with different wind-wave conditions in which the measurements were conducted. The depiction of cubic wind speed dependence of whitecap fraction in different wave field conditions was also reported by Sugihara et al. (2007). These authors observed a more rapid increase of whitecap fraction with wind speed in pure wind-sea than in counter and cross swell. They also show a stronger relationship between whitecap fraction and wind speed (it is almost perfect, with a correlation coefficient r = 0.99) in the presence of wind-sea, but the number of samples recorded in wind-sea conditions are notably smaller, so this relationship may not be well generalized by the regression model until more data is available. Interestingly,

whitecap fraction has been observed to be more sensitive to wind speed in older seas (larger wave age) than in younger ones (Sugihara et al., 2007). This appears surprising, given that younger waves are usually driven by local winds (whereas swell is not), so their dynamics (including breaking) closely responds to wind variation. However, in both older and younger seas, there are only few samples, so the level of significance of these relationships may be lower.

Bibliography

Ainslie, M. A. (2004), 'The sonar equation and the definitions of propagation loss', *Journal of Acoustical Society of America* **115**, 131–134.

Ainslie, M. A. and Leighton, T. G. (2011), 'Review of scattering and extinction cross-sections, damping factors, and resonance frequencies of a spherical gas bubble', *Journal of Acoustical Society of America* **130**, 3184.

Al-Lashi, R. (2016), 'Toward omnidirectional and automated imaging system for measuring oceanic whitecap coverage', *J. Opt. Soc. Am. A* **33**, 1589–1597.

Al-Lashi, R., Gunn, R. S. and H., C. (2016), 'Automated processing of oceanic bubble images for measuring bubble size distributions underneath breaking waves', *Journal of Atmospheric and Oceanic Technology* **33**, 1701–1714.

Al-Lashi, R., Gunn, R. S., Webb, E. G. and Czerski, H. (2017), 'A novel high-resolution optical instrument for imaging oceanic bubbles.', *IEEE Journal of Oceanic Engineering* pp. 1–11.

Anguelova, M. D. and Huq, P. (2012), 'Characteristics of bubble clouds at various wind speeds', *Journal Geophysical Research* **117**(C03036).

Asher, W. E. and Wanninkhof, R. (1998), 'The effect of bubble-mediated gas transfer on purposeful dual-gaseous tracer experiments', *Journal of Geophysical Research* **103**(C5), 10555–10560.

Asher, W., Farley, P. J., Higgins, B. J., Karle, L. M., Monahan, E. C. and Leifer, I. (1996), 'The influence of bubble plumes on air/seawater gas transfer velocities', *Journal of Geophysical Research* **101**(C5), 12027–12041.

Bigg, E. K. and Leck, C. (2008), 'The composition of fragments of bubbles bursting at the ocean surface', *Journal of Geophysical Research* **113**(D11).

Blanchard, D. C. (1963), 'The electrification of the atmosphere by particles from bubbles in the sea', *Progress in Oceanography* **1**, 73–112.

Blenkinsopp, C. E. and Chaplin, J. R. (2007), 'Void fraction measurements in breaking waves', *Proceedings of the Royal Society of London A: Mathematical, Physical and Engineering Sciences* **463**, 3151–3170.

Blenkinsopp, C. E. and Chaplin, J. R. (2011), 'Void fraction measurements and scale effects in breaking waves in freshwater and seawater', *Coastal Engineering* **58**, 417–428.

Blomquist, B. W., Brumer, S. E., Fairall, C. W., Huebert, B. J., Zappa, C. J., Brooks, I. M., Yang, M., Bariteau, L., Prytherch, J., Hare, J. E., Czerski, H., Matei, A. and Pascal, R. W. (2017), 'Advances in quantifying air-sea gas exchange in environmental forcing', *Journal of Geophysical Research* **122**, n/a–n/a.

Bowyer, P. A. (2001), 'Video measurements of near-surface bubble spectra', *Journal of Geophysical Research* **106**, 14179–14190.

Brumer, S. E., Zappa, C. J., Brooks, I. M., Tamura, H. and Brown, S. M. (2017), 'Whitecap coverage dependence on wind and wave statistics as observed during so gasex and hiwings', *Journal of Phyical Oceanography* **47**, 2211–2235.

Bye, J. A. T. and Jenkins, A. D. (2006), 'Drag coefficient reduction at very high wind speeds', *Journal of Geophysical Research* **111**(C3).

Callaghan, A. H., Deane, G. B. and Stokes, M. D. (2013), 'Two regimes of laboratory whitecap foam decay: bubble-plume controlled and surfactant stabilized', *Journal of Physical Oceanography* **43**, 1114–1126.

Callaghan, A. H., Deane, G. B., Stokes, M. D. and Ward, B. (2012), 'Observed variation in the decay time of oceanic whitecap foam', *Journal of Geophysical Research* **117**, 1–20.

Carpenter, J. H. (1966), 'New measurements of oxygen solubility in pure and natural water', *Limnology and Oceanography* **11**, 264–277.

Caruthers, J. W., Stanic, S. J., Elmore, P. A. and Goodman, R. R. (1999), 'Acoustic attenuation in very shallow water due to the presence of bubbles in rip currents', *Journal of Acoustical Society of America* **106**, 617–625.

Casas-Prat, M. and Holthuijsen, L. H. (2010), 'Shortterm statistics of waves observed in deep water', *Journal of Geophysical Research* **115**(C09024).

Cavaleri, L. and Malanotte-Rizzoli, P. (2010), 'Wind wave prediction in shallow water: theory and application', *Journal of Geophysical Research* **86**(C11), 10961–10973.

Chapman, R. B. and Plesset, M. S. (1971), 'Thermal effects in the free oscillation of gas bubbles', *Journal of Basic Engineering* **93**, 373–376.

Charnock, H. (1955), 'Wind stress on a water surface', *Q. J. R. Meteorol. Soc.* **81**, 639–640.

Cipriano, R. J. and Blanchard, D. C. (1981), 'Bubble and aerosol spectra produced by a laboratory 'breaking wave", *Journal of Geophysical Research* **86**, 8085–8092.

Clay, C. S. and Medwin, H. (1977), *Acoustical Oceanography: Principles and Applications*, John Wiley.

Commander, K. W. and McDonald, R. J. (1991), 'Finite-element solution of the inverse problem in bubble swarm acoustics', *Journal of Acoustical Society of America* **89**, 592.

Commander, K. W. and Moritz, E. (1989), 'Off-resonance contributions to acoustical bubble spectra off-resonance contributions to acoustical bubble spectra', *The Journal of the Acoustical Society of America* **85**, 2665.

Crawford, G. B. and Farmer, D. M. (1987), 'On the spatial distribution of ocean bubbles', *Journal of Geophysical Research* **92**, 8231–8243.

Czerski, H. (2012), 'An inversion of acoustical attenuation measurements to deduce bubble populations', *Journal of Atmospheric and Oceanic Technology* **29**, 1139–1148.

Czerski, H., Twardowski, M., Zhang, X. and Vagle, S. (2011), 'Resolving size distributions of bubbles with radii less than 30 μm with optical and acoustical methods', *Journal of Geophysical Research* **116**, 1–13.

Czerski, H., Vagle, S., Farmer, D. M. and Hall-Patch, N. (2011), 'Improvements to the methods used to measure bubble attenuation using and underwater acoustical resonator', *Journal of Acoustical Society of America* **130**, 3421–3430.

Dahl, P. H. (2003), 'The contribution of bubbles to high-frequency sea surface backscatter: A 24-h time series of field measurements', *Journal of Acoustical Society of America* **113**, 769–780.

Dahl, P. H. and Jessup, A. T. (1995), 'On bubble clouds produced by break- ing waves: An event analysis of ocean acoustic measurements', *Journal of Geophysical Research* **100**, 5007–5020.

Dahl, P. H., Plant, W. J., Ntzel, B., Schmidt, A., Herwig, H. and Terray, E. A. (1997), 'Simultaneous acoustic and microwave backscattering from the sea surface', *Journal of Acoustical Society of America* **101**, 2583–2595.

D'Asaro, E. and McNeil, C. (2007), 'Airsea gas exchange at extreme wind speeds', *Journal of Marine Systems* **66**, 92–109.

Deane, G. B. (2016), 'The performance of high-frequency doppler sonars in actively breaking wave crests', *IEEE Journal of Oceanic Engineering* **41**, 1028–1034.

Deane, G. B., Preisig, J. C. and Andone, C. L. (2013), 'The suspension of large bubbles near the sea surface by turbulence and their role in absorbing forward-scattered sound', *IEEE Journal of Ocean Engineering* **38**, 632–640.

Deane, G. B. and Stokes, M. D. (2002), 'Scale dependence of bubble creation mechanisms in breaking waves', *Nature* **418**, 839–844.

Deane, G. B. and Stokes, M. D. (2008), 'The acoustic excitation of air bubbles fragmenting in sheared flow', *The Journal of the Acoustical Society of America* **124**(6), 3450–3463.

Deike, L., Lenain, L. and Melville, W. K. (2017), 'Air entrainment by breaking waves', *Geophysical Research Letters* **44**(8), 3779–3787.

Devin, C. (1959), 'Survey of thermal, radiation, and viscous damping of pulsating air bubbles in water', *Journal of Acoustical Society of America* **31**, 1654.

Donelan, M. A., Dobson, F. W., Smith, S. D. and Anderson, R. J. (1993), 'On the dependence of sea surface roughness on wave development', *Journal of Physical Oceanography* **23**, 2143–2149.

Drazen, D. A., Melville, W. K. and Lenain, L. (2008), 'Inertial scaling of dissipation in unsteady breaking waves', *Journal of Fluid Mechanics* **611**, 307–332.

Duncan, J. H. (1981), 'An experimental investigation of breaking waves produced by a towed hydrofoil', *Proc. R. Soc. Lond. A* **377**, 331–348.

Duncan, J. H., Philomin, V., Behres, M. and Kimmel, J. (1994), 'The formation of spilling breaking water waves', *Physics of Fluids* **6**, 2558–2560.

Duncan, J. H., Qiao, H., Philomin, V. and Wenz, A. (1999), 'Gentle spilling breakers: crest profile evolution', *Journal of Fluid Mechanics* **379**, 191–222.

Falkowski, P. G. (1997), 'Evolution of the nitrogen cycle and its influence on the biological sequestration of CO_2 in the ocean', *Nature* **387**, 272–274.

Farmer, D. M., Deane, G. B. and Vagle, S. (2001), 'The influence of bubble clouds on acoustic propagation in the surf zone', *IEEE Journal Oceanic Engineering* **26**, 113–124.

Farmer, D. M., McNeil, C. L. and Johnson, B. D. (1993), 'Evidence for the importance of bubbles in increasing airsea gas flux', *Nature* **361**, 620–623.

Farmer, D. M. and Vagle, S. (1989), 'Waveguide propagation of ambient sound in the oceansurface bubble layer', *Journal of Acoustical Society of America* **86**(5), 1897–1908.

Farmer, D. M., Vagle, S. and Booth, D. A. (1998), 'A free-flooding acoustical resonator for measurement of bubble size distributions', *Journal of Atmospheric and Oceanic Technology* **15**, 1132–1146.

Forristall, G. Z. (1978), 'On the statistical distribution of wave heights in a storm', *Journal Geophysical Research* **83**(C5), 2353–2358.

Galvin, C. J. (1968), 'Breaker type classification on three laboratory beaches', *Journal of Geophysical Research* **73**, 3651–3659.

Gargett, A. E. (1994), 'Observing turbulence with a modified acoustic doppler current profiler', *Journal of Atmospheric and Oceanic Technology* **11**(6), 1592–1610.

Gargett, A. E. (2017), 'Comment on using an adcp to estimate turbulent kinetic energy dissipation rate in sheltered coastal waters', *Journal of Atmospheric and Oceanic Technology* **34**(6), 1387–1390.

Geernaert, G. L. (1990), *Bulk parameterizations for the wind stress and heat fluxes*, Vol. 7, Springer.

Gemmrich, J. R. and Farmer, D. M. (1999), 'Observations of the scale and occurrence of breaking surface waves', *Journal of Physical Oceanography* **29**, 2595–2606.

Graham, A., Woolf, D. J. and Hall, A. J. (2004), 'Aeration due to breaking waves. part 1: bubble populations', *Journal of Physical Oceanography* **34**, 989–1007.

Green, E. J. and Carritt, D. E. (1967), 'Oxygen solubility in sea water: Thermodynamic influence of sea salt', *Science* **157**, 191–193.

Hall, M. V. (1989), 'A comprehensive model of wind-generated bubbles in the ocean and predictions of the effects on sound propagation at frequencies up to 40 kHz', *Journal of Acoustical Society of America* **86**, 1103–1117.

Hanson, J. L. and Jensen, R. E. (2004), 'Wave system diagnostics for numerical wave models', *Proc. Eighth Int. Workshop on Wave Hindcasting and Forecasting, Oahu, HI, Joint WMO/IOC Technical Commission for Oceanography and Marine Meteorology* **29**, 1–19.

Hanson, J. L. and Philips, O. M. (2001), 'Automated analysis of ocean surface directional wave spectra', *Journal of Atmospheric and Oceanic Technology* **18**, 277–293.

Hanwright, J., Zhou, J., Evans, G. M. and Galvin, K. P. (2005), 'Influence of surfactant on gas bubble stability', *Langmuir* **21**, 4912–4920.

Hashimoto, N., Nagai, T. and Asai, T. (1993), 'Wave system diagnostics for numerical wave models', *Rept. Of P.H.R.I.* **32**, 25–47.

Hasselmann, K. (1974), 'On the spectral dissipation of ocean waves due to white capping', *Boundary-Layer Meteorology* **6**, 107–127.

Hasselmann, K., Barnett, T. P., Bouws, E., Carlson, H., Cartwright, D. E., Enke, K., Ewing, J. A., Gienapp, H., Hasselmann, D. E., Kruseman, P., Meerburg, A., Mller, P., Olbers, D. J., Richter, K., Sell, W. and Walden, H. (1973), 'Measurements of wind-wave growth and swell decay during the joint north sea wave project (jonswap)', *Ergänzung zur Deutschen Hydrographischen Zeitschrift Reihe A (8)* **12**, 32–37.

Haugan, P. M. and Drange, H. (1992), 'Sequestration of CO_2 in the deep ocean by shallow injection', *Nature* **357**, 318–320.

Hoff, L., Sontum, P. C. and Hovem, J. M. (2000), 'Oscillations of polymeric microbubbles: Effect of the encapsulating shell', *The Journal of the Acoustical Society of America* **107**, 2272.

Holthuijsen, L. H. (2007), *Waves in oceanic and coastal waters*, Cambridge Univ. Press.

Jeffrey, C. D., Robinson, I. S. and Woolf, D. K. (2000), 'Tuning a physically-based model of the airsea gas transfer velocity', *Ocean Modelling* **31**, 28–35.

Jessup, A. T., Zappa, C. J., Loewen, M. R. and Hesany, V. (1997), 'Infrared remote sensing of breaking waves', *Nature* **385**, 52–55.

Johnson, B. D. and Cooke, R. (1979), 'Bubble populations and spectra in coastal waters: A photographic approach', *Journal of Geophysical Research* **84**.

Keeling, R. F. (1993), 'On the role of large bubbles in air-sea gas exchange and supersaturation in the ocean', *Journal of Marine Research* **51**, 237–271.

Kinsler, L. E., Frey, A. R., Coppens, A. B. and Sanders, J. V. (1982), *Fundamentals of Acoustics*, John Wiley.

Kleiss, J. M. and Melville, W. K. (2010), 'Observations of wave breaking kinematics in fetch-limited seas', *Journal of Physical Oceanography* **40**(12), 2575–2604.

Kleiss, J. M. and Melville, W. K. (2011), 'The analysis of sea surface imagery for whitecap kinematics', *Journal of Atmospheric and Oceanic Technology* **28**(2), 219–243.

Lamarre, E. and Melville, W. K. (1991), 'Air entrainment and dissipation in breaking waves', *Nature* **351**, 469–472.

Leifer, I., Guillemette, C. and Gerrit, D. L. (2007), 'Characteristics of bubble plumes bubble-plume bubbles and waves from wind-steepened wave breaking', *Journal of Marine Systems* **66**(1), 61–70.

Leifer, I., Leeuw, G. D. and Cohen, L. H. (2003), 'Optical measurement of bubbles: system design and application', *Journal of Atmospheric and Oceanic Technology* **20**, 1317–1332.

Leighton, T. G. (1994), *The Acoustic Bubble*, Academic Press.

Leighton, T. and Walton, A. (1959), 'An experimental study of the sound emitted from gas bubbles in a liquid', *European Journal of Physics* **8**, 98–104.

Li, S., Li, M., Gerbi, G. P. and Song, J.-B. (2013), 'Roles of breaking waves and langmuir circulation in the surface boundary layer of a coastal ocean', *Journal of Geophysical Research* **118**, 5173–5187.

Liss, P. S. and Merlivat, L. (1986), *Air-Sea Gas Exchange Rates: Introduction and Synthesis*, Springer.

Liu, X. and Duncan, J. H. (2003), 'The effects of surfactants on spilling breaking waves', *Nature* **421**, 520–523.

Liu, X. and Duncan, J. H. (2006), 'An experimental study of surfactant effects on spilling breakers', *Journal of Fluid Mechanics* **567**, 433–455.

Longuet-Higgins, M. S. (1952), 'On the statistical distributions of the heights of sea waves', *Journal of Marine Research* **11**, 245–265.

Macpherson, J. D. (1957), 'The effect of gas bubbles on sound propagation in water', *Proc. Phys. Soc. London, Sect. B* **70**, 85–92.

Marage, J. P. and Mori, Y. (2013), *Sonars and Underwater Acoustics*, John Wiley.

Mason, B. J. (2001), 'The role of seasalt particles as cloud condensation nuclei over the remote oceans', *Q. J. R. Meteorol. Soc.* **127**, 2023–2032.

McConnell, S. O. and Dahl, P. H. (1989), 'Vertical incidence backscatter and surface forward scattering loss from near-surface bubbles', *Oceans '91 Proceeding* **1**, 434–441.

McGillis, W. R., Dacey, J. W., Frew, N. M., Bock, E. J. and Nelson, R. K. (2000), 'Water-air flux of dimethylsulfide', *Journal of Geophysical Research* **105**(C1), 1187–1193.

McNeil, C. and D'Asaro, E. (2007), 'Parameterization of airsea gas exchange at extreme wind speeds', *Journal of Marine Systems* **66**, 110–121.

Medwin, H. (1974), 'Acoustic fluctuations due to microbubbles in the near-surface ocean', *Journal of Acoustical Society of America* **56**, 1100–1104.

Medwin, H. (1977*a*), 'Acoustical determinations of bubble-size spectra', *Journal of Acoustical Society of America* **62**, 1041.

Medwin, H. (1977*b*), 'Counting bubbles acoustically : a review', *Ultrasonics* pp. 7–13.

Medwin, H. (1977*c*), 'In situ acoustic measurements of microbubbles at sea', *Journal of Geophysical Research* **82**, 971–976.

Medwin, H. (2005), *Sounds in the Sea*, Cambridge Univ. Press.

Medwin, H. and Breitz, N. D. (1989), 'Ambient and transient bubble spectral densities in quiescent seas and under spilling breakers', *Journal of Geophysical Research* **94**, 12751–12759.

Medwin, H. and Clay, C. S. (1997), *Fundamentals of Acoustical Oceanography*, Elsevier Science.

Melville, W. K. (1993), 'Energy dissipation by breaking waves', *Journal of Physical Oceanography* **24**, 2041–2049.

Melville, W. K. (1996), 'The role or surface-wave breaking in air-sea interaction', *Annual Review of Fluid Mechanics* **28**, 279–321.

Miles, J. W. (1957), 'On the generation of surface waves by shear flows', *Journal of Fluid Mechanics* **3**, 185–204.

Modini, R. L., Russell, L. M., Deane, G. B. and Stokes, M. D. (2013), 'Effect of soluble surfactant on bubble persistence and bubble-produced aerosol particles', *Journal Geophysical Research* **118**, 1388–1400.

Monahan, E. C. (1971), 'Oceanic whitecaps', *Journal of Physical Oceanography* **1**, 139–144.

Monahan, E. C. (1993), 'Occurrence and evolution of acoustically relevant sub-surface bubble plumes and their associated, remotely monitorable, surface whitecaps', *Natural Physical Sources of Underwater Sound: Sea Surface Sound* **2**, 503–517.

Monahan, E. C. and Lu, M. (1990), 'Acoustically relevant bubble assemblages and their dependence on meteorological parameters', *IEEE Journal of Oceanic Engineering* **15**, 340–349.

Nayar, K. G., Sharqawy, M. H., Banchik, L. D. and Lienhard V, J. H. (2016), 'Thermophysical properties of seawater: a review and new correlations that include pressure dependence', *Desalination* **390**, 1–24.

Novarini, J. C. and Bruno, D. R. (1982), 'Effects of the subsurface bubble layer on sound propagation', *Journal of Acoustical Society of America* **72**(2), 510–514.

Nützel, B., Herwig, H., Koenigs, P. D. and Monti, J. M. (1994), 'Acoustic backscatter measurements in the north sea: 318 khz', *Journal of Acoustical Society of America* **95**(5), 2488–2494.

O'Dowd, C. D. and Smith, M. H. (1993), 'Physicochemical properties of aerosols over the northeast atlantic: Evidence for wind-speed-related submicron sea-salt aerosol production', *Journal of Geophysical Research* **98**(D1), 1137–1149.

Osborn, T., Farmer, D. M., S., V., Thorpe, S. A. and Cure, M. (1992), 'Measurements of bubble plumes and turbulence from a submarine', *Atmosphere-Ocean* **30**(3), 419–440.

Pascal, R. W. (2011), 'A spar buoy for high-frequency wave measurements and detection of wave breaking in the open ocean', *Journal of Atmospheric and Oceanic Technology* **28**, 590–605.

Phillips, O. M. (1957), 'On the generation of waves by turbulent wind', *Journal of Fluid Mechanics* **2**, 417–445.

Phillips, O. M. (1958), 'The equilibrium range in the spectrum of wind-generated waves', *Journal of Fluid Mechanics* **4**, 426–434.

Phillips, O. M. (1977), *The dynamics of the upper ocean*, Cambridge University Press.

Phillips, O. M. (1985), 'Spectral and statistical properties of the equilibrium range in wind-generated gravity waves', *Journal of Fluid Mechanics* **156**, 505–531.

Pierson, W. J. and Moskowitz, L. (1964), 'A proposed spectral form for fully developed wind seas based on the similarity theory of s. a. kitaigorodskii', *Journal of Geophysical Research* **69**, 5181–5190.

Plant, W. J. (1982), 'A relationship between wind stress and wave slope', *Journal of Geophysical Research* **87**, 1961–1967.

Portilla, J., Ocampo-Torres, F. L. and Monabaliu, J. (2008), 'Spectral partitioning and identification of wind sea and swell', *Journal of Atmospheric and Oceanic Technology* **26**, 107–122.

Powell, M. D., Vickery, P. J. and Reinhold, T. A. (2003), 'Reduced drag coefficient for high wind speeds in tropical cyclones', *Nature* **422**, 279–283.

Qiao, H. and Duncan, J. H. (2001), 'Gentle spilling breakers: crest flow-field evolution', *Journal of Fluid Mechanics* **439**, 57–85.

Rice, S. O. (1954), *Mathematical analysis of random noise*, Dover Publications Inc.

Romero, L., Melville, W. K. and Kleiss, J. M. (2012), 'Spectral energy dissipation due to surface wave breaking', *Journal of Physical Oceanography* **42**(9), 1421–1444.

Ross, D. B. and Cardone, V. (1974), 'Observations of oceanic whitecaps and their relation to remote measurements of surface winds speed', *Journal of Geophysical Research* **79**(3), 444–452.

Scandella, B. P., Pillsbury, L., Weber, T., Ruppel, C., Hemond, H. F. and Juanes, R. (2016), 'Ephemerality of discrete methane vents in lake sediments', *Geophysical Research Letters* **43**, 4374–4381.

Scanlon, B. and Ward, B. (2013), 'Oceanic wave breaking coverage separation techniques for active and maturing whitecaps', *Methods in Oceanography* **8**, 1–12.

Simmonds, J. and MacLennan, D. N. (2008), *Fisheries Acoustics: Theory and Practice*, John Wiley.

Snyder, R. L., Dobson, F. W., Elliott, J. A. and Long, R. B. (1981), 'Array measurement of atmospheric pressure fluctuations above surface gravity waves', *Journal of Fluid Mechanics* **102**, 1–59.

Soloviev, A. and Lukas, R. (2013), *The near-surface layer of the ocean: structure, dynamics and applications*, Springer.

Stokes, M. D. and Deane, G. B. (1999), 'A new optical instrument for the study of bubbles at high void fractions within breaking waves', *IEEE Journal of Oceanic Engineering* **24**, 300–311.

Sugihara, Y., Tsumori, H., Ohga, T., Yoshioka, H. and Serizawa, S. (2007), 'Variation of white-cap coverage with wave-field conditions', *Journal of Marine Systems* **66**, 47–60.

Takahashi, T., Sutherland, S. C., Sweeney, C., Poisson, A., Metzl, N., Tilbrook, B., Bates, N., Wanninkhof, R., A., F. R., Sabine, C., Olafsson, J. and Nojiri, Y. (2002), 'Global seaair CO_2 flux based on climatological surface ocean pCO_2, and seasonal biological and temperature effects', *Deep Sea Research Part II: Topical Studies in Oceanography* **49**(9), 1601–1622.

Terray, E. A., Donelan, M. A., Agrawal, Y. C., Drennan, W. M., Kahma, K. K., Williams III, A. J., Hwang, P. A. and Kitaigorodskii, S. A. (1995), 'Estimates of kinetic energy dissipation under breaking waves', *Journal of Physical Oceanography* **26**, 792–807.

Terril, E. J., Melville, W. K. and Stramski, D. (2001), 'Bubble entrainment by breaking waves and their influence on optical scattering in the upper ocean', *Journal of Geophysical Research* **106**, 16,815–16,823.

Thornton, E. B. (1977), 'Rederivation of the saturation range in the frequency spectrum of wind-generated gravity waves', *Journal of Physical Oceanography* **7**, 137–140.

Thorpe, S. A. (1982), 'On the clouds of bubbles formed by breaking wind-waves in deep water, and their role in air-sea gas transfer', *Philos. Trans. R. Soc. London A, Math. Phys. Sci.* **304**, 155–210.

Thorpe, S. A. (1986), 'Measurements with an automatically recording inverted echo sounder; aries and the bubble clouds', *Journal of Physical Oceanography* **16**, 1462–1478.

Thorpe, S. A. (1992), 'Bubble clouds and the dynamics of the upper ocean', *Q. J. R. Meteorol. Soc.* **118**, 1–22.

Thorpe, S. A., Bowyer, P. and Woolf, D. K. (1992), 'Some factors affecting the size distributions of oceanic bubbles', *Journal of Physical Oceanography* **22**, 382–389.

Thorpe, S. A. and Hall, A. J. (1983), 'The characteristics of breaking waves, bubble clouds, and near-surface currents observed using side-scan sonar', *Continental Shelf Research* **1**, 353–384.

Thorpe, S. A. and Humphries, P. N. (1980), 'Bubbles and breaking waves', *Nature* **283**, 463–465.

Toba, Y. (1972), 'Local balance in the air-sea boundary processes', *Journal of Oceanography* **28**(3), 109–120.

Toba, Y. and Chaen, M. (1973), 'Quantitative expression of the breaking of wind waves on the sea surface', *Rec. Oceanogr. Works Jpn.* **12**, 2–11.

Trevorrow, M. V. (2003), 'Measurements of nearsurface bubble plumes in the open ocean', *Journal of Acoustical Society of America* **114**, 2672–2684.

Trevorrow, M. V., Vagle, S. and Farmer, D. M. (1994), 'Acoustical measurements of microbubbles within ship wakes', *Journal of Acoustical Society of America* **95**(4), 1922–1930.

Vagle, S. and Farmer, D. M. (1992), 'The measurement of bubble-size distributions by acoustical backscatter', *Journal of Atmospheric and Oceanic Technology* **9**, 630–644.

Vagle, S. and Farmer, D. M. (1998), 'A comparison of four methods for bubble size and void fraction measurements', *IEEE Journal of Oceanic Engineering* **23**(3), 211–222.

Vagle, S., McNeil, C. and Steiner, N. (2010), 'Upper ocean bubble measurements from the ne pacific and estimates of their role in airsea gas transfer of the weakly soluble gases nitrogen and oxygen', *Journal of Geophysical Research* **115**, 1–16.

Wang, D. W. and Hwang, P. A. (2001), 'An operational method for separating wind sea and swell from ocean wave spectra', *Journal of Atmospheric and Oceanic Technology* **18**, 2052–2062.

Wang, D. W., Wijesekera, H. W., Teague, W. J., Rogers, W. E. and Jarosz, E. (2011), 'Bubble cloud depth under a hurricane', *Geophysical Research Letters* **38**, n/a–n/a.

Wanninkhof, R. (1992), 'Relationship between gas exchange and wind speed over the ocean', *Journal of Geophysical Research* **97**, 7373–7381.

Wanninkhof, R., Asher, W. E., Ho, D. T., Sweeney, C. and McGillis, W. R. (2008), 'Advances in quantifying air-sea gas exchange in environmental forcing', *Annual Review of Marine Science* **1**, 213–244.

Wanninkhof, R., Asher, W. and Monahan, E. C. (1995), *The influence of bubbles on air-water gas exchange: results from gas transfer experiments during WABEX-93*, Third International Symposium on Air-Water Gas Transfer.

Wanninkhof, R. and Jessup, A. T. (1999), 'A cubic relationship between air-sea CO_2 exchange and wind speed', *Geophysical Research Letters* **26**, 1889–1892.

Wanninkhof, R., Ledwell, J. R. and Broecker, W. S. (1985), 'Gas exchange-wind speed relation measured with sulfur hexafluoride on a lake', *Science* **227**, 1224–1226.

Weiss, R. F. (1970), 'The solubility of nitrogen, oxygen and argon in water and seawater', *Deep Sea Res. and Oceanogr. Abstr.* **17**, 721–735.

Wildt, R. (1946), 'Acoustic theory of bubbles'.

Wilson, P. S. and Roy, R. A. (2008), 'An audible demonstration of the speed of sound in bubbly liquids', *American Journal of Physics* **76**, 975.

Wood, A. B. (1930), *A Textbook of Sound*, MacMillan.

Woolf, D. K. (1993), 'Bubbles and the airsea transfer velocity of gases', *Atmosphere-Ocean* **31**(4), 517–540.

Woolf, D. K. (1997), *Bubbles and their role in gas exchange, in The Sea Surface and Global Change*, Cambridge Univ. Press.

Woolf, D. K. (2005), 'Parametrization of gas transfer velocities and sea-state-dependent wave breaking', *Tellus B: Chemical and Physical Meteorology* **57**(2), 87–94.

Woolf, D. K. and Thorpe, S. A. (1991), 'Bubbles and the air-sea exchange of gases in near-saturation conditions', *Journal of Marine Research* **49**, 435–466.

Yelland, M. J. and Taylor, P. K. (1996), 'Wind stress measurements from the open ocean', *Journal of Physical Oceanography* **26**, 541–558.

Zappa, C. J., Banner, M. L., Schultz, H., Gemmrich, J. R., Morison, R. P., LeBel, D. A. and Dickey, T. (2012), 'An overview of sea state conditions and air-sea fluxes during RaDyO', *Journal of Geophysical Research* **117**(C7).

Zedel, L. and Farmer, D. (1991), 'Organized structures in subsurface bubble clouds: Langmuir circulation in the open ocean', *Journal of Geophysical Research* **96**, 8889–8900.

Zhao, D. and Toba, Y. (2001), 'Dependence of whitecap coverage on wind and wind-wave properties', *Journal of Oceanography* **57**, 603–616.